Takagi-Sugeno Methods with Application to Wind Power Systems

Von der Fakultät Wirtschaftswissenschaften
der Leuphana Universität Lüneburg zur Erlangung des Grades

Doktor der Ingenieurwissenschaften
Dr.–Ing.

genehmigte Dissertation von Florian Pöschke

geboren am 15. Januar 1988 in Beeskow.

Die einzelnen Beiträge des kumulativen Dissertationsvorhabens sind wie folgt veröffentlicht:

Florian Pöschke, Eckhard Gauterin, Horst Schulte: LMI region-based non-linear disturbance observer with application to robust wind turbine control. In: O Boubaker, Q Zhu, M S Mahmoud, J Ragot, H R Karimi, J Dávila, eds. *New Trends in Observer-based Control*, p. 35-75. Academic Press. 2019. DOI: 10.1016/B978-0-12-817034-2.00015-0

Florian Pöschke, Eckhard Gauterin, Martin Kühn, Jens Fortmann, Horst Schulte: Load mitigation and power tracking capability for wind turbines using LMI-based control design. *Wind Energy*, Vol. 23, No. 9, p. 1792-1809. 2020. DOI: 10.1002/we.2516

Florian Pöschke, Vlaho Petrović, Frederik Berger, Lars Neuhaus, Michael Hölling, Martin Kühn, Horst Schulte: Model-based wind turbine control design with power tracking capability: a wind-tunnel validation. *Control Engineering Practice*, Vol. 120, p. 105014. 2022.
DOI: 10.1016/j.conengprac.2021.105014

Florian Pöschke, Horst Schulte: Model-based nonlinear filter design for tower load reduction of wind power plants with active power control capability. *2020 IEEE International Conference on Fuzzy Systems (FUZZ-IEEE)*, p. 1-6. Glasgow, Scotland, United Kingdom. 2020.
DOI: 10.1109/FUZZ48607.2020.9177658

Veröffentlichungsjahr: 2022

Abstract

The transition of our energy system towards a generation by renewables, and the corresponding developments of wind power technology enlarge the requirements that must be met by a wind turbine control scheme. Within this thesis, the role of modern, model-based control approaches in providing an answer to present and future challenges faced by wind energy conversion systems is discussed. While many different control loops shape the power system in general, and the energy conversion process from the wind to the electrical grid specifically, this work addresses the problem of power output regulation of an individual turbine. To this end, the considered control task focuses on the operation of the turbine on the nonlinear power conversion curve, which is dictated by the aerodynamic interaction of the wind turbine structure and the current inflow. To enable a power tracking functionality, and thereby account for requirements of the electrical grid instead of operating the turbine at maximum efficiency constantly, an extended operational range is explicitly considered in the implemented control scheme. This allows for an adjustment of the produced power depending on the current state of the electrical grid and is one component in constructing a reliable and stable power system based on renewable generation.

To account for the nonlinear dynamics involved, a linear matrix inequalities approach to control based on Takagi-Sugeno modeling is investigated. This structure is capable of integrating several degrees of freedom into an automated control design, where, additionally to stability, performance constraints are integrated into the design to account for the sensitive dynamical behavior of turbines in operation and the loading experienced by the turbine components. For this purpose, a disturbance observer is designed that provides an estimate of the current effective wind speed from the evolution of the measurements. This information is used to adjust the control scheme to the varying operating points and dynamics. Using this controller, a detailed simulation study is performed that illustrates the experienced loading of the turbine structure due to a dynamic variation of the power output. It is found that a dedicated controller allows wind turbines to provide such functionality.

Additionally to the conducted simulations, the control scheme is validated experimentally. For this purpose, a fully controllable wind turbine is operated in a wind tunnel setup that is capable of generating reproducible wind conditions, including turbulence, in a wide operational range. This allows for an assessment of the power tracking performance enforced by the controller and analysis of the wind speed estimation error with the uncertainties present in the physical application. The controller showed to operate the turbine smoothly in all considered operating scenarios, while the implementation in the real-time environment revealed no limitations in the application of the approach within the experiments. Hence, the high flexibility in adjusting the turbine operating trajectories and structural design characteristics within the model-based design allows for efficient controller synthesis for wind turbines with increasing functionality and complexity.

Danksagung

Contents

3   Load mitigation and power tracking capability for wind turbines using LMI-based control design   67

List of Figures

List of Tables

1 | Synopsis I

1.1 Introduction and context

The global annual primary energy consumption and simultaneously the carbon dioxide emissions rose by approx. 70% within three decades from 1987 [1, 2, 3]. Industrialized countries like Germany play a major role in this process with carbon dioxide emissions per capita twice as high compared to the global average in 2018 [1]. The annual growth rate of global primary energy consumption averages 1.5% over the last decade [1], indicating the exponential slope of our thirst for energy. Our planet is a complex dynamical system that is excited by the disturbances in form of our emissions and global warming of 0.87±0.12°C compared to the preindustrial level is already observable [4]. The possibly fatal short- and long-term consequences reveal the vulnerability of ecosystems and human systems [5]. In control theory, a system that exhibits an exponential growth is considered unstable, where the main idea underlying all control approaches is to break the exponential growth and influence the controllable inputs to achieve stability and thus enforce convergence to the desired state. One vital component for mitigating the consequences for us and our habitat lies in the de-carbonization of the energy sector.

In 2017, electricity generation was the second-largest emitter after transportation and accounted for 28% of greenhouse gas emissions in the US [6]. From an energy generation perspective, the inter-governmental panel on climate change identifies 'strong upscaling of renewables [...]' as one key characteristic for a successful limitation of global warming to 1.5 °C [7]. Guided by this, a transformation of the existing energy system towards electricity provided by renewables is a major challenge addressed across the globe and results in an average annual growth rate for generation by renewables of 16.4% from 2007 to 2017 [1]. Globally, the proportion of electricity produced by renewables rose from 3% in 2008 to 9.3% in 2018, of which the share in Europe was 18.7% in 2018 [1]. In the same year, renewables contributed 40.2% of the generated electricity in Germany and with 20.4% wind power covered half of it [8]. Wind energy is considered as the backbone of the future energy system and is predicted to provide one-quarter to one-third of the electricity demand globally by 2050 [9].

Wind turbines are nonlinear dynamical systems driven by stochastic inputs and interact in a network formed by the electrical grid. Interdisciplinary research is a key driver for enhancing wind energy to satisfy the increasing requirements of current and future energy systems [9]. This includes, but is not limited to, disciplines like engineering, natural and social sciences, information technology, and mathematics. In the effort to reduce the levelized cost of energy, the ongoing research led to the production of turbines with a power capacity in the range of 10 MW-20 MW [10], making wind turbines the largest dynamical, rotating machines in the world [9]. For example, the rotor of a recently erected

GE 12 MW turbine prototype covers an area with a diameter of 220 m, while capable of supplying sixteen thousand European homes and avoiding an approx. amount of 42 million tonnes of carbon dioxide emissions [11]. These developments determine the cost of generating electricity from the wind resource. In 2018, it is found that utility-scale photovoltaic and onshore wind turbines are, on average, the least expensive technology for the production of electricity with an anticipated further reduction of costs well below all fossil power plants by 2035 [12]. Thus, wind energy is not only an ecologically favorable option for energy production but also shows to be economically superior to fossil-based electricity generation.

1.2   A control perspective on wind energy

The energy conversion process from the wind resource to the electrical grid inherits a variety of simultaneously active control loops at different levels and time scales of the wind-based generation system. This ranges from a wind farm controller respecting the electrical and/or aerodynamic interaction of several closely located turbines, down to the power electronics level, where the transfer of the electrical energy to the grid is supervised by a control scheme [13]. The available power of the wind resource is determined by turbulent, atmospheric flows [14] with a nonlinear dependency to the current wind speed $P_{\mathrm{wind}} \propto v^3$. Thus, for modern variable speed wind turbines appropriate state operating trajectories that determine the energy conversion process depending on the varying wind speed need to be enforced by the controller. This control loop has different scopes depending on the current operating region, while the applied control scheme must cope with a highly nonlinear aeroelastic process and is the main subject of this work.

Traditionally, two main control loops are established to regulate the nonlinear power control problem subject to the varying wind. The first comprises a strategy, where the generator torque of the turbine is adjusted proportionally to the square of the current generator speed, i.e., $T = K_{\mathrm{opt}}\, \omega^2$, and aims to track the optimal tip speed ratio and operate the turbine with maximum efficiency [13, 15]. The gain K_{opt} therein is derived from the relation of the optimal power coefficient to the tip speed ratio, which depends on the inflow and the rotational speed. This strategy is used until the rated power of the turbine is reached, where a second control loop initializes the actuation of the blade pitch positions from this operating point to alter the efficiency of the aerodynamic conversion, and thus limits the power output to the turbine's rated capacity [13, 15]. While the strategy in partial load region involving the generator torque can be applied rather straightforward, especially the interconnection of the control loops and the gain-scheduled PI pitch controller for limitation of power output involves a possible arduous tuning of gains to account for operation on the nonlinear power coefficient surface sensitive to changes in the pitch angle [16]. While the operating trajectory defines the overall

energy capture, the turbine's lifetime is determined by the occurring loads faced by the mechanical and electrical components due to the rotation and operation in a stochastic three-dimensional wind field.

By an appropriately fast reaction to the varying wind speed, the control interference is vital for remaining below the admissible ultimate loading that would destroy the components. The control action, however, also excites the structural dynamics of the turbine [15], e.g., through the coupling of changes in the generator torque to the drivetrain oscillation or the sensitivity of the tower fore-aft motion to blade pitching. When operating in a stochastic wind field, the interaction of the closed-loop turbine with the varying inflow is, additionally to the inevitable gravitational loads from rotation, a major cause for the fatigue of the structures. Thus, it ultimately determines the turbine's lifetime and in consequence cost of energy. Therefore, Bossanyi states load reduction as an explicit objective of wind turbine control design and proposes several independently designed control loops to mitigate the experienced structural loading in [15], which can be considered as the standard industrial approach.

The scaling laws used to increase the turbine dimensions with the aim of reducing the levelized cost of energy necessitate the use of innovative materials, production techniques and design concepts [9], including flexible blades with bend twist coupling [10] or so-called soft-soft tower configurations that shift the eigenfrequency into an operating region located within the rotational speed range [17]. Therefore, enforcing desired closed-loop dynamics is of vital importance, where the loading faced by the turbine is determined by the interaction of the controller with the varying wind speed in operation. Innovative sensing devices like LIDAR (light detection and ranging) used for a measurement of the upcoming inflow, and actuators like active flaps on the blades to induce local aerodynamic effects, are introduced into the wind energy system [10]. As a consequence, the increasing number of coupled subsystems, dynamically interacting in the operation of the turbine, and a greater number of sensors connected to an actuator elevate the complexity of the multi-input, multi-output control problem. Additional to the academic concerns involving missing stability considerations when closing individual feedback loops using PI controllers without accounting for relevant couplings, in a competitive economic environment, manufacturers are forced to reduce the development cycles, and thus increasingly complex controller tuning to yield a desired dynamical response is not a favorable option.

In the light of this increasing control complexity, model-based approaches have shifted into focus for the control design of wind turbines. Their inherent ability to include relevant dynamical properties into the control design stage makes them attractive for a dedicated definition of desired closed-loop properties and therefore implicitly, or even explicitly, account for the associated loading. Further, nonlinear approaches can incorporate the variation of dynamics depending on the current inflow to account for changes in the operating point. In that way, essential characteristics for the operation of a wind turbine can be portrayed when designing the necessary control loops, and promising results

from a loading perspective were reported, see e.g., [18, 19, 20, 21, 22, 17].

Additionally, with the higher share of renewables in the electrical grid, the requirements for wind energy systems increase. Reliable operation of the electrical grid, which is a large-scale dynamical system active in time scales from microseconds to hours, necessitates various stabilizing mechanisms that are traditionally accomplished by large power plants supplying energy through synchronous generators with power ratings of 100 MW-1300 MW [23]. To replace those power plants with a larger number of decentralized generators based on renewable sources, a contribution of wind power systems to the stabilization of the electrical grid is inevitable.

Three main stability measures determine a reliable operation of the electrical grid: (i) rotor angle stability, (ii) frequency stability, and (iii) voltage stability [23]. (i) addresses the (possibly virtual) inertial response of generating units and determines the synchronism of coupled generators in case of disturbances such as short-circuits. Within this process that is governed by the impedance characteristics of the electrical grid connection and the dynamic response of the generating unit, a variation of active power to an altered steady-state operating point and in form of damping power occurs [23]. (ii) frequency stability is determined by the inherent characteristic of a synchronous generator that traditionally supplies the electrical grid, i.e., automatically emitting or absorbing energy stored in the rotation and thereby conditioning the frequency depending on a load imbalance. As a result, an imbalance in load and generation causes the frequency to deviate from its nominal value (possibly after an event causing the phenomena captured by (i)). Thus, the frequency can be considered as a carrier of information on the current state of the electric grid. Even though the large rotating masses of wind turbines exhibit inertial time constants comparable to that of conventional power plants [24], the generator of a wind energy system is decoupled from the electrical grid by its power electronics to operate at variable rotational speed. As a result, a grid stabilizing functionality in these cases is determined by the applied control schemes [25], and necessarily involves a variation of the turbines active power setpoint. (iii) is mainly associated with reactive power injection, which due to the converter characteristics may also involve active power variations of the produced turbine power [26].

The ability of a power system to retain its nominal frequency depends on the generation characteristic and effectively defines the slope at which the sum of generating units in the grid reacts to a frequency deviation with an adjustment of active power [23]. This measure is inevitably connected to decentralized control loops within the generating units usually termed automatic generation control for traditional power plants [23]. Consequently, to enhance the generation characteristic of the power system while replacing conventional power plants with renewables, wind energy systems must provide a variable active power output depending on the state of the electrical grid. This opens a new perspective on the operation of wind turbines, which were historically designed to maximize its energy yield by operating on the optimal power trajectory depending on the current inflow only.

Additionally to the power system stability considerations, a variable power generation provides the basis for optimized operation of wind farms in meeting the power output demands. A dedicated power tracking of the individual turbines within a farm can mitigate the experienced loading [27] and level them among the participating turbines [28] by solving the non-unique distribution of power commands among the turbines in a wind farm. As discussed in [29], a power reference tracking is also applicable for preventing wind turbine states from exceeding their maximum values by designing an envelope protection control strategy. Further, in [30] it is discussed that a dynamic control of the effective power coefficient yields an optimized wake interaction, capable of improving the overall efficiency of the wind farm at cost of a continuous actuation.

Effectively, these requirements transfer to an enlarged operating range on the surface that determines the aerodynamic conversion process and nonlinear operating behavior of the individual turbine. As a result, a wind turbine controller must be capable of adjusting the power output not only depending on the current wind speed but also tracking externally conditioned power demands depending on e.g., the state of the electrical grid, which is termed shifting from "wind-driven" to "grid-driven" operation in [31]. This, however, induces additional excitation from actuation into the mechanical structures of the turbine, underlining the need for a control design involving load optimized behavior defined as desired closed-loop dynamical properties. As the operating range coped by the turbine greatly increases, controller tuning of individual gains to yield a desired operational behavior is also increasing in complexity.

1.3 Methodical approach: Takagi-Sugeno systems and LMI-based control design

The applied control approach needs to take into account the varying dynamics in a large operating range while ensuring a narrowly defined closed-loop response to meet the loading criteria. An appropriate adjustment of the feedback gains has benefits from a loading perspective [32], and thus ensuring the robustness of the controller by fully integrating the nonlinearity in e.g., a $\mathcal{H}_2$ attenuation framework is not a favorable option [33]. Therefore, the control design needs to dedicatedly account for the dominating system nonlinearities from modeling to the controller synthesis. Throughout my studies, I found that so-called *Takagi-Sugeno systems* (TS) provide a useful approach for the discussed requirements.

Its simple yet effective idea based on a combination of linear submodels to describe a nonlinear function originally emerged in the context of fuzzy systems [34]. This approach paved the way for a wide variety of tools including optimal control, robust control, or inclusion of input/output constraints [35].

These design methods can be usually derived as straightforward extensions of their linear counterparts involving Lyapunov functions. A key characteristic exploited in those approaches is given by the *convexity* of the modeling framework, which allows for controller and observer design using *linear matrix inequalities* (LMIs). Therein, the overall nonlinear design problem is enveloped into an interconnected discrete set of constraints. A variety of standard problems in systems and control theory can be cast into convex or quasi-convex LMI constraints that can be solved numerically efficient [36].

The blending of submodels in the TS framework depends on the states of the premise variable z, which serves as an indicator of the current operating condition. The blending is conducted by the membership function $h_i(z)$ that are designed to fulfill the convexity conditions within the considered operating range. A basic state-space representation with states $x \in \mathrm{R}^n$, inputs $u \in \mathrm{R}^m$ and outputs $y \in \mathrm{R}^p$ of a TS model is given by

$$\dot{x} = \sum_{i=1}^{N} h_i(z)\big(A_i x + B_i u\big) \quad , \quad y = \sum_{i=1}^{N} h_i(z) C_i x \quad . \tag{1.1}$$

Therein, the linear submodel dynamics are described by the state A_i, input B_i, and output matrix C_i blended by the membership functions $h_i(z)$ to portray an overall nonlinear behavior of the modeled system. The premise variables z may consist of states, inputs, disturbances or external variables. The measurability of the premise variables determines if the separation principle of control and observer design applies [35]. While the following introduction to TS systems assumes measurable premise variables, a discussion on the joint control and observer design in case of unmeasurable premise variables is found in chapter 4.

The definition of a TS description and appropriate control design models can be derived by two general approaches in case of a given nonlinear model of the system dynamics. The first is usually referred to as *sector nonlinearity approach* (SNL) [37] and builds on the definition of membership functions by enveloping the occurring nonlinearities of a designable state-space realization into the membership functions. The main idea of the SNL can be illustrated by considering the following equation describing a function $f(x)$ within an operating range that satisfies the upper bound $\bar{f} \geq f(x)$ and lower bound $\underline{f} \leq f(x)$

$$\begin{aligned}
f(x) &= \frac{\bar{f} - \underline{f}}{\bar{f} - \underline{f}} f(x) = \frac{(\bar{f} - \underline{f})f(x) + (\bar{f}\underline{f} - \bar{f}\underline{f})}{\bar{f} - \underline{f}} \\
&= \underbrace{\frac{\bar{f} - f(x)}{\bar{f} - \underline{f}}}_{w^1(f(x))} \underline{f} + \underbrace{\frac{f(x) - \underline{f}}{\bar{f} - \underline{f}}}_{w^2(f(x))} \bar{f} = w^1(f(x))\underline{f} + w^2(f(x))\bar{f} \quad .
\end{aligned} \tag{1.2}$$

In this description, the function $f(x)$ is represented as a weighted combination of its operational

bounds $\bar{f}$, $\underline{f}$. The derived weighting functions $w^1(f(x))$, $w^2(f(x))$ satisfy the convexity condition

$$0 \leq w^l(f(x)) \leq 1 \quad \text{for} \quad l = 1, 2 \text{ and} \quad w^1(f(x)) + w^2(f(x)) = 1 \tag{1.3}$$

for any trajectories in the state-space spanned by x that obey $\underline{f} \leq f(x) \leq \bar{f}$. This procedure is repeated for every nonlinear relation $f(x)$ occurring in the system description and determines the number of premise variables nz with $z \in \mathrm{R}^{nz}$. As a result, for each premise variable z_j in $z = [z_1, ..., z_j, ... z_{nz}]$, a pair of weighting functions $w_j^l(z_j)$ is obtained.

Using the SNL, a convex description results, in which, except for the vertices of the operational range, all submodels are active at the same time characterizing the dynamics. While this approach yields an *exact* description of the underlying nonlinear dynamics within a defined operating space, this interconnection has consequences for the design complexity and conservatism in terms of the number of obtained submodels and their interconnection within the posing of the LMIs. Additionally, the handling of the nonlinearities in the sector nonlinearity approach can cause structural properties like controllability or observability to be violated, especially for the wind turbine application as discussed in [38, 39].

Therefore, a second approach is used for the wind turbine application in this work, which is based on *Taylor linearization* (Lin) at several operating points along the considered range to form the TS model description [40]. The linearization procedure builds on an approximation of the Taylor series for $f(x)$, where the function value $f(x_{0i})$ in the considered operating point x_{0i} is reflected along with its first partial derivative

$$f(x) \approx f(x_{0i}) + \frac{\partial f(x)}{\partial x}\big|_{x_{0i}}(x - x_{0i}) \quad . \tag{1.4}$$

This yields an approximation of the possibly nonlinear function $f(x)$ within a limited region around the considered operating point x_{0i}. Usually, linearization is conducted in stationary operating points, i.e., $f(x_{0i}) = 0$ holds. The premise variables $z \in \mathrm{R}^{nz}$ of the TS model are then defined by the states that are contained in the partial derivative $\frac{\partial f(x)}{\partial x} = A(x)$. For each operating point, $A_i = \frac{\partial f(x)}{\partial x}\big|_{x_{0i}} = A(x_{0i})$ holds.

For each of the premise variables z_j, the linearization points z_j^{0l} that form the foundation of the TS description are chosen by the control engineer. Convex weighting functions $w_{l,j}(z_j)$ fulfilling (1.3) are constructed for each premise variable z_j. While the weighting functions may have different shapes including (possibly screwed) trapezoidal or gaussian distribution forms, within this work, triangular

weighting functions are used that can be formalized as follows (and are visualized in chapter 4)

$$w^l j(z_j) = \begin{cases} \frac{z_j - z_j^{0(l-1)}}{z_j^{0l} - z_j^{0(l-1)}} & \text{if } z_j^{0(l-1)} < z_j \le z_j^{0l} \\ 1 - \frac{z_j - z_j^{0l}}{z_j^{0(l+1)} - z_j^{0l}} & \text{if } z_j^{0l} < z_j \le z_j^{0(l+1)} \\ 0 & \text{else} \end{cases} \quad . \tag{1.5}$$

In both construction ways, i.e., using SNL or Lin, for each premise variable z_j a number of $l_{j,\max}$ weighting functions $w_{l,j}$ is obtained. In case of the SNL $l_{j,\max} = 2$, while $l_{j,\max}$ for the Lin procedure depends on the choice of linearization points. To obtain the membership functions $h_i(z)$ depending on the premise variables z used in the TS state-space description (1.1), the sum of each weighting function $\sum_{l=1}^{l_{j,\max}} w_j^l(z_j) = 1$ is multiplied, where the membership functions h_i are formed by the unique products of several weighting functions. This can be described as

$$\sum_{i=1}^{N} h_i(z) = \prod_{j=1}^{nz} \sum_{l=1}^{l_{j,\max}} w_{l,j}(z_j) \quad , \tag{1.6}$$

and yields a description where the membership functions h_i also fulfill the convexity condition as formulated for the weighting functions in (1.3).

When applying the Lin approach to derive the TS model (and opposed to the SNL), only a limited number of simultaneously active submodels contribute to portraying the dynamics for a certain operating point defined by the premise variable z. This affects the design conservativeness and flexibility of the LMI-based approach significantly.

In case of a non-autonomous system $f(x, u)$, for both, SNL and Lin, an equivalent procedure as discussed before can be applied to treat the inputs of the system to obtain the input matrix B_i in (1.1) when deriving the TS model [35, 41]. To enforce a stable closed-loop behavior using the input u, state feedback can be assigned that follows the structure of the TS description by blending N gains K_k corresponding to the linear submodels (but also interacting with at least the neighboring submodels in operation). Using the membership functions of the TS model in (1.1), a basic state feedback control law is given as

$$u = -\sum_{k=1}^{N} h_k(z) K_k x \quad . \tag{1.7}$$

To derive the feedback gains K_k, stability measures in the sense of Lyapunov can be used. A well studied approach for deriving a set of stability constraints uses a quadratic Lyapunov candidate function

of the closed-loop dynamics to obtain a set of stability constraints. When introducing (1.7) to (1.1),

$$\dot{x} = \sum_{i=1}^{N} h_i(z) \sum_{k=1}^{N} h_k(z)\big((A_i - B_i K_k)x\big) \tag{1.8}$$

is obtained. Then, a quadratic Lyapunov candidate function $V(x) = x^{\mathrm{T}} P x$ with the matrix variable $P = P^{\mathrm{T}} \succ 0$ is assigned to the closed-loop dynamics. The time derivative of the Lyapunov candidate function using (1.8) is then given as

$$\dot{V}(x) = \dot{x}^{\mathrm{T}} P x + x^{\mathrm{T}} P \dot{x} = \sum_{i=1}^{N} h_i(z) \sum_{k=1}^{N} h_k(z)\big(x^{\mathrm{T}}(A_i^{\mathrm{T}} P + P A_i - K_k^{\mathrm{T}} B_i^{\mathrm{T}} P - P B_i K_k)x\big) \quad . \tag{1.9}$$

Consequently, the quadratic description above fulfills the Lyapunov stability requirement on the negative definiteness of the time derivative $\dot{V}(x) < 0$, if the following bilinear matrix inequalities for the design variables P and K_k hold

$$A_i^{\mathrm{T}} P + P A_i - K_k^{\mathrm{T}} B_i^{\mathrm{T}} P - P B_i K_k \prec 0 \quad . \tag{1.10}$$

As bilinear matrix inequalities are computationally much more difficult to handle [42], the condition is recast into an LMI. To this end, the auxiliary variable $M_k = K_k P^{-1}$ is defined along with $X = P^{-1}$, and substitution yields a basic set of LMI stability constraints as

$$X A_i^{\mathrm{T}} + A_i X - M_k^{\mathrm{T}} B_i^{\mathrm{T}} - B_i M_k \prec 0 \quad . \tag{1.11}$$

One of various LMI solvers can be used to obtain a solution for X and the auxiliary variables $M_k = K_k X$, which defines the necessary feedback gains K_k of (1.7). The combination for i, k in (1.11) and thus number of LMIs is determined by the number of linear submodels N and the construction of the membership functions h_i by the SNL or Lin. It can be seen that all posed LMIs are interconnected by the matrix $X = P^{-1}$ that characterizes the Lyapunov candidate function. The main idea of the proof of stability is based on the inclusion of the convex model description into a positive definite, continuously decreasing function along the trajectories of x, where P conditions the shared energy function that fulfills the requirements in the sense of Lyapunov stability [43]. While the system dynamics are weighted by the membership functions in (1.8), the LMIs constrain all possible combinations of simultaneously active submodels as if fully activated at all times without a weighting but exploiting the convex property of the system description. While this approach allows to provide stabiltiy constraints for nonlinear systems, it is evident that information about the system dynamics is externalized to the membership functions, and thus conservatism is introduced into the stability constraints. A possible way to mitigate this is the construction of piecewise or fuzzy Lyapunov functions

[44].

While the constraints in (1.11) provide basic stability guarantees, the formulation of LMIs can be widely enhanced to include performance measures like disturbance attenuation and region constraints to enforce a desired closed-loop response. To illustrate this, consider introducing a restriction on the time derivative of the Lyapunov candidate function in form of $\dot{V}(x) < -2\alpha V(x)$. Following the previously described approach then yields

$$XA_i^{\mathrm{T}} + A_i X - M_k^{\mathrm{T}} B_i^{\mathrm{T}} - B_i M_k + 2\alpha X \prec 0 \quad , \tag{1.12}$$

and thus influences the obtained feedback gains K_k that are used for the system feedback. Therein, $\alpha > 0$ determines the minimum decay rate of the closed-loop system dynamics. Extending basic LMI stability conditions with additional performance constraints allows for a dedicated design framework, where engineering knowledge in terms of decay rates or damping ratios can be directly introduced into the synthesis of the controller gains before evaluating their performance based on simulation or measurement studies. Due to the convex TS structure, the approach is capable of integrating a wide range of operating points and thus varying dynamics at once, and therefore controller tuning at several locations within the operational range to obtain an appropriate control performance is avoided.

As the TS description (1.1) relies on a basic state-space representation, the discussed implications of the modeling and control synthesis apply to the dual problem of observer design analogously for the reconstruction of unmeasurable but observable states. For this purpose, an observer in the TS framework is given as

$$\dot{\hat{x}} = \sum_{l=1}^{N} h_l(z)\big(A_l\hat{x} + B_l u + L_l(y - \hat{y})\big) \quad , \quad \hat{y} = \sum_{i=1}^{N} h_l(z)C_l\hat{x} \quad . \tag{1.13}$$

The model-based observer design aims for a stabilization of the error dynamics $\dot{e} = \dot{x} - \dot{\hat{x}}$ to ensure the convergence of $\hat{x} \to x$. Using (1.1), (1.13) and assigning a quadratic Lyapunov function candidate to the error dynamics, i.e., $V(e) = e^{\mathrm{T}} P e$, the LMI stability conditions can be deduced as

$$A_i^{\mathrm{T}} P + P A_i - C_l^{\mathrm{T}} N_i^{\mathrm{T}} - N_i C_l \prec 0 \quad , \tag{1.14}$$

where $P \succ 0$ and N_i are the variables determined in the optimization problem. The desired feedback gains L_l of (1.13) can then be recovered from $L_l = P^{-1} N_l$.

A detailed derivation of the control and observer LMIs is given in chapter 2. The TS description provides a powerful framework for the nonlinear control tasks, as variable gains individually shaping the dynamics by depending on the current operating point are implicitly considered in the modeling and

design approach. Since this is vital to a well-performing wind turbine operation, the usefulness and applicability of the described approach to wind energy are explored within this thesis.

Illustrative example: Rössler attractor   To illustrate the application of the TS modeling framework for both, the SNL and Lin, consider the strange attractor $x = [x_1, x_2, x_3]^{\mathrm{T}}$ that exhibits nonlinear dynamics and was studied by Rössler in the context of chaos theory [45]

$$\dot{x} = g(x, u) = \begin{bmatrix} -x_2 - x_3 \\ x_1 + ax_2 \\ bx_1 - cx_3 + x_1x_3 + u \end{bmatrix} \quad , \quad y = [x_1, x_3]^{\mathrm{T}} = Cx \quad . \tag{1.15}$$

The parametrization of the dynamics is chosen as $a = 0.5$, $b = 0.4$ and $c = 4.5$. Compared to the original work in [45], the differential equation is augmented with an additional input u term and an output matrix $C = \begin{bmatrix} 1 & 0 & 0 \\ 0 & 0 & 1 \end{bmatrix}$ to allow an illustration of the observer-based control design.

To apply the SNL, the system is rewritten as

$$\dot{x} = g(x, u) = \begin{bmatrix} 0 & -1 & -1 \\ 1 & a & 0 \\ b + x_3 & 0 & -c \end{bmatrix} \begin{bmatrix} x_1 \\ x_2 \\ x_3 \end{bmatrix} + \begin{bmatrix} 0 \\ 0 \\ 1 \end{bmatrix} u \quad , \tag{1.16}$$

and the function inducing the nonlinearity is defined as $f(x_3) = x_3$. The function $f(x_3)$ is treated as shown in (1.2) within the (state) limits $\bar{f}(x_3) = 100$, $\underline{f}(x_3) = -100$, such that the following model is derived

$$\dot{x} = g(x, u) = \begin{bmatrix} 0 & -1 & -1 \\ 1 & a & 0 \\ b + (w^1(x_3)\underline{f} + w^2(x_3)\bar{f}) & 0 & -c \end{bmatrix} \begin{bmatrix} x_1 \\ x_2 \\ x_3 \end{bmatrix} + \begin{bmatrix} 0 \\ 0 \\ 1 \end{bmatrix} u \quad . \tag{1.17}$$

Every entry in the system matrices can be multiplied by $1 = w^1(x_3) + w^2(x_3)$ and for only one function treated with $z = x_3$, $w^1(x_3) = h_1(z)$ and $w^2(x_3) = h_2(z)$ follows from (1.6). Consequently,

the system description in a TS form derived by the SNL can be given as

$$\dot{x} = \left(h_1(z) \underbrace{\begin{bmatrix} 0 & -1 & -1 \\ 1 & a & 0 \\ b+\underline{f} & 0 & -c \end{bmatrix}}_{A_1} + h_2(z) \underbrace{\begin{bmatrix} 0 & -1 & -1 \\ 1 & a & 0 \\ b+\bar{f} & 0 & -c \end{bmatrix}}_{A_2} \right) \begin{bmatrix} x_1 \\ x_2 \\ x_3 \end{bmatrix} + \underbrace{\begin{bmatrix} 0 \\ 0 \\ 1 \end{bmatrix}}_{B} u \quad .$$

$$= g(x,u) = \sum_{i=1}^{2} h_i(z) A_i x + Bu$$

(1.18)

For the Lin approach, the partial derivative of the function $g(x,u)$ with respect to the states is evaluated, which yields

$$\frac{\partial g(x,u)}{\partial x} = \begin{bmatrix} 0 & -1 & -1 \\ 1 & a & 0 \\ b+x_3 & 0 & -c+x_1 \end{bmatrix} = A(x) \quad .$$

(1.19)

To obtain the input matrix B (in this case common as $B \neq f(x)$), the partial derivative with respect to the input u of the function $g(x,u)$ is evaluated

$$\frac{\partial g(x,u)}{\partial u} = \begin{bmatrix} 0 \\ 0 \\ 1 \end{bmatrix} = B \quad .$$

(1.20)

As a result, the system dynamics in the linearization points $x_{0i} = [x_{10i}, x_2, x_{30i}]^{\mathrm{T}}$ for any x_2 as $A(x) \neq f(x_2)$ can be approximated by

$$g(x,u) \approx \dot{x} = g(x_{0i}, u) + A(x_{0i})(x - x_{0i}) + Bu \quad .$$

(1.21)

This procedure is repeated for both premise variables $z = [x_1, x_3]^{\mathrm{T}}$ along a chosen operating range spanned by $x_{10i} \in [-10, 0, 10]$ $(l_{1,max} = 3)$ and $x_{30i} \in [-100, -60, -20, 20, 60, 100]$ $(l_{2,max} = 6)$. Definition of the weighting functions according to (1.5) for each premise variable, using (1.6) to obtain the membership functions and subsequently interconnecting the individually gained linear submodels results in the following TS model description derived by Lin

$$g(x,u) \approx \dot{x} = g(x_{0i}, u) + \sum_{i=1}^{18} h_i(z) A_i (x - x_{0i}) + Bu$$

$$= \sum_{i=1}^{18} h_i(z)(A_i x + a_i) + Bu \quad \text{with} \quad a_i = g(x_{0i}, u) - A_i x_{0i}$$

(1.22)
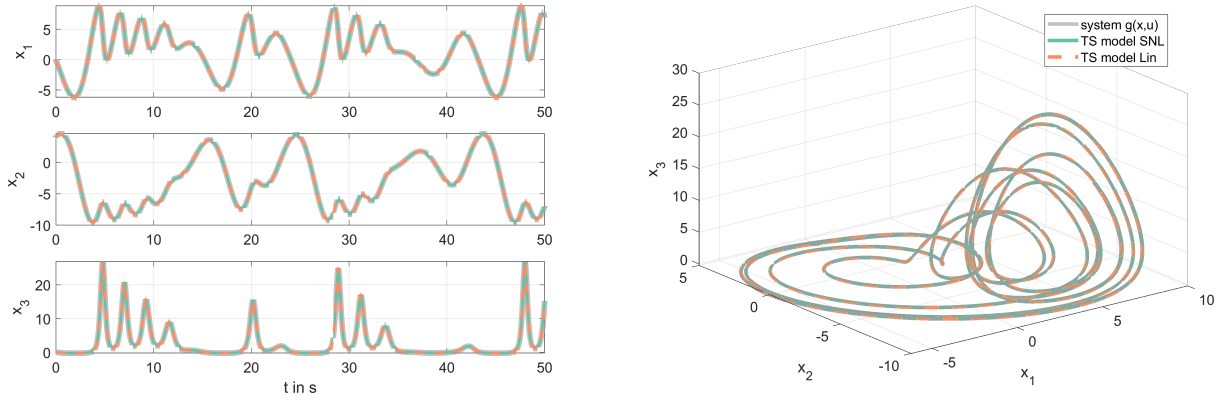
Figure 1.1: Comparison of state-space trajectories of the Rössler attractor and the TS models derived by the SNL or Lin. The initial value of the system is chosen as $x(0) = [0, 4, 0]^{\mathrm{T}}$.

The combination of each operating point defined in the premise space $z \in \mathrm{R}^2$, results in $N = l_{1,max} \cdot l_{2,max} = 18$ linear submodels.

A comparison of the state trajectories of the original attractor $g(x, u)$ and the derived TS models is shown in Fig. 1.1. The state trajectories of both TS models align well with the evolution of the attractor states that exhibits its typical chaotic behavior.
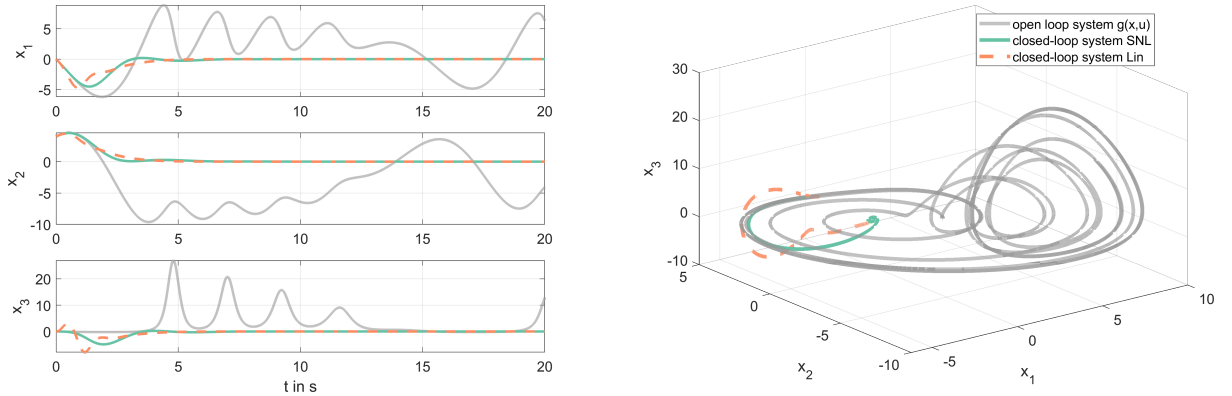
Figure 1.2: Comparison of state-space trajectories of the open-loop and the closed-loop attractor governed by a TS controller based on SNL or Lin. The initial value of the system is chosen as $x(0) = [0, 4, 0]^{\mathrm{T}}$ and the observer is initialized with $\hat{x}(0) = [0, 0, 0]^{\mathrm{T}}$.

An observer-based controller is designed for both TS descriptions, where the observers follow the structure defined in (1.13). To achieve state feedback stabilization, the following control law is implemented

$$u = -\sum_{i=1}^{N} h_k(z) K_k \hat{x} \quad , \tag{1.23}$$

that uses the reconstructed states from the observer $\hat{x}$. LMI-based design is applied to obtain the necessary feedback gains K_k. As the considered TS systems have a common input matrix B, i.e., they
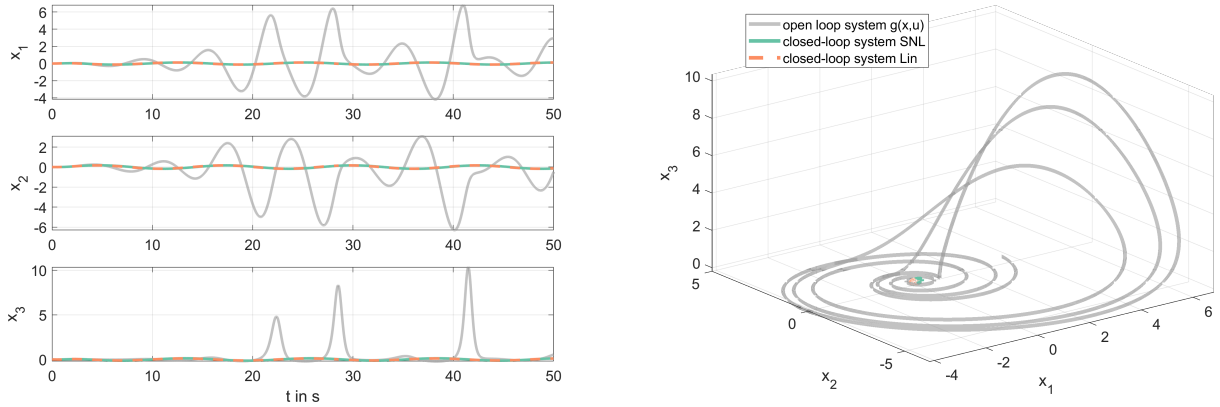
Figure 1.3: Comparison of state-space trajectories of the open-loop and the closed-loop attractor governed by a TS controller based on SNL or Lin when excited by a disturbance $d(t) = 0.01\sin(\pi\,1\mathrm{Hz}\,t)$. The initial value of the system is chosen as $x(0) = [0,0,0]^{\mathrm{T}}$ and the observer is initialized with $\hat{x}(0) = [0,0,0]^{\mathrm{T}}$.

remain constant irrespective of the evolution of z, the decay rate stability constraints in (1.12) can be restated as

$$XA_i^{\mathrm{T}} + A_i X - M_i^{\mathrm{T}} B^{\mathrm{T}} - BM_i + 2\alpha X \prec 0 \qquad . \tag{1.24}$$

This effectively means that M_k needs to fulfill the constraint for every submodel of the TS description individually, i.e., $k = i$ only, while being only connected by the common design matrix X. These LMIs are applied for both TS models (1.18) and (1.22) with a desired decay rate $\alpha = 0.5$ and the necessary feedback gains contained in (1.23) are derived.

Dually to the feedback gain design, the common output matrix of the studied attractor in (1.15), i.e., $C_i = C\,\forall i$, results in reduced LMI stability conditions for deriving the observer feedback gains compared to (1.14). Including a desired decay rate of α_O, they can be stated as

$$A_i^{\mathrm{T}} P + PA_i - C^{\mathrm{T}} N_i^{\mathrm{T}} - N_i C + 2\alpha_O P \prec 0 \quad , \tag{1.25}$$

where a design parameter of $\alpha_O = 1$ for the system at hand was chosen.

A comparison of the open-loop state trajectories compared to the closed-loop trajectories governed by the observer-based TS controller is shown in Fig. 1.2. It is observed that the feedback results in a decay of the closed-loop system into the stable equilibrium of $x = [0, 0, 0]^{\mathrm{T}}$. To additionally illustrate the disturbance rejection potential, the attractor is augmented with a disturbance input d, i.e., $\dot{x} = g(x, u) + B_d d$ with $B_d = [10, 0, 2]^{\mathrm{T}}$. As shown in Fig. 1.3, the controllers are capable of effectively rejecting the disturbance acting on the system and thus the state trajectories vary only slightly due to the disturbance opposed to the open-loop system dynamics.

1.4 Overview and connection of the individual contributions

The employed approach, i.e., using TS modeling to obtain LMI-based design constraints, and the subsequent application to wind turbines, interconnects the four scientific contributions. The proposed control structure integrates a feedback and feedforward term as input to the system, where an observer is designed to estimate the unknown inflow that drives the energy conversion process and influences the dynamical properties of the wind turbine. However, the focus and perspective of the contributions differ, and to a certain degree build on each other. Overall, the objective of this work is to explore the TS approach for providing a flexible, load mitigating and grid supporting control scheme for wind turbines.

In the first work presented in chapter 2, the formulation of LMIs for TS systems in the Lyapunov framework are reviewed in detail. Therein, basic stability constraints are derived for observer and controller design based on existing literature, where quadratic Lyapunov candidate functions are used, see e.g., [35, 41]. The $\mathcal{D}$-stability framework [46] is discussed for a restriction of the resulting closed-loop system eigenvalues into a subregion in the complex plane. As a potential method to disturbance rejection especially with regard to the wind speed as the governing energy source of the process, the $\mathcal{H}_2$ disturbance attenuation framework [35] is explicated. To account for the unmeasurable premise variable in the stability considerations of the estimation error dynamics, the input-to-state stability concept [47] is discussed and applied. A technique to influence the conservatism of the solution and thereby closed-loop dynamics after solving the LMI-based optimization problem without leaving the grounding stability constraints is discussed. Originally, the concept was proposed in [48], and is applied to the wind turbine control problem in this chapter. This overview of the different LMI constraints for TS systems forms a theoretical basis of the following contributions.

The implications from exploiting a closed-loop shaping and observer-based approach for the wind turbine control problem in full load region is investigated through simulation studies. A detailed model of a 5MW reference turbine [49] implemented within the aeroelastic simulator [50] is operated with the proposed control approach. The TS description captures the aerodynamic conversion process in the rotational dynamics of the turbine model as only considered state. A comparison to an integral-based feedback structure resembling the common approach for wind turbine control is drawn. It is discussed how this controller can be equivalently derived using the presented LMI constraints. In summary, it is found that the use of an observer-based scheme increases the design flexibility to alter the resulting closed-loop dynamics, and in consequence the control performance by the possibility of the control engineer to dedicatedly influence the operating behavior of the turbine.

The performance of the discussed methods in providing a specifically shaped operating behaviour

are then assessed based on detailed simulation studies for the 5MW reference turbine [49] within the aero-elastic simulator [50]. This work is presented in chapter 3. It illustrates the load mitigation capabilities for wind turbines from the proposed framework when considering several components in the control design simultaneously. This includes tower fore-aft and side-to-side motion and drivetrain dynamics. Further, the operating range is extended such that partial load operation of the turbine is simultaneously considered in the control design stage. The experienced loading of the turbine is compared to a reference control implementation [51], where the provision of active damping by the control scheme is seen to result in a relevantly load reduced operation. The considered design load cases for comparison to the reference controller are operation at turbulent wind according to the normal turbulence model across the wind operating range and extreme operating gusts within the crucial operating range around rated wind speed.

To obtain specifically shaped closed-loop dynamics despite the conservatism inherited in stability considerations based on candidate functions, the control design is separated for the individual components allowing a componentwise, specific definition of desired closed-loop dynamics. The nature of the multi-variate control problem in the TS structure is considered in a subsequent stability consideration including all individually synthesized controller gains and their interaction within the closed-loop system description. In contrast, the disturbance observer for wind speed and state reconstruction is formulated as a single LMI-based optimization problem considering the entire operating range of interest.

Additionally, the concept of capturing a power tracking functionality within the distribution of operating points that constitute the TS model of the wind turbine is introduced. The controller is used to analyze the resulting loading of the turbine structure while following different demand scenarios emulating continuous grid stabilizing behavior. The results suggest that turbines are suitable for a fast variation of the power output enforced by a dedicated control scheme while experiencing no additional ultimate loading compared to nominal operation in the considered scenarios. At the same time, the turbine operation shows an expected increase in fatigue loading due to the continuous actuation to enforce the demanded variation of the power output.

In the previously discussed works that illustrate the potential of the proposed method for wind turbine control design, the assumption of time-scale separation of estimation error dynamics and closed-loop system dynamics is inherited in the stability considerations. This assumption holds for TS systems with measurable premise variables within the defined operating range, effectively allowing for separate controller and observer design [35, 41]. In the wind turbine control approach discussed here, however, a disturbance observer provides an estimate of the current effective wind speed and determines the evolution of the premise variables. For this purpose, an augmented state-space is created, inheriting the estimated wind speed as state of the system description. In consequence, this problem

treatment yields a purely nonlinear estimation problem with unknown but estimated premise variables. This increases the design complexity for controller and observer design [52, 53, 54] compared to parameter-varying estimation error dynamics in case of measurable premise variables. The works in chapter 2 and 3 consider the unmeasurable premise variable within the input-to-state stability framework for observer design only, while independently designing the closed-loop system dynamics assuming that adequately shaped estimation error and system dynamics fulfill the separation principle.

Beyond the assumption of this time-scale separation, in chapter 4, a framework for the stability analysis of the coupled closed-loop system and estimation error dynamics in case of unmeasurable premise variables is proposed. The stability framework embeds a wind speed estimation error possibly occurring during application of the control scheme into an increased number of interconnected LMIs constraining the Lyapunov candidate function. The approach exploits specific structural properties of the TS formulation to capture the nonlinear estimation process globally within the defined operating range. The assumption of a maximum estimation error defines a subspace of the state-space, where the closed-loop turbine model dynamics are proven to be stable despite of the unmeasurable premise variable if a solution is found. In the upper limit, i.e., when the wind speed estimation error $\rightarrow \infty$, the proposed LMI constraints constitute a global proof of stability within the defined operating range of the TS description. In the lower limit, i.e., when the wind speed estimation error $\rightarrow 0$, the stability constraints conincide with their counterparts when assuming measurable premise variables. The control and observer design to synthesize the necessary feedback gains is conducted in a previous step using the methods described in chapter 2 and 3.

An experimental validation of the model-based control concept in a wind tunnel campaign is presented in chapter 4. A scaled wind turbine [55] is operated by the designed TS controller in a large operating range of different wind speeds. An active grid [56] is used to generate turbulent inflow conditions resembling realistic operating conditions that turbines face during operation in the field [57]. Additionally, the response of the closed-loop wind turbine at different operating gusts is examined to explore possible limitations due to extreme wind conditions. The measurement campaign focuses on the capability of wind turbines to provide grid stabilizing behavior emulated through challenging power variation demand. The measured power output of the turbine can be seen to adequately follow the demand while showing a suitable operating behavior in all considered operational scenarios. The application of the model- and observer-based control scheme in an experimental setting with great uncertainties show the real-time capabilities and robustness of the approach.

As described above, the proposed stability framework incorporates an assumption on the maximum occurring wind speed estimation error, for this specific problem. Through a measurement device supplying an estimate of the current effective wind speed, the experimental validation allows to assess

the adherence of this assumption in operation of the turbine commanded by the proposed disturbance observer-based control scheme.

Finally, the fourth contribution addresses a load mitigating filter design for the interaction of the electrical grid and a wind turbine in chapter 5. For this purpose, a simple analytical grid model is used and interconnected to the wind turbine through a droop control scheme [58]. As a result, a deviation of the frequency in the electrical grid results in a variation of the produced power by the wind energy system. Effectively, this aims at a reduction of the causing power imbalance in the electrical grid and a limitation of the frequency deviation from its nominal value. However, this actuation based on the frequency evolution induces additional excitation into the wind turbine structure. Especially the tower is stressed by the continuous variation of the blade pitch positions. To address this, a filter design is proposed that dynamically alters the power output demand from the droop-control scheme before passing it to the wind turbine controller. The discussed filter design is reformulated into a feedback control problem, effectively allowing for the application of the LMI-based approaches discussed for the wind turbine control problem before. From the simulation studies involving the 5 MW reference turbine [49] within FAST [50], it is found that the filter reduces the impact of frequency stabilizing behavior on the mechanical loading of the turbine structure in fore-aft direction significantly. At the same time, the evolution and settling value of the simulated grid frequency is only minorly altered due to the filter, underlining the usefulness of the discussed LMI-based approaches in a variety of different control problems.

References

[1] BP. Statistical review of world energy. Technical report, 2019.

[2] D Gilfillan, G Marland, T Boden, and R Andres. Global, Regional, and National Fossil-Fuel CO2 Emissions. Technical report, Carbon Dioxide Information Analysis Center at Appalachian State University, 2019.

[3] United Nations Framework Convention on Climate Change. National Inventory Submissions 2019. Technical report, United Nations, 2019.

[4] M R Allen, O P Dube, W Solecki, F Aragón-Durand, W Cramer, S Humphreys, M Kainuma, J Kala, N Mahowald, Y Mulugetta, R Perez, M Wairiu, and K Zickfeld. *Framing and Context*. In V Masson-Delmotte, P Zhai, H-O Pörtner, D Roberts, J Skea, P R Shukla, A Pirani, W Moufouma-Okia, C Péan, R Pidcock, S Connors, J B R Matthews, Y Chen, X Zhou, M I Gomis, E Lonnoy, T Maycock, M Tignor, and T Waterfield, editors, *Global Warming of 1.5℃. An IPCC Special Report on the impacts of global warming of 1.5℃ above pre-industrial levels and related global greenhouse gas emission pathways, in the context of strengthening the global response to the threat of climate change, sustainable development, and efforts to eradicate poverty.* 2018.

[5] The Intergovernmental Panel on Climate Change. Climate Change 2014: Impacts, Adaptation, and Vulnerability. Part A: Global and Sectoral Aspects. Contribution of Working Group II to the Fifth Assessment Report of the Intergovernmental Panel on Climate Change. Cambridge UniversityPress, Cambridge, United Kingdom and New York, NY, USA, 2014.

[6] United States Environmental Protection Agency. Sources of Greenhouse Gas Emissions, September 2019. `https://www.epa.gov/ghgemissions/sources-greenhouse-gas-emissions` (02.11.2020).

[7] J Rogelj, D Shindell, K Jiang, S Fifita, P Forster, V Ginzburg, C Handa, H Kheshgi, S Kobayashi, E Kriegler, L Mundaca, R. Séférian, and M V Vilariño. *Mitigation Pathways Compatible with 1.5℃ in the Context of Sustainable Development*. In V Masson-Delmotte, P Zhai, H-O Pörtner, D Roberts, J Skea, P R Shukla, A Pirani, W Moufouma-Okia, C Péan, R Pidcock, S Connors, J B R Matthews, Y Chen, X Zhou, M I Gomis, E Lonnoy, T Maycock, M Tignor, and T Waterfield, editors, *Global Warming of 1.5℃. An IPCC Special Report on the impacts of global warming of 1.5℃ above pre-industrial levels and related global greenhouse gas emission pathways, in the context of strengthening the global response to the threat of climate change, sustainable development, and efforts to eradicate poverty.* 2018.

[8] B Burger. Öffentliche Nettostromerzeugung in Deutschland im Jahr 2018. Technical report, Fraunhofer-Institut für Solare Energiesysteme ISE, 2019.

[9] P Veers, K Dykes, E Lantz, S Barth, C L Bottasso, O Carlson, A Clifton, J Green, P Green, H Holttinen, Dl Laird, V Lehtomäki, J K Lundquist, J Manwell, M Marquis, C Meneveau, P Moriarty, X Munduate, M Muskulus, J Naughton, L Pao, J Paquette, J Peinke, A Robertson, J Sanz Rodrigo, A M Sempreviva, J C Smith, A Tuohy, and R Wiser. Grand challenges in the science of wind energy. *Science*, 2019. DOI: 10.1126/science.aau2027.

[10] INNWIND.EU. LCOE reduction for the next generation offshore wind turbines. Technical report, 2017.

[11] V Petrova.   GE installs 12-MW wind turbine prototype in Rotterdam,   October   2019.   `https://renewablesnow.com/news/ge-installs-12-mw-wind-turbine-prototype-in-rotterdam-673053` (02.11.2020).

[12] C Kost, S Shammugam, V Jülch, H-T Nguyen, and T Schlegl. Levelized Cost of Eectricity Renewable Energy Technologies. Technical report, Fraunhofer Institute for Solar Energy Systems ISE, March 2018.

[13] L Y Pao and K E Johnson. Control of Wind Turbines. *IEEE Control Systems Magazine*, 2011. DOI: 10.1109/MCS.2010.939962.

[14] M Wächter, H Heißelmann, M Hölling, A Morales, P Milan, T Mücke, J Peinke, N Reinke, and P Rinn. The turbulent nature of the atmospheric boundary layer and its impact on the wind energy conversion process. *Journal of Turbulence*, 2012. DOI: 10.1080/14685248.2012.696118.

[15] E A Bossanyi. Wind turbine control for load reduction. *Wind Energy*, 2003. DOI: 10.1002/we.95.

[16] F D Bianchi, R J Mantz, and C F Christiansen. Control of variable-speed wind turbines by LPV gain scheduling. *Wind Energy*, 2004. DOI: 10.1002/we.103.

[17] S P Mulders, T G Hovgaard, J D Grunnet, and J-W van Wingerden. Preventing wind turbine tower natural frequency excitation with a quasi-LPV model predictive control scheme. *Wind Energy*, 2020. DOI: 10.1002/we.2447.

[18] K Z Østergaard, J Stoustrup, and P Brath. Linear parameter varying control of wind turbines covering both partial load and full load conditions. *Int. J. Robust and Nonlinear Control*, 2009. DOI: 10.1002/rnc.1340.

[19] A Koerber and R King. Combined Feedback–Feedforward Control of Wind Turbines Using State-Constrained Model Predictive Control. *IEEE Transactions on Control Systems Technology*, 2013. DOI: 10.1109/TCST.2013.2260749.

[20] S Schuler, D Schlipf, P W Cheng, and F Allgöwer. ℓ_1-optimal control of large wind turbines. *IEEE Transactions on Control Systems Technology*, 2013. DOI: 10.1109/TCST.2013.2261068.

[21] V Pascu, S Kanev, and J-W van Wingerden. Adaptive tower damping control for offshore wind turbines. *Wind Energy*, 2017. DOI: 10.1002/we.2058.

[22] J Kersten and H Aschemann. Aktive Schwingungsdämpfung einer Windkraftanlage mit hydrostatischem Getriebe und permanenterregtem Synchrongenerator: Berücksichtigung von Parametervariabilitäten, Eigenwertbereichsbeschränkungen und Optimalitätsanforderungen mittels LMI-Ansätzen. *at - Automatisierungstechnik*, 2019. DOI: 10.1515/auto-2018-0032.

[23] J Machowski, J W Bialek, and J Bumby. *Power System Dynamics: Stability and Control*. Wiley, 2011.

[24] J Morren, J P, and S WH de Haan. Inertial response of variable speed wind turbines. *Electric Power Systems Research*, 2006. DOI: 10.1016/j.epsr.2005.12.002.

[25] U Markovic, O Stanojev, P Aristidou, E Vrettos, C Callaway, and G Hug. Understanding small-signal stability of low-inertia systems. *IEEE Transactions on Power Systems*, 2021. DOI: 10.1109/T-PWRS.2021.3061434.

[26] N R Ullah, T Thiringer, and D Karlsson. Voltage and transient stability support by wind farms complying with the E.ON Netz grid code. *IEEE Transactions on Power Systems*, 2007. DOI: 10.1109/TPWRS.2007.907523.

[27] J Kazda, K Merz, J O Tande, and N A Cutululis. Mitigating Turbine Mechanical Loads Using Engineering Model Predictive Wind Farm Controller. *Journal of Physics: Conference Series*, 2018. DOI: 10.1088/1742-6596/1104/1/012036.

[28] M Vali, V Petrović, G Steinfeld, L Y Pao, and M Kühn. An active power control approach for wake-induced load alleviation in a fully developed wind farm boundary layer. *Wind Energy Science*, 2019. DOI: 10.5194/wes-4-139-2019.

[29] V Petrović and C L Bottasso. Wind turbine envelope protection control over the full wind speed range. *Renewable Energy*, 2017. DOI: 10.1016/j.renene.2017.04.021.

[30] W Munters and J Meyers. Towards practical dynamic induction control of wind farms: analysis of optimally controlled wind-farm boundary layers and sinusoidal induction control of first-row turbines. *Wind Energy Science*, 2018. DOI: 10.5194/wes-3-409-2018.

[31] M Shan, W Shan, F Welck, and D Duckwitz. Design and laboratory test of black-start control mode for wind turbines. *Wind Energy*, 2020. DOI: 10.1002/we.2457.

[32] C Galinos, A M Urbán, and W H Lio. Optimised de-rated wind turbine response and loading through extended controller gain-scheduling. *Journal of Physics: Conference Series*, 2019.

[33] F D Bianchi, R J Mantz, and C F Christiansen. Gain scheduling control of variable-speed wind energy conversion systems using quasi-lpv models. *Control Engineering Practice*, 2005. DOI: 10.1016/j.conengprac.2004.03.006.

[34] T Takagi and M Sugeno. Fuzzy identification of systems and its applications to modeling and control. *IEEE Transactions on Systems, Man, and Cybernetics*, 1985. DOI: 10.1109/TSMC.1985.6313399.

[35] K Tanaka and H O Wang. *Fuzzy Control Systems Design and Analysis: A Linear Matrix Inequality Approach*. John Wiley & Sons, Inc., 2001.

[36] S Boyd, L El Ghaoui, E Feron, and V Balakrishnan. *Linear Matrix Inequalities in System and Control Theory*. Society for Industrial and Applied Mathematics, 1994.

[37] H Ohtake, K Tanaka, and H O Wang. Fuzzy modeling via sector nonlinearity concept. In *Proceedings Joint 9th IFSA World Congress and 20th NAFIPS International Conference*, 2001. DOI: 10.1109/NAFIPS.2001.944239.

[38] S Georg. *Fault Diagnosis and Fault-Tolerant Control of Wind Turbines – Nonlinear Takagi-Sugeno and Sliding Mode Techniques*. PhD thesis, Fakultät für Maschinenbau und Schiffstechnik der Universität Rostock, 2015.

[39] F Pöschke, J Fortmann, and H Schulte. Nonlinear wind turbine controller for variable power generation in full load region. In *2017 American Control Conference (ACC)*, 2017. DOI: 10.23919/ACC.2017.7963148.

[40] T A Johansen, R Shorten, and R Murray-Smith. On the interpretation and identification of dynamic takagi-sugeno fuzzy models. *IEEE Transactions on Fuzzy Systems*, 2000. DOI: 10.1109/91.855918.

[41] Z Lendek, T M Guerra, R Babuska, and B De Schutter. *Stability Analysis and Nonlinear Observer Design Using Takagi-Sugeno Fuzzy Models*. Springer-Verlag Berlin Heidelberg, 2010.

[42] J G VanAntwerp and R D Braatz. A tutorial on linear and bilinear matrix inequalities. *Journal of Process Control*, 2000. DOI: 10.1016/S0959-1524(99)00056-6.

[43] H J Marquez. *Nonlinear Control Systems – Analysis and Design*. John Wiley and Sons, Inc., 2003.

[44] G Feng. A survey on analysis and design of model-based fuzzy control systems. *IEEE Transactions on Fuzzy Systems*, 2006. DOI: 10.1109/TFUZZ.2006.883415.

[45] O E Rössler. Continuous chaos—four prototype equations. *Annals of the New York Academy of Sciences*, 1979. DOI: 10.1111/j.1749-6632.1979.tb29482.x.

[46] M Chilali and P Gahinet. H_∞ design with pole placement constraints: an LMI approach. *IEEE Transactions on Automatic Control*, 1996. DOI: 10.1109/9.486637.

[47] E D Sontag. On the Input-to-State Stability Property. *European Journal of Control*, 1995. DOI: 10.1016/S0947-3580(95)70005-X.

[48] F Pöschke and H Schulte. Optimization of takagi-sugeno observers with application to fault estimation. *IFAC-PapersOnLine*, 2018. DOI: 10.1016/j.ifacol.2018.06.249.

[49] J Jonkman, S Butterfield, W Musial, and G Scott. Definition of a 5-MW Reference Wind Turbine for Offshore System Development. Technical report, 2009.

[50] J Jonkman and M L Buhl Jr. FAST User's Guide. Technical report, 2005.

[51] S P Mulders and J W van Wingerden. Delft Research Controller: an open-source and community-driven wind turbine baseline controller. *Journal of Physics: Conference Series*, 2018. DOI: 10.1088/1742-6596/1037/3/032009.

[52] K Tanaka, T Ikeda, and H O Wang. Fuzzy regulators and fuzzy observers: relaxed stability conditions and LMI-based designs. *IEEE Transactions on Fuzzy Systems*, 1998. DOI: 10.1109/91.669023.

[53] T M Guerra, A Kruszewski, L Vermeiren, and H Tirmant. Conditions of output stabilization for nonlinear models in the takagi–sugeno's form. *Fuzzy Sets and Systems*, 2006. DOI: 10.1016/j.fss.2005.12.006.

[54] H K Lam, H Li, and H Liu. Stability analysis and control synthesis for fuzzy-observer-based controller of nonlinear systems: a fuzzy-model-based control approach. *IET Control Theory & Applications*, 2013. DOI: 10.1049/iet-cta.2012.0465.

[55] F Berger, L Kröger, D Onnen, V Petrović, and M Kühn. Scaled wind turbine setup in a turbulent wind tunnel. *Journal of Physics: Conference Series*, 2018. DOI: 10.1088/1742-6596/1104/1/012026.

[56] L Kröger, J Frederik, J-W van Wingerden, J Peinke, and M Hölling. Generation of user defined turbulent inflow conditions by an active grid for validation experiments. *Journal of Physics: Conference Series*, 2018. DOI: 10.1088/1742-6596/1037/5/052002.

[57] L Neuhaus, F Berger, J Peinke, and M Hölling. Exploring the capabilities of active grids. *Experiments in Fluids*, 2021. DOI: 10.1007/s00348-021-03224-5.

[58] J Van de Vyver, J D M De Kooning, B Meersman, L Vandevelde, and T L Vandoorn. Droop Control as an Alternative Inertial Response Strategy for the Synthetic Inertia on Wind Turbines. *IEEE Transactions on Power Systems*, 2016. DOI: 10.1109/TPWRS.2015.2417758.

2 | LMI region-based non-linear disturbance observer with application to robust wind turbine control

Abstract

This chapter investigates the Takagi-Sugeno modeling approach for non-linear control and observer design. Several results from the literature based on linear matrix inequalities are summarized and combined to provide a useful control design framework for non-linear systems. Stability constraints, techniques to include region constraints of the resulting closed-loop dynamics and robust criteria are discussed and formulated as linear matrix inequalities. A linear matrix inequality constraint for Takagi-Sugeno observers with unmeasurable premise variables based on the input-to-state property is proposed. By combining the presented LMIs for the application to a wind turbine, two different non-linear control schemes based on the convex system description are derived, and the implications from introducing the observer for the wind turbine application are discussed.

2.1 Introduction

This contribution deals with non-linear model-based observer and control design techniques in the Takagi-Sugeno (TS) framework. TS modeling is employed to obtain a convex representation of the non-linear system dynamics. The derived convex model description allows for stability analysis, feedback gain synthesis and the introduction of performance criteria formulated in terms of linear matrix inequalities (LMI). LMIs can be efficiently solved numerically using various available solvers [1], and thus provide a powerful framework for the automated generation of feedback gains with respect to stability conditions and performance constraints. The Lyapunov function approach is used to derive convex constraints that account for the non-linear nature of the models by combining the linear sub-models of the vertices in the TS description. A collection of LMI constraints is reviewed simultaneously for both observer and control design that allow for a shaping of the resulting closed-loop dynamics, providing a useful overview for design of non-linear control schemes in the TS framework. This includes the formulation of desired closed-loop pole regions in the complex plane, robust disturbance attenuation and a mixture of them. The derived stability constraints form the basis for the controller design of a wind turbine application.

The premise variables in the TS description govern the blending of the linear sub-models, and thus provide information on the current operating point of the non-linear system and adequate feedback signal. For systems, where the premise variables are measurable, this is conducted by calculation of the membership functions based on the current measurement of the premise variable. However, in some applications like discussed for the wind turbine, the premise variables may be unmeasurable. A non-linear TS observer can be used to estimate the premise variable, but the design needs to account for the unmeasurability as the observer relies on its own estimate of the premise variable. The input-to-state stability concept (ISS) is employed for the formulation of LMIs of a TS observer with unmeasurable premise variable and subsequently applied to the wind speed estimation for wind turbine control.

As wind turbines take a major role in the transformation of the energy sector towards a renewable supply, they need to produce energy at a competitive cost. The cost of energy of renewable energy conversion systems have to be lowered while retaining or increasing energy yield and decreasing systems cost. For wind turbines the costs are are among others governed by material expenses. Therefore, achieving mitigation of the loads acting on the mechanical components of the wind turbine by adequate control of the available actuators is a focus of both industry and research as the size of wind turbine steadily increases with the aim of achieving greater power production capabilities [2, 3].

In the design of control algorithms, two characteristic effects of different time scale need to be considered: While the wind, accelerating the wind turbine's rotor and drive-train, is highly fluctuating

within milliseconds, the wind turbine (i.e. its rotor and drive-train) possesses a high rotational inertia resulting in time constants of some seconds. A precise wind speed measurement is hardly feasible with conventional, cost-effective wind speed sensors [4]. Therefore, in common approaches the information on the wind is estimated from the current control input to the system, i.e. the pitch angle of the wind turbine blades. However, since the estimate of the current wind speed in this concept is coupled to the dynamics of the closed-loop system, the derived estimate is delayed in the time range of the occurring closed-loop dynamics of the wind turbine. Therefore, the employment of wind speed observers is proposed to establish an observer-based wind turbine control algorithm, effectuating in adjustable dynamics of the wind speed estimate. Further, by using the observer for wind speed estimation, the calculation of the current operating point based on the estimated wind speed can be decoupled from the actual stabilizing feedback control action.

The concept of using the rotational dynamics of the wind turbine to estimate the effective wind speed has been addressed in several contributions and with different techniques. Surveys and comparison between different methods can be found in [5, 6, 7]. In [7] a wind speed disturbance observer in a TS form has been proposed and the performance is compared to Kalman filtering techniques. However, in this contribution it is shown how the information gained by the TS observer can be exploited in a feedforward scheme. Further, the estimated wind speed is used in the calculation of the feedback gains, complementing the observation to an overall non-linear control scheme in the TS framework for wind turbines in the full-load region.

An observer-based non-linear control algorithm is presented, exploiting only the measurement of the rotational speed of the turbine ω, which is the common approach in industrial wind turbine control. It is discussed how the proposed observer-based non-linear control algorithm allows for assessing an increased sensitivity of the resulting closed-loop dynamic to the design process, and it is compared to a TS controller resembling the common approach for wind turbine control. Further, the proposed non-linear control considers the structural integrity of the wind turbine system by avoiding conflicting natural frequencies of the major, mechanical wind turbine components in closed-loop rotational dynamics through the LMI pole placement technique.

After an introduction to the TS modeling technique in Sec. 2.2, LMIs for feedback design are derived for both controller and observer purposes in Sec. 2.3. The derivation of the wind turbine TS model follows, and the general LMI formulations in the TS framework are applied for observer and controller design of the wind turbine in Sec. 2.4. The implications of the LMI region constraints are discussed along with a variation of the different design parameters, such that their effect can be discussed in Sec. 2.4. An overview of the entire chapter is given in Fig. 2.1.
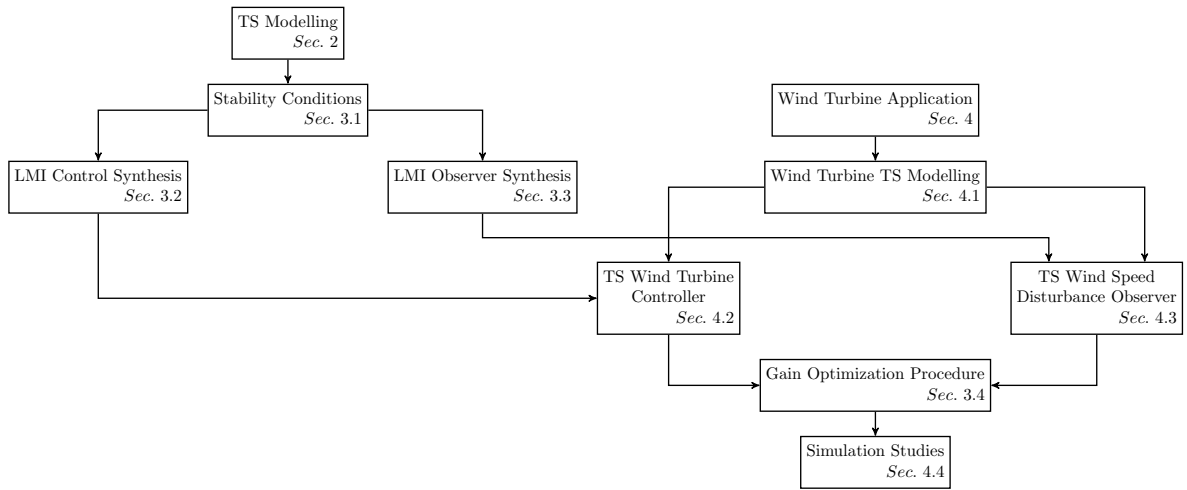
Figure 2.1: Overview of the chapter

2.2 Takagi-Sugeno modeling

Throughout this chapter, non-linear state-space models, as well as control laws and observer models, are formulated in terms of the TS model structure. TS models provide a useful and uniform framework for non-linear controller and observer design. Originally introduced in the context of fuzzy systems [8], TS models are weighted combinations of linear sub-models. These can either be derived from input-output data using system identification techniques or from mathematical models of non-linear systems. In the latter, the TS model is analytically constructed by the sector non-linearity approach [9] or by local linearization around a set of different representative points, which may or may not be equilibria. The sector non-linearity approach is one of the most frequently used approaches for constructing TS models for non-linear control and observer design, as an exact representation of a given non-linear system in a compact set of the state space is obtained [10]. The disadvantage of this method is that all sub-models are always interconnected in the membership functions, which may impose conservative constraints to the automated feedback synthesis. Further, all non-linear terms are concentrated in the membership functions. For some models this may result in the loss of structural information on dynamics in the local models and may affect properties like observability or controllability. For a discussion on this aspect regarding the formulation of a wind turbine in the TS structure, see [11].

In contrast, the local linearization of a given non-linear model by Taylor series expansion, which is used for the wind turbine in Sec. 2.4, generates locally valid sub-models which are summarized in a TS model via weighted combination of local overlapping normalized membership functions and thus the non-linear dynamics are preserved in the overall interconnected TS model. The local validity reduces

the coupling of linear sub-models in description of the defined operating range. However, models derived by local linearization yield an approximation of the underlying non-linear model description that depends on the number of chosen operating points.

The non-linear control and disturbance observer design uses the following TS state-space model structure

$$\dot{\mathbf{x}} = \sum_{i=1}^{N_r} h_i(\mathbf{z}) \left(\mathbf{A}_i \mathbf{x} + \mathbf{B}_i \mathbf{u} + \mathbf{D}_i \, \mathbf{d}\right) , \qquad \mathbf{y} = \mathbf{C} \mathbf{x} , \tag{2.1}$$

where $\mathbf{z} \in \mathbb{R}^{n_z}$ denotes the vector of premise variables, $\mathbf{x} \in \mathbb{R}^n$ the vector of system states, $\mathbf{u} \in \mathbb{R}^m$ the input vector, and $\mathbf{y} \in \mathbb{R}^p$ the vector of outputs. The disturbance is represented by the vector $\mathbf{d} \in \mathbb{R}^{n_d}$ and their distribution by $\mathbf{D}_i$. The system and input matrices, and output matrix are given by $\mathbf{A}_i \in \mathbb{R}^{n \times n}$, $\mathbf{B}_i \in \mathbb{R}^{n \times m}$ with $i = 1, \dots, N_r$, and $\mathbf{C} \in \mathbb{R}^{p \times n}$, respectively. The membership functions $h_i : \mathbb{R}^{n_z} \to \mathbb{R}$ in the TS model description are designed to fulfill the convex sum condition

$$\sum_{i=1}^{N_r} h_i(\mathbf{z}) = 1 , \quad h_i(\mathbf{z}) \geq 0 , \quad i = 1, \dots, N_r . \tag{2.2}$$

2.3 LMI control and observer synthesis

The description of non-linear systems in a convex structure allows for the formulation of autonomous and closed-loop stability criteria as LMIs [12]. LMIs are convex constraints that can be solved efficiently employing various available solvers such as SeDuMi [13], which is used throughout this contribution for all deployed LMIs. As a result, the proof of stability of the non-linear system can be reduced to the feasibility of a set of LMIs. The definition of feedback gains as variables in the LMI feasibility problem allows for an automated generation of stabilizing controller and observer gains from a set of given LMIs. Various problems from the control theory such as Lyapunov or Riccati inequalities can be reformulated and thus solved as LMIs [1].

This section first describes stability conditions for TS systems emerging from Lyapunov theory. The derived stability conditions are extended to include robustness criteria. This includes a decay rate, a desired location of the resulting closed-loop poles in the complex plane and guaranteed $\mathcal{H}_2$ attenuation of the disturbance acting on the process. Additionally, a mixed criterion involving the closed-loop location of the poles along with the guaranteed H_2 attenuation is formulated.

Preliminaries In the definition of the LMIs, $\mathbf{X} \prec 0 \, (\mathbf{X} \succ 0)$ describes a negative (positive) definite matrix, i.e. all eigenvalues of the matrix λ, fulfilling $\det(\mathbf{X} - \lambda \mathbf{I}) = 0$, are negative (positive). For

scalars the notation $<$ and $>$ is used. The euclidean norm is denoted as $\|\mathbf{x}\|_2 = \sqrt{\mathbf{x}^{\mathrm{T}}\mathbf{x}}$. The real and imaginary part of a complex vector is described by $\mathrm{Re}(\cdot)$ and $\mathrm{Im}(\cdot)$, respectively.

Congruence [10]

For a symmetric matrix $\mathbf{X}$ and a full column rank matrix $\mathbf{Q}$ the following property holds

$$\mathbf{X} \succ 0 \Rightarrow \mathbf{Q}^{\mathrm{T}}\mathbf{X}\mathbf{Q} \succ 0 \ .$$

Completion of Squares

For two matrices $\mathbf{X}$ and $\mathbf{Y}$ of appropriate dimensions and a symmetric positive definite matrix $\mathbf{Q} = \mathbf{Q}^{\mathrm{T}} \succ 0$, from $(\mathbf{X} - \mathbf{Q}^{-1}\mathbf{Y})^{\mathrm{T}}\mathbf{Q}(\mathbf{X} - \mathbf{Q}^{-1}\mathbf{Y}) \succeq 0$, the following inequality

$$\mathbf{X}^{\mathrm{T}}\mathbf{Y} + \mathbf{Y}^{\mathrm{T}}\mathbf{X} \preceq \mathbf{X}^{\mathrm{T}}\mathbf{Q}\mathbf{X} + \mathbf{Y}^{\mathrm{T}}\mathbf{Q}^{-1}\mathbf{Y}$$

can be derived.

Schur Complement [10]

For a symmetric matrix $\mathbf{X} = \mathbf{X}^{\mathrm{T}} = \begin{bmatrix} \mathbf{X}_{11} & \mathbf{X}_{12} \\ \mathbf{X}_{12}^{\mathrm{T}} & \mathbf{X}_{22} \end{bmatrix}$, the following conditions are equivalent

$$\mathbf{X} \prec 0 \Leftrightarrow \begin{cases} \mathbf{X}_{22} \prec 0 \\ \mathbf{X}_{11} - \mathbf{X}_{12}\mathbf{X}_{22}^{-1}\mathbf{X}_{12}^{\mathrm{T}} \prec 0 \end{cases} .$$

2.3.1 Stability conditions

Consider a non-linear closed-loop or autonomous TS system given by

$$\dot{\mathbf{x}} = \sum_{i=1}^{N_r} h_i(\mathbf{z})\,\mathbf{G}_i\mathbf{x} \ . \tag{2.3}$$

From the direct Lyapunov method it is well known that a system is globally asymptotically stable, if a function $V(\mathbf{x})$ satisfying

$$V(\mathbf{x}) > 0 \quad \text{and} \quad \dot{V}(\mathbf{x}) < 0 \tag{2.4}$$

exists. Setting a quadratic Lyapunov function candidate as $V(\mathbf{x}) = \mathbf{x}^{\mathrm{T}}\mathbf{P}\mathbf{x}$, where $\mathbf{P}$ is defined as a symmetric positive matrix to be determined, i.e. $\mathbf{P} = \mathbf{P}^{\mathrm{T}}$ and $\mathbf{P} \succ 0$, the aim is to verify the negativity of the time derivative $\dot{V}(\mathbf{x})$ resulting from the Lyapunov function candidate. The given candidate functions derivative is

$$\dot{V}(\mathbf{x}) = \dot{\mathbf{x}}^{\mathrm{T}}\mathbf{P}\mathbf{x} + \mathbf{x}^{\mathrm{T}}\mathbf{P}\dot{\mathbf{x}} \ , \tag{2.5}$$

such that with (2.3)

$$\dot{V}(\mathbf{x}) = \sum_{i=1}^{N_r} h_i(\mathbf{z}) \, \mathbf{x}^{\mathrm{T}} \big(\mathbf{G}_i^{\mathrm{T}}\mathbf{P} + \mathbf{P}\mathbf{G}_i\big)\mathbf{x} \qquad (2.6)$$

results. Thus, stability of the non-linear system (2.3) is verified if a matrix $\mathbf{P} = \mathbf{P}^{\mathrm{T}} \succ 0$ is found fulfilling the set of LMIs for $i = 1, ..., N_r$ given by

$$\mathbf{G}_i^{\mathrm{T}}\mathbf{P} + \mathbf{P}\mathbf{G}_i \prec 0 \,. \qquad (2.7)$$

The LMIs in (2.7) verify stability of the non-linear system by determination of a common positive symmetric matrix $\mathbf{P}$ that fulfills the requirements of the Lyapunov function approach at every vertex of the polytopic description. Therefore, due to the convex blending of the linear sub-models that represent the vertices, the overall non-linear operation of the system in the confined operating range is stable as well.

2.3.1.1 Input to State Stability (ISS)

Consider the TS system (2.3) subject to a bounded input δ

$$\dot{\mathbf{x}} = \sum_{i=1}^{N_r} h_i(\mathbf{z}) \big(\mathbf{G}_i\mathbf{x} + \mathbf{F}_i\delta\big) \,. \qquad (2.8)$$

Assuming that condition (2.7) for system (2.8) holds, there $\exists \bar{\lambda} > 0$ for which the following is verified

$$\mathbf{x}^{\mathrm{T}}(\mathbf{G}_i^{\mathrm{T}}\mathbf{P} + \mathbf{P}\mathbf{G}_i)\mathbf{x} \prec -\bar{\lambda}\mathbf{I} \,\|\mathbf{x}\|_2^2 = -\bar{\lambda}\mathbf{x}^{\mathrm{T}}\mathbf{x} \,. \qquad (2.9)$$

Employing a quadratic Lyapunov function approach, an upper bound of the corresponding derivative is denoted as [10]

$$\dot{V}(\mathbf{x}) < -\frac{\bar{\lambda}}{2}\|x\|_2^2 + \frac{2\overline{\mathbf{PF}_i}^2}{\bar{\lambda}}\|\delta\|_2^2 \,, \qquad (2.10)$$

where $\overline{\mathbf{PF}_i} = \max_i\|\mathbf{PF}_i\|$ can be calculated from the solution of the LMI-based stability analysis of the system in (2.7). Thus, the derivative of the quadratic Lyapunov function in (2.10) is guaranteed to be negative as long as

$$\frac{2\overline{\mathbf{PF}_i}^2}{\bar{\lambda}}\|\delta\|_2^2 < \frac{\bar{\lambda}}{2}\|\mathbf{x}\|_2^2 \qquad (2.11)$$

holds. The input-to-state stability property of a system $\dot{\mathbf{x}} = \mathbf{f}(\mathbf{x}) + \mathbf{g}(\mathbf{x})\delta$ is presented in [14]. The concept proposes to assess the ISS property, by finding a Lyapunov function candidate $V(0) = 0$, $V(\mathbf{x}) > 0 \,\, \forall \mathbf{x} \neq \mathbf{0}$ and monotonically increasing functions $\chi_1(\cdot), \chi_2(\cdot), \chi_3(\cdot) : \mathbb{R}_{\geq 0} \to \mathbb{R}_{\geq 0}$, $\chi_1(0) = 0, \chi_2(0) = 0, \chi_3(0) = 0$, such that $\dot{V}(\mathbf{x}) \leq -\chi_1(\|\mathbf{x}\|_2) + \chi_2(\|\delta\|_2)$ with $\|\mathbf{x}\|_2 \geq \chi_3(\|\delta\|_2)$

for all $\mathbf{x}$ and δ. Then system (2.8) subject to a bounded input δ is ISS. From the definitions

$$\chi_1(\|\mathbf{x}\|_2) := \frac{\bar{\lambda}}{2}\|x\|_2^2, \quad \chi_2(\|\delta\|_2) := \frac{2\overline{\mathbf{PF}}_i^2}{\bar{\lambda}}\|\delta\|_2^2 \quad \text{and} \quad \chi_3(\|\delta\|_2) = \frac{4\overline{\mathbf{PF}}_i^2}{\bar{\lambda}^2}\|\delta\|_2^2 \tag{2.12}$$

it is apparent that (2.10) and (2.11) fulfill the ISS properties derived in [14]. Further, condition (2.11) allows for an estimate on the guaranteed resulting stability margin around the origin under impact of the bounded input, where $V(\mathbf{x})$ is decreasing as long as (2.11) holds.

In fact, for bounded inputs of the system, guaranteeing the autonomous closed-loop stability of the TS model (2.3) results in the ISS property, since there always $\exists\bar{\lambda}$ in (2.9) [10]. However, as will be discussed for the observer design with unmeasurable premise variables, introducing a restriction in form of (2.11) in the LMI design process can be used to impose a desired stability margin around the origin.

2.3.1.2   Decay rate

LMIs (2.7) constrain the eigenvalues of the solution at the vertices λ_i, i.e., $\det(\mathbf{G}_i - \lambda_i\mathbf{I}) = 0$, to lie anywhere within the left half of the complex plane. It is well known for linear systems that the transient response is governed by the location of the eigenvalues in the complex plane. Due to the non-linear nature of the system, TS systems perform with variable transient responses depending on the current operating point. However, a good indicator of the transient properties of the overall non-linear system is the location of the eigenvalues at the vertices of the polytopic description. Consequently, by influencing the location of the eigenvalues of the linear closed-loop sub-models, the dynamic behavior of the non-linear system can be designed to account for requirements that arise from e.g. the physical application.

The introduction of an additional term to the LMIs (2.7) guarantees a decay rate α at which system (2.3) at least moves towards a stable equilibrium [9]. It results from restricting the Lyapunov function candidates derivate to an upper bound $\dot{V}(\mathbf{x}) < -2\alpha V(\mathbf{x})$ and is given in terms of LMIs as

$$\mathbf{G}_i^{\mathrm{T}}\mathbf{P} + \mathbf{P}\mathbf{G}_i + 2\alpha\mathbf{P} \prec 0 \tag{2.13}$$

for $i = 1, ..., N_r$, where the reformulation to $\mathbf{G}_i^{\mathrm{T}}\mathbf{P} + \mathbf{P}\mathbf{G}_i \prec -\alpha\mathbf{P} - \alpha\mathbf{P}$ directly indicates that all real parts of the eigenvalues of $\mathbf{G}_i$ attain at least $\mathrm{Re}(\lambda_i) < -\alpha$.
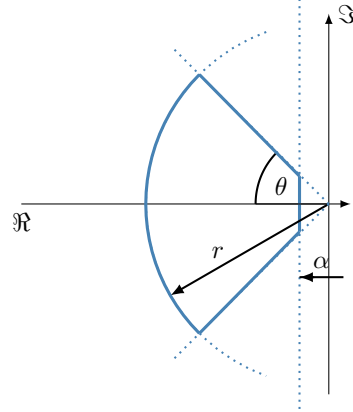
Figure 2.2: Graphical representation of the subset $\mathcal{S}(\alpha, r, \theta)$ in the complex plane defined by (2.14)

2.3.1.3 LMI region in the complex plane

In many applications there is a limit to the maximum attainable decay rate of the systems response, e.g. from loading aspects or acutator saturation. Further, the transient response of the system is often restricted by certain natural frequencies of the process, which can be characterized as the imaginary part of the closed-loop eigenvalue $\mathrm{Im}(\lambda_i)$, as discussed for the wind turbine in Sec. 2.4. Therefore, the excitation of un-modeled dynamics may be prevented by imposing a restriction of the resulting eigenvalues λ_i on the admissible subset in the complex plane, such that a desired transient behavior of the system occurs.

In [15] a LMI representation for eigenvalues of a linear system to be located in region $\mathcal{S}(\alpha, r, \theta)$, which is shown in Fig. 2.2, is presented. This formulation can be extended to TS models by the following LMIs for $i = 1, ..., N_r$ [16]

$$\mathbf{G}_i^{\mathrm{T}}\mathbf{P} + \mathbf{P}\mathbf{G}_i + 2\alpha\mathbf{P} \prec 0 \,,$$

$$\begin{bmatrix} -r\mathbf{P} & \mathbf{P}\mathbf{G}_i \\ \mathbf{G}_i^{\mathrm{T}}\mathbf{P} & -r\mathbf{P} \end{bmatrix} \prec 0 \,, \tag{2.14}$$

$$\begin{bmatrix} \sin\theta\big(\mathbf{G}_i^{\mathrm{T}}\mathbf{P} + \mathbf{P}\mathbf{G}_i\big) & \cos\theta\big(\mathbf{P}\mathbf{G}_i - \mathbf{G}_i^{\mathrm{T}}\mathbf{P}\big) \\ \cos\theta\big(\mathbf{G}_i^{\mathrm{T}}\mathbf{P} - \mathbf{P}\mathbf{G}_i\big) & \sin\theta\big(\mathbf{G}_i^{\mathrm{T}}\mathbf{P} + \mathbf{P}\mathbf{G}_i\big) \end{bmatrix} \prec 0 \,.$$

If the LMIs in (2.14) hold, the system is said to be quadratically $\mathcal{D}$-stable and all poles of the vertices of the system $\mathbf{G}_i$, $i = 1, ..., N_r$ lie inside of $\mathcal{D}$, where $\mathcal{S}(\alpha, r, \theta)$ is one possible representation of a subset $\mathcal{D}$ of the complex plane. It consists of an α-stability region (2.13), a disk with a center at the origin and a cone given by $\mathcal{S}(0, 0, \theta)$ as the first, second and third LMI in (2.14), respectively.

2.3.1.4   Disturbance attenuation by $\mathcal{H}_2$ approach

Now consider a TS system subject to a disturbance $\mathbf{d} \in \mathbb{R}^{m_d}$ and given by

$$\dot{\mathbf{x}} = \sum_{i=1}^{N_r} h_i(\mathbf{z}) \left(\mathbf{G}_i \mathbf{x} + \mathbf{D}_i \mathbf{d} \right) , \tag{2.15}$$

where $\mathbf{D}_i$ is the non-linear disturbance distribution matrix in TS formulation. The impact of the disturbance on the system can be characterized in terms of the $\mathcal{L}_2 \to \mathcal{L}_2$ gain $\gamma > 0$

$$\frac{\|\mathbf{x}\|_2}{\|\mathbf{d}\|_2} \leq \gamma \quad \Longleftrightarrow \quad \mathbf{x}^{\mathrm{T}} \mathbf{x} - \gamma^2 \mathbf{d}^{\mathrm{T}} \mathbf{d} \leq 0 . \tag{2.16}$$

The aim of the control synthesis is to minimize gain γ, which implies an attenuation of the disturbance $\mathbf{d}$ on the system states $\mathbf{x}$ of γ. The characterization of the $\mathcal{L}_2 \to \mathcal{L}_2$ gain in (2.16) is a LMI and can be introduced into negativity condition of the Lyapunov function candidates derivative in (2.4) to form [10]

$$\dot{V}(\mathbf{x}) + \mathbf{x}^{\mathrm{T}} \mathbf{x} - \gamma^2 \mathbf{d}^{\mathrm{T}} \mathbf{d} < 0 . \tag{2.17}$$

From integrating expression (2.17), assuming a resulting stable system $V(\mathbf{x}(\infty)) = 0$, and setting the initial condition to $\mathbf{x}(0) = \mathbf{0}$

$$\int_0^\infty (\gamma^2 \mathbf{d}^{\mathrm{T}} \mathbf{d} - \mathbf{x}^{\mathrm{T}} \mathbf{x}) \mathrm{d}t > 0 \tag{2.18}$$

is obtained as the solution to the corresponding Lyapunov function. This is equivalent to the attenuation condition represented by (2.16). Therefore, using the system description subject to disturbance in (2.15), the derivative of the Lyapunov function candidate in (2.5) and expansion with respect to the property of the membership functions $\sum_{i=1}^{N_r} h_i(\mathbf{z}) = 1$, stability condition (2.17) results in

$$\sum_{i=1}^{N_r} h_i(\mathbf{z}) \left(\mathbf{x}^{\mathrm{T}} \mathbf{G}_i^{\mathrm{T}} \mathbf{P} \mathbf{x} + \mathbf{x}^{\mathrm{T}} \mathbf{P} \mathbf{G}_i \mathbf{x} + \mathbf{d}^{\mathrm{T}} \mathbf{D}_i^{\mathrm{T}} \mathbf{P} \mathbf{x} + \mathbf{x}^{\mathrm{T}} \mathbf{P} \mathbf{D}_i \mathbf{d} + \mathbf{x}^{\mathrm{T}} \mathbf{x} - \gamma^2 \mathbf{d}^{\mathrm{T}} \mathbf{d} \right) < 0 , \tag{2.19}$$

or equivalently

$$\sum_{i=1}^{N_r} h_i(\mathbf{z}) \begin{bmatrix} \mathbf{x}^{\mathrm{T}} & \mathbf{d}^{\mathrm{T}} \end{bmatrix} \begin{bmatrix} \mathbf{G}_i^{\mathrm{T}} \mathbf{P} + \mathbf{P} \mathbf{G}_i + \mathbf{I}_n & \mathbf{P} \mathbf{D}_i \\ \mathbf{D}_i^{\mathrm{T}} \mathbf{P} & -\gamma^2 \mathbf{I}_{m_d} \end{bmatrix} \begin{bmatrix} \mathbf{x} \\ \mathbf{d} \end{bmatrix} < 0 . \tag{2.20}$$

As a result, stability of the system and an attenuation $\gamma > 0$ from the disturbance to the states of the system is verified if

$$\begin{bmatrix} \mathbf{G}_i^{\mathrm{T}} \mathbf{P} + \mathbf{P} \mathbf{G}_i + \mathbf{I}_n & \mathbf{P} \mathbf{D}_i \\ \mathbf{D}_i^{\mathrm{T}} \mathbf{P} & -\gamma^2 \mathbf{I}_{m_d} \end{bmatrix} \prec 0 \tag{2.21}$$

with respect to a matrix $\mathbf{P} = \mathbf{P}^{\mathrm{T}} \succ 0$ holds.

The presented stability conditions form the basis for both the following observer and controller synthesis. In the remainder of the section, the proposed controller is described, and the synthesis of the necessary feedback gains are formulated in terms of LMIs.

2.3.2 Control synthesis

The control design is based on the disturbed TS system in form of

$$\dot{\mathbf{x}} = \sum_{i=1}^{N_r} h_i(\mathbf{z})\big(\mathbf{A}_i\mathbf{x} + \mathbf{B}_i\mathbf{u} + \mathbf{D}_i\mathbf{d}\big) \ . \tag{2.22}$$

For control design it is assumed that the N_r pairs $(\mathbf{A}_i, \mathbf{B}_i)$ are controllable. The proposed state feedback is the Parallel-Distributed Compensation (PDC) control law [9, 10], which accordingly to the TS structure consists of N_r feedback matrices $\mathbf{K}_i$ blended by the membership functions $h_i(\mathbf{z})$ or as will be derived for the wind turbine application on the estimate of the membership functions $\sum_{j=1}^{N_r} h_j(\hat{\mathbf{z}})$. Consequently, the PDC control law is given by [9, 10]

$$\mathbf{u} = -\sum_{j=1}^{N_r} h_j(\mathbf{z})\mathbf{K}_j\mathbf{x} \ . \tag{2.23}$$

As a result, the closed-loop TS system under impact of the PDC control (2.23) is denoted as

$$\dot{\mathbf{x}} = \sum_{i=1}^{N_r} h_i(\mathbf{z})\bigg(\big(\mathbf{A}_i - \sum_{j=1}^{N_r} h_j(\mathbf{z})\mathbf{B}_i\mathbf{K}_j\big)\mathbf{x} + \mathbf{D}_i\mathbf{d} \bigg) = \sum_{i=1}^{N_r} h_i(\mathbf{z})\big(\mathbf{G}_i\mathbf{x} + \mathbf{D}_i\mathbf{d}\big) \ , \tag{2.24}$$

where from expansion with respect to the convex sum property $\sum_{j=1}^{N_r} h_j(\mathbf{z}) = 1$ the closed-loop system matrix is given by $\mathbf{G}_i = \sum_{j=1}^{N_r} h_j(\mathbf{z})(\mathbf{A}_i - \mathbf{B}_i\mathbf{K}_j)$.

2.3.2.1 Control synthesis: decay rate

Assuming an undisturbed system, i.e. $\mathbf{d} = 0$, stability condition (2.13) from a quadratic Lyapunov function approach for the closed-loop TS system in (2.24) reads as

$$\mathbf{A}_i^{\mathrm{T}}\mathbf{P} + \mathbf{P}\mathbf{A}_i - \mathbf{K}_j^{\mathrm{T}}\mathbf{B}_i^{\mathrm{T}}\mathbf{P} - \mathbf{P}\mathbf{B}_i\mathbf{K}_j + 2\alpha\mathbf{P} \prec 0 \ . \tag{2.25}$$

Since the objective of the LMI solver is to determine $\mathbf{P}$ and $\mathbf{K}_j$ simultaneously, the given constraint is bi-linear. By employing the matrix $\mathbf{X} = \mathbf{X}^{\mathrm{T}} = \mathbf{P}^{-1}$ to derive a congruent inequality $\mathbf{X}(2.25)\mathbf{X}$, the control synthesis of the N_r feedback gains $\mathbf{K}_i$ with respect to a guaranteed decay rate $\alpha > 0$ can be formulated as LMIs in the following way.

Determine the matrix $\mathbf{X} = \mathbf{X}^{\mathrm{T}} \succ 0$ and N_r matrices $\mathbf{M}_j$ with respect to a decay rate α constraint by [9]

$$\mathbf{X}\mathbf{A}_i^{\mathrm{T}} + \mathbf{A}_i\mathbf{X} - \mathbf{M}_j^{\mathrm{T}}\mathbf{B}_i^{\mathrm{T}} - \mathbf{B}_i\mathbf{M}_j + 2\alpha\mathbf{X} \prec 0 \tag{2.26}$$

for every combination $i, j = 1, ..., N_r$ such that $h_i \cdot h_j \neq 0$. The positive definite matrix fulfilling the Lyapunov function in (2.4) is given by $\mathbf{P} = \mathbf{X}^{-1}$ and the N_r feedback matrices ensuring stability of the closed-loop non-linear TS system (2.24) are calculated by $\mathbf{K}_j = \mathbf{M}_j\mathbf{X}^{-1}$.

Remark. *The combination of i and j in LMIs (2.26) of the control synthesis plays an important role with respect to both feasibility and performance of the resulting feedback gains. In general, stability of the TS system is verified, if all possible combinations of $i = 1, ..., N_r$ and $j = 1, ..., N_r$ are respected in the synthesis. However, this results in a large number of LMIs and might impede the search for appropriate feedback gains $\mathbf{K}_i$, which need to ensure the stability and performance imposed by the LMIs at every vertex of the polytopic description. The additional condition $h_i \cdot h_j \neq 0$ accounts for the property of systems, where not every membership function may be active, i.e. $h_i \neq 0$, at the same time (or operational point), see e.g. the discussion in Sec. 2.4.4 for the control syntheses of the wind turbine application. Thus, the conservativeness of the LMIs is reduced by accounting for $h_i \cdot h_j \neq 0$. This consideration holds for all control and observer synthesis LMIs discussed in this contribution, where the double sum $\sum_{i=1}^{N_r} h_i(\mathbf{z}) \sum_{j=1}^{N_r} h_j(\mathbf{z})$ or $\sum_{i=1}^{N_r} h_i(\mathbf{z}) \sum_{j=1}^{N_r} h_j(\hat{\mathbf{z}})$ occurs.*

Remark. *For the derivation of the LMIs in the control synthesis by introducing $\mathbf{G}_i = \sum_{j=1}^{N_r} h_j(\mathbf{z})(\mathbf{A}_i - \mathbf{B}_i\mathbf{K}_j)$ into the LMIs presented in Sec. 2.3.1, all necessary terms can be expanded using the property $\sum_{j=1}^{N_r} h_j(\mathbf{z}) = 1$ to form e.g. $\sum_{j=1}^{N_r} h_j(\mathbf{z})(\mathbf{X}\mathbf{A}_i^{\mathrm{T}} + \mathbf{A}_i\mathbf{X} - \mathbf{M}_j^{\mathrm{T}}\mathbf{B}_i^{\mathrm{T}} - \mathbf{B}_i\mathbf{M}_j + 2\alpha\mathbf{X}) \prec 0$ from (2.26), which holds if (2.26) holds for the necessary combinations of i and j as discussed before.*

2.3.2.2 Control synthesis: LMI region constraint

Employing substitution $(\mathbf{P}, \mathbf{P}\mathbf{G}_i, \mathbf{G}_i^{\mathrm{T}}\mathbf{P}) \leftrightarrow (\mathbf{X}, \mathbf{G}_i\mathbf{X}, \mathbf{X}\mathbf{G}_i^{\mathrm{T}})$ [15], stability of the closed-loop system $\mathbf{G}_i$ in (2.24) constraint to the region $\mathcal{S}(\alpha, r, \theta)$ can be expressed based on (2.14), such that the following synthesis results.

Determine the matrix $\mathbf{X} = \mathbf{X}^{\mathrm{T}} \succ 0$ and N_r matrices $\mathbf{M}_j$ for a desired $\alpha > 0$, $r > 0$ and $\theta > 0$

constraint by

$$\mathbf{X}\mathbf{A}_i^{\mathrm{T}} + \mathbf{A}_i\mathbf{X} - \mathbf{M}_j^{\mathrm{T}}\mathbf{B}_i^{\mathrm{T}} - \mathbf{B}_i\mathbf{M}_j + 2\alpha\mathbf{X} \prec 0 \,,$$

$$\begin{bmatrix} -r\mathbf{X} & \mathbf{A}_i\mathbf{X} - \mathbf{B}_i\mathbf{M}_j \\ \mathbf{X}\mathbf{A}_i^{\mathrm{T}} - \mathbf{M}_j^{\mathrm{T}}\mathbf{B}_i^{\mathrm{T}} & -r\mathbf{X} \end{bmatrix} \prec 0 \,, \quad (2.27)$$

$$\begin{bmatrix} \sin\theta\big(\mathbf{X}\mathbf{A}_i^{\mathrm{T}} + \mathbf{A}_i\mathbf{X} - \mathbf{M}_j^{\mathrm{T}}\mathbf{B}_i^{\mathrm{T}} - \mathbf{B}_i\mathbf{M}_j\big) & \cos\theta\big(\mathbf{A}_i\mathbf{X} - \mathbf{B}_i\mathbf{M}_j - \mathbf{X}\mathbf{A}_i^{\mathrm{T}} + \mathbf{M}_j^{\mathrm{T}}\mathbf{B}_i^{\mathrm{T}}\big) \\ \cos\theta\big(\mathbf{X}\mathbf{A}_i^{\mathrm{T}} - \mathbf{M}_j^{\mathrm{T}}\mathbf{B}_i^{\mathrm{T}} - \mathbf{A}_i\mathbf{X} + \mathbf{B}_i\mathbf{M}_j\big) & \sin\theta\big(\mathbf{A}_i\mathbf{X} - \mathbf{B}_i\mathbf{M}_j + \mathbf{X}\mathbf{A}_i^{\mathrm{T}} - \mathbf{M}_j^{\mathrm{T}}\mathbf{B}_i^{\mathrm{T}}\big) \end{bmatrix} \prec 0$$

for all $i, j = 1, ..., N_r$ such that $h_i \cdot h_j \neq 0$. If (2.27) is solved, the eigenvalues of the closed-loop system (2.24) are located in $\mathcal{S}(\alpha, r, \theta)$, and the positive definite matrix fulfilling the Lyapunov function in (2.4) is given by $\mathbf{P} = \mathbf{X}^{-1}$. The N_r feedback matrices ensuring stability of the closed-loop non-linear TS system are calculated by $\mathbf{K}_j = \mathbf{M}_j\mathbf{X}^{-1}$.

2.3.2.3 Control synthesis: $\mathcal{H}_2$ disturbance attenuation

Inserting the closed-loop TS system (2.24) into (2.21) and applying the congruence matrix $\begin{pmatrix} \mathbf{X} & \mathbf{0} \\ \mathbf{0} & \mathbf{I} \end{pmatrix}$ yields

$$\begin{bmatrix} \mathbf{X}\mathbf{A}_i^{\mathrm{T}} + \mathbf{A}_i\mathbf{X} - \mathbf{M}_j^{\mathrm{T}}\mathbf{B}_i^{\mathrm{T}} - \mathbf{B}_i\mathbf{M}_j + \mathbf{X}\mathbf{X} & \mathbf{D}_i \\ \mathbf{D}_i^{\mathrm{T}} & -\gamma^2\mathbf{I}_{m_d} \end{bmatrix} \prec 0 \qquad (2.28)$$

and from separation of the quadratic term gives

$$\begin{bmatrix} \mathbf{X}\mathbf{A}_i^{\mathrm{T}} + \mathbf{A}_i\mathbf{X} - \mathbf{M}_j^{\mathrm{T}}\mathbf{B}_i^{\mathrm{T}} - \mathbf{B}_i\mathbf{M}_j & \mathbf{D}_i \\ \mathbf{D}_i^{\mathrm{T}} & -\gamma^2\mathbf{I}_{m_d} \end{bmatrix} + \begin{bmatrix} \mathbf{X} \\ \mathbf{0} \end{bmatrix} \begin{bmatrix} \mathbf{X} & \mathbf{0} \end{bmatrix} \prec 0 \,. \qquad (2.29)$$

Applying the Schur complement to (2.29) results in the following set of LMIs for a control synthesis guaranteeing an attenuation of γ.

Determine the matrix $\mathbf{X} = \mathbf{X}^{\mathrm{T}} \succ 0$ and N_r matrices $\mathbf{M}_j$ with respect to a desired γ constraint by

$$\begin{bmatrix} \mathbf{X}\mathbf{A}_i^{\mathrm{T}} + \mathbf{A}_i\mathbf{X} - \mathbf{M}_j^{\mathrm{T}}\mathbf{B}_i^{\mathrm{T}} - \mathbf{B}_i\mathbf{M}_j & \mathbf{D}_i & \mathbf{X} \\ \mathbf{D}_i^{\mathrm{T}} & -\gamma^2\mathbf{I}_{m_d} & \mathbf{0} \\ \mathbf{X} & \mathbf{0} & -\mathbf{I}_n \end{bmatrix} \prec 0 \qquad (2.30)$$

for $i = 1, ..., N_r$, $j = 1, ..., N_r$ such that $h_i \cdot h_j \neq 0$. Moreover, by a change of variable $\Gamma = \gamma^2$, the LMI solver can be employed to minimize Γ.

2.3.2.4   Control synthesis: mixed $\mathcal{H}_2$ disturbance attenuation and LMI region constraint

In some applications, like discussed for the wind turbine in Sec. 2.4, minimizing the disturbance attenuation within a particular LMI region might be favorable. For that reason, a mixed LMI constraint from the previously discussed LMIs can be formed similar to the approach for linear systems in [15]. Increasing the attenuation from the disturbance to the system states pushes the resulting eigenvalue of the closed-loop system further into left half of the complex plane, see e.g. Tab. 2.1 in Sec. 2.4, and consequently has similar effects like introducing a decay rate α in (2.27). Since stability of the closed-loop system is verified by (2.30), combining it with (2.27), where the first LMI respecting the guaranteed decay rate α is omitted, results in a mixed criterion ensuring an attenuation of γ with eigenvalues of the closed-loop system restricted to $\mathcal{S}(0, r, \theta)$. Formulated in terms of LMIs, this property is verified if for all $i, j = 1, ..., N_r$ such that $h_i \cdot h_j \neq 0$, $\mathbf{X} = \mathbf{X}^\mathrm{T} \succ 0$ and N_r matrices $\mathbf{M}_j$ the following LMI conditions hold

$$
\begin{bmatrix}
\mathbf{X}\mathbf{A}_i^\mathrm{T} + \mathbf{A}_i\mathbf{X} - \mathbf{M}_j^\mathrm{T}\mathbf{B}_i^\mathrm{T} - \mathbf{B}_i\mathbf{M}_j & \mathbf{D}_i & \mathbf{X} \\
\mathbf{D}_i^\mathrm{T} & -\gamma^2\mathbf{I}_{m_d} & \mathbf{0} \\
\mathbf{X} & \mathbf{0} & -\mathbf{I}_n
\end{bmatrix} \prec 0 \,,
$$

$$
\begin{bmatrix}
-r\mathbf{X} & \mathbf{A}_i\mathbf{X} - \mathbf{B}_i\mathbf{M}_j \\
\mathbf{X}\mathbf{A}_i^\mathrm{T} - \mathbf{M}_j^\mathrm{T}\mathbf{B}_i^\mathrm{T} & -r\mathbf{X}
\end{bmatrix} \prec 0 \,, \tag{2.31}
$$

$$
\begin{bmatrix}
\sin\theta\big(\mathbf{X}\mathbf{A}_i^\mathrm{T} + \mathbf{A}_i\mathbf{X} - \mathbf{M}_j^\mathrm{T}\mathbf{B}_i^\mathrm{T} - \mathbf{B}_i\mathbf{M}_j\big) & \cos\theta\big(\mathbf{A}_i\mathbf{X} - \mathbf{B}_i\mathbf{M}_j - \mathbf{X}\mathbf{A}_i^\mathrm{T} + \mathbf{M}_j^\mathrm{T}\mathbf{B}_i^\mathrm{T}\big) \\
\cos\theta\big(\mathbf{X}\mathbf{A}_i^\mathrm{T} - \mathbf{M}_j^\mathrm{T}\mathbf{B}_i^\mathrm{T} - \mathbf{A}_i\mathbf{X} + \mathbf{B}_i\mathbf{M}_j\big) & \sin\theta\big(\mathbf{A}_i\mathbf{X} - \mathbf{B}_i\mathbf{M}_j + \mathbf{X}\mathbf{A}_i^\mathrm{T} - \mathbf{M}_j^\mathrm{T}\mathbf{B}_i^\mathrm{T}\big)
\end{bmatrix} \prec 0 \,.
$$

2.3.3   Observer synthesis

An observer for the TS system represented by (2.22) with a linear output defined as $\mathbf{y} = \mathbf{C}\mathbf{x}$ and estimated premise variables $\hat{\mathbf{z}}$ is denoted as [10]

$$
\dot{\hat{\mathbf{x}}} = \sum_{i=1}^{N_r} h_i(\hat{\mathbf{z}})\big(\mathbf{A}_i\hat{\mathbf{x}} + \mathbf{B}_i\mathbf{u} + \mathbf{L}_i(\mathbf{y} - \hat{\mathbf{y}})\big) \,,
$$

$$
\hat{\mathbf{y}} = \mathbf{C}\hat{\mathbf{x}} \,, \tag{2.32}
$$

where in the following it is assumed that the N_r pairs $\big(\mathbf{A}_i, \mathbf{C}\big)$ are observable. The structure of the observer described by (2.32) resembles the well-known Luenberger observer with a feedback term blended by the convex membership functions $\sum_{i=1}^{N_r} h_i(\hat{\mathbf{z}})\mathbf{L}_i$. By ensuring stability of the observation error $\mathbf{e} = \mathbf{x} - \hat{\mathbf{x}}$, the convergence of the estimated states to the real states $\hat{\mathbf{x}} \to \mathbf{x}$ is verified. Therefore,

consider the observer error dynamics $\dot{\mathbf{e}}$ of system (2.22) specified as [17]

$$\dot{\mathbf{e}} = \dot{\mathbf{x}} - \dot{\hat{\mathbf{x}}} + \underbrace{\sum_{i=1}^{N_r} h_i(\hat{\mathbf{z}})\big(\mathbf{A}_i\mathbf{x} + \mathbf{B}_i\mathbf{u} + \mathbf{D}_i\mathbf{d}\big) - \sum_{i=1}^{N_r} h_i(\hat{\mathbf{z}})\big(\mathbf{A}_i\mathbf{x} + \mathbf{B}_i\mathbf{u} + \mathbf{D}_i\mathbf{d}\big)}_{=0} \qquad (2.33)$$

resulting in

$$\dot{\mathbf{e}} = \sum_{i=1}^{N_r} h_i(\hat{\mathbf{z}})\big((\mathbf{A}_i - \mathbf{L}_i\mathbf{C})\mathbf{e} + \mathbf{D}_i\mathbf{d}\big) + \underbrace{\Big(\sum_{i=1}^{N_r} h_i(\mathbf{z}) - \sum_{i=1}^{N_r} h_i(\hat{\mathbf{z}})\Big)\big(\mathbf{A}_i\mathbf{x} + \mathbf{B}_i\mathbf{u} + \mathbf{D}_i\mathbf{d}\big)}_{:=\Delta(\mathbf{z},\hat{\mathbf{z}},\mathbf{x},\mathbf{u},\mathbf{d})} . \qquad (2.34)$$

The premise vector $\mathbf{z}$ may be unmeasurable but estimated, which is accounted for by the notation $\sum_{i=1}^{N_r} h_i(\hat{\mathbf{z}})$.

2.3.3.1 Observer synthesis: measurable premise variable

In many applications the premise variables may depend on an output or a measurable exogenous signal of the process. In those cases, where $\mathbf{z}$ is completely measurable, the error dynamic reduces to

$$\dot{\mathbf{e}} = \sum_{i=1}^{N_r} h_i(\mathbf{z})\big((\mathbf{A}_i - \mathbf{L}_i\mathbf{C})\mathbf{e} + \mathbf{D}_i\mathbf{d}\big) . \qquad (2.35)$$

The error dynamic given by (2.35) is compatible with the structure of the system represented by (2.24), and thus a quadratic Lyapunov candidate function $V(\mathbf{e}) = \mathbf{e}^{\mathrm{T}}\mathbf{P}\mathbf{e}$ can be applied accordingly. Therefore the results from deriving the stability condition in Sec. 2.3.1 can be readily applied for the observer synthesis by introducing the closed-loop state matrices $\mathbf{G}_i = \mathbf{A}_i - \mathbf{L}_i\mathbf{C}$. As a result, a **minimum decay rate** α in the convergence from the observer to the system states $\hat{\mathbf{x}} \to \mathbf{x}$ is guaranteed, if a positive definite matrix $\mathbf{P} = \mathbf{P}^{\mathrm{T}} \succ 0$ and N_r matrices $\mathbf{N}_i$ for $i = 1, ..., N_r$ are found fulfilling

$$\mathbf{A}_i^{\mathrm{T}}\mathbf{P} + \mathbf{P}\mathbf{A}_i - \mathbf{N}_i\mathbf{C} - \mathbf{C}^{\mathrm{T}}\mathbf{N}_i^{\mathrm{T}} + 2\alpha\mathbf{P} \prec 0 , \qquad (2.36)$$

where the feedback gains are obtained from $\mathbf{L}_i = \mathbf{P}^{-1}\mathbf{N}_i$. In addition, $\mathcal{D}$-**stability** implying that the closed-loop eigenvalues of the error dynamic at the vertices of the convex description are restricted to the **subset** $\mathcal{S}(\alpha, r, \theta)$ for a given $\alpha > 0$, $r > 0$ and $\theta > 0$ is verified, if a positive definite matrix

$\mathbf{P} = \mathbf{P}^{\mathrm{T}} \succ 0$ and N_r matrices $\mathbf{N}_i$ for $i = 1, ..., N_r$ constrained by

$$\mathbf{A}_i^{\mathrm{T}}\mathbf{P} + \mathbf{PA}_i - \mathbf{N}_i\mathbf{C} - \mathbf{C}^{\mathrm{T}}\mathbf{N}_i^{\mathrm{T}} + 2\alpha\mathbf{P} \prec 0$$

$$\begin{bmatrix} -r\mathbf{P} & \mathbf{PA}_i - \mathbf{N}_i\mathbf{C} \\ \mathbf{A}_i^{\mathrm{T}}\mathbf{P} - \mathbf{C}^{\mathrm{T}}\mathbf{N}_i^{\mathrm{T}} & -r\mathbf{P} \end{bmatrix} \prec 0 \tag{2.37}$$

$$\begin{bmatrix} \sin\theta\left(\mathbf{A}_i^{\mathrm{T}}\mathbf{P} + \mathbf{PA}_i - \mathbf{N}_i\mathbf{C} - \mathbf{C}^{\mathrm{T}}\mathbf{N}_i^{\mathrm{T}}\right) & \cos\theta\left(\mathbf{PA}_i - \mathbf{N}_i\mathbf{C} - \mathbf{A}_i^{\mathrm{T}}\mathbf{P} + \mathbf{C}^{\mathrm{T}}\mathbf{N}_i^{\mathrm{T}}\right) \\ \cos\theta\left(\mathbf{A}_i^{\mathrm{T}}\mathbf{P} - \mathbf{C}^{\mathrm{T}}\mathbf{N}_i^{\mathrm{T}} - \mathbf{PA}_i + \mathbf{N}_i\mathbf{C}\right) & \sin\theta\left(\mathbf{A}_i^{\mathrm{T}}\mathbf{P} + \mathbf{PA}_i - \mathbf{N}_i\mathbf{C} - \mathbf{C}^{\mathrm{T}}\mathbf{N}_i^{\mathrm{T}}\right) \end{bmatrix} \prec 0$$

are determined. Accordingly, a **disturbance attenuation** to the error states $\|\mathbf{e}\|_2 \leq \gamma\|\mathbf{d}\|_2$ of γ is verified, if a solution for $\mathbf{P} = \mathbf{P}^{\mathrm{T}} \succ 0$ and N_r matrices $\mathbf{N}_i$ for $i = 1, ..., N_r$ constraint by

$$\begin{bmatrix} \mathbf{A}_i^{\mathrm{T}}\mathbf{P} + \mathbf{PA}_i - \mathbf{C}^{\mathrm{T}}\mathbf{N}_i^{\mathrm{T}} - \mathbf{N}_i\mathbf{C} + \mathbf{I}_n & \mathbf{PD}_i \\ \mathbf{D}_i^{\mathrm{T}}\mathbf{P} & -\gamma^2\mathbf{I}_{m_d} \end{bmatrix} \prec 0 \tag{2.38}$$

is determined.

2.3.3.2   Observer synthesis: unmeasurable premise variable

For applications that depend on an unmeasurable state as premise variable, the estimated states of the observer can be used to calculate the membership functions of the TS feedback loop. However, in the transient region where the observer states $\hat{\mathbf{x}}$ converge to the real states $\mathbf{x}$, this induces an additional disturbance term denoted as Δ in (2.34), which stems from the error in the calculation of the membership function $\sum_{i=1}^{N_r} h_i(\mathbf{z}) - \sum_{i=1}^{N_r} h_i(\hat{\mathbf{z}})$. This error term converges $\rightarrow 0$ as the states of the observer move towards the real states of the system.

To ensure stability with respect to unmeasurable premise variables that are states of the TS systems, in [18] a synthesis is proposed. However, as also stated in [19], the synthesis is conservative when accounting for the unmeasurable premise variable. For that reason in [19] an observer design is presented that employs an assumption on the maximum occurring mismatch from the calculation of the estimated membership functions $h_i(\hat{\mathbf{x}})$. The negativity of the Lyapunov derivative is ensured despite of $\Delta(\mathbf{x}, \hat{\mathbf{x}}, \mathbf{u})$ influencing system (2.34). The impact on the Lyapunov function derivative is upper bounded by $\|h_i(\mathbf{x})\mathbf{x} - h_i(\hat{\mathbf{x}})\hat{\mathbf{x}}\|_2 \leq O_i\|\mathbf{e}\|_2$ and $\|\left(h_i(\mathbf{x}) - h_i(\hat{\mathbf{x}})\right)\mathbf{u}\|_2 \leq U_i\|\mathbf{e}\|_2$, where O_i and U_i are appropriate real matrices with all components being positive definite.

Here, TS observers with states as unmeasurable premise variables are considered by a different approach. The error in the calculation will be accounted by combining the necessary linear sub-models in the observer synthesis to ensure convergence to a defined stability margin imposed by the ISS concept, see Sec. 2.3.1.1. The presented LMI condition is less restrictive with respect to the influence

of the error term from the unknown premise variable, i.e. to the bounded disturbance induced by the mismatch of the calculated membership functions. In the feedback synthesis term $\Delta(\mathbf{x}, \hat{\mathbf{x}}, \mathbf{u})$ is not entirely included in the presented approach. However, this property is derived at cost of combining more linear sub-models within the synthesis, imposing a different source of conservatism on this LMI-based approach.

Therefore, consider rewriting the error dynamics with respect to convexity $\sum_{j=1}^{N_r} h_j(\hat{\mathbf{z}}) = \sum_{i=1}^{N_r} h_i(\mathbf{z}) = 1$ as $\dot{\mathbf{e}} = \sum_{j=1}^{N_r} h_j(\hat{z})\dot{\mathbf{x}} - \sum_{i=1}^{N_r} h_i(\mathbf{z})\dot{\hat{\mathbf{x}}}$ and reformulating the state matrix of the observer as $\mathbf{A}_j = (\mathbf{A}_j + \mathbf{A}_i - \mathbf{A}_i)$.

This yields

$$\dot{\mathbf{e}} = \sum_{i=1}^{N_r} h_i(\mathbf{z}) \sum_{j=1}^{N_r} h_j(\hat{\mathbf{z}})\big((\mathbf{A}_i - \mathbf{L}_j\mathbf{C})\mathbf{e} + \Delta\mathbf{A}_{i,j}\hat{\mathbf{x}} + \Delta\mathbf{B}_{i,j}\mathbf{u}\big) , \qquad (2.39)$$

with $\Delta\mathbf{A}_{i,j} = (\mathbf{A}_i - \mathbf{A}_j)$ and $\Delta\mathbf{B}_{i,j} = (\mathbf{B}_i - \mathbf{B}_j)$. By inserting $\hat{\mathbf{x}} = (\mathbf{x} - \mathbf{e})$, the error dynamics are given by

$$\dot{\mathbf{e}} = \sum_{i=1}^{N_r} h_i(\mathbf{z}) \sum_{j=1}^{N_r} h_j(\hat{\mathbf{z}})\big((\mathbf{A}_i - \mathbf{L}_j\mathbf{C} - \Delta\mathbf{A}_{i,j})\mathbf{e} + \Delta\mathbf{A}_{i,j}\mathbf{x} + \Delta\mathbf{B}_{i,j}\mathbf{u}\big) . \qquad (2.40)$$

As also argued in [19], if the membership functions are Lipschitz and the input $\mathbf{u}$ of the system is bounded, then the state $\mathbf{x}$ is also bounded. Thus the ISS property is applicable to the disturbance resulting from the mismatch in the estimation and the current state $\mathbf{x}$ and input $\mathbf{u}$ of the system. Therefore, only the closed-loop system matrix $(\mathbf{A}_i - \Delta\mathbf{A}_{i,j} - \mathbf{L}_j\mathbf{C})$ determines the ISS property. In case of an unmeasurable premise variable, here the disturbance in (2.34) is assumed to be $\mathbf{d} = 0$. This is reasonable for the presented application of the wind turbine, since the main task of the observer is to estimate the current wind speed, and thus the disturbance of the system is included as an augmented state in the system description. The following theorems provide the basis for the wind speed observer design.

Theorem. *The observer with unmeasurable states as premise variables and a closed-loop error dynamic of* (2.40) *is ISS if a positive definite matrix* $\mathbf{P} = \mathbf{P}^{\mathrm{T}} \succ 0$ *for* $V(\mathbf{e}) = \mathbf{e}^{\mathrm{T}}\mathbf{P}\mathbf{e}$ *and* N_r *matrices* $\mathbf{N}_j$ *for* $i, j = 1, ..., N_r$ *are found fulfilling*

$$(\mathbf{A}_i - \Delta\mathbf{A}_{i,j})^{\mathrm{T}}\mathbf{P} + \mathbf{P}(\mathbf{A}_i - \Delta\mathbf{A}_{i,j}) - \mathbf{N}_j\mathbf{C} - \mathbf{C}^{\mathrm{T}}\mathbf{N}_j^{\mathrm{T}} \prec 0 , \qquad (2.41)$$

where the feedback gains are obtained from $\mathbf{L}_j = \mathbf{P}^{-1}\mathbf{N}_j$.

Proof. The bounded inputs $\mathbf{x}$ and $\mathbf{u}$ can omitted for applying ISS property, and and thus the derivative

of the quadratic Lyapunov function $V(\mathbf{e}) = \mathbf{e}^{\mathrm{T}}\mathbf{P}\mathbf{e}$ is denoted as

$$\dot{V}(\mathbf{e}) = \sum_{i=1}^{N_r} h_i(\mathbf{z}) \sum_{j=1}^{N_r} h_j(\hat{\mathbf{z}})\mathbf{e}^{\mathrm{T}}\big((\mathbf{A}_i - \Delta\mathbf{A}_{i,j})^{\mathrm{T}}\mathbf{P} + \mathbf{P}(\mathbf{A}_i - \Delta\mathbf{A}_{i,j}) - \mathbf{C}^{\mathrm{T}}\mathbf{N}_j^{\mathrm{T}} - \mathbf{N}_j\mathbf{C}\big)\mathbf{e} < 0 \ , \quad (2.42)$$

which holds if (2.41) is verified. $\qquad\qquad\qquad\qquad\qquad\qquad\qquad\qquad\qquad\qquad\qquad\qquad\qquad\square$

It is interesting to notice that by inserting $\Delta\mathbf{A}_{i,j} = (\mathbf{A}_i - \mathbf{A}_j)$ in (2.41), condition (2.36) with $\alpha = 0$ results, since $\mathbf{A}_i - \Delta\mathbf{A}_{i,j} = \mathbf{A}_j$. However, the given description with respect to a variation of i and j allows for the derivation of the following theorem that ensures the convergence to a defined stability margin with respect to a bounded input in case of an estimation error of the premise variable.

Theorem. *The observer with unmeasurable states as premise variables and a closed-loop error dynamic of (2.40) is ISS and the occurring error due to the bounded input $\mathbf{x}$ is confined to a stability margin defined by ϵ, if a positive definite matrix $\mathbf{P} = \mathbf{P}^{\mathrm{T}} \succ 0$ for $V(\mathbf{e}) = \mathbf{e}^{\mathrm{T}}\mathbf{P}\mathbf{e}$ and N_r matrices $\mathbf{N}_j$ are determined for $i, j = 1, ..., N_r$ and a given matrix $\mathbf{Q} = \mathbf{Q}^{\mathrm{T}} \succ 0$ fulfilling*

$$\begin{bmatrix} (\mathbf{A}_i - \Delta\mathbf{A}_{i,j})^{\mathrm{T}}\mathbf{P} + \mathbf{P}(\mathbf{A}_i - \Delta\mathbf{A}_{i,j}) - \mathbf{N}_j\mathbf{C} - \mathbf{C}^{\mathrm{T}}\mathbf{N}_j + \epsilon^2\mathbf{Q} & \mathbf{P}\Delta\mathbf{A}_{i,j} \\ \Delta\mathbf{A}_{i,j}^{\mathrm{T}}\mathbf{P} & -\mathbf{Q} \end{bmatrix} \prec 0 \ . \qquad (2.43)$$

Proof. The resulting error from the bounded inputs is confined to a stability margin around the origin depending on $\mathbf{x}$, $\mathbf{u}$ and the resulting closed-loop dynamic of the observer in (2.40). However, a margin of stability can also be defined beforehand, such that if the LMIs are solved, the desired margin around the origin is verified. So consider the case whenever

$$\|\mathbf{x}\|_2 \le \epsilon\|\mathbf{e}\|_2 \quad (\text{or} \quad \|\mathbf{u}\|_2 \le \epsilon\|\mathbf{e}\|_2) \qquad (2.44)$$

holds in operation, which by employing in the estimate of the Lyapunov function derivative implies that the observer error $\mathbf{e}$ decays to (2.44) as long as the condition holds, see also the margin given by (2.11).

Since it can be addressed by the ISS property, neglecting the term introduced by $\mathbf{u}$ in (2.40) does not violate the stability conditions. The derivative of a quadratic Lyapunov function with respect to the bounded input $\mathbf{x}$ is given by

$$\dot{V}(\mathbf{e}) = \sum_{i=1}^{N_r} h_i(\mathbf{z}) \sum_{j=1}^{N_r} h_j(\hat{\mathbf{z}})\Big(\mathbf{e}^{\mathrm{T}}\big((\mathbf{A}_i - \Delta\mathbf{A}_{i,j})^{\mathrm{T}}\mathbf{P} + \mathbf{P}(\mathbf{A}_i - \Delta\mathbf{A}_{i,j}) - \mathbf{C}^{\mathrm{T}}\mathbf{N}_j^{\mathrm{T}} - \mathbf{N}_j\mathbf{C}\big)\mathbf{e}$$
$$+\mathbf{x}^{\mathrm{T}}\Delta\mathbf{A}_{i,j}^{\mathrm{T}}\mathbf{P}\mathbf{e} + \mathbf{e}^{\mathrm{T}}\mathbf{P}\Delta\mathbf{A}_{i,j}\mathbf{x}\Big) \ . \qquad (2.45)$$

An upper bound of the Lyapunov function derivative outside of the stability margin imposed by (2.44) and using *Completion of Squares* property to achieve

$$\mathbf{x}^{\mathrm{T}} \Delta \mathbf{A}_{i,j}^{\mathrm{T}} \mathbf{P} \mathbf{e} + \mathbf{e}^{\mathrm{T}} \mathbf{P} \Delta \mathbf{A}_{i,j} \mathbf{x} \leq$$
$$\mathbf{x}^{\mathrm{T}} \mathbf{Q} \mathbf{x} + \mathbf{e}^{\mathrm{T}} \mathbf{P} \Delta \mathbf{A}_{i,j} \mathbf{Q}^{-1} \Delta \mathbf{A}_{i,j}^{\mathrm{T}} \mathbf{P} \mathbf{e} \leq$$
$$\epsilon^2 \mathbf{e}^{\mathrm{T}} \mathbf{Q} \mathbf{e} + \mathbf{e}^{\mathrm{T}} \mathbf{P} \Delta \mathbf{A}_{i,j} \mathbf{Q}^{-1} \Delta \mathbf{A}_{i,j}^{\mathrm{T}} \mathbf{P} \mathbf{e}$$

is denoted as

$$\dot{V}(\mathbf{e}) < \sum_{i=1}^{N_r} h_i(\mathbf{z}) \sum_{j=1}^{N_r} h_j(\hat{\mathbf{z}}) \big(\mathbf{e}^{\mathrm{T}} ((\mathbf{A}_i - \Delta \mathbf{A}_{i,j})^{\mathrm{T}} \mathbf{P} + \mathbf{P}(\mathbf{A}_i - \Delta \mathbf{A}_{i,j}) - \mathbf{N}_j \mathbf{C} - \mathbf{C}^{\mathrm{T}} \mathbf{N}_j$$
$$+ \epsilon^2 \mathbf{Q} + \mathbf{P} \Delta \mathbf{A}_{i,j} \mathbf{Q}^{-1} \Delta \mathbf{A}_{i,j}^{\mathrm{T}} \mathbf{P}) \mathbf{e} \big) < 0 \,, \tag{2.46}$$

which holds, if

$$(\mathbf{A}_i - \Delta \mathbf{A}_{i,j})^{\mathrm{T}} \mathbf{P} + \mathbf{P}(\mathbf{A}_i - \Delta \mathbf{A}_{i,j}) - \mathbf{N}_j \mathbf{C} - \mathbf{C}^{\mathrm{T}} \mathbf{N}_j + \epsilon^2 \mathbf{Q} + \mathbf{P} \Delta \mathbf{A}_{i,j} \mathbf{Q}^{-1} \Delta \mathbf{A}_{i,j}^{\mathrm{T}} \mathbf{P} \prec 0$$

is verified. This expression can be rearranged by applying the *Schur Complement*, such that (2.43) results. □

As a result, the observer synthesis with respect to stability margin (2.44) with unmeasurable premise variables can be formulated in the following approach. Determine $\mathbf{P} = \mathbf{P}^{\mathrm{T}} \succ 0$ and N_r matrices $\mathbf{N}_j$ for a given $\mathbf{Q} = \mathbf{Q}^{\mathrm{T}} \succ 0$ constraint by (2.43) for $i,j = 1,...,N_r$. If the problem is found feasible, calculate the feedback matrices from $\mathbf{L}_j = \mathbf{P}^{-1} \mathbf{N}_j$.

2.3.4 Gain optimization procedure

The TS model description allows for an additional and subsequent optimization procedure of the derived controller, observer or performance gains. It is based on a two step synthesis, where the first step consists in solving the former introduced LMIs. After a solution to the initial synthesis is found, properties resulting from the convex model structure are used to separate the feedback gain synthesis for each of the N_r gains individually. Originally introduced in [20], the procedure was employed for performance optimization of a TS proportional multi-integral observer for the fault reconstruction in non-linear systems subject to noise. Anyhow, here the optimization process is formulated in a generalized fashion, such that it can be applied to all presented LMIs in this contribution.

Essentially, the optimization procedure consists in finding a feasible solution to the same LMIs as in

the first design step. However, since the derived feedback gains from the LMI solver depend on the formulation of the posed problem, the introduction of results from the initial design stage enables for a reduction of the complexity for the employed LMI solver, where at the same time stability of the closed-loop system is still guaranteed. The reduction of complexity stems from a reduced number of matrix variables to be determined and a reduced number of LMIs constraining the solver operation. That way different feedback gains may be attained by the LMI solver compared to the initial LMI design step.

The optimization procedure employs the derived solution of the positive definite matrix $\mathbf{P} = \mathbf{P}^{\mathrm{T}} \succ 0$ from the initial design step. The LMI solver is used only to determine a feasible solution for each of the N_r feedback gains $\{\mathbf{L}_i, \mathbf{K}_i\}$ individually and only for the necessary combinations of i and j, see also the remark in Sec. 2.3.2. Since the originally derived matrix $\mathbf{P}$ is introduced in the LMI definitions for each of the N_r LMI solver operations, the initial stability conditions resulting from the Lyapunov function approach is not violated. Therefore, if the proposed optimization procedure is found feasible, employing the resulting N_r controller or observer gains and $\mathbf{P}$, condition (2.4) is verified and the performance imposed by the LMIs are attained. Therefore the overall control or observer synthesis in this contribution can be given as the following two step procedure, where the notation $(\star) \prec 0$ means that any LMI described in Sec. 2.3.2 may be introduced into this procedure. It is simultaneously denoted for both, the controller $\{\mathbf{X}, \mathbf{K}_i\}$ and observer design task $\{\mathbf{P}, \mathbf{N}_i\}$, see Sec. 2.3.2.

Step 1 - Initial design:
Determine the symmetric positive definite matrix $\{\mathbf{X}, \mathbf{P}\}$ and N_r matrices $\{\mathbf{M}_j, \mathbf{N}_j\}$ constraint by $(\star) \prec 0$ for all $i, j = 1, ..., N_r$ such that $h_i \cdot h_j \neq 0$.

Step 2 - Optimization:
If the initial design step is feasible, use the resulting $\{\mathbf{X}, \mathbf{P}\}$ from Step 1 and determine the matrix $\{\mathbf{M}_j, \mathbf{N}_j\}$ constraint by $(\star) \prec 0$ for each $j = 1, ..., N_r$ *individually* subject to a variation $i = 1, ..., N_r$ such that $h_i \cdot h_j \neq 0$.

Even though the two steps appear similar, and essentially describe the same formal stability problem, there are some differences with regard to the LMI solver. Whereas in the *first* design step there are $N_r + 1$ matrix variables to be determined, i.e. $\{\mathbf{M}_j, \mathbf{N}_j\}$ for $j = 1, ..., N_r$ and $\{\mathbf{X}, \mathbf{P}\}$, the *second* step consists in determining only 1 matrix variable $\{\mathbf{M}_j, \mathbf{N}_j\}$ for a given $\{\mathbf{X}, \mathbf{P}\}$. Additionally, the number of LMIs that constrain the feasible solution are reduced from a maximum of N_r^2 if all sub-models are interconnected, i.e. $h_i \cdot h_j \neq 0, \; \forall i, j$, to a maximum number of N_r in the optimization step for entirely interconnected sub-models. Therefore, the two steps describe the same stability problem, but the reformulation in the optimization procedure is numerically less extensive due to knowledge

from the first design step and stability is verified due to the convex properties of the TS description.

2.4 Application to wind turbine control

Wind turbines are highly non-linear systems with many dynamically interacting components. Its dynamics depend heavily on the current wind speed that at the same time represents the disturbance of the process [4].

In general, the aim of the controller depends on the current operating region of the wind turbine [21]. The aim in partial load region is to optimize the extraction of power from the incoming wind field. In full load region, where the wind results in rated power production, the aim is to reduce the structural loads by varying the efficiency of the energy conversion from the wind to the rotational components of the wind turbine.

The power optimization in partial load region is conducted by a variation of the generator torque. Usually a quadratic law $T_g \propto \omega^2$ governs the generator torque T_g depending on the current rotational speed ω of the wind turbine. When the rated wind speed is reached, thus the turbine operates in full load region, the generator torque set-point reaches its rated value along with the rated power production. From this operating point on, the wind turbines pitch actuators are employed to adjust the angle-of-attack by pitching the blades, and consequently decreasing the efficiency of the energy conversion process. The adjustment of the pitch angle aims for a limitation of the power to the rated values to prevent the mechanical and electrical components of the wind turbine from overloading.

Components of the wind turbine are optimized with regard to cost and lifetime, and thus rely on a well defined operational range that fits predicted loads over the entire lifetime in the mechanical and electrical design. For that reason, the main aim of the wind turbine controller in full-load region is to shape the dynamics by appropriate controller feedback and adjust the pitch angle according to the current operating point. Controllers that are designed for the wind turbine implementation need to perform well in a large amount of operational settings, which are assessed during the wind turbine development through simulations that need to fulfill criteria on lifetime prediction for the certification process [22]. This includes considerations of both fatigue and extreme loads with respect to the operation in a small band around the rated values of the components.

The range of admirable dynamics as the closed-loop response of the wind turbine is however narrow. This results from the dynamically interacting components of the wind turbine such as the tower, blades or drive-train, where each component might introduce several orders of considerable natural frequencies. For that reason, it is desirable to place the resulting closed-loop poles of the system into

a certain region, avoiding conflicting natural frequencies of the unmodeled components. As will be demonstrated, this can be achieved by employing the LMI region constraints in the control synthesis discussed in Sec. 2.3.

Another important aspect in the operation of wind turbines, which at the same time is the source of energy, is the wind field acting on the components of the wind turbine. From a control point of view, the wind speed is considered as disturbance of the system. Consequently, the results on $\mathcal{H}_2$ attenuation expressed as LMIs from Sec. 2.3.2 will be used for the control feedback gain syntheses.

Up to now, conventional wind turbines are equipped with measurements of the wind speed that are unsubstantial for control purposes. More recent sensor techniques under consideration involve e.g. LIDAR [23] or spinner anemometer [24] to assess information on the upcoming and current wind field. Such information can be employed to introduce a feedforward term into the pitch angle command, for example as shown in [25]. Contrarily, here a TS disturbance observer will be employed to estimate the current effective wind speed from augmenting a TS wind turbine model by a wind state. The estimated wind speed of the observer represents an effective wind speed, which causes the excitation of the rotational dynamics of the wind turbine. This estimated wind speed will be employed for both, the calculation of the operating point of the TS controller by determination of the feedback gains $\sum_{i=1}^{N_r} h_i(\hat{\mathbf{z}})\mathbf{K}_i$ and introducing a feedforward term.

Since the designed observer is based on an augmented TS description of the wind turbine with the effective wind speed as a state, the premise variable of the TS wind turbine description is unmeasurable. The presented stability conditions for TS observers from Sec. 2.3.2 with unmeasurable premise variables will be employed to derive the observer feedback gains.

The common approach to pitch control in full-load region is usually conducted by a gain-scheduled PI controller with a feedback of the measured generator speed, for example as described in [26]. However, classical PI controllers lack of a proof of stability. The gain-scheduling for adjusting the resulting gains to the current operating point in these applications is calculated based on the current pitch angle of the wind turbine, which at the same time is the input to the system governed by the controller. The integral action of the PI controller plays a crucial role in the scheduling, since integrating the state adjusts the current operating point by in- or decreasing the pitch angle depending on the evolution of the rotational speed. As a result, the integral action adjusts the offset of the pitch angle to the current operating point. The information on the operating point is gained from the current pitch angle connecting the pitch angle to a wind speed by inversion of the curve in Fig. 2.3. The curve is obtained by trimming analysis employing a wind turbine model executed as FAST code v8 [27].

To derive a similar controller to the common gain-scheduling technique with the presented framework,
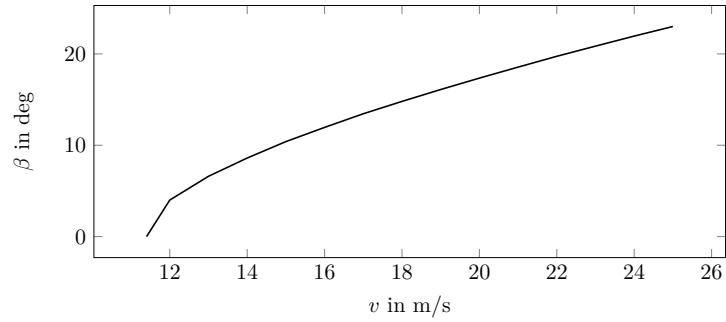
Figure 2.3: Equilibria $\dot{\omega}(\omega_d, \beta, v) = 0$ of the non-linear wind turbine connecting each wind speed v in the operating range to a corresponding pitch angle β and being derived by simulation analysis of the 5-MW reference turbine [26] under investigation.
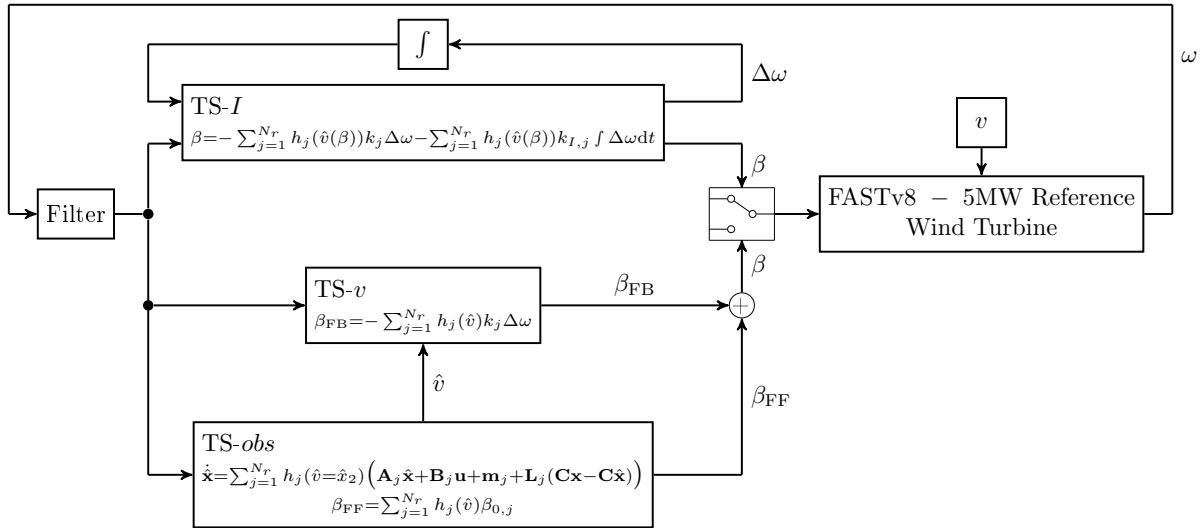
Figure 2.4: Block diagram of the simulation studies, where the wind turbine is either controlled by the presented TS-I approach or the combination TS-v&obs of observer TS-obs and corresponding feedback term TS-v.

the TS model of the wind turbine is augmented by an integrator state with respect to the error of the angular dynamics. Based on this augmented system a TS controller is derived, which calculates the membership functions of the TS representation from the current pitch angle. It resembles the discussed gain-scheduled PI technique and thus employs no information from the derived wind speed disturbance observer, see Fig. 2.4. However, since the PDC feedback gains are derived from Lyapunov theory, stability of the closed-loop design model is verified. For a simple notation and since an integral action is included, this controller is denoted as TS-I in the following.

Additionally, a second PDC feedback in the TS framework is presented and denoted as TS-v. It employs information from a disturbance observer TS-obs that is designed to estimate the current wind speed and in combination they form the closed-loop system referred to as TS-v&obs. It combines a

feedback and feedforward term as input to the system, see Fig. 2.4. Stability criteria based on LMIs from the previous section are employed to derive both, the PDC feedback gains for the controller and the observer. Properties of the TS system description are used to ensure the stability of the combined controller/observer feedback. By respecting these properties, the estimation of the wind speed and thus the determination of the current operating point by the feedforward term are decoupled from the control action resulting from the feedback loop, as the observer and controller gains can be derived separately in terms of LMI. The separation of identifying the current operating point from the immediate feedback control action results in a more flexible structure, allowing for an increased shaping capability of the closed-loop dynamics based on the presented LMI syntheses.

2.4.1 Wind turbine model

The FAST code offers linearization analysis at some definable time instant of the simulation [28]. This feature is used to derive linear sub-models of the non-linear rotational dynamics of the wind turbine. The specified linearization points are located on the equilibria of the system in Fig. 2.3. As suggested in [28], the linearization analysis is conducted three times, evenly distributed along the rotor azimuth angle within one revolution of the wind turbine rotor. The resulting values represent the rotational dynamics of the system in this operating point and are calculated as the mean of the three derived linear sub-models. This procedure is repeated for each operating point and results in linear sub-models with corresponding a_i, b_i and $b_{d,i}$ as state, input and disturbance coefficient illustrated in Fig. 2.5.

The rotational dynamics of the wind turbine based on Taylor series expansion in a neighborhood of the i-th operating point is given by

$$\dot{\omega}(\omega, \beta, v) = \dot{\omega}(\omega_d + \Delta\omega, \beta_{0,i} + \Delta\beta, v_{0,i} + \Delta v) = \underbrace{\dot{\omega}(\omega_d, \beta_{0,i}, v_{0,i})}_{=0} + a_i\Delta\omega + b_i\Delta\beta + b_{d,i}\Delta v \ , \quad (2.47)$$

where $\Delta\omega = \omega - \omega_d$, $\Delta\beta = \beta - \beta_{0,i}$ and $\Delta v = v - v_{0,i}$ are the distance of the rotational speed, pitch angle and wind speed from their nominal value in the i-th operating point. The desired rotational speed of the wind turbine in the full load region is constant in the entire operating range, resulting in a constant ω_d. Since the operating points illustrated in Fig. 2.3 are stationary points of the non-linear system, the term $\dot{\omega}(\omega, \beta, v_{0,i})$ converges to $\rightarrow 0$ as the rotational speed approaches its rated value $\omega \rightarrow \omega_d$ and the pitch angle its i-th operating point $\beta \rightarrow \beta_{0,i}$ for a given wind speed $v_{0,i}$. As a consequence, there are two objectives for the wind turbine controller in full load region, firstly to adjust the pitch angle to converge towards the desired operating value $\beta \rightarrow \beta_{0,i}$, such that the system description using the Taylor expansion in (2.47) holds, and consequently control the deviation $\Delta\omega \rightarrow 0$ in the current operating point, such that $\omega \rightarrow \omega_d$.
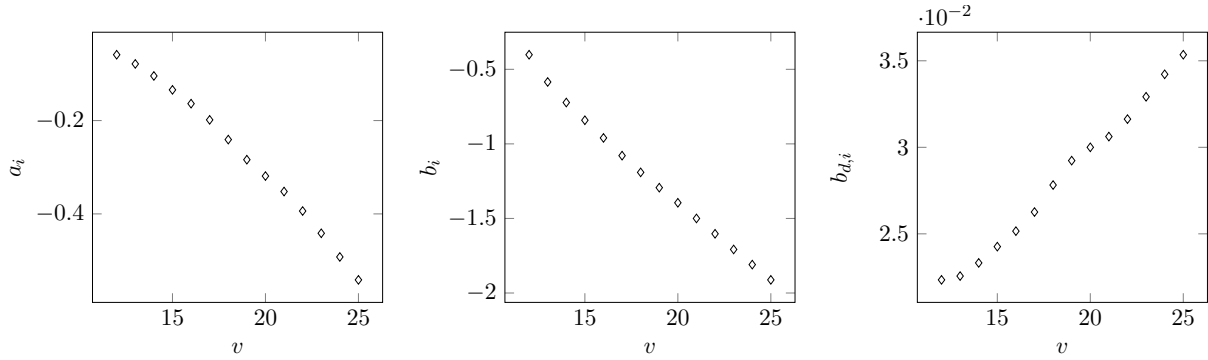
Figure 2.5: Linear sub-models representing the vertices of the TS description and obtained from linearization analysis employing the FAST code [28].
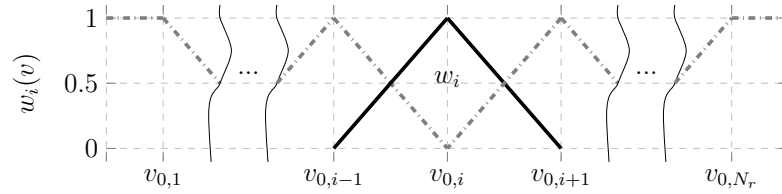
Figure 2.6: Triangular membership functions are employed to interconnect the N_r individual linear sub-models derived in equilibria of the system.

2.4.1.1 WT TS model

Based on the $N_r = 14$ linear model descriptions, a non-linear TS representation of the system over the defined operating range can be constructed. Triangular membership functions as shown in Fig. 2.6 are used to interconnect the N_r individual linear dynamics in a convex TS formulation. The triangular weighting functions w_i are calculated by

$$w_i(v) = \begin{cases} \frac{v-v_{0,i}}{v_{0,i}-v_{0,(i-1)}} & \text{if } v_{0,(i-1)} < v \leq v_{0,i} \\ 1 - \frac{v-v_{0,i}}{v_{0,(i+1)}-v_{0,i}} & \text{if } v_{0,i} < v \leq v_{0,(i+1)} \\ 0 & \text{else} \end{cases} \quad . \tag{2.48}$$

Since in this description only one premise variable is present, i.e. $\mathbf{z} = v$, the weighting functions are the membership functions in the general TS description, i.e. $w_i(v) = h_i(\mathbf{z})$ in (2.1). As a result, the non-linear TS model of the wind turbine gained by linearization around N_r operating points based on

Taylor series expansion is given by

$$
\begin{aligned}
\dot{\omega}(\omega, \beta, v) &= \sum_{i=1}^{N_r} h_i(v) \underbrace{\dot{\omega}(\omega_d, \beta_{0,i}, v_{0,i})}_{=0} + \sum_{i=1}^{N_r} h_i(v)\big(a_i \Delta\omega + b_i \Delta\beta + b_{d,i} \Delta v\big) \\
&= \sum_{i=1}^{N_r} h_i(v)\big(a_i \Delta\omega + b_i \Delta\beta + b_{d,i} \Delta v\big)
\end{aligned}
\qquad (2.49)
$$

where in this form the distance from the desired or nominal value $\Delta\omega$, $\Delta\beta$ and Δv is considered as the state, input and disturbance of the system. From (2.49) it follows that the term $\sum_{i=1}^{N_r} h_i(v)\big(a_i \Delta\omega + b_i \Delta\beta + b_{d,i} \Delta v\big)$ approximates – in the vertices of the convex description exactly represents [10] – the non-linear rotational dynamics within the defined operational range of the wind turbine.

Using system description (2.49) essentially means that the coordinate system of the TS formulation is moving along the stationary points illustrated in Fig. 2.3. If this description of the non-linear rotational dynamics at the stationary points is used to derive appropriate feedback gains, the role of the wind speed observer is vital as the calculation of the stationary values in the operating point is based on the estimate of the wind speed. For the control design employing the wind speed observer, the aim of the derived PDC feedback gains is to shape the dynamics appropriately in the stationary points, whereas the observer is used to add the stationary pitch values depending on the current operating point.

2.4.1.2 TS model validation

The derived TS model given by (2.49) is simulated along the FAST code to assess the quality of the TS approximation of the non-linear dynamics. For this simulation, the wind speed is assessed as an output of the FAST code at runtime of the simulation, and therefore is used to calculate the membership functions $h_i(v)$ in (2.49). Simulation studies under different wind conditions have shown that the derived TS model approximates the non-linear rotational dynamics of the system well, as long as the turbine remains close enough to the operating points illustrated in Fig. 2.3. The evolution of the rotational speed of the FAST model is compared to the TS model in Fig. 2.7, which is subject to a turbulent wind field with a mean of $\bar{v} = 18 \text{ m/s}$ as an example. Even though only the downwind component at hub height in the rotor plane is used as the wind signal to calculate the membership functions, which represents an important indicator of the wind speed but still only provides one of many vectors in the spatial three dimensional wind field, the accuracy of the approximation in the evolution of the state is satisfying. The wind sequence at hub height is shown in the upper plot of Fig. 2.7. In the time range from 400 s to 450 s the wind speed partly declines to values below the defined operating range of the linearization analysis yielding the linear sub-models in Fig. 2.5, and consequently the modeling mismatch between the FAST code and TS model increases in this range,
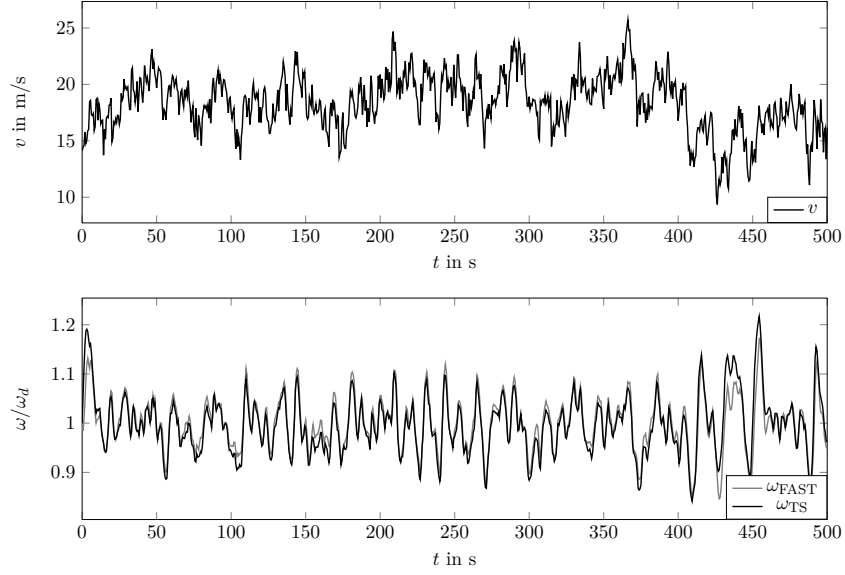
Figure 2.7: Validation of the derived TS wind turbine model under influence of a turbulent wind field with a mean wind speed $\bar{v} = 18 \text{ m}/s$.

reflected by an increased error in the rotational speed.

2.4.2 WT control

2.4.2.1 Closed-loop TS-$v\&obs$

The closed-loop dynamics of the wind turbine is derived from the TS description of the wind turbine in (2.49). For the PDC feedback approach employing a wind speed disturbance observer, consider the pitch angle for a deviation from the operational point of $\Delta\omega = \omega - \omega_d$ to be commanded by

$$\beta_{\text{TS}-v\&obs} = -\sum_{j=1}^{N_r} h_j(\hat{v}) k_j \Delta\omega + \sum_{j=1}^{N_r} h_j(\hat{v}) \beta_{0,j} \, , \tag{2.50}$$

which combines a feedback β_{FB} and feedforward β_{FF} term, and depends on the current estimate of the wind speed $\hat{v}$ from the observer, see Fig. 2.4.

By adding $\sum_{i=1}^{N_r} h_i(v)\beta_{0,i} - \sum_{i=1}^{N_r} h_i(v)\beta_{0,i} = 0$ to (2.50), which depends on the real wind speed v, we obtain

$$\beta_{\text{TS}-v\&obs} = \underbrace{\sum_{i=1}^{N_r} h_i(v)\beta_{0,i}}_{\approx\beta_0} \underbrace{- \sum_{j=1}^{N_r} h_j(\hat{v}) k_j \Delta\omega + \sum_{j=1}^{N_r} h_j(\hat{v}) \beta_{0,j} - \sum_{i=1}^{N_r} h_i(v)\beta_{0,i}}_{\Delta\beta} \, . \tag{2.51}$$

Therefore, the non-linear closed-loop dynamics of the wind turbine is reformulated based on Taylor series expansion in TS formulation (2.49) as

$$\dot{\omega}(\omega, \beta_{\text{TS}-v\&obs}, v) = \sum_{i=1}^{N_r} h_i(v) \underbrace{\dot{\omega}(\omega_d, \beta_0, v_{0,i})}_{=0}$$

$$+ \sum_{i=1}^{N_r} h_i(v)\big(a_i \Delta\omega + b_i \underbrace{(-\sum_{j=1}^{N_r} h_j(\hat{v})k_j \Delta\omega + \sum_{j=1}^{N_r} h_j(\hat{v})\beta_{0,j} - \sum_{i=1}^{N_r} h_i(v)\beta_{0,i})}_{=\Delta\beta} + b_{d,i}\Delta v\big)$$

$$\Leftrightarrow$$

$$\dot{\omega}(\omega, \beta_{\text{TS}-v\&obs}, v) = \sum_{i=1}^{N_r} h_i(v) \sum_{j=1}^{N_r} h_j(\hat{v})\big((a_i - b_i k_j)\Delta\omega + b_{d,i}\Delta v\big)$$

$$+ \sum_{i=1}^{N_r} h_i(v)b_i\big(\sum_{j=1}^{N_r} h_j(\hat{v})\beta_{0,j} - \sum_{i=1}^{N_r} h_i(v)\beta_{0,i}\big) \ .$$

(2.52)

Neglecting the derivative $\dot{\omega}(\omega_d, \beta_{0,i}, v_{0,i})$ is based on the assumption that the model approximates the real dynamics in the blending from one operating point to the other well enough, such that $\sum_{i=1}^{N_r} h_i(v)\beta_{0,i} \approx \beta_0$ for the current operating point. By formulating the TS model based on the linearized sub-models, in each vertex of the polytopic description the corresponding pitch angle is an exact representation of the pitch angle from the euqilibria of the system determined in the linearization analysis, such that $\sum_{i=1}^{N_r} h_i(v_{0,i})\beta_{0,i} = \beta_0$ holds [10].

2.4.2.2 Closed-loop TS-I

The integral-based control law resembling the state-of-the-art wind turbine control scheme is given by

$$\beta_{\text{TS-}I} = -\sum_{j=1}^{N_r} h_j(\hat{v}(\beta_{\text{TS-}I}))k_j \Delta\omega - \sum_{j=1}^{N_r} h_j(\hat{v}(\beta_{\text{TS-}I}))k_{I,j} \int \Delta\omega \ \mathrm{d}t \ ,$$

(2.53)

where $\hat{v}(\beta_{\text{TS-}I})$ indicates the calculation of the current operating point employing the input to the system $\beta_{\text{TS-}I}$ and the curve given by Fig. 2.3. This incorporates the assumption that the current input represents an equilibrium of the system, which is the commonly used in gain-scheduled PI control schemes for wind turbines. However, the presented TS-I approach accounts for the mismatch induced by this assumption by a variation of combined sub-models in the formulation of the LMI synthesis.

Adding $\sum_{i=1}^{N_r} h_i(v)\beta_{0,i} - \sum_{i=1}^{N_r} h_i(v)\beta_{0,i} = 0$ to control law (2.53) and reformulating $\dot{\omega}(\omega, \beta_{\text{TS-}I}, v)$

as shown for the TS-v approach in (2.52) results in closed-loop dynamics of

$$
\begin{bmatrix} \dot{\omega} \\ \dot{x}_I \end{bmatrix} = \sum_{i=1}^{N_r} h_i(v) \sum_{j=1}^{N_r} h_j(\hat{v}(\beta)) \left(\left(\begin{bmatrix} a_i & 0 \\ 1 & 0 \end{bmatrix} - \begin{bmatrix} b_i \\ 0 \end{bmatrix} \begin{bmatrix} k_j & k_{I,j} \end{bmatrix} \right) \begin{bmatrix} \Delta\omega \\ x_I \end{bmatrix} + \begin{bmatrix} b_{d,i} \\ 0 \end{bmatrix} \Delta v \right)
$$
$$
+ \sum_{i=1}^{N_r} h_i(v) \begin{bmatrix} b_i \\ 0 \end{bmatrix} \left(- \sum_{i=1}^{N_r} h_i(v)\beta_{0,i} \right)
$$

(2.54)

where $x_I = \int \Delta\omega \, \mathrm{d}t$ is the integral state of the deviation from the desired rotational speed of the wind turbine.

2.4.2.3   Control synthesis

The system description of the general control synthesis in Sec. 2.3 is employed to match the resulting closed-loop system descriptions in (2.52) and (2.54). The disturbance from the wind is respected by the robust disturbance gain attenuation approach. The remaining bounded input terms resulting from the unknown wind speed in (2.52) and (2.54) will be neglected in the controller synthesis, to apply the ISS stability analysis of the closed-loop system subject to the bounded input.

In the following part, stability of the closed-loop dynamics (2.52) and (2.54) is studied, and appropriate feedback gains are derived based on the LMI constraints. Stability in the defined operating range is therefore verified as long as the wind turbine remains within the defined operational range. The violation of this assumption may happen due to two reasons. The first results from a decrease of the effective wind speed, resulting in a power production below rated. From this point on a different controller governs the dynamical operation of the turbine, and therefore the presented controller is no longer applicable. The other scenario includes the derived pitch controller under consideration. If the dynamics of the closed-loop system is maladjusted to the characteristics of the wind turbine, the defined operational range may be left, such that the Taylor series expansion represents no proper approximation of the system behavior as discussed in the derivation of the TS model in Sec. 2.4.1.1. An impression of the resulting closed-loop dynamics can be studied by the locations of the poles of the linear sub-systems. Therefore, the LMI region restrictions are essentially the key in shaping the resulting dynamics from knowledge on the technical implementation of the turbine, and thus the dynamics are assumed to perform adequate if the technical restrictions are respected by the choice of the LMI region.

TS-v   Stability of the closed loop system (2.52) under impact of control law (2.50) is verified and the resulting closed-loop poles are located in $\mathcal{S}(0, r, \theta)$, if a matrix $\mathbf{X} = \mathbf{X}^{\mathrm{T}} \succ 0$ and N_r matrices

$\mathbf{M}_j = k_j \mathbf{X}$ can be found constraint by (2.31). Additionally, if (2.31) holds, an attenuation of γ from the wind disturbance to the rotational speed of the wind turbine is ensured. The LMI solver is used to minimize Γ, which results from a change of variable $\Gamma = \gamma^2$. The corresponding matrices in (2.52) are defined as

$$\mathbf{A}_i := a_i, \quad \mathbf{B}_i := b_i \quad \text{and} \quad \mathbf{D}_i := b_{d,i} \, .$$

Assuming that the LMI constraints are found feasible, there exists some $\bar{\lambda} > 0$ fulfilling (2.9). For the bounded input $\delta := \sum_{j=1}^{N_r} h_j(\hat{v})\beta_{0,j} - \sum_{i=1}^{N_r} h_i(v)\beta_{0,i}$ and $\overline{\mathbf{PF}_i} := \max_i \|\mathbf{PB}_i\|$ the ISS property is verified. The stability margin around the origin is governed by $\bar{\lambda}$, which is defined by the maximum real parts of the N_r closed-loop eigenvalues λ_i by $-\bar{\lambda}/2 = \max\Re(\lambda_i) < -\alpha$.

TS-I Stability of the closed loop system (2.54) under impact of control law (2.53) is verified and the resulting closed-loop poles are located in $\mathcal{S}(0, r, \theta)$, if a matrix $\mathbf{X} = \mathbf{X}^{\mathrm{T}} \succ 0$ and N_r matrices $\mathbf{M}_j = \begin{bmatrix} k_j & k_{I,j} \end{bmatrix} \mathbf{X}$ can be found constraint by (2.31). Additionally, if (2.31) holds, an attenuation of γ from the wind disturbance to the rotational speed of the wind turbine is verified. The LMI solver is used to minimize Γ, which results from a change of variable $\Gamma = \gamma^2$. The corresponding matrices in (2.54) are defined as

$$\mathbf{A}_i := \begin{bmatrix} a_i & 0 \\ 1 & 0 \end{bmatrix}, \quad \mathbf{B}_i := \begin{bmatrix} b_i \\ 0 \end{bmatrix} \quad \text{and} \quad \mathbf{D}_i := \begin{bmatrix} b_{d,i} \\ 0 \end{bmatrix} \, .$$

Assuming that the LMI constraints are found feasible, there exists some $\bar{\lambda} > 0$ fulfilling (2.9). For the bounded input $\delta := -\sum_{i=1}^{N_r} h_i(v)\beta_{0,i}$ and $\overline{\mathbf{PF}_i} := \max_i \|\mathbf{PB}_i\|$ the ISS property is verified. The stability margin around the origin is governed by $\bar{\lambda}$, which is defined by the maximum real parts of the N_r closed-loop eigenvalues λ_i by $-\bar{\lambda}/2 = \max\Re(\lambda_i) < -\alpha$.

Remark. *The term, which is handled by the ISS property, differs depending on whether the TS-v or the TS-I is designed. While for the observer-based TS-v approach, the bounded input decreases as the wind speed observer converges towards the real wind speed, the TS-I always shows an offset in the states, which will not vanish. This represents the integral state that needs to emerge to some value to reject the mismatch from the unknown operating point when employing the TS-I approach.*

2.4.3 Wind speed disturbance observer

As discussed previously, the wind field acting on the rotor of the wind turbine plays a major role from a control perspective. Therefore, a disturbance observer in TS formulation will be employed to derive

an estimate of the current effective wind speed, such that the membership functions of the TS-v and the feedforward term β_{FF} accounting for the current operating point in (2.50) can be calculated. The TS model of the wind turbine (2.49) is augmented by a state that represents the effective wind speed. For augmenting the system, the information from the disturbance distribution matrix $b_{d,i}$ is used. The wind dynamics are considered as a first order transfer function $\dot{v} = -\frac{1}{\tau}v$ as suggested in [29], where the time constant is defined as $\tau = 4\mathrm{s}$. The augmented TS model of the wind turbine is given by

$$\dot{\mathbf{x}} = \begin{bmatrix} \dot{\omega} \\ \dot{v} \end{bmatrix} = \sum_{i=1}^{N_r} h_i(v) \left(\begin{bmatrix} a_i & b_{d,i} \\ 0 & -\frac{1}{\tau} \end{bmatrix} \begin{bmatrix} \Delta\omega \\ v \end{bmatrix} + \begin{bmatrix} b_i \\ 0 \end{bmatrix} \Delta\beta - \begin{bmatrix} b_{d,i} \\ 0 \end{bmatrix} v_{0,i} \right) , \tag{2.55}$$

where the term $-b_{d,i}v_{0,i}$ accounts for $b_{d,i}$ characterizing the disturbance distribution around the current operating point, i.e. $b_{d,i}\Delta v = b_{d,i}v - b_{d,i}v_{0,i}$. The output is the deviation of the rotational speed from the desired value $\Delta\omega$, such that $\mathbf{C} = [1\ 0]$ is obtained.

As a result, by defining a TS observer for the augmented system (2.32) with the matrices $\mathbf{A}_i$, $\mathbf{B}_i$ and vectors $\mathbf{m}_i$

$$\mathbf{A}_i := \begin{bmatrix} a_i & b_{d,i} \\ -\frac{1}{\tau} & 0 \end{bmatrix} \quad \text{and} \quad \mathbf{B}_i := \begin{bmatrix} b_i \\ 0 \end{bmatrix} \quad \mathbf{m}_i = - \begin{bmatrix} b_{d,i} \\ 0 \end{bmatrix} v_{0,i} .$$

and defining an observer similar to (2.32)

$$\dot{\hat{\mathbf{x}}} = \sum_{j=1}^{N_r} h_j(\hat{v} = \hat{x}_2)\big(\mathbf{A}_j\hat{\mathbf{x}} + \mathbf{B}_j\mathbf{u} + \mathbf{m}_j + \mathbf{L}_j(\mathbf{C}\mathbf{x} - \mathbf{C}\hat{\mathbf{x}})\big) \tag{2.56}$$

yields the dynamics of the observation error $\mathbf{e} = \mathbf{x} - \hat{\mathbf{x}}$ as

$$\dot{\mathbf{e}} = \sum_{j=1}^{N_r} h_j(\hat{v}) \sum_{i=1}^{N_r} h_i(v)\big((\mathbf{A}_i - \mathbf{L}_j\mathbf{C} - \Delta\mathbf{A}_{i,j})\mathbf{e} + \Delta\mathbf{A}_{i,j}\mathbf{x} + \Delta\mathbf{B}_{i,j}\mathbf{u} + \Delta\mathbf{m}_{i,j}\big) , \tag{2.57}$$

where $\Delta\mathbf{m}_{i,j} = \mathbf{m}_i - \mathbf{m}_j$ is bounded and consequently can be addressed by the ISS property, see Sec. 2.3.1.1 with $\delta := \Delta\mathbf{m}_{i,j}$.

As discussed in the derivation of the TS observer with unmeasurable states as variables in Sec. 2.3.3, the convergence of the observer to a stability margin from determining ϵ can be verified. Let us define the maximum state $\mathbf{x}_{\max} = [\Delta\omega\ v]^{\mathrm{T}} = [1.5\frac{\mathrm{rad}}{\mathrm{s}}\ 35\frac{\mathrm{m}}{\mathrm{s}}]^{\mathrm{T}}$. Condition (2.44) allows us to derive an error and therefore ϵ, for which the Lyapunov functions derivative is guaranteed to be negative definite if a feasible solution to the LMIs in (2.43) is found. Therefore, we define the maximum resulting error (only with regard to the offset stemming from the states) as $\mathbf{e}_{\max} = [.5\frac{\mathrm{rad}}{\mathrm{s}}\ .5\frac{\mathrm{m}}{\mathrm{s}}]^{\mathrm{T}}$. From these conditions an $\epsilon \approx 42$ results, which is used in the observer synthesis. For all observers discussed here, a design matrix of $\mathbf{Q} = .0001 \cdot \mathbf{I}$ is chosen in (2.43).

2.4.4 Simulation studies

The simulation studies were conducted using the FAST code [27] and employing the presented controllers in the full-load region along the combination with other controllers for the adjacent operating ranges, for example the quadratic control law $T_g \propto \omega^2$. For a detailed description of the entire control scheme of the wind turbine out of full-load region see [26]. However, in the full load region, where each of the presented results is located, the dynamics of the wind turbine are governed by the proposed TS approach. As suggested in [26], a single-pole filter on the generator speed measurement with a corner frequency of .25 Hz is used before processing the measurement signal of the rotational speed to the controller. An overview of the simulation environment and the resulting signal flow for the two presented control schemes is depicted in Fig. 2.4.

To illustrate and compare the two approaches (TS-I and TS-$v\&obs$), a variation of the design parameters is conducted. The employed parameters for the syntheses are given in Tab. 2.1. For improved readability the different parameters and dynamics feedback loops are denoted as *slow, nominal* or *fast* depending on the design parameters forcing the closed-loop poles further into the left half of the complex plane.

2.4.4.1 LMI Implementation with respect to wind turbine characteristics

The variation of sub-models indicated by a variation of i and j in the LMIs depends on the purpose of the design and an overview is given in Tab. 2.1. The TS-obs synthesis is conducted based on the LMI criterion emerging from the unmeasurable premise variable (2.43) with respect to (w.r.t.) a variation of i and j based on (2.58). It accounts for every combination of model and feedback gains as proposed in deriving the LMI to ensure stability despite a mismatch in the estimation of the wind speed. Additionally, LMIs (2.37) for $i = 1, ..., N_r$, $j = i$ in Tab. 2.1 constrain the solution to a desired LMI region at instances where the estimation error is close to 0. This accounts for a shaping of the dynamics in the proper operational point, i.e. when the estimated wind speed is close to the real wind speed.

The control design for both, the TS-v and TS-I is based on the same synthesis. However, as discussed with different models and inputs to the system. The LMIs for the TS-v design given by (2.31) with respect to a variation of (2.59) account for two adjacent sub-model combinations of the LMI criterion with regard to the LMI region and disturbance attenuation γ. LMI (2.25) with a decay rate $\alpha = 0$ ensures stability of the 6 adjacent models before and after the i-the sub-model controller combination, and is introduced to ensure stability in case of an estimation error of the wind speed, irregardless if it stems from the pitch angle measurement for the TS-I or from the wind speed observer TS-obs. However, since the minimization of the disturbance attenuation gain yields a minimum decay rate, α is

set to zero, to verify stability but propose no further restriction to the LMI solver. This approach verifies stability even if the information on the current operating point is inaccurate in a wider neighborhood of the real operating point.

$$i = 1, ..., N_r, \quad j = 1, ..., N_r \tag{2.58}$$

$$i = 1, ..., N_r, \quad j = i - 2, \ i - 1, \ i, \ i + 1, \ i + 2 \quad \text{if } j \in [1, ..., N_r] \tag{2.59}$$

$$i = 1, ..., N_r, \quad j = i - 6, \ i - 5, ..., \ i, ..., \ i + 6 \quad \text{if } j \in [1, ..., N_r] \tag{2.60}$$

The attainable disturbance attenuation gain γ as given in Tab. 2.1 decreases as the dynamics are getting faster and the LMI region is constraint further into the left half of the complex plane, indicated by an increasing r. The choice of the restricting radius r and the damping coefficient D is based on the description of the gain-scheduled PI controller for the employed wind turbine in [26]. The discussed gain-scheduled PI control scheme in [26] aims for a closed-loop natural frequency of $\omega_n = .6\text{rad/s}$ with a damping ratio of $D = .7$. This corresponds to a radius with length $r = \sqrt{\omega_n^2 + (\omega_n\sqrt{1 - D^2})^2}$. In fact, from the design with parameters in Tab. 2.1, the resulting closed-loop eigenvalues as shown in Fig. 2.8 are in the range of the proposed dynamics as suggested in [26], but since the damping is restricted by the LMI region in the complex plane by $\theta = \cos^{-1}(D)$, the resulting damping ratios are well above the desired damping ratio. Therefore, the achieved damped frequencies $\omega_n\sqrt{1 - D^2}$ are below the considerable frequencies of the unmodeled wind turbine components given in [26].

2.4.4.2 Application of the gain optimization procedure

The resulting eigenvalues of the nominal closed-loop TS models before and after the optimization are illustrated in Fig. 2.8 with respect to (2.59) for the TS-v and the TS-I controller. The closed-loop poles of the disturbance observer TS-obs are illustrated with respect to a variation of $i = 1, ..., N_r, j = i$, since the LMI region was only imposed to this combination in the control design. As can be seen, the resulting closed-loop eigenvalues are confined to the LMI region $\mathcal{S}(\alpha, r, \theta)$. The subsequent optimization aim in this design step was changed from minimizing $\min(\Gamma)$, with $\Gamma = \gamma^2$ to the minimization of the trace of the resulting feedback gains, i.e. $\min(\text{trace}(\mathbf{M}_j^T\mathbf{M}_j))$ for the control design and $\min(\text{trace}(\mathbf{N}_j^T\mathbf{N}_j))$ observer. This is conducted to reduce the magnitude of the gains, such that with respect to the LMI region and the attained disturbance attenuation gains γ from the initial step,

Table 2.1: Overview of the LMI design parameters:
TS-I: TS integral feedback control (2.53)
(TS-obs & TS-v): TS wind speed disturbance observer & corresponding feedback (2.50).

Design Notation	Type	LMIs	r	D	α	attained γ
slow	TS-I	$\star$	.8	.7	0	.1405
nominal	TS-I	(2.31) w.r.t. (2.59) & (2.25) w.r.t. (2.60)	1	.7	0	.0907
fast	TS-I	$\star$	1.2	.7	0	.0651
slow	TS-v	$\star$	.8	.7	0	.0505
nominal	TS-v	(2.31) w.r.t. (2.59) & (2.25) w.r.t. (2.60)	1	.7	0	.0403
fast	TS-v	$\star$	1.2	.7	0	.0335
slow	TS-obs	$\star$	.8	.7	.5	—
nominal	TS-obs	(2.43) w.r.t. (2.58) & (2.37) w.r.t. $i = j$	1	.7	.7	—
fast	TS-obs	$\star$	1.2	.7	.8	—

the feedback gains are as small as possible. This reduces the necessary actuator activity with respect to the dynamical constraints of the actuator, and the noise sensitivity in the implementation of the observer, see [20] for details. In Fig. 2.8 the optimization yields the biggest location change in the complex plane for the TS-obs, as the closed-loop eigenvalues are pushed towards the minimum decay rate α. For the control syntheses of TS-v and TS-I the change from the optimization is rather small, however resulting in a more evenly distribution of the eigenvalues along the range of attained values.

2.4.4.3 Step response

To assess the dynamical properties of the resulting closed-loop dynamics, a synthetic wind speed signal is used. Due to the inertia of a natural incoming wind field, a wind signal like presented in the upper plot of Fig. 2.9 will not occur. Further, a single vector signal is used to represent the incoming wind field, such that no three dimensional wind field is represented that acts distributed at the different rotor blade positions. However, this wind signal allows for a direct comparison with the estimated effective wind speed $\hat{v}$ by the observer and the resulting feedback signals for the two evaluated control concepts TS-I and TS-v&obs.

As can be seen in Fig. 2.9, the resulting wind speed estimation from the observer based on the *nominal* design converges to the real wind speed after the step within ≈ 10 s. As a result, the offset in the pitch angle accounting for the operating point is adjusted through the feedforward term. In combination with the additional feedback by the *nominal* TS-v, the pitch signal in the middle plot of Fig. 2.9 is formed. Especially for steps to a higher wind speed, the pitch signal of the observer-based control
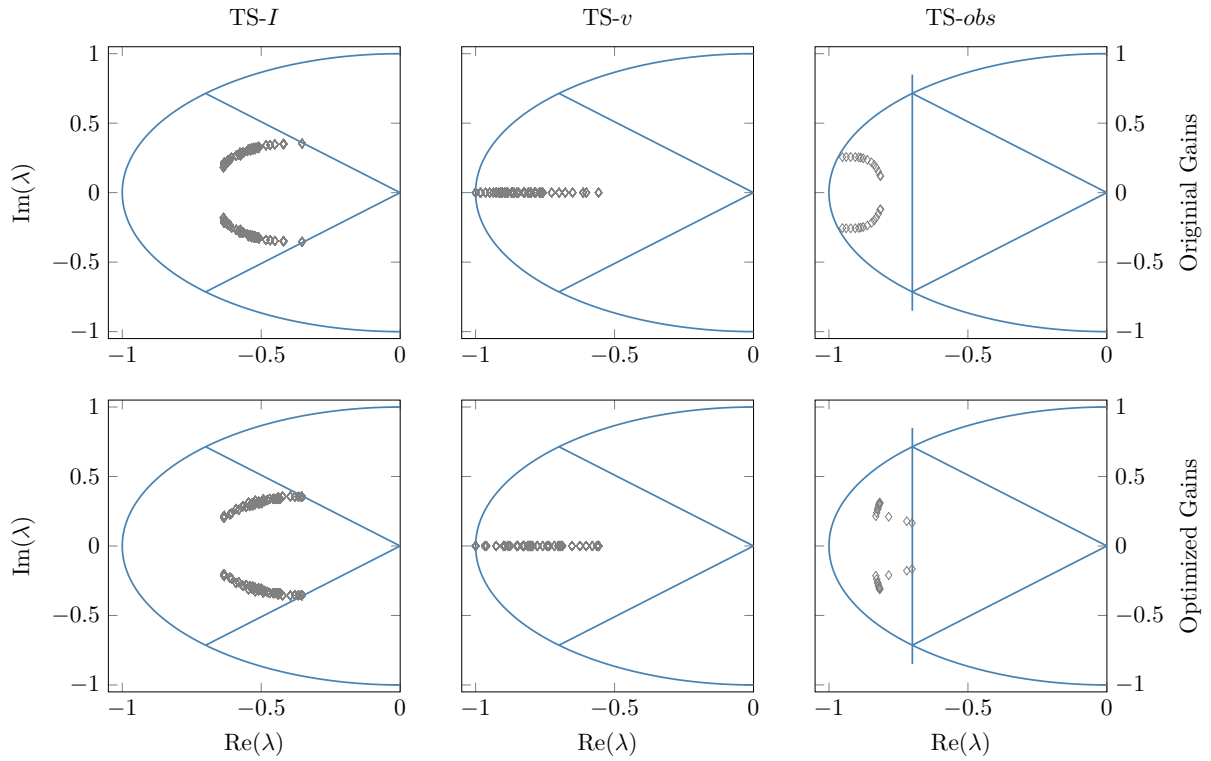
Figure 2.8: Eigenvalues of the derived closed-loop systems TS-I, TS-v and TS-obs in the complex plane within the desired LMI region of the control synthesis. The eigenvalues are illustrated before and after the optimization procedure from Sec. 2.3.4 is conducted.

approach decays faster towards its stationary value compared to the pitch signal from the *nominal* TS-I. This results in reduced over-speeding of the rotor as can be seen in the lower plot of Fig. 2.9.

2.4.4.4 Analysis of the pitch signal components

To directly assess the influence of the proposed observer, in Fig. 2.10 the components of the pitch angle signal in the upper plot of Fig. 2.10 are separated depending on their origin. As discussed, the signal is the sum of a component respecting the current operating point through the feedforward term and a direct feedback depending on the current deviation from the desired rotational speed $\Delta\omega$. The feedback is depicted in the middle plot of Fig. 2.10, whereas the observer-based feedforward component β_{FF} in (2.50) can be seen in the lower plot along with the resulting feedback from the integrator state in (2.53) for the TS-I.

As can be seen, the TS-I signal resulting from the integral term in the lower plot of Fig. 2.10 declines before increasing the pitch angle to adjust the current operating point. This stems from a reduction of the feedback gains $\sum_{j=1}^{N_r} h_j(\hat{v}(\beta))k_{I,j}$ due to an increase of the pitch angle from the immediate
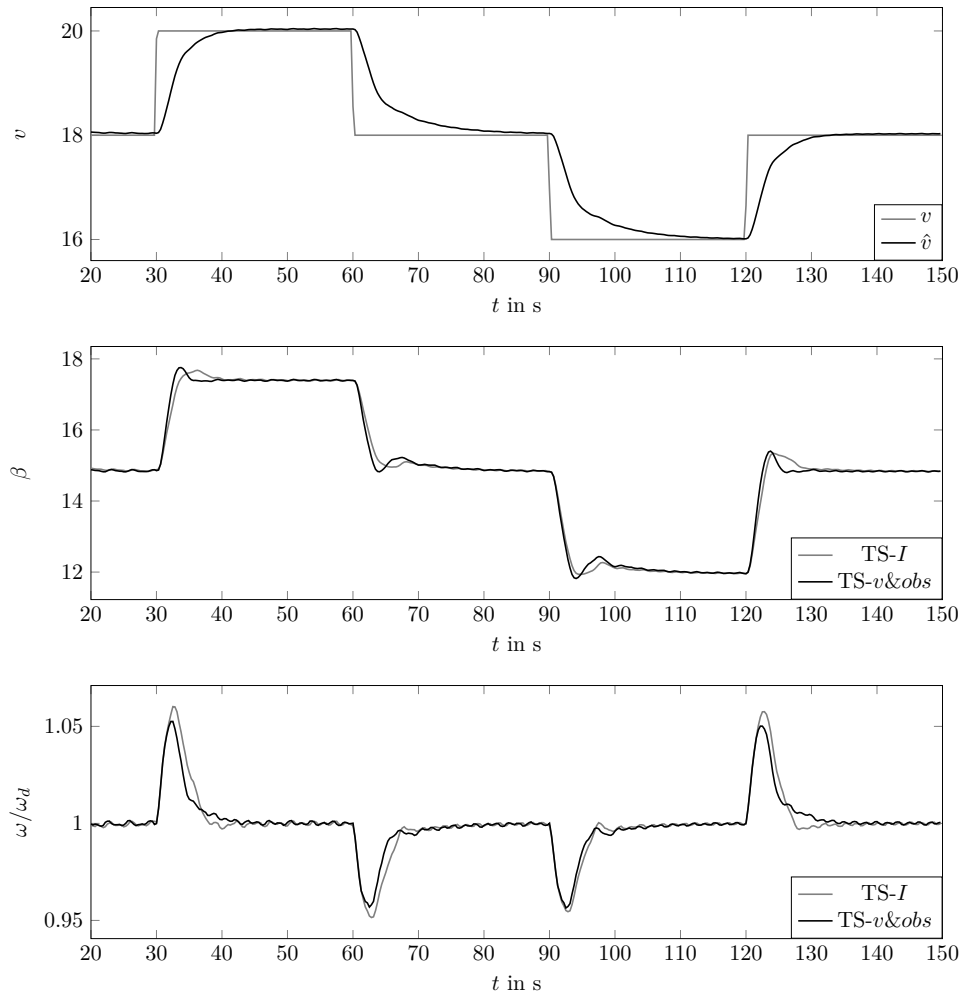
Figure 2.9: Step response of the non-linear wind turbine simulated by FAST code, and governed by the presented control approaches TS-I and TS-$v\&obs$ in the full load-region.

feedback term in the middle plot of Fig. 2.10. This follows from $\sum_{j=1}^{N_r} h_j(\hat{v}(\beta))k_{I,j}$ decreasing for an increasing pitch angle, which is based on the property of wind turbines to possess a higher sensitivity to changes in the pitch angle as the wind evolves towards higher speeds, see also the equilibria of the system in Fig. 2.3. Therefore, in the first seconds after the step change of the wind speed, the TS-I controller performs oppositely to the desired behavior until due to the integration of the error, the integrator state governs the increasing pitch angle. Contrarily, the observer-based approach TS-$v\&obs$ adjusts the pitch angle by estimating the current wind speed into the desired direction from the beginning.

The feedback components shown in the middle plot of Fig. 2.10 are only active in the transient region, thus when a deviation from the desired rotational speed occurs. However, the term β_{FB} produced by the TS-v remains below the counterpart in the TS-I, TS-$v\&obs$ due to the superior adjustment of
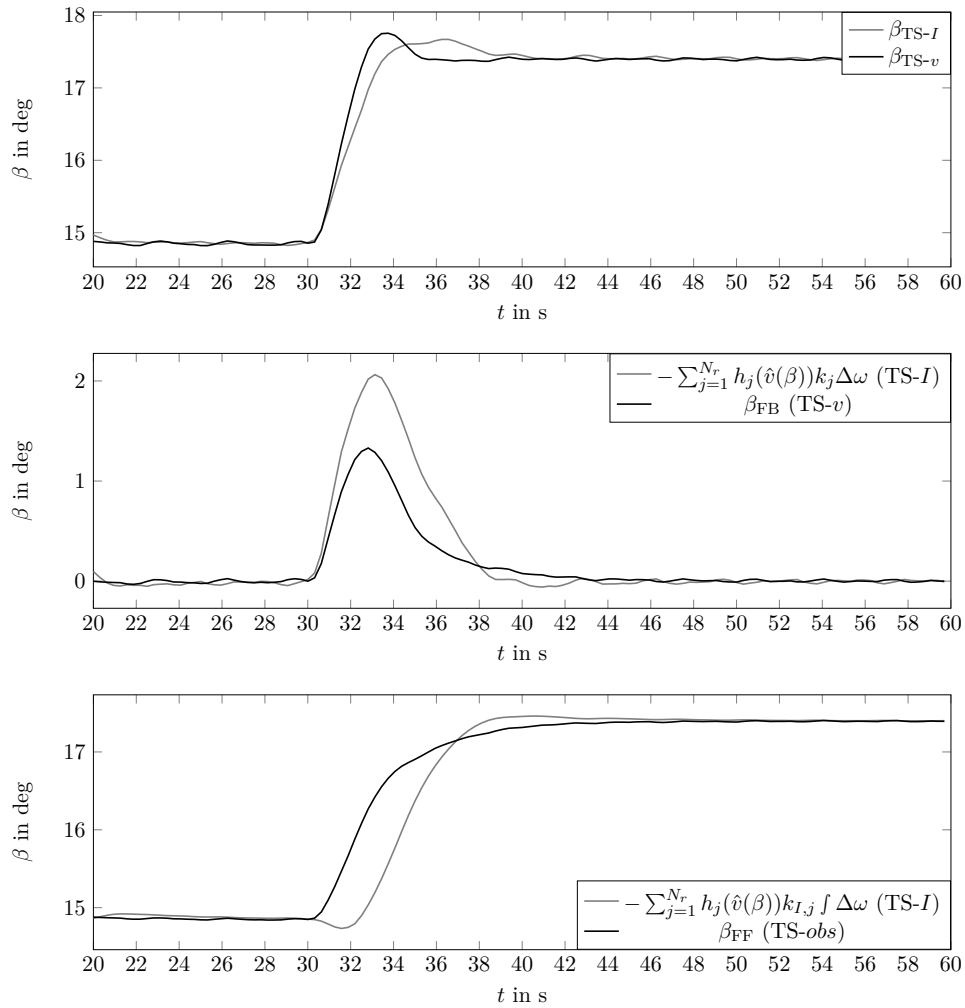
Figure 2.10: Detail view of the pitch angle signal β of the presented approaches TS-I and TS-$v\&obs$, which is separated into the the steady state and transient component of the pitch signal to assess the effect of the derived disturbance observer.

the current operating from the deployment of the wind speed disturbance observer. This results in a faster convergence of the pitch angle to the desired value as seen in the upper plot of Fig. 2.10 and to a smoother transition of the rotational speed into the desired value as also illustrated in Fig. 2.9.

2.4.4.5 Wind turbine closed-loop dynamics variation

As mentioned in the introduction to the wind turbine application section 2.4, the TS wind speed disturbance observer allows us to decouple the calculation of the current operating point from the feedback in the estimated operating point. The TS-I approach combines the latter two, and thus the controller formulation incorporates both aspects. The design of the observer TS-obs allows us to define the dy-

namics of the transients from one operating point to the other independently from the closed-loop dynamics within the current operating point.

From a wind turbine life predictions perspective, a lot of effort is devoted to the simulation of fatigue and extreme loads. Depending on the investigated scenario, the control in these analyses have different scopes, where in extreme events the maximum load from fast changes in the wind speed are of prior interest, in the fatigue case the number of cycles and corresponding magnitudes are considered from a load spectrum. Therefore by shaping the dynamics of the two effects individually, a decoupling from the fatigue and extreme load might be attained to a certain degree.

This can also be assessed by analyzing Fig. 2.11, where the *slow* and *fast* designed feedback loops are compared to the *nominal* design case. As can be seen in Tab. 2.1, the design parameters for the TS-I, TS-v and TS-obs are equivalently adjusted to provide *faster* or *slower* dynamical responses. From Fig. 2.11 it is apparent that the small variation of the targeted dynamics in the design process is more directly adjustable for the TS-$v\&obs$ combination, as both the *slow* and *fast* variant significantly affect the resulting dynamics compared to the *nominal* case.

The variation for the TS-I results in a *faster* decay compared to the *nominal* case as can be seen in the upper plot of Fig. 2.11. However, imposing a *slower* dynamics within this small variation of desired LMI region results in a response of the closed-loop system with no significant difference from the *nominal* design. This indicates the additional complexity by the coupling of the adjustment of operating point and feedback loop through the integral state in a coupled design. As a result, the degree of freedom in the design is increased by employing a wind speed disturbance observer compared to the integral-based approach TS-I.

2.5   Conclusion

Within this contribution, the TS modeling technique is discussed as a framework for the control and observer design of non-linear systems, where stability constraints and feedback gain syntheses are formulated as LMIs. By adding further constraints to the LMI stability problem, a desired performance can be imposed on the closed-loop dynamic. This facilitates for the shaping of the resulting closed-loop system towards a desired dynamical response for non-linear systems.

Further, the formulation of a TS observer with unmeasurable premise variables enables for the estimation of a wider class of systems compared to TS observers with the assumption of a measurable premise variable. The derived stability conditions of TS observers with unmeasurable premise variable differs from the existing approaches, such that the ISS property is used to account for the unmeasur-
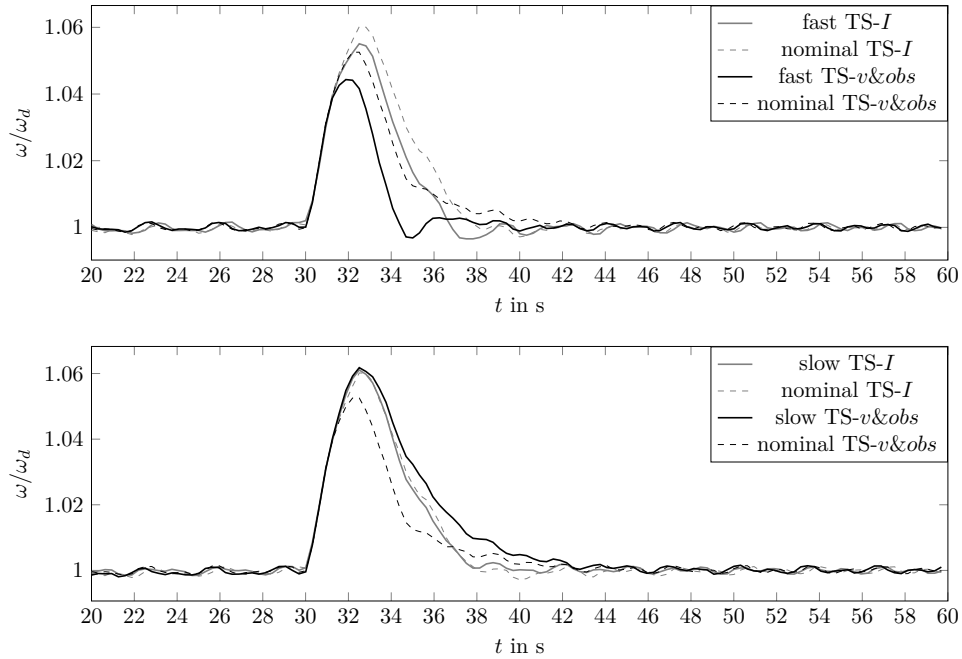
Figure 2.11: Detail view of the step response for different LMI region constraints (slow, nominal, fast) of the presented approaches TS-I and TS-$v\&obs$, where the resulting dynamics by variation of design parameters in the LMI synthesis is studied.

able premise variables, and a stability margin is verified even in a mismatch from the estimation of the premise variable. This results in a satisfying performance for the developed wind speed disturbance observer of the wind turbine application.

The estimation of the wind speed by the presented observer in TS form employs no additional sensor components in the presented wind turbine application compared to the state-of-the-art control concept. Therefore, compared to other approaches involving additional measurements, no hardware costs or chances of hardware failure necessitating costly maintenance are introduced to the application. The approach can be interpreted as using the rotor of the wind turbine as wind speed sensor, and the model-based observer design is used to convert the information from the rotational dynamics into an estimated wind speed signal. With regard to the different time scales governing the dynamics of the wind turbine, the information on the current wind speed is delayed by the inertia of the wind turbine, but by appropriate LMI-based observer design, a desired dynamic to the estimation error and the resulting feedforward term can be imposed. The resulting estimate of the wind speed represents an effective measure, which yields the excitation of the rotational dynamics, and therefore the stochastic three dimensional wind field can not be recovered in detail. Anyhow, for the presented approach this is not necessary, as the aim is to calculate a collective signal for the pitch angle of all blades simultaneously.

The obtained results from the simulation studies point towards the increased flexibility in the control design due the observer-based concept. By formulating the disturbance observer, the adjustment of the feedback terms to the current operating point is separated from the actual feedback signal. Stability and closed-loop dynamic constraints can be formulated in terms of LMIs in the design synthesis. As a result, a desired closed-loop dynamic of the combined TS-$v\&obs$ can be imposed, such that the effects of different time scales, i.e. the rotational dynamics of the wind turbine and the wind speed change can be shaped individually with respect to the limitations arising from the technical implementation such as conflicting natural frequencies of the application components.

References

[1] J G VanAntwerp and R D Braatz. A tutorial on linear and bilinear matrix inequalities. *Journal of Process Control*, 2000. DOI: 10.1016/S0959-1524(99)00056-6.

[2] G A M van Kuik, J Peinke, R Nijssen, D Lekou, J Mann, J N Sørensen, C Ferreira, J W van Wingerden, D Schlipf, P Gebraad, H Polinder, A Abrahamsen, G J W van Bussel, J D Sørensen, P Tavner, C L Bottasso, M Muskulus, D Matha, H J Lindeboom, S Degraer, O Kramer, S Lehnhoff, M Sonnenschein, P E Sørensen, R W Künneke, P E Morthorst, and K Skytte. Long-term research challenges in wind energy – a research agenda by the European Academy of Wind Energy. *Wind Energy Science*, 2016. DOI: 10.5194/wes-1-1-2016.

[3] J G Njiri and D Söfker. State-of-the-art in wind turbine control: Trends and challenges. *Renewable and Sustainable Energy Reviews*, 60, 2016. DOI: 10.1016/j.rser.2016.01.110.

[4] K Z Østergaard, P Brath, and J Stoustrup. Estimation of effective wind speed. *Journal of Physics: Conference Series*, 2007. DOI: 10.1088/1742-6596/75/1/012082.

[5] M N Soltani, T Knudsen, M Svenstrup, R Wisniewski, P Brath, R Ortega, and K Johnson. Estimation of rotor effective wind speed: a comparison. *IEEE Transactions on Control Systems Technology*, 2013. DOI: 10.1109/TCST.2013.2260751.

[6] D Jena and S Rajendran. A review of estimation of effective wind speed based control of wind turbines. *Renewable and Sustainable Energy Reviews*, 2015. DOI: 10.1016/j.rser.2014.11.088.

[7] E Gauterin, P Kammerer, M Kühn, and H Schulte. Effective wind speed estimation: comparison between Kalman Filter and Takagi–Sugeno observer techniques. *ISA Transactions*, 2016. DOI: 10.1016/j.isatra.2015.11.016.

[8] T Takagi and M Sugeno. Fuzzy identification of systems and its applications to modeling and control. *IEEE Transactions on Systems, Man, and Cybernetics*, 1985. DOI: 10.1109/TSMC.1985.6313399.

[9] K Tanaka and H O Wang. *Fuzzy Control Systems Design and Analysis: A Linear Matrix Inequality Approach*. John Wiley & Sons, Inc., 2001.

[10] Z Lendek, T M Guerra, R Babuska, and B De Schutter. *Stability Analysis and Nonlinear Observer Design Using Takagi-Sugeno Fuzzy Models*. Springer-Verlag Berlin Heidelberg, 2010.

[11] F Pöschke, J Fortmann, and H Schulte. Nonlinear wind turbine controller for variable power generation in full load region. In *2017 American Control Conference (ACC)*, 2017. DOI: 10.23919/ACC.2017.7963148.

[12] S Boyd, L El Ghaoui, E Feron, and V Balakrishnan. *Linear Matrix Inequalities in System and Control Theory*. Society for Industrial and Applied Mathematics, 1994.

[13] J F Sturm. Using SeDuMi 1.02, A Matlab toolbox for optimization over symmetric cones. *Optimization Methods and Software*, 1999. DOI: 10.1080/10556789908805766.

[14] E D Sontag. On the Input-to-State Stability Property. *European Journal of Control*, 1995. DOI: 10.1016/S0947-3580(95)70005-X.

[15] M Chilali and P Gahinet. H_∞ design with pole placement constraints: an LMI approach. *IEEE Transactions on Automatic Control*, 1996. DOI: 10.1109/9.486637.

[16] D Rotondo, V Puig, F Nejjari, and M Witczak. Automated generation and comparison of Takagi-−Sugeno and polytopic quasi-LPV models. *Fuzzy Sets and Systems*, 2015. DOI: 10.1016/j.fss.2015.02.002.

[17] H Schulte. On nonlinear observers in Takagi−Sugeno form based on fixed and variable structure. In *2016 IEEE International Conference on Fuzzy Systems (FUZZ-IEEE)*, 2016. DOI: 10.1109/FUZZ-IEEE.2016.7737989.

[18] P Bergsten. *Observers and Controllers for Takagi−Sugeno Fuzzy Systems*. PhD thesis, Orebro University, Schweden, 2001.

[19] D Ichalal, B Marx, J Ragot, and D Maquin. Brief paper: state estimation of Takagi-Sugeno systems with unmeasurable premise variables. *IET Control Theory Applications*, 2010. DOI: 10.1049/iet-cta.2009.0054.

[20] F Pöschke and H Schulte. Optimization of Takagi-Sugeno Observers with Application to Fault Estimation. In *Proceedings of the 3rd IFAC Conference on Embedded Systems, Computational Intelligence and Telematics in Control (CESCIT 2018)*, 2018. DOI: 10.1016/j.ifacol.2018.06.249.

[21] T Burton, N Jenkins, D Sharpe, and E Bossanyi. *Wind Energy Handbook*, chapter The Controller. John Wiley & Sons, Ltd, 2011.

[22] T Burton, N Jenkins, D Sharpe, and E Bossanyi. *Wind Energy Handbook*, chapter Design Loads for Horizontal Axis Wind Turbines. John Wiley & Sons, Ltd, 2011.

[23] P Towers and B Ll Jones. Real-time wind field reconstruction from LiDAR measurements using a dynamic wind model and state estimation. *Wind Energy*, 2016. DOI: 10.1002/we.1824.

[24] T F Pedersen, G Demurtas, and F Zahle. Calibration of a spinner anemometer for yaw misalignment measurements. *Wind Energy*, 2015. DOI: 10.1002/we.1798.

[25] F Dunne and L Y Pao. Optimal blade pitch control with realistic preview wind measurements. *Wind Energy*, 2016. DOI: 10.1002/we.1973.

[26] J Jonkman, S Butterfield, W Musial, and G Scott. Definition of a 5-MW Reference Wind Turbine for Offshore System Development. Technical report, National Renewable Energy Laboratory, 2009.

[27] B Jonkman and J Jonkman. *FAST v8.16.00a-bjj*. National Renewable Energy Laboratory, July 2016. Manual.

[28] J Jonkman and M L Buhl Jr. FAST User's Guide. Technical report, National Renewable Energy Laboratory, 2005.

[29] T Ekelund. Speed control of wind turbines in the stall region. In *1994 Proceedings of IEEE International Conference on Control and Applications*, 1994. DOI: 10.1109/CCA.1994.381194.

3 | Load mitigation and power tracking capability for wind turbines using LMI-based control design

Abstract

This article deals with non-linear model-based control design for wind turbines. By systematically integrating several mechanical degrees of freedom in the control design model, the load mitigation potential from the proposed multi-variable control framework is demonstrated. The application of the linear matrix inequality-based (LMI) control design is discussed in detail. Apart from the commonly considered power production mode, an extended operating range to provide stabilization of the electrical grid through power tracking is considered. This control functionality allows for an evaluation of the resulting fatigue and ultimate loads for power tracking at different dynamic requirements. The results indicate that under the impact of a dedicated control scheme this functionality is feasible with respect to the occurring loads and operational behavior of the wind turbine.

3.1 Introduction

In the process of reducing wind turbines' levelized cost of energy, research and industry focus on the up-scaling in spatial size and implemented technology [1]. This results in more flexible structures and an increasing number of couplings in the dynamical system. While employing an actuator to yield a desired objective, the unintended excitement of coupled structures requires an elaborate control design respecting several dynamically interacting sub-systems. A turbine's lifetime is determined by the occurring loads, resulting in load reduction being an explicit objective of control design [2]. Non-linear model-based approaches introduce a description of the complex wind turbine dynamics into the design and allow for a subsequent definition of desired closed-loop dynamics [3]. This allows to account for different performance objectives of the non-linear multi-input, multi-output wind turbine system before the control performance is evaluated by simulation or measurement studies, providing the basis for purposeful controller design.

Due to an increasing share of wind energy in the electrical grid, wind turbines' ability to provide ancillary services is central for providing a reliable and stable power supply [4]. Effectively, the envisaged concepts involve adjustment of the power output depending on the electrical grid's current state. While power system research studies the capability of wind turbines to replace conventional power plants in frequency stabilization of the electrical grid, see e.g., Morren et al. [5], the considerations usually comprise simple turbine representations neglecting mechanical loading. As the nominal power production trajectory is left due to power tracking, the covered operating range of the turbine increases significantly. Wind turbines exhibit a non-linear behavior governed by stochastic inflow as the main disturbance to be rejected by the control system. Consequently, the applied controller is required to handle highly varying system dynamics while accounting for the loads by enforcing desired closed-loop dynamics in a wide operating range.

The parallel implementation of several single-input, single-output control loops based on linear considerations and the subsequent interconnection through gain-scheduling to account for the non-linearity raises stability concerns. As the design complexity due to increasingly flexible and coupled structures in a wide operating range rises, stability considerations provide an effective measure for detecting unintended control interaction in the design process. Multi-variable model-based control design constrains the solution based on stability measures and therefore accounts for the dynamical representation integrated in the turbine model, while capable of integrating a wide operating range. Additional performance constraints are capable of shaping the closed-loop behavior in operation [3], where the translation from engineering requirements to an appropriate constraint formulation in the model-based design is of particular importance for the applicability.

The design of wind turbines usually is a process based on iterations among specialists [4], where few aspects in the wind turbine dynamics can be studied without respecting interaction with the controller [6]. A reproducible and modular design allows for a dedicated and fast controller adaption based on adjusted wind turbine model descriptions. This is beneficial for development processes, and consequently the adjustment to fast-evolving markets that turbine manufacturers have to withstand.

Model-based approaches have been proven to provide a valuable contribution to the advancement of wind turbine control in various works, e.g., by applying model-predictive control [7, 8, 9, 10]. The possibility to cope with non-linear dynamics attracted intensive research employing linear parameter-varying concepts [11, 12, 13, 14, 15] . However, some schemes only cover a limited region within normal operation mode and therefore do not incorporate the crucial blending between partial and full load in the proposed design [10, 13]. Other works remain short of the resulting loads from the controller action in operation [7, 10, 11, 14]. While Østergaard et al. [12], Schlipf et al. [8] and Koerber and King [9] provide promising results with respect to the operational behavior of the turbine, a variable output power tracking for grid stabilization is not discussed. In the work from Inthamoussou et al. [15] an approach towards a variable power control is presented. However, the authors do not illustrate the effects of tower loading, which plays a dominant role due to the strong feedback from pitch actuation [2] when altering the power output of the turbine.

In this article, a non-linear model- and observer-based control in the Takagi-Sugeno (TS) framework [16] is proposed, incorporating the following features:

- Reproducible non-linear model-based control design based on stability constraints

- Integrated approach with respect to several degrees of freedom to achieve load mitigation from control action

- Wind speed estimation by disturbance observer

- Extended operating range enabling electrical grid stabilization by power tracking

By enforcing active load reduction, enabling grid stabilizing behavior and providing a detailed illustration of design parameters in the proposed scheme, the purpose of this paper is to illustrate the merits of model-based control approaches offer for the wind turbine application. Further, the explicit consideration of the power tracking functionality allows for an assessment of loads resulting from power tracking operation at different dynamic requirements. In that way we can contribute to the discussion on the development of wind turbines capable of providing ancillary services.

The article is structured as follows. In Sec. 3.2 the non-linear TS model description is presented. The control and observer synthesis is described generally and subsequently applied to the wind turbine

control problem. In Sec. 3.3 the proposed controller's performance is evaluated and compared to a reference controller [17] based on simulation studies. The proposed control scheme is brought into a broader perspective within the discussion in Sec. 3.4, and a conclusion is drawn in Sec. 3.5.

3.2 Method

Linearized models carry valuable information for wind turbine controller design in the evaluated operating point [2]. However, due to the non-linear system dynamics involved, controller tuning in a particular operating point does not necessarily have positive effects on other operating points, giving rise to a possibly arduous controller tuning and scheduling design [11]. TS and linear parameter-varying concepts have a close connection [18] and can incorporate a variety of operating points and their corresponding linear models at once. By imposing performance constraints within the linear matrix inequalities (LMI) framework that can be solved efficiently by employing convex optimization [19], these concepts can enforce a desired transient response on the non-linear plant in operation.

The beginning of this section is therefore devoted to an introduction of the TS concept. While an in-depth description and derivation of the TS method would outreach the scope of this contribution, the theoretical foundation of the LMI-based design of this contribution is given in a previous work [20]. Application of the model-based design to wind turbine control is then discussed in detail. The design complexity is governed by the integration of different component models in the control synthesis (e.g., tower fore-aft motion or drivetrain oscillation) over a wide operating range, as each component possesses specific characteristics and thus the desired operational behavior differ depending on the considered component model. To illustrate the applicability of the general LMIs from the theoretical framework, an exemplary wind turbine, and the corresponding control design is studied in detail.

3.2.1 Theoretical framework

3.2.1.1 Non-linear Takagi-Sugeno modeling

By linearizing non-linear dynamics $\dot{x} = f(x, u, d)$ at a stationary operating point, models in form of

$$\dot{x} = A_i(x - x_{0i}) + B_i(u - u_{0i}) + B_{\mathrm{d}i}(d - d_{0i}) \tag{3.1}$$

can be derived, where x, u and d denote the state, input and disturbance, respectively. The state matrix A_i, input matrix B_i and disturbance matrix $B_{\mathrm{d}i}$ characterize the linear model dynamics at the evaluated operating point.

TS models describe non-linear systems as convex combination of linear sub-models that contribute to the overall non-linear behavior. The non-linear system dynamics in a TS structure within the defined operating range is given as [16]

$$\dot{x} = \sum_{i=1}^{N} h_i(z)\big(A_i(x - x_{0i}) + B_i(u - u_{0i}) + B_{\mathrm{d}i}(d - d_{0i})\big) \quad .$$

$$(3.2)$$

Depending on the premise vector z of dimension $j_{\max}$, which may be functions of inputs, states or external variables, the convex membership functions $h_i(z)$ adjust the current operating point of the model. They can be constructed by defining triangular weighting functions $w_{l,j}(z_j)$ conditioned on the value in l-th linearization point z_{0l} within the operating range [21] and are given by

$$w_{l,j}(z_j) = \begin{cases} \frac{z_j - z_{0(l-1)}}{z_{0l} - z_{0(l-1)}} & \text{if } z_{0(l-1)} < z_j \leq z_{0l} \\ 1 - \frac{z_j - z_{0l}}{z_{0(l+1)} - z_{0l}} & \text{if } z_{0l} < z_j \leq z_{0(l+1)} \\ 0 & \text{else} \end{cases}$$

$$(3.3)$$

for each premise variable z_j, $j = 1...j_{\max}$. If the premise vector is of dimension one, i.e., $j_{\max} = 1$, the weighting functions coincide with the membership function. Otherwise, the weighting functions are combined to form the membership functions that are used in the non-linear TS description of the system

$$\sum_{i=1}^{N} h_i(z) = \prod_{j=1}^{j_{\max}} \big(\sum_{l=1}^{l_{j,\max}} w_{l,j}(z_j)\big) \quad ,$$

$$(3.4)$$

where $l_{j,\max}$ is the resolution of the j-th premise variable. This approach gives an uniform and convex scheduling law design in several dimensions that is determined by definition of the linearization points of the premise variable z. The number of linear sub-models is given by the product $N = \prod_{j=1}^{j_{\max}} l_{j,\max}$.

3.2.1.2 LMI constraints for control design

The parallel distributed compensation law [16] following the TS structure forms the system input u

$$u = -\underbrace{\sum_{j=1}^{N} h_j(z)K_j(x - x_{0j})}_{u_{\mathrm{FB}}} + \underbrace{\sum_{j=1}^{N} h_j(z)\,u_{0j}}_{u_{\mathrm{FF}}} \quad ,$$

$$(3.5)$$

and consists of a feedback u_{FB} and feedforward u_{FF} term. Inserting (3.5) into (3.2), the closed-loop dynamics can be derived as

$$\dot{x} = \sum_{i=1}^{N} h_i(z) \sum_{j=1}^{N} h_j(z)\big((A_i - B_i K_j)(x - x_{0i}) + B_{\mathrm{d}i}(d - d_{0i})\big) \quad , \tag{3.6}$$

where the state matrix $(A_i - B_i K_j)$ under the impact of the feedback gains K_j to be designed describes the dynamical properties of the system.

When having a convex system description, a quadratic Lyapunov function $V(x) = x^{\mathrm{T}} X^{-1} x$ is a common approach for deriving LMI stability constraints [16], where $X = X^{\mathrm{T}} \succ 0$ is a symmetric positive definite matrix to be determined by the LMI solver. From stability conditions $V(x) \succ 0$ and $\dot{V}(x) = \dot{x}^{\mathrm{T}} X^{-1} x + x^{\mathrm{T}} X^{-1} \dot{x} \prec 0$ the following constraints can be obtained [16]

$$X A_i^{\mathrm{T}} + A_i X - M_j^{\mathrm{T}} B_i^{\mathrm{T}} - B_i M_j \prec 0 \quad . \tag{3.7}$$

The approach embeds all necessary combinations of i and j sub-models, i.e., $h_i h_j \neq 0 \ \forall i, j$ [16], into a common Lyapunov function characterized by X. Additionally, M_j is a variable determined by the LMI solver, where the desired feedback gains are calculated from $K_j = M_j X^{-1}$.

By introducing a lower and upper restriction in terms of the decay rate of the Lyapunov function candidate $\dot{V}(x) = -2\alpha V(x)$ with $\alpha_{\min} < \alpha < \alpha_{\max}$, the LMIs [16]

$$X A_i^{\mathrm{T}} + A_i X - M_j^{\mathrm{T}} B_i^{\mathrm{T}} - B_i M_j \prec -2\alpha_{\min} X \tag{3.8}$$

$$X A_i^{\mathrm{T}} + A_i X - M_j^{\mathrm{T}} B_i^{\mathrm{T}} - B_i M_j \succ -2\alpha_{\max} X \tag{3.9}$$

result. This allows us to define a minimum $\alpha_{\min}$ and maximum $\alpha_{\max}$ decay rate of the states and shape the closed-loop dynamics.

Further, the system's desired damping ratio D actively enforced by the controller can be characterized in terms of a line angle θ to the real axis [22] in the complex plane, and is calculated as $\theta = \arccos(D)$. The diagonal lines in later discussed Fig. 3.3 (c)-(e) split the complex plane, whereas every eigenvalue located to the left exhibits transient responses with a damping of at least D. Formulated in terms of LMIs this reads as [22]

$$\begin{bmatrix} \sin\theta\big(X A_i^{\mathrm{T}} + A_i X - M_j^{\mathrm{T}} B_i^{\mathrm{T}} - B_i M_j\big) & \cos\theta\big(A_i X - B_i M_j - X A_i^{\mathrm{T}} + M_j^{\mathrm{T}} B_i^{\mathrm{T}}\big) \\ \cos\theta\big(X A_i^{\mathrm{T}} - M_j^{\mathrm{T}} B_i^{\mathrm{T}} - A_i X + B_i M_j\big) & \sin\theta\big(A_i X - B_i M_j + X A_i^{\mathrm{T}} - M_j^{\mathrm{T}} B_i^{\mathrm{T}}\big) \end{bmatrix} \prec 0 \quad . \tag{3.10}$$

Unnecessary control activity within the dynamical constraints can be mitigated by a decrease of M_j's

gain magnitude. Characterized in terms of the euclidean norm $M_j^{\mathrm{T}} M_j \prec \gamma \mathrm{I}_{n \times n}$, where m and n denote the number of inputs and states, respectively, this can be formulated as

$$\min(\gamma) \quad \text{subject to} \quad \begin{bmatrix} -\gamma \mathrm{I}_{n \times n} & M_j^{\mathrm{T}} \\ M_j & -\mathrm{I}_{m \times m} \end{bmatrix} \prec 0 \quad , \tag{3.11}$$

where the LMI solver is used to minimize the optimization variable γ.

The discussed LMIs of this section are then flexibly combined within the wind turbine control procedure discussed in Sec. 3.2.2 to account for different dynamical requirements of the wind turbine components.

3.2.1.3   Disturbance observer

To provide an effective operating point adaption, an estimate of the disturbance acting on the system is reconstructed by an observer. Generating an estimate of the disturbance, which represents the current inflow of the wind turbine, based on the available measurements of the turbine has been applied in previous research, where comparison of different techniques can be found in e.g., [23, 24, 25] and applied in a closed-loop scheme in e.g., [7, 9].

The estimation scheme in this work is also formulated in the TS framework, and LMI-based observer design yields the necessary feedback gains [21]. Along with scheduling of the control scheme, the disturbance estimate provides a feedforward term that is part of the system input in (3.5). The possibility to assess unmeasurable but observable states $\hat{x}$ is exploited in calculation of the feedback term in (3.5). The observer closed-loop dynamics is therefore central to the overall performance of the control scheme.

The disturbance observer using the system output y is defined as

$$\dot{\hat{x}} = \sum_{i=1}^{N} h_i(z) \Big(\underbrace{\begin{bmatrix} A_i & B_{\mathrm{d}i} \\ 0 & -1/\tau \end{bmatrix}}_{\hat{A}_i} \begin{bmatrix} \hat{x} - x_{0i} \\ \hat{d} - d_{0i} \end{bmatrix} + \underbrace{\begin{bmatrix} B_i \\ 0 \end{bmatrix}}_{\hat{B}_i} (u - u_{0i}) + L_i(y - \hat{y}) \Big) \quad , \tag{3.12}$$

where an artificial state $\hat{d}$ represents the estimated disturbance within the augmented system description. While the real wind disturbance is a stochastic variable acting at various timescales, this first-order model description assigns a virtual inertia characterized by τ to the disturbance. Augmentation of the system can be performed if the resulting model remains observable. The disturbance input gains $B_{\mathrm{d}i}$ from the linearization analysis in (3.14) are used for definition of the state matrices

$\hat{A}_i$. The observation error dynamics $\dot{e} = \dot{\tilde{x}} - \dot{\hat{\tilde{x}}}$, with $\tilde{x} = [x^{\mathrm{T}}\ d]^{\mathrm{T}}$ based on (3.2) and the system output matrix C with $y = Cx$, can then be found as

$$\dot{e} = \sum_{i=1}^{N} h_i(z)(\hat{A}_i - L_iC)e \quad . \tag{3.13}$$

By employing a quadratic Lyapunov function on the error dynamics dually to the LMI-based controller feedback design, stability and performance region constraints for the observer can be obtained [20, 21].

3.2.2 Application of method to wind turbine control

3.2.2.1 Non-linear model of the reference wind turbine

Without limiting the general applicability, we employ NREL's well-known 5 MW reference turbine [26] for our investigation. Due to the interpretability of the modeled system disturbance as the rotor effective wind speed, the disturbance term is denoted as $d = v$ in the following. The considered control design model comprises four degrees of freedom. We include the aerodynamic conversion process affecting the rotational dynamics characterized by the rotor speed ω_r and generator speed ω_g, and the coupled drivetrain torsion $\Delta\theta_{\mathrm{DT}}$. The tower fore-aft (TwFA) and side-to-side (TwSS) motion is considered in the control design model, completing the model description in (3.14). The system matrix A_i comprises the first tower eigenmodes and -frequencies along with its corresponding damping. From the later discussed Fig. 3.3 (a), it can be observed that two complex conjugate pole pairs characterize the tower fore-aft and side-to-side motion of the N sub-models. An additional conjugate complex pole pair along with a real-valued decaying state represent the rotational and drivetrain dynamics of the turbine.

We define the premise variables that govern the membership functions as the current wind speed and power tracking signal, i.e., $z = [v \quad \Delta p]^{\mathrm{T}}$. While the estimated wind from the disturbance observer is used in controller operation, the power tracking signal Δp can be adjusted by an external operator or a higher level control scheme to adjust the power output depending on the current requirements from the electrical grid.

Wind turbine models in form of

$$\dot{x} = \underbrace{\begin{bmatrix} A_{i\mathrm{TwSS}} & 0_{2\times2} & 0_{2\times3} \\ 0_{2\times2} & A_{i\mathrm{TwFA}} & 0_{2\times3} \\ 0_{3\times2} & 0_{3\times2} & A_{i\mathrm{DT}} \end{bmatrix}}_{A_i} (x - x_{0i}) + \underbrace{\begin{bmatrix} 0_{2\times1} & B_{i\mathrm{TwSS}} \\ B_{i\mathrm{TwFA}} & 0_{2\times1} \\ B_{i\mathrm{DT}\beta} & B_{i\mathrm{DT}T} \end{bmatrix}}_{B_i} \underbrace{\begin{bmatrix} \beta - \beta_{0i} \\ T - T_{0i} \end{bmatrix}}_{u - u_{0i}} + B_{\mathrm{d}i}(v - v_{0i}) \tag{3.14}$$

are constructed from the linearization analysis at stationary points $|_{c_{0i}} = |_{x_{0i}, u_{0i}, v_{0i}, \Delta p_{0i}}$, where c_{0i} denotes the set of operational values that determine the location within the operating range. The state vector is given by $x = \begin{bmatrix} x_{\text{TwSS}} & \dot{x}_{\text{TwSS}} & x_{\text{TwFA}} & \dot{x}_{\text{TwFA}} & \omega_r & \omega_g & \theta_{\text{DT}} \end{bmatrix}^{\text{T}}$, while the inputs β and T denote the collective pitch angle and generator torque, respectively. The proposed structure of the model yields a convenient model description for control design, where the structure of the input matrices B_i results in coupling of the considered degrees of freedom, but possible structural coupling within the system matrices A_i is neglected. The TwSS and TwFA open-loop dynamics are modeled as second-order transfer functions in accordance to FAST [27]

$$A_{i\text{TwSS}} = \begin{bmatrix} 0 & 1 \\ \frac{\partial f_2(x,u,v)}{\partial x_{\text{TwSS}}}|_{c_{0i}} & \frac{\partial f_2(x,u,v)}{\partial \dot{x}_{\text{TwSS}}}|_{c_{0i}} \end{bmatrix}, \quad A_{i\text{TwFA}} = \begin{bmatrix} 0 & 1 \\ \frac{\partial f_4(x,u,v)}{\partial x_{\text{TwFA}}}|_{c_{0i}} & \frac{\partial f_4(x,u,v)}{\partial \dot{x}_{\text{TwFA}}}|_{c_{0i}} \end{bmatrix}$$

and $A_{i\text{DT}}$ follows the widely employed modeling structure of the drivetrain [7, 12, 14, 15]. The input matrices are defined as

$$B_{i\text{TwSS}} = \begin{bmatrix} 0 \\ \frac{\partial f_2(x,u,v)}{\partial T}|_{c_{0i}} \end{bmatrix}, \quad B_{i\text{TwFA}} = \begin{bmatrix} 0 \\ \frac{\partial f_4(x,u,v)}{\partial \beta}|_{c_{0i}} \end{bmatrix},$$

$$B_{i\text{DT}\beta} = \begin{bmatrix} \frac{\partial f_5(x,u,v)}{\partial \beta}|_{c_{0i}} \\ 0_{2\times 1} \end{bmatrix}, \quad B_{i\text{DT}T} = \begin{bmatrix} 0 \\ \frac{\partial f_6(x,u,v)}{\partial T}|_{c_{0i}} \\ 0 \end{bmatrix},$$

such that in this model description pitching acts on the rotor speed ω_r and the tower fore-aft motion $\dot{x}_{\text{TwFA}}$, while a variation of the generator torque T affects the generator speed ω_g and tower side-to-side oscillation $\dot{x}_{\text{TwSS}}$.

For definition of the model dynamics at each operating point, the partial derivatives are used that result from the linearization analysis conducted with FAST [27]. Here, they are denoted using the corresponding position of the considered state in the vector function of the overall dynamics $\dot{x} = f(x, u, v)$, where e.g., $f_2(x, u, v) = \ddot{x}_{\text{TwSS}}$ refers to the second entry and in this case defines the dynamics of the tower side-to-side motion. In Figure 3.1 (a), (b) and (c) the resulting partial derivatives are illustrated. While the sensitivity to pitching varies significantly in operation underlining the non-linear dynamics, see Figure 3.1 (a) and (b), the component's sensitivity to torque variations is constant, see Figure 3.1 (c).

Based on N linear sub-models locally describing the dynamics at the corresponding operating points in (3.14), an overall non-linear description in the TS framework can be obtained, which follows the model description in (3.2).
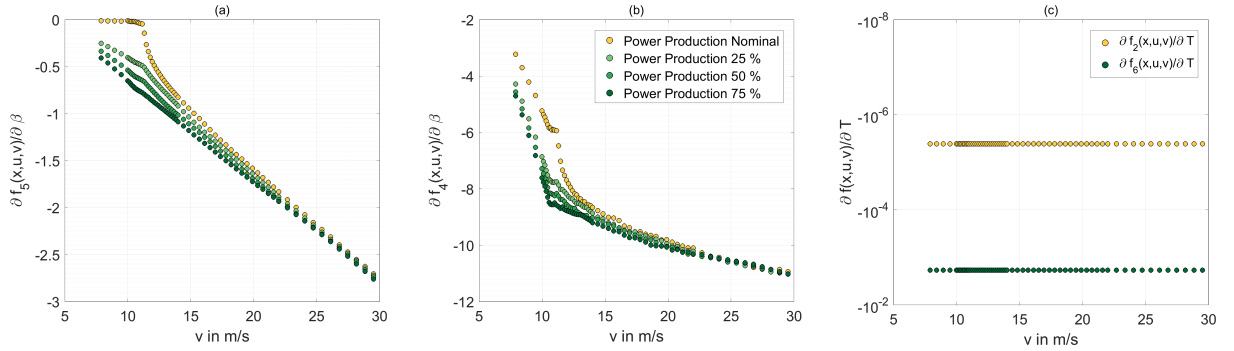
Figure 3.1: Wind turbine model coefficients at the evaluated stationary operating points. Sensitivity of (a) the rotor speed to changes in the pitch angle (b) fore-aft tower top displacement to changes in the pitch angle (c) generator speed and side-to-side tower top displacement to changes in the generator torque. The coefficients are gained by linearization analysis and used to create linear sub-models of the wind turbine components. Combined in the TS framework, the linear sub-models describe the overall non-linear wind turbine dynamics.

3.2.2.2 Operational concept

In the presented approach, the choice of linearization points determines the desired operating trajectory of the turbine that is enforced by the applied controller. As usual in wind turbine control, different actuators govern the rotational speed feedback depending on the current operating region. During nominal power production below rated wind speed, the torque is active for optimal tip speed ratio tracking and the pitch angle is fixed at 0 deg (see Figure 3.2) until the rated rotational speed is reached. From this point the generator torque is used to regulate the rotation until rated generator torque is reached, where for increasing wind inflow the pitch angle is used to perform regulation of the rotational speed. This approach follows the commonly applied concept for wind turbine operation [26, 17] and can be identified from *nominal* power production in Figure 3.2, where the inputs inducing stationary behavior at the considered operating points of the linearization analysis are depicted. The linearization is conducted at $l_{1,\mathrm{max}} = 63$ operating points in a range of $v = [7.89...30]$ m/s unevenly distributed along the operating range as can be identified from Figure 3.2, where the lower bound corresponds to the beginning of the optimal tip speed tracking region [26].

To enable the power tracking functionality, linearization is not only conducted on the nominal power production curve, i.e. $\Delta p = 0$, but we sought for stationary points with reduced power output for the same wind speed at $l_{2,\mathrm{max}} = 4$ discrete steps. The power tracking signal Δp is normalized to the power output on the nominal power trajectory, which depends on the current inflow condition. By definition of the power tracking signal range $\Delta p = [0\ .25\ .5\ .75]$ from the *nominal* power production $\Delta p = 0$ at a given wind speed and rotational speed, a reduced generator torque T_0 varies the power output. This is coped by an adjustment of the pitch angle to obtain stationary behavior, i.e., $\dot{x} = 0$.
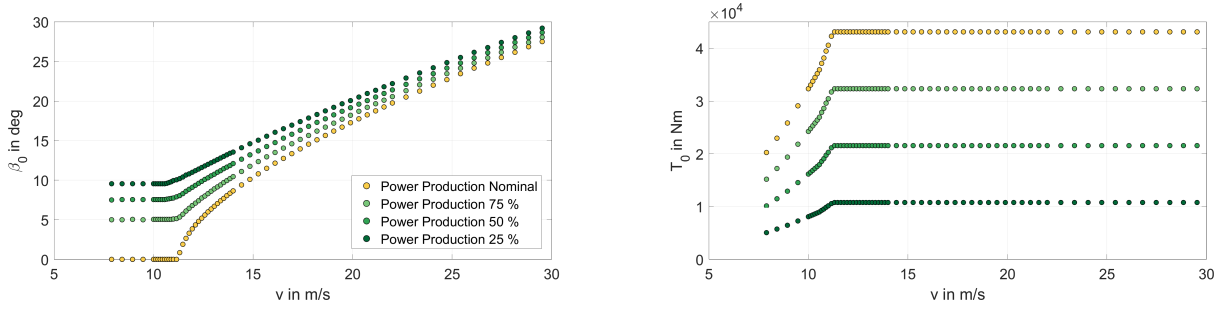
Figure 3.2: Input of the wind turbine at different stationary points. The operating points comprise the nominal production mode and reduced power output at steps of 75%, 50% and 25% relative to the current available wind power. Governed by the estimated wind speed of the observer, the values of the pitch angle β_0 and generator torque T_0 provide the basis for the feedforward term in the control scheme, see Figure 3.5.

This approach results in a total number of $N = 63 \cdot 4 = 252$ linearized models. From Figure 3.2 it can be observed that the inputs inducing stationary behavior at a given wind speed deviate significantly for different desired power outputs of the turbine, as the torque is varied to match the desired power output, while the pitch angle is employed to balance the aerodynamic torque to the applied generator torque in full and partial load operation with reduced power output compared to the nominal power trajectory.

3.2.2.3 Control design

The inherent dynamical response of the turbine model in an operating point is characterized by the poles λ_i of A_i in (3.14). Consequently, by influencing the pole location under the impact of the individual feedback gains, a desired transient behavior of the turbine can be enforced by the controller. Convexly blended in operation, the dynamical properties of the closed-loop linear sub-models shape the non-linear system response of the wind turbine. In Figure 3.3 the poles of the state matrices A_i are captured open- (a) and closed-loop (b)-(f) depending on the control design stage. Depending on the considered component and objective, different LMI stability and performance constraints can be combined to form a powerful control design concept.
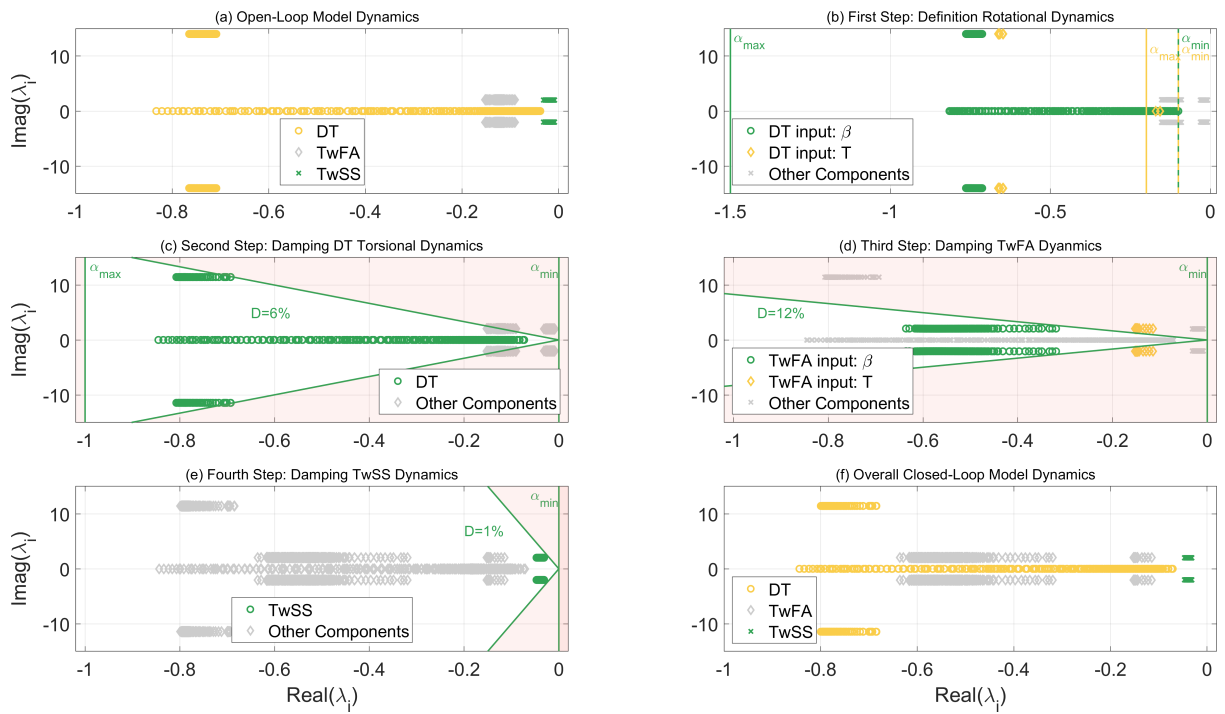
Figure 3.3: Pole locations of the wind turbine model at N stationary operating points in the complex plane at individual steps of the control design. Subfigures (a) and (f) provide an impression of the open-loop and closed-loop wind turbine dynamics. Subfigures (b)-(e) illustrate the relocation of the poles of certain wind turbine components within the individual feedback design steps due to the LMI-based performance criteria.

The feedback gains of (3.5) in the overall form are defined as

$$K_j = \begin{bmatrix} 0_{1\times2} & 0_{1\times2} & 0_{1\times3} \\ K_{j\mathrm{TwSS}} & 0_{1\times2} & K_{j\widetilde{\mathrm{DT}}} \end{bmatrix}, \quad \text{if input T}$$

$$\text{or} \tag{3.15}$$

$$K_j = \begin{bmatrix} 0_{1\times2} & K_{j\mathrm{TwFA}} & [K_{j\omega_r\beta}\, 0_{1\times2}] \\ K_{j\mathrm{TwSS}} & 0_{1\times2} & K_{j\mathrm{DT}} \end{bmatrix}, \quad \text{if input } \beta \quad .$$

The gain structure reflects the employed actuator for the corresponding j-th operating point. If the turbine is operated on the nominal power trajectory below rated power, i.e., $P < P_{\mathrm{rated}}$ with $\Delta p = 0$, only the generator torque control is used to provide feedback to the rotational speed, while the pitch angle is employed in all other operating points. The blending of controller gains based on the estimated wind speed and power tracking signal automatically incorporates this conceptual change in operation of the plant in the TS framework, and therefore no separate treatment of transitional regions is necessary in the proposed scheme.

The structure is chosen to suppress some couplings from the control action in the multi-variable control problem. This prevents unnecessary control action from interfering with other modeled but uncoupled states of the system model by feedback calculation, as would result from a full state feedback. I.e., from the definition of inputs $u = [\beta \quad T]^{\mathrm{T}}$ and the above definition of the feedback gains, the TwSS observer states act on the generator torque T only, while the TwFA observer states influence the pitch angle, both aiming for an active damping in operation. The individual feedback gains $K_{j\mathrm{TwSS}}$, $K_{j\mathrm{TwFA}}$, $K_{j\mathrm{DT}}$ and $K_{j\omega_r\beta}$ represent the feedback for the TwSS and TwFA motion, as well as the feedback of the drivetrain oscillation or rotor speed depending on the current operating point. The gains $K_{j\widetilde{\mathrm{DT}}}$ are constructed to combine rotational speed feedback $K_{j\omega_r T}$ with damping characteristics imposed on the drivetrain oscillation in the design of $K_{j\mathrm{DT}}$ at operating points where the generator torque is employed for both purposes. The feedback gains are derived sequentially and are subsequently integrated into the overall structure of K_j.

The control design is composed of different steps. This accounts for the sensitive dynamical behavior of the wind turbine by enforcing a desired performance for each modeled component individually employing LMIs presented within the theoretical framework. It allows for a modular handling of different turbine components for control design.

Step 1: definition of the rotational dynamics   A feedback from the drivetrain oscillation to the pitch is avoided as this severely excites tower and blade oscillations. For that reason, a rigid drivetrain model representing the non-linear rotational dynamics ω_r as combinations of first-order transfer functions and neglecting the drivetrain flexibility is used in the first design step.

The model is analogously derived in operating points from Figure 3.2, but only the rotor degree of freedom is enabled in the linearization analysis using FAST [27], which results in reduced a wind turbine model following $\dot{\omega} = f(\omega, \beta, T, v)$ as shown in [20]. This yields a model description in form of

$$
\dot{\omega}_r = \sum_{i=1}^{N} h_i(v, \Delta p) \Bigg(\bigg[\underbrace{\frac{\partial f(\omega, \beta, T, v)}{\partial \omega_r}\big|_{c_{0i}}}_{A_{\omega_r,i}} \bigg] (\omega_r - \omega_{r0i})
$$
$$
+ \bigg[\underbrace{\frac{\partial f(\omega, \beta, T, v)}{\partial \beta}\big|_{c_{0i}}}_{B_{\omega_r\beta,i}} \quad \underbrace{\frac{\partial f(\omega, \beta, T, v)}{\partial T}\big|_{c_{0i}}}_{B_{\omega_r T,i}} \bigg] (u - u_{0i}) \Bigg) \quad ,
$$

(3.16)

where depending on the feedback actuator of the j-th operating point in the control design either $B_{\omega_r T,i}$ or $B_{\omega_r\beta,i}$ is employed for definition of the LMIs. The input u is equivalently given by the pitch and generator torque as described in (3.14).

A favorable starting point for the definition of a desired rotational behavior is provided by the open-loop dynamics in Figure 3.3 (a). Whereas in lower wind speed the turbine exhibits a slower transient response, in higher wind speed the pole locations move further into the left half of the complex plane, which is also reflected by a decreasing standard deviation of the rotor speed as illustrated in Figure 3.9 (f). This basic behavior is reproduced by our control concept, where the rotational dynamics when the torque is used as feedback (yellow in Figure 3.3 (b)) is defined in a narrow range close to the origin of the complex plane. For operating points governed by pitching, a wider range of dynamics is accepted, resulting in the green region constraints illustrated in Figure 3.3 (b) and given by (3.8), (3.9). Additionally, (3.11) is applied for matrices incorporating a pitch feedback to optimize for reduced pitch activity.

This design step results in feedback matrices $K_{j\omega_r\beta}$ and $K_{j\omega_r T}$ depending on the operating point. While the rotational speed feedback for the pitching $K_{j\omega_r\beta}$ can be readily introduced into the description (3.15), the operating points with torque feedback to the rotational speed $K_{j\omega_r T}$ are combined with the drivetrain damper gains in the next step as they act through the same input.

Step 2: damping drivetrain torsional dynamics   By employing LMIs (3.8), (3.9), (3.10) and (3.11) to the drivetrain model $A_{i\mathrm{DT}}$ and generator torque input matrix $B_{i\mathrm{DT}T}$, a damping ratio of $D =$

6% on the torsional oscillation can be enforced. As illustrated in Figure 3.3 (c), the imposed region constraints result in a damped closed-loop behavior indicated by a reduced imaginary part of the conjugate complex pole pair, i.e., lowering $\mathrm{Imag}(\lambda_i) \approx 14\,\mathrm{s}^{-1}$ to $\mathrm{Imag}(\lambda_i) \approx 11\,\mathrm{s}^{-1}$ while retaining similar real parts. This damping ratio yields appropriate drivetrain dynamics as will be shown in the load analysis in Sec. 3.3.2.

This design step results in feedback gains $K_{j\mathrm{DT}}$. For operating points that employ the pitch angle for the rotational speed feedback, the derived gains are incorporated as shown in (3.15). If the torque is used for rotational feedback, the drivetrain damping gains are combined with the previously synthesized gains for rotation feedback from torque

$$K_{j\widetilde{\mathrm{DT}}} = \begin{bmatrix} K_{j\omega_r T} & 0_{1\times 2} \end{bmatrix} + K_{j\mathrm{DT}} \quad . \tag{3.17}$$

Step 3 and 4: damping TwFA/TwSS dynamics   By applying LMI constraints (3.8), (3.10) and (3.11) to the TwFA model $A_{i\mathrm{TwFA}}$ and $B_{i\mathrm{TwFA}}$, a damping of the motion by pitching is enforced. As we (optionally) only incorporated TwFA feedback when the pitch rotational feedback loop is active, in some operating points the pole locations of the TwFA motion remain constant (yellow in Figure 3.3 (d)). We imposed a damping ratio of $D = 12\%$ to the remaining operating points, resulting in a movement of the TwFA poles further into the left half, compare Figure 3.3 (a) and (d).

The same approach is applied to the TwSS model $A_{i\mathrm{TwSS}}$ and $B_{i\mathrm{TwSS}}$ using the torque input for all modeled operating points. This pushes the TwSS poles further to the left, compare Figure 3.3 (a) and (e), and results in a guaranteed damping ratio of at least $D = 1\%$. This small damping shows great consequences for the resulting loads, as this motion is highly undamped in open-loop mode indicated by its location close to the imaginary axis. The resulting feedback gains $K_{j\mathrm{TwFA}}$ and $K_{j\mathrm{TwSS}}$ can then be incorporated into the overall model description as shown in (3.15).

Step 5: justification of stability   Even though in the previous steps LMI constraints that verify stability of the considered component models are used, through the interaction of all feedback loops couplings of the previously decoupled system result. The effects for stability of the considered wind turbine model can be evaluated in the discussed LMI framework. The proposed stepwise control design allows for great flexibility with regard to different degrees of freedom of the wind turbine structure at cost of a possible iterative final justification of stability that interconnects all individually derived feedback gains.

The last step consists of finding a quadratic Lyapunov function for the overall closed-loop dynamics under the impact of K_j, which is illustrated in Figure 3.3 (f). Through combination of all necessary i

and j, i.e. $h_i h_j \neq 0 \; \forall i, j$ [16], in the LMIs

$$X(A_i - B_i K_j)^{\mathrm{T}} + (A_i - B_i K_j)X \prec 0 \tag{3.18}$$

and deriving a solution for X, stability of the non-linear closed-loop design model on the considered operating trajectory is verified. The justification of stability does not incorporate robust measures that account for additional disturbance terms induced by a wind speed estimation error, and the associated model uncertainty. However, by enveloping the entire considered operating region into a Lyapunov function including the conceptual change in actuation from generator torque to pitch, this step at the end provides a valuable verification of the derived controller's effectiveness.

3.2.2.4   Observer design

In the considered model we assume the tower top displacement (TwFA and TwSS) as measurable. While direct measurements of the tower top deflection are hardly feasible, a tower acceleration signal can be used to provide the velocities and position of the tower top [2] in application of the approach. The drivetrain torsional angle θ_{DT} is estimated from measurements of both the rotor and generator speed. This yields an output matrix C in form of

$$y = C\tilde{x} = \begin{bmatrix} 1 & 0 & 0 & 0 & 0 & 0 & 0 & 0 \\ 0 & 0 & 1 & 0 & 0 & 0 & 0 & 0 \\ 0 & 0 & 0 & 0 & 1 & 0 & 0 & 0 \\ 0 & 0 & 0 & 0 & 0 & 1 & 0 & 0 \end{bmatrix} \tilde{x} \quad .$$

The time constant of the first-order disturbance model is defined as $\tau = 4\;s$, and the estimated disturbance represents the current effective wind speed, i.e., $\hat{d} = \hat{v}$. While the inflow acts among various time scales, this parameter can be chosen such that the modeled dynamics represent a relevant time scale relative to the rotational wind turbine dynamics (see also location of wind model in the complex plane in Figure 3.4). The effective wind speed estimated by the observer portrays a virtual one-dimensional wind speed that excites the modeled system in a representative manner compared to the turbulent, three-dimensional inflow.

The definition of adequate observer dynamics is central to the proposed control scheme. On the one hand, a fast decaying estimation error is favorable as this means scheduling and decay of the estimated states $\hat{x}$ in the feedback loop at a short timescale. However, as a change in the wind disturbance estimate $\hat{v}$ directly varies the pitch angle through the feedforward term u_{FF}, a trade-off due to limitations of the pitch activity and resulting loads is required.
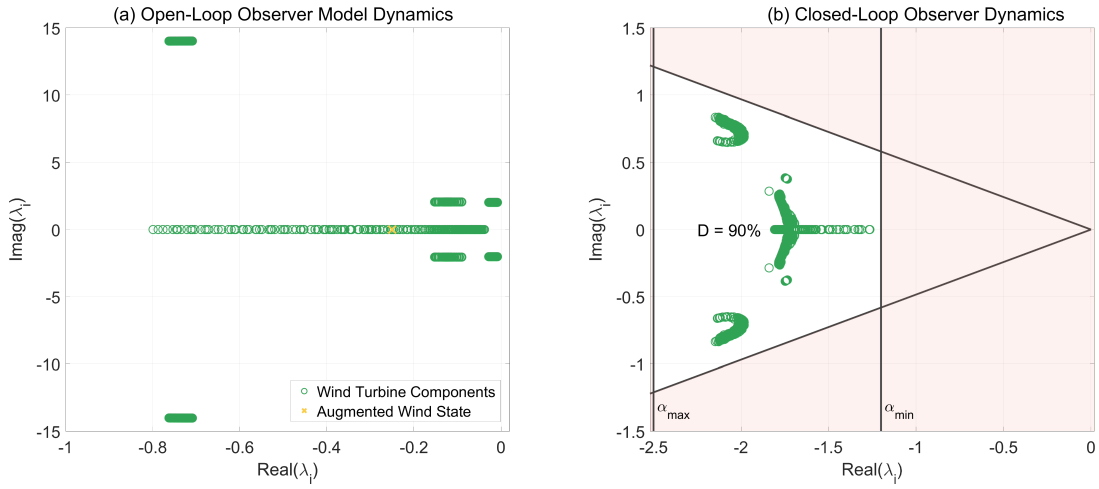
Figure 3.4: Pole locations of the observer model (a) open-loop and (b) closed-loop after LMI-based observer feedback gain synthesis. The model comprises an augmented wind state, which in closed-loop provides an estimate for scheduling of feedback gains and is used for calculation of a feedforward term.

To achieve this, an LMI formulation is chosen that defines the closed-loop dynamics to lie within a particular region in the complex plane. This region is shaped by employing the observer equivalent formulation [20] for the conical sector defined by θ in (3.10), $\alpha_{\min}$ in (3.8) and $\alpha_{\max}$ in (3.9). Assigning a damping of at least $D = 90\%$ and $\alpha_{\min} = 1.2$ and $\alpha_{\max} = 2.5$ results in Figure 3.4 (b), where the closed-loop observation error dynamics are depicted.

The open-loop pole locations in Figure 3.4 (a) are identical to the poles of the control design model in Figure 3.3 (a), except for the additional poles introduced by the augmented wind state in (3.12). The closed-loop error dynamics is posed faster than closed-loop system dynamics to ensure an adequate scheduling of the control gains and feedforward action. The observer dynamics can be separated dynamically from the closed-loop system by assigning an adequate $\alpha_{\min}$ (compare pole locations in Figure 3.3 (f) to Figure 3.4 (b)), while the bandwidth of the observer is limited using the design parameter $\alpha_{\max}$. The assigned damping ratio prevents the observer from inducing oscillations into the wind turbine structure from the feedfoward term. The application of an observer is capable of separating the design of desired closed-loop behavior enforced by the feedback gains and the adjustment to changes in the operating point due to a variation in the wind speed.

3.3   Simulation studies

The proposed controller is evaluated in different deterministic and turbulent wind inflow scenarios connected to FAST [27], which is configured as NREL's 5 MW reference turbine [26]. The resulting

$$y = [\omega_{\mathrm{r}} \ \omega_{\mathrm{g}} \ x_{\mathrm{TwFA}} \ x_{\mathrm{TwSS}}]^{\mathrm{T}}$$

TS Feedback Controller
$u_{\mathrm{FB}} = -\sum_{j=1}^{N_r} h_j(\hat{v}, \Delta p) K_j(\hat{x} - x_{0j})$

Aeroelastic wind turbine model
Input : $u = u_{\mathrm{FF}} + u_{\mathrm{FB}} = [\beta, \ T]^{\mathrm{T}}$

$\hat{\tilde{x}} = [\hat{x}^{\mathrm{T}} \ \hat{v}]^{\mathrm{T}}$

TS Wind Speed Observer
$\dot{\hat{\tilde{x}}} = \sum_{i=1}^{N_r} h_i(\hat{v}, \Delta p)\big(\hat{A}_i(\hat{\tilde{x}} - \tilde{x}_{0i}) + \hat{B}_i(u - u_{0i}) + L_i(y - \hat{y})\big)$
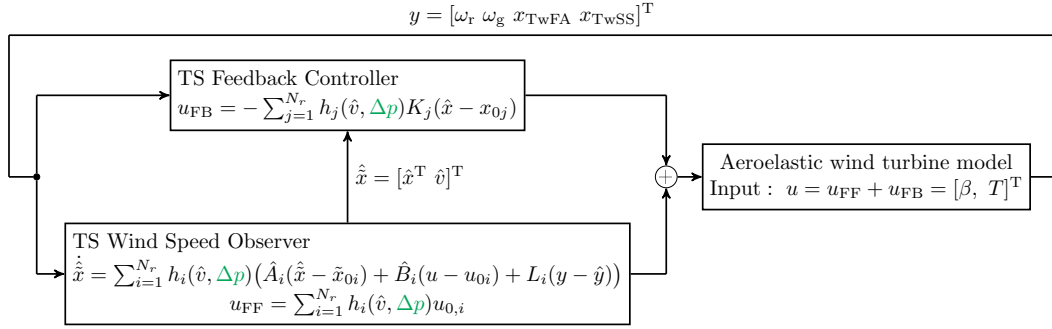$u_{\mathrm{FF}} = \sum_{i=1}^{N_r} h_i(\hat{v}, \Delta p)u_{0,i}$

Figure 3.5: Block diagram of the presented control scheme. The control functionality is captured in the model and feedback matrices along with an on-line calculation of the TS membership functions based on the estimated wind speed $\hat{v}$ and power tracking signal Δp. The observer states $\hat{x}$ are used in calculation of the feedback loop.

state trajectories and occurring loads are compared to the Delft Research Controller (DRC) [17]. The DRC software package comprises a configuration for the evaluated 5 MW turbine, which is used as reference control implementation. The entire TS control functionality in operation is captured in the block diagram Figure 3.5.

Design load cases   We analyze the wind turbine under the impact of step wind signals (see Figure 3.6). Additionally, the occurring loads in typical inflow conditions are analyzed based on the following Design Load Cases (DLC) [28]:

- DLC 1.1 : Turbulent inflow, according to the *normal turbulence model* to obtain fatigue and ultimate loads with mean wind speeds $v_{j,\mathrm{mean}}$ in the range of $v_{j,\mathrm{mean}}$ = 8 m/s to $v_{8,\mathrm{mean}}$ = 22 m/s with $\Delta v_{\mathrm{mean}} = 2$ m/s.

- DLC 1.6 : A deterministic *extreme operating gust* at four different wind speeds $v_{\mathrm{r}-2\,\mathrm{m/s}}$, v_{r}, $v_{\mathrm{r}+2\,\mathrm{m/s}}$ and v_{CutOut} (with the rated wind speed v_{r}) to obtain ultimate loads.

Load assessment   For performance evaluation of different control configurations and scenarios, the loads during simulation are mapped onto a comparable quantity. To assess the controllers capability to maintain the desired rotational speed despite of the disturbing wind, standard deviation $\mathrm{std}(\omega)$ of the rotational speed is analyzed. The pitch wear from controller activity is accounted for by the actuator duty cycle (ADC) [29], i.e., ADC = $1/T \int_0^T |\dot{\beta}(t)|\mathrm{d}t$ over simulation time T.

Fatigue loading of the mechanical structure is estimated in terms of the damage equivalent load (DEL) that depends on the material parameter k, i.e., the inverse slope of the *S/N-curve*, and loading history over simulation time. For that purpose we chose $k = 4$ for the steel tower and $k = 10$ for the blades

made of reinforced glass or carbon fibre [30]. The equivalent load cycle number n_{eq} corresponds for the blades to the number of rotor revolutions at rated rotor speed during a period of 600 s, and for the tower to a three times higher number, i.e., the number of blade passages at the tower. To identify the individual load cycles $S_{a,i}$ and number of occurrences n_i, the package provided by Niesłony [31] is used, such that the damage equivalent load is then calculated from $\mathrm{DEL} = (\frac{1}{n_{\mathrm{eq}}} \sum_i n_i S_{a,i}^k)^{\frac{1}{k}}$.

The DEL is analyzed for the tower base fore-aft moment (TwrBsMyt), tower base side-to-side moment (TwrBsMxt), Blade 1 flapwise moment (RootMyb1) and drivetrain shaft torque ΔT as representative components of the wind turbine structure. Within the ultimate load analysis, the same load sensors are investigated.

Power tracking specification   To study turbine loading of power tracking at different gradients, the TS controller performance is evaluated for different power tracking signals with identical wind inputs. In that way an analysis of grid stabilizing behavior on the wind turbine operation under the impact of a dedicated control scheme can be assessed. The turbine's loading history is influenced by the form and evolution of the power tracking and therefore affected by the requirements of transmission grid operators.

For instance, Hydro-Québec as Canadian transmission system operator requires wind farms to vary the power output by at least 5% "dynamically and rapidly" for 10 s [32]. Assuming a time of 0.5 s as fast enough to adjust the power output by 5%, results in a power gradient of $\mathrm{d}\Delta p/\mathrm{d}t = 10\%\mathrm{s}^{-1}$. This requirement provides the center of evaluated power tracking scenarios (Sc2) with a faster (Sc3) and slower configuration (Sc1), which are summarized in Table 3.1.
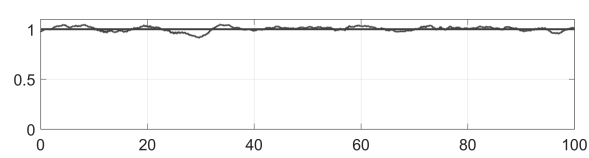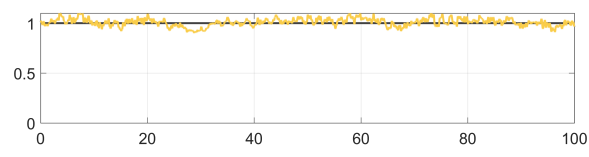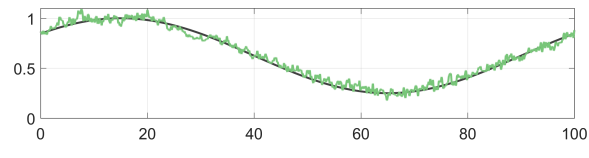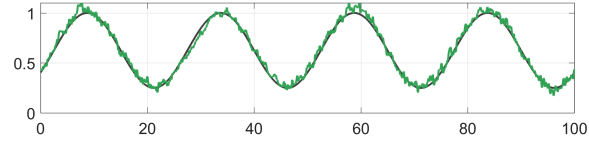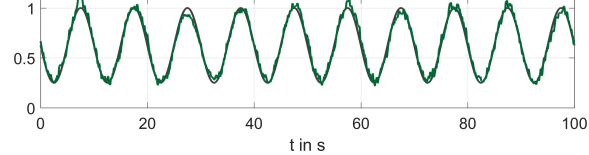
3.3.1   Step response of the system dynamics

A comparison of the response to step changes in the wind speed is presented in Figure 3.6 for the DRC and TS controller. In Figure 3.6 (a) the wind speed at hub height and the estimated effective wind speed by the disturbance observer are depicted. After a step change, the wind estimate decays towards the altered wind condition, and consequently adjusts the feedback gains and feedforward term to the new operating point, resulting in the control action in Figure 3.6 (g) and (h). As noted in the observer synthesis Sec. 3.2.2.4, a trade-off between the need for fast scheduling and state estimation in the feedback is confronted with limitations in the pitch rates and corresponding loads, that directly result from the pitch angle feedforward term.

By design, the DRC and TS controller in operating scenario Sc0 drive the turbine into the same stationary operating points. However, due to the additional incorporated feedback terms and the wind

Table 3.1: Overview of the operating scenarios for the TS controller (Sc0-Sc3) and DRC reference controller. The third column illustrates the power tracking signal Δp (gray) along with the normalized power output (colorized) under the impact of the different controllers, scenarios and identical turbulent wind input for 100 s at a mean of 22 m/s. The following columns specify the employed power tracking signals in terms of maximum reduced power $\max(\Delta p)$, frequency and maximum power gradient $\max(\frac{\mathrm{d}\Delta p}{\mathrm{d}t})$ in operation.

Label	Cntrl	Power Tracking Signal Δp	$\max(\Delta p)$	Freq.	$\max(\frac{\mathrm{d}\Delta p}{\mathrm{d}t})$
DRC	Delft Research Cntrl.[17]		0%	–	–
Sc0	TS		0%	–	–
Sc1	TS		75%	0.01 Hz	$2\%\mathrm{s}^{-1}$
Sc2	TS		75%	0.04 Hz	$10\%\mathrm{s}^{-1}$
Sc3	TS		75%	0.1 Hz	$20\%\mathrm{s}^{-1}$
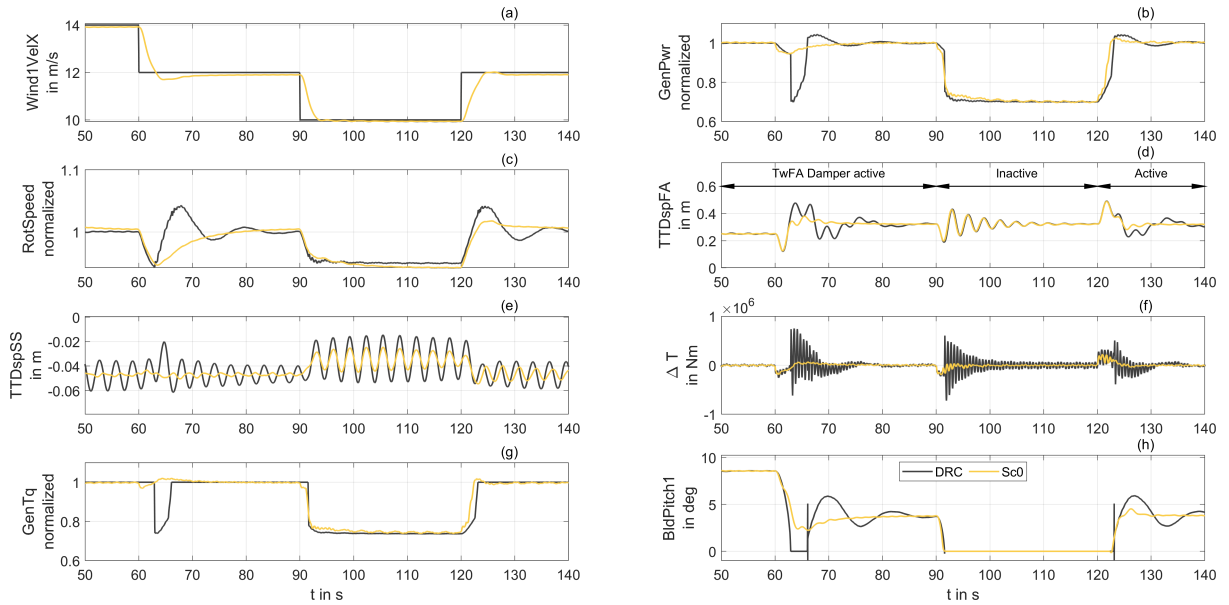
Figure 3.6: Wind turbine time series of different states as a response to step changes in the wind speed evaluated for the DRC (gray) and the TS controller in Sc0 (yellow). Subplots: (a) Hub-height and estimated wind speed (b) normalized generator power (c) normalized rotor speed (d) tower top fore-aft displacement (e) tower top side-to-side displacement (f) drivetrain shaft torque (g) normalized generator torque (h) pitch angle of blade 1

speed estimation in the TS control scheme, the state evolution of the turbine's components differ. The rotor speed governed by the TS controller settles into the new operating point without oscillation (Figure 3.6 (c)). Further, the damping properties of the feedback design are reflected by a reduction of tower top (Figure 3.6 (d) and (e)) and drivetrain torque oscillation (Figure 3.6 (f)). The effect of control system properties becomes apparent by comparing the active and inactive TwFA damping in Figure 3.6 (d) due to a change in the operating point from full to partial load and back.

3.3.2   Loads in nominal operation

To illustrate the load mitigation potential of the TS controller from introducing different wind turbine component models in the control design, the DEL in DLC 1.1 is compared to the DRC's performance. The normalized performance measures are illustrated in Figure 3.7.

The incorporated damping of the TS controller results in reduction of tower base DEL in fore-aft direction along the entire operating range above 10 m/s with values around -10% as depicted in Figure 3.7 (a). However, for a turbulent mean wind speed of 8 m/s an increase of DEL is visible, which results from an operational difference of the controllers when the inflow drops below the optimal tip speed tracking range (and therefore design range of the TS scheme is left). Due to the active damping
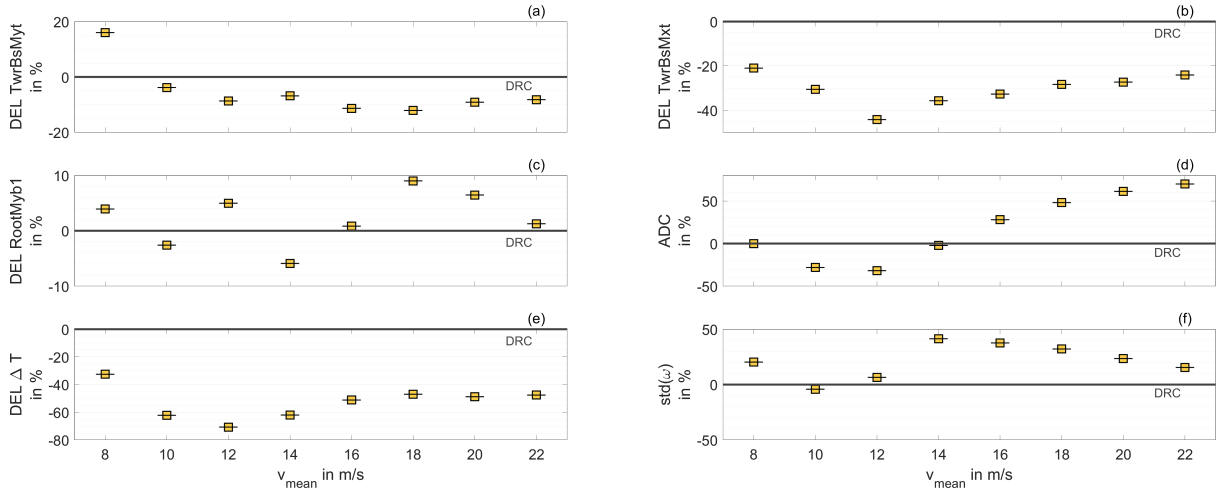
Figure 3.7: Performance of the TS controller in normal operation (Sc0) normalized to the DRCs' performance for DLC 1.1. Damage Equivalent Loads: (a) tower base fore-aft moment (b) tower base side-to-side moment (c) blade 1 root flapwise moment (e) drivetrain shaft torque; Other measures: (d) actuator duty cycle (f) standard deviation of rotational speed

from generator torque actuation, the tower base side-to-side DELs (Figure 3.7 (b)) and drivetrain DELs (Figure 3.7 (e)) are reduced around -30% and -50%, respectively.

While in some operating points the blade root DELs reduction can be observed, others increase as depicted in Figure 3.7 (c). By exhibiting varying values between -10% and +10% the DEL range is comparable, as neither of the applied controller actively acts on the blade motion.

The standard deviation of the rotational speed in Figure 3.7 (f) reflects the control design concept, where the feedback for rotation is designed to enable a behavior close to the open-loop rotational dynamics of the turbine. This aims for a reduction in control activity in a close vicinity of an operating point, while critical components as the tower are individually damped by purposefully designed feedback gains. In this concept, the observer dynamics is mainly responsible for an adjustment to a changing operating point, reducing the need for feedback activity from rotational speed. This allows for an increased standard deviation of the rotor speed in turbulent inflow, while the maximum speed overshoot in extreme gust operations is reduced as depicted in Figure 3.10 (e).

A comparable pitch activity for the simulation studies in lower wind speeds, and an increased relative ADC (up to 70%) in higher wind speeds can be identified from Figure 3.7 (d). As can be seen in Figure 3.9 (d), this increase in relative ADC originates from decreasing ADC of the DRC for higher wind speeds, while the TS controller's activity almost remains at a constant level for providing tower fore-aft damping.
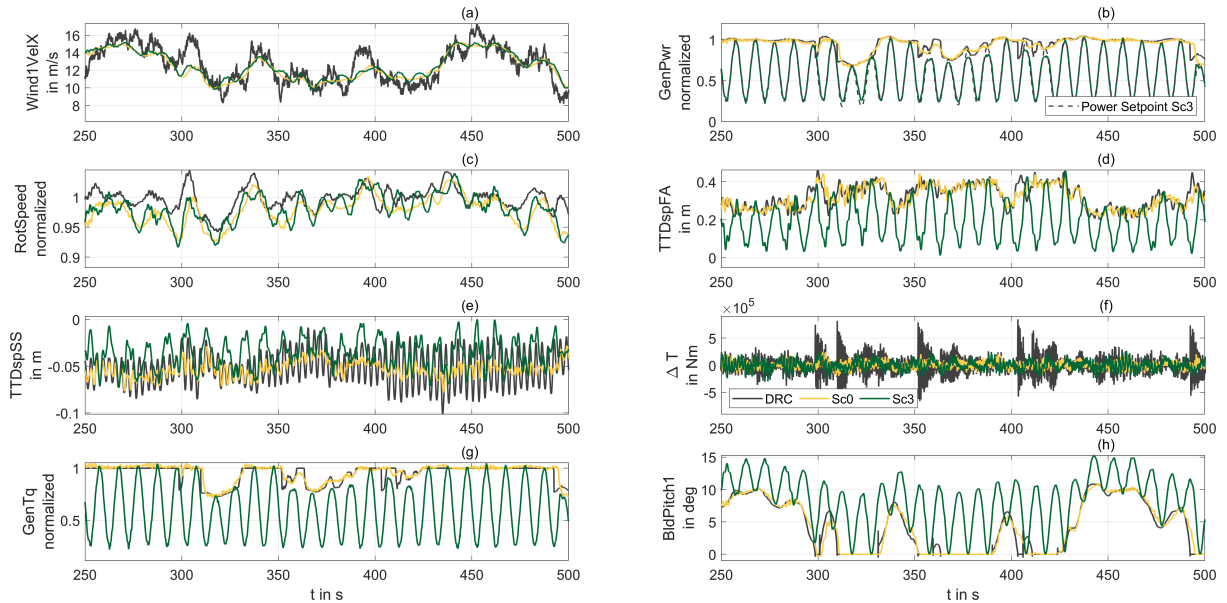
Figure 3.8: Wind turbine time series of different states as a response to turbulent inflow at a mean wind speed of 12 m/s evaluated for the DRC and TS controller (Sc0 and Sc3). Subplots: (a) Hub-height and estimated wind speed (b) normalized generator power (c) normalized rotor speed (d) tower top fore-aft displacement (e) tower top side-to-side displacement (f) drivetrain shaft torque (g) normalized generator torque (h) pitch angle of blade 1

3.3.3 Power tracking operation

The power tracking signals in operating scenarios Sc1-Sc3 are parametrized as sinusoidal variations to fulfill different power gradient requirements, and consequently a varying number of operating point changes of the components in operation occur. While in Sc1 the operating point is varied six times within the simulation at each mean wind speed, Sc3 enforces sixty operating point changes from nominal power production to 25% and back, see Figure 3.8 (b) enabled by generator and pitch angle actuation depicted in Figure 3.8 (g) and (h). As illustrated in Figure 3.8 (d) and (e) this mainly affects the tower displacement of the turbine, while other components behave similarly when compared with nominal operation by the DRC and TS controller in Sc0, see Figure 3.8 (c) and (f). Even though the power is varied at a maximum rate of 20%/s in Sc3, the TS controller is capable of smoothly varying the operating point of the turbine without showing additional oscillations building up induced by the power tracking capability.

3.3.4 Loads in power tracking operation

In Figure 3.9 and 3.10 fatigue and ultimate loads resulting from DLC 1.1 and DLC 1.6 are depicted, respectively. The control approach is able to perform a stable operation of the turbine in all considered

scenarios, which is reflected by comparable standard deviations of the rotation irregardless of the power tracking requirements in Figure 3.9 (f).

While the tower base side-to-side and drivetrain DELs in Figure 3.9 (b) and (e) suggest only slight increases in loading due to the power tracking in Sc1-3 and yielding load reduction compared to the implemented DRC, other components' fatigue loading is intensively affected.

The change in stationary tower fore-aft displacement for varying operating points has its maximum around rated wind speed, and consequently the traveled distance due to power tracking by the tower top is greatest. This is reflected by the maximum increase in tower base fore-aft fatigue loading (approx. doubling of DEL in Sc3 compared to DRC) around wind speeds with a mean of 12 m/s in Figure 3.9 (a). This value declines to 20% increased fatigue loading at 22 m/s in Sc3. The resulting DEL depends on the dynamic requirements (i.e., operating point changes and gradients) of the power tracking, reflected by a severely lower DEL in Sc2 and Sc1 compared to Sc3 along the entire operating range.

Further, pitch activity is greatly increased due to the power tracking operation as can be seen in Figure 3.9 (d). As depicted in Figure 3.2, the difference in stationary pitch angle is greatest around rated wind, resulting in the largest increase of ADC to cope with the varying power output of the turbine around 12 m/s and almost decreasing to a level comparable to nominal operation in Sc0 for higher wind speeds. The difference due to the dynamic requirements of the power tracking is severe, where only a moderate ADC growth for Sc1 and Sc2 compared to Sc0 is identified.

The blade root's flapwise loading also increases due to the power tracking operation (35% at 12 m/s and 10% at 22 m/s in Sc3 compared to DRC) as can be seen from Figure 3.9 (c). As discussed for tower fore-aft loading and ADC, the dynamic requirements of power tracking signal determine the increase in blade loading.

While we identify an increase in some components' fatigue loading, the ultimate loads for extreme operating gusts in DLC 1.6 underline the smooth closed-loop behavior induced by the TS controller in both nominal and power tracking operation. As can be seen in Figure 3.10, all considered ultimate loads are reduced compared to the DRC performance regardless of the scenario. While in fatigue loading an increase due to a faster dynamic tracking signal is apparent, the ultimate loads show no trend with regard to the power tracking signal. They are certainly influenced by the phase shift of the wind gust to the current position of the power tracking signal, which motivated us to configure the individual signals in Sc1-3 to perform at a maximum power gradient at the gust's beginning, while in e.g., Sc3 the power output is varied more than an entire cycle (from rated power to 25% and back) for an active wind gust of about 15 s.
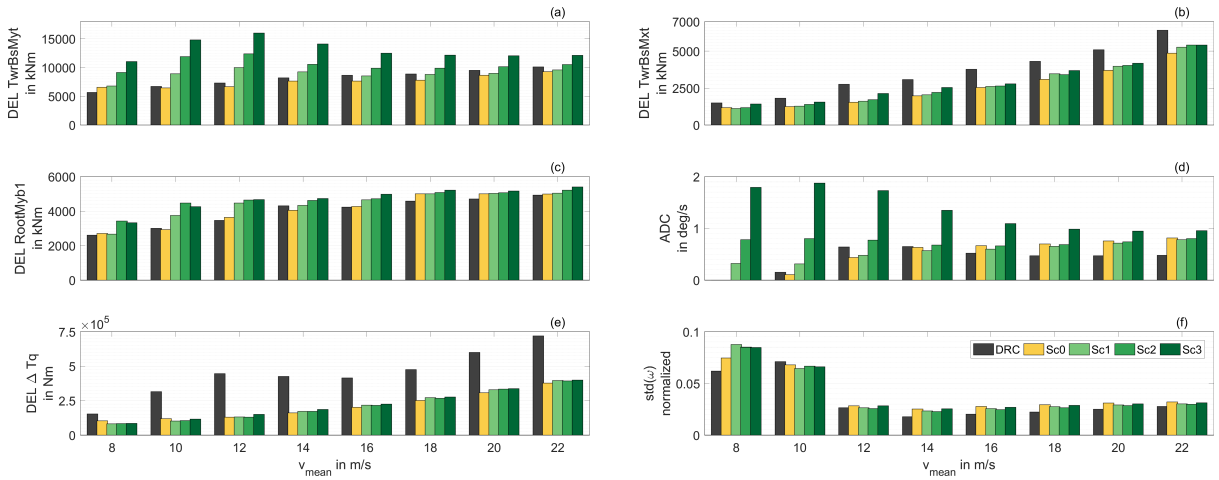
Figure 3.9: Fatigue loads of the DRC and TS controller in different operation modes (Sc0-Sc3) for DLC 1.1. As the same TS controller and wind inputs are used in the different scenarios (Sc0-Sc3), the resulting loads for different turbine components due to power tracking are accessible. Damage Equivalent Loads: (a) tower base fore-aft moment (b) tower base side-to-side moment (c) blade 1 root flapwise moment (e) drivetrain shaft torque; Other measures: (d) actuator duty cycle (f) standard deviation of rotational speed

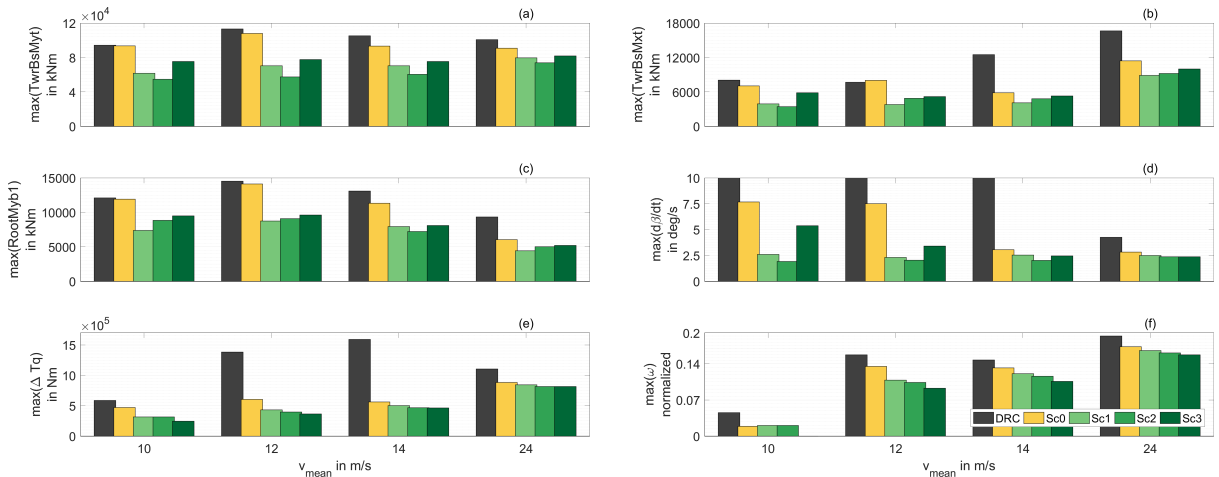Figure 3.10: Ultimate loads of the DRC and TS controller in different operation modes (Sc0-Sc3) for DLC 1.6. The evaluation of the power tracking scenarios in Sc1-Sc3 reveal no additional ultimate loads faced by the turbine. Maximum values of: (a) tower base fore-aft moment (b) tower base side-to-side moment (c) blade 1 root flapwise moment (d) pitch speed (e) drivetrain shaft torque (f) normalized rotor speed

3.4 Discussion

The considered operating range in the control design allows for a variation of the turbine's power output to perform grid stabilizing behavior. In Fleming et al. [33] the effects of constant power reserve on the turbine's structural loading are investigated. They find a decrease in ultimate loading along with an increasing pitch actuation, especially in lower wind speed. The reported results align with the findings using the TS controller in the discussed scenarios, where pitch activity increased most in lower wind speeds and ultimate loads are positively affected by the power tracking scenarios. In contrast to the constantly applied power reserve strategies from Fleming et al. [33], in this study the controller is employed to dynamically track a given power command, resulting in a continuous and inevitable excitation of especially the tower top in fore-aft direction. Where Fleming et al. [33] found a reduction due to constantly reduced power output, our fatigue load analysis of the tower base fore-aft moments reveals the dependence on the dynamic requirements of the power tracking. Other fatigue measures including the drivetrain shaft torque, blade flapwise loading or tower base side-to-side moment show smaller dependence on the evolution of the power tracking signal. The increased fatigue loading at different dynamic scenarios follows a clear trend, indicating that a characterization of the additional fatigue loading by enforcing a desired power output is quantifiable.

As noted by Mulders and van Wingerden [17], the different reference implementations aggravate the comparison of load reduction capabilities from control schemes proposed in research. By employing preview-based, model predictive control, Schlipf et al. [8] and Koerber and King [9] report tower fore-aft fatigue load reduction potential in a range of 30-40%, which outperforms the results in nominal operation normalized to the DRC [17] in Figure 3.7. In the non-preview investigation of Koerber and King [9], where an Extended Kalman Filter comparable to the TS disturbance observer [25] is employed, an increase on tower fatigue loading of approx. 19% compared to the preview case is reported. Averaging the load reduction potential of the TS controller around 10% along the considered operating range, an introduction of preview information in the TS control functionality might promise a total load reduction potential on a similar level in a range of 30%.

Compared to the proposed TS controller, ultimate loads could be reduced significantly in both reports [8, 9]. However, as pointed out by Koerber and King [9], ultimate loads are mitigated mainly by preview, as this effect vanishes when using the non-preview controller version. This is caused by the propagation time from the wind gust to the measurement as a result of the involved dynamics. Further, they note that in the case of the non-preview scheme, the load reduction is achieved at the cost of an increased pitch activity. This effect is also revealed in Figure 3.7, where especially in higher wind speed the actuator duty cycle is increased compared to the reference controller for providing damping to the tower fore-aft motion.

Different from the mentioned model-predictive control schemes [8, 9], no explicit formulation of state and input constraints is incorporated in the proposed LMI-based approach, which might provide lower confidence in keeping the turbine's operational constraints. Instead, this is coped by a priori shaped closed-loop state dynamics to prevent exceedance of limits and saturation in operation. However, Koerber and King [9] note that while greatly decreasing the risk of overspeeding, even the state constrained control scheme can not provide guarantee in all gust situations, as a gust might excite the turbine such that no feasible solution under the given constraints exists.

Model-predictive control schemes with their inherited capability to handle preview information, especially with the emergence of LIDAR (light detection and ranging) systems, provide a promising field of advancement in wind turbine control. However, they suffer from real-time implementation issues, as also reported by Schlipf et al. [8]. While research will certainly decrease these issues, the proposed TS scheme represents an interesting alternative, especially for non-preview operation. The control design complexity is shifted into the reproducible off-line model-based synthesis and the scheme can be implemented in a few lines of code, see Figure 3.5. This allows for an efficient evaluation, maintenance and real-time implementation of the controller code.

In this contribution, the TS scheme is investigated for a well-known 5 MW reference case, but the control design is not limited to this turbine. The performance in operation with regard to state trajectories and occurring loads depends, however, on the employed design parameters in terms of LMI region and damping constraints. As the controller "needs careful design" [2], the optimal set of design parameters differs depending on the wind turbine specifications. The analysis of the open-loop models in the complex plane yields an impression of the autonomous turbine dynamics, and thus provides a valuable starting point for the definition of a desired closed-loop behavior enforced by the control scheme in operation. While the control design remains an iterative procedure depending on the occurring loads, the general formulation of the control synthesis and the interpretability of the design parameters allow for an efficient controller adjustment. The proposed modular structure facilitates the dedicated integration or isolation of specific feedback loops, resulting in a flexible control procedure with respect to the considered wind turbine components.

The TS scheme envelops a wide operating range into an overall convex description that is integrated into the design process. Stability and performance constraints imposed by the LMIs are valid within the defined operating range. If the turbine exceeds the boundaries of this range, a controller adjustment to the alternating turbine dynamics is disabled. Effectively, this results in locking of the TS model description in the boundary operating point of the defined range, and consequently, the real dynamics of the turbine in operation and the model diverge. While the TS controller still provides feedback, the feedforward action and desired operational values represented by x_{0j} freeze at the boundary operating point, such that the controller tries to enforce these stationary values. For example, this effect

leads to a relative increase in tower fore-aft loading for a mean wind of 8 m/s in Figure 3.7 (a) when the wind drops below the lower bound of the operating range. In contrast to the TS controller, the DRC incorporates a strategy for this operating range. Anyhow, the TS controller performs robust, stable operation of the turbine, but the state trajectories differ as by design the TS controller possesses no information on the desired states and input values of the turbine in this range. To circumvent this malady, either the operational range of the TS scheme can be enlarged by including this range in the linearization analysis, or a simple linear dependence of the torque to the generator speed could be applied as suggested by Jonkman et al. [26].

In general, the choice of operating points and their distribution in the TS scheme depends on the purpose of the designed controller and considered dynamics. An increasing number of linearized models within an operating range results in an increased accuracy of the model approximation [21]. On the other hand, the computational cost of the design also increases, such that a balance between accuracy and complexity needs to be designed by the control engineer. For example, a validation of the TS model for the rotational dynamics used in the control design in Sec. 3.2.2.3 is shown in [20] for the full load region. The linearization points in this work as depicted in Figure 3.2 ($N = 252$) are unevenly distributed, such that a denser model description is derived in the crucial range around rated wind speed, where the feedback loop actuator changes from generator torque to pitch angle for increasing wind speeds. The contribution follows a heuristic approach, where we analyzed the variation of eigenvalues due to a change in operating point. While the rotational dynamics of the turbine varies significantly for different wind speeds, the influence of a power output adjustment at a given wind speed varies the resulting dynamics similarly across the entire wind spectrum. This is the reason for the different resolutions of the incorporated premise variables.

Extensions to the presented LMI framework exist, where the conservativeness of the design can be further decreased by employing e.g., non-quadratic Lyapunov approaches [34, 35] or relaxation schemes [36]. While the considered LMI techniques in this work due to the un-relaxed quadratic Lyapunov approach constitute rather basic and conservative design constraints, the results underline the usefulness of the LMI-based design for the wind turbine application, leaving room for further advancements employing a variety of rich methods existing for handling of systems modeled in a TS framework [37]. For example, an approach towards active power control for wind turbines employing LMIs using an on-line optimal and off-line sub-optimal output feedback design is considered in the work of Bayat and Bahmani [38].

By accounting for nominal and reduced power production at arbitrary inflow in the multi-variable stability framework, scheduling is implicitly integrated in the TS approach. Further, tuning of operating point-dependent control loops as necessary in state-of-the-art proportional-integral control schemes is avoided due to the TS scheme's capability to capture the varying dynamics in a unified framework.

As a result, the combination of an automated model-based control synthesis over a wide operating range and a lean implementation allows for an efficient control design procedure.

3.5 Conclusion

A non-linear model-based TS controller was presented that proves to be effective for the complex task of wind turbine control design. It is capable of integrating several degrees of freedom in the model and subsequent control design in an extended operating range to enable dynamic power tracking. Through the model-based controller synthesis based on linear matrix inequalities, desired dynamical properties within the Lyapunov stability framework can be enforced. As a result, the controller shows significant load reduction potential for the incorporated dynamics in the description compared to the employed reference controller.

The effects of power tracking with different dynamic requirements on the wind turbine structure were evaluated to provide a measure of the resulting loads. For that purpose, artificial grid stabilization scenarios modeled by sinusoidal variations of the power demand with different frequencies are enforced by the controller. The results reveal the increased fatigue loading affecting the lifetime of the wind turbine from grid stabilizing behavior. In the ultimate load analysis, no increase due to the power tracking operation was observed, such that mechanical dimensioning of the structures from the considered DLCs is unaffected.

As a result, the controller's power tracking capability allows for a dedicated variation of the turbine's power output to support the stabilization of the electrical grid, potentially even without a turbine redesign. The results suggest that under appropriate control action the turbine can be employed to provide active power control with the necessary dynamics to the electrical grid, leaving the question of financial compensation for the additional fatigue loading. As the levelized cost of energy depends on the included services and their revenue [4], the provision of ancillary services for the electrical grid may become a competitive and technical advantage, if not a necessity, when replacing conventional power plants with renewable sources in the energy generation mix.

References

[1] INNWIND.EU. LCOE reduction for the next generation offshore wind turbines. Technical report, 2017.

[2] E A Bossanyi. Wind turbine control for load reduction. *Wind Energy*, 2003. DOI: 10.1002/we.95.

[3] S Schuler, D Schlipf, P W Cheng, and F Allgöwer. ℓ_1-Optimal Control of Large Wind Turbines. *IEEE Transactions on Control Systems Technology*, 2013. DOI: 10.1109/TCST.2013.2261068.

[4] G A M van Kuik, J Peinke, R Nijssen, D Lekou, J Mann, J N Sørensen, C Ferreira, J W van Wingerden, D Schlipf, P Gebraad, H Polinder, A Abrahamsen, G J W van Bussel, J D Sørensen, P Tavner, C L Bottasso, M Muskulus, D Matha, H J Lindeboom, S Degraer, O Kramer, S Lehnhoff, M Sonnenschein, P E Sørensen, R W Künneke, P E Morthorst, and K Skytte. Long-term research challenges in wind energy – a research agenda by the European Academy of Wind Energy. *Wind Energy Science*, 2016. DOI: 10.5194/wes-1-1-2016.

[5] J Morren, J Pierik, and S W H de Haan. Inertial response of variable speed wind turbines. *Electric Power Systems Research*, 2006. DOI: 10.1016/j.epsr.2005.12.002.

[6] K O Merz. Basic controller tuning for large offshore wind turbines. *Wind Energy Science*, 2016. DOI: 10.5194/wes-1-153-2016.

[7] L C Henriksen, M H Hansen, and N K Poulsen. Wind turbine control with constraint handling: a model predictive control approach. *IET Control Theory & Applications*, 2012. DOI: 10.1049/iet-cta.2011.0488.

[8] D Schlipf, D J Schlipf, and M Kühn. Nonlinear model predictive control of wind turbines using LIDAR. *Wind Energy*, 2013. DOI: 10.1002/we.1533.

[9] A Koerber and R King. Combined Feedback–Feedforward Control of Wind Turbines Using State-Constrained Model Predictive Control. *IEEE Transactions on Control Systems Technology*, 2013. DOI: 10.1109/TCST.2013.2260749.

[10] A Lasheen and A L Elshafei. Wind-turbine collective-pitch control via a fuzzy predictive algorithm. *Renewable Energy*, 2016. DOI: 10.1016/j.renene.2015.10.030.

[11] F D Bianchi, R J Mantz, and C F Christiansen. Control of variable-speed wind turbines by LPV gain scheduling. *Wind Energy*, 2004. DOI: 10.1002/we.103.

[12] K Z Østergaard, J Stoustrup, and P Brath. Linear parameter varying control of wind turbines covering both partial load and full load conditions. *Int. J. Robust and Nonlinear Control*, 2009. DOI: 10.1002/rnc.1340.

[13] A Diaz de Corcuera, A Pujana-Arrese, J M Ezquerra, A Milo, and J Landaluze. Linear models-based LPV modelling and control for wind turbines. *Wind Energy*, 2015. DOI: 10.1002/we.1751.

[14] M Meisami-Azad and K M Grigoriadis. Anti-windup linear parameter-varying control of pitch actuators in wind turbines. *Wind Energy*, 2015. DOI: 10.1002/we.1689.

[15] F A Inthamoussou, H De Battista, and R J Mantz. LPV-based active power control of wind turbines covering the complete wind speed range. *Renewable Energy*, 2016. DOI: 10.1016/j.renene.2016.07.064.

[16] K Tanaka and H O Wang. *Fuzzy Control Systems Design and Analysis: A Linear Matrix Inequality Approach*. John Wiley & Sons, Inc., 2001.

[17] S P Mulders and J W van Wingerden. Delft Research Controller: an open-source and community-driven wind turbine baseline controller. *Journal of Physics: Conference Series*, 2018. DOI: 10.1088/1742-6596/1037/3/032009.

[18] D Rotondo, V Puig, F Nejjari, and M Witczak. Automated generation and comparison of Takagi–Sugeno and polytopic quasi-LPV models. *Fuzzy Sets and Systems*, 2015. DOI: 10.1016/j.fss.2015.02.002.

[19] J G VanAntwerp and R D Braatz. A tutorial on linear and bilinear matrix inequalities. *Journal of Process Control*, 2000. DOI: 10.1016/S0959-1524(99)00056-6.

[20] F Pöschke, E Gauterin, and H Schulte. LMI Region-based Non-linear Disturbance Observer with Application to Robust Wind Turbine Control. In Olfa Boubaker, Quanmin Zhu, Magdi Mahmoud, Jose Ragot, Hamid Reza, and Karimi Jorge Dávila, editors, *New Trends in Observer-based Control.* . Academic Press, 2019.

[21] Z Lendek, T M Guerra, R Babuska, and B De Schutter. *Stability Analysis and Nonlinear Observer Design Using Takagi-Sugeno Fuzzy Models*. Springer-Verlag Berlin Heidelberg, 2010.

[22] M Chilali and P Gahinet. H_∞ design with pole placement constraints: an LMI approach. *IEEE Transactions on Automatic Control*, 1996. DOI: 10.1109/9.486637.

[23] M N Soltani, T Knudsen, M Svenstrup, R Wisniewski, P Brath, R Ortega, and K Johnson. Estimation of Rotor Effective Wind Speed: A Comparison. *IEEE Transactions on Control Systems Technology*, 2013. DOI: 10.1109/TCST.2013.2260751.

[24] D Jena and S Rajendran. A review of estimation of effective wind speed based control of wind turbines. *Renewable and Sustainable Energy Reviews*, 2015. DOI: 10.1016/j.rser.2014.11.088.

[25] E Gauterin, P Kammerer, M Kühn, and H Schulte. Effective wind speed estimation: Comparison between Kalman Filter and Takagi–Sugeno observer techniques. *ISA Transactions*, 2016. DOI: 10.1016/j.isatra.2015.11.016.

[26] J M Jonkman, S Butterfield, W Musial, and G Scott. Definition of a 5-MW Reference Wind Turbine for Offshore System Development. Technical report, National Renewable Energy Laboratory, 2009.

[27] J M Jonkman and M L Buhl. FAST Users Guide. Technical report, National Renewable Energy Laboratory, 2005.

[28] GL Wind. Guideline for the Certification of Wind Turbines. Standard, Germanischer Lloyd, 2010.

[29] C E D Riboldi. On the optimal tuning of individual pitch control for horizontal–axis wind turbines. *Wind Engineering*, 2016. DOI: 10.1177/0309524X16651545.

[30] M O L Hansen. *Aerodynamics of Wind Turbines*. Earthscan, 2nd edition, 2008.

[31] A Niesłony. Determination of fragments of multiaxial service loading strongly influencing the fatigue of machine components. *Mechanical Systems and Signal Processing*, 2009. DOI: 10.1016/j.ymssp.2009.05.010.

[32] Hydro-Québec. Technical Requirements for the Connection of Generation Facilities to the Hydro–Québec Transmission System: Supplementary Requirements for Wind Generation. Technical report, 2009.

[33] P A Fleming, J Aho, A Buckspan, E Ela, Y Zhang, V Gevorgian, A Scholbrock, L Pao, and R Damiani. Effects of power reserve control on wind turbine structural loading. *Wind Energy*, 2016. DOI: 10.1002/we.1844.

[34] K Tanaka, T Hori, and H O Wang. A multiple lyapunov function approach to stabilization of fuzzy control systems. *IEEE Transactions on Fuzzy Systems*, 2003. DOI: 10.1109/TFUZZ.2003.814861.

[35] T M Guerra, M Bernal, K Guelton, and S Labiod. Non-quadratic local stabilization for continuous-time Takagi–Sugeno models. *Fuzzy Sets and Systems*, 2012. DOI: 10.1016/j.fss.2011.12.003.

[36] K Tanaka, T Ikeda, and H O Wang. Fuzzy regulators and fuzzy observers: relaxed stability conditions and LMI-based designs. *IEEE Transactions on Fuzzy Systems*, 1998. DOI: 10.1109/91.669023.

[37] G Feng. A Survey on Analysis and Design of Model-Based Fuzzy Control Systems. *IEEE Transactions on Fuzzy Systems*, 2006. DOI: 10.1109/TFUZZ.2006.883415.

[38] F Bayat and H Bahmani. Power regulation and control of wind turbines: LMI-based output feedback approach. *International Transactions on Electrical Energy Systems*, 2017. DOI: 10.1002/etep.2450.

4 | Model-based wind turbine control design with power tracking capability: a wind-tunnel validation

Abstract

Owing to the aerodynamic conversion process, wind turbines exhibit a nonlinear behavior and encounter turbulent operating conditions that demand well-defined closed-loop dynamics to withstand accumulated loading over the lifetime. Wind excitation is the main disturbance and driving force for the system and determines the necessary operating strategy, but it usually represents an unmeasurable quantity. In this study, we used a linear-matrix-inequalities-based control and observer design to operate a variable-speed, variable-pitch wind turbine in a wind tunnel experiment at different reproducible inflow conditions while relying on a wind speed estimate obtained from a disturbance observer. The computational complexity of the stability framework incorporating the reconstruction of the unknown wind speed is reduced by exploiting characteristics of the modeling approach based on a convex combination of linear submodels. The assumption used in the proposed stability consideration is evaluated based on measurement data. We introduced an extended operating range compared to the commonly considered operating trajectory of wind turbines in the control design. A controller based on Takagi–Sugeno modeling is used to operate the turbine at challenging power tracking requirements demonstrating the capability to support fast stabilization of the electrical grid while discussing the loading and operational constraints observed during the experiments.

Graphical abstract
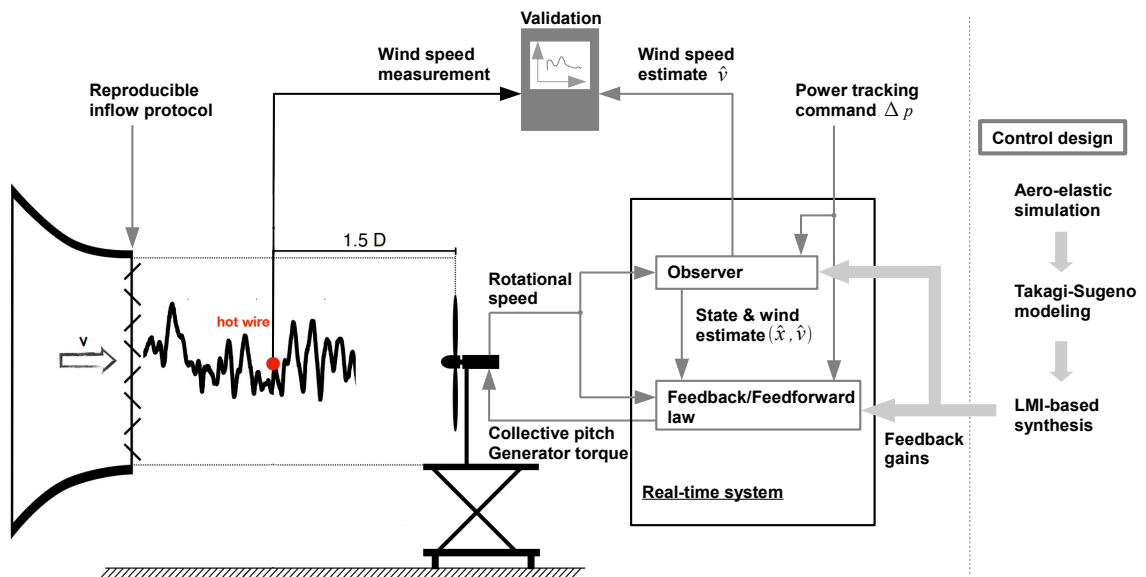
4.1 | Introduction

Wind turbines are nonlinear systems carefully designed to withstand operational loads occurring over the lifetime. To reduce the cost of energy, scaling approaches are used [1]. This results in increasingly flexible and larger components dynamically interacting that the controller needs to handle appropriately [2]. Therefore, a well-defined closed-loop behavior actively enforced by the controller is vital for the wind turbine performance during the lifetime.

This has led to intensive control research. Various promising results have been achieved by applying modern model-based control strategies. These strategies comprise model predictive control [3, 4, 5], optimal control [6, 7] or linear parameter varying approaches [2, 8, 9, 10]. Relevant fatigue load reduction in several degrees of freedom has been achieved [2, 4, 5, 6, 7, 10, 11] compared to the classically used gain-scheduled PI approaches. This shows the potential of model-based methods based on simulation studies, but few experimental studies have been conducted. Data-driven identification of a closed-loop turbine model based on field data in turbulent conditions has been performed [12]. Wind-

tunnel validation has also been reported [13], where predictive control for a small-scale wind turbine was investigated. The strategy is based on wind speed measurements using a Pitot tube and covers generator torque control. It is discussed that knowledge of the incoming flow in advance can increase the control performance. Further, subspace predictive repetitive control has been evaluated in wind-tunnel experiments [14, 15], which focused on the mitigation of periodic blade loading by individually pitching the turbine's rotor blades without addressing the power regulation problem.

The increasing share of wind power in the energy generation mix demands a higher contribution of wind turbines to grid services, such as providing frequency stabilization of electrical grids [7, 16] or contributing to black-start [17] by dynamic power tracking. Besides the benefits for electrical grids, power tracking can improve conversion performance, such as limiting turbine loading [18, 19], reducing or balancing structural loads in wind farms [20, 21] or increasing wind farm power production [22]. To enable power tracking functionality, turbines are forced out of the commonly considered operating trajectory that maximizes the power output [17, 11], and consequently, the operational range for the applied controller is effectively increased. In [23], it has been reported that turbine loading is affected by the associated variation in dynamics when the controller gains derived for the nominal power trajectory are applied. Thus, an extension of the commonly applied gain-scheduled PI controller has been proposed to account for this effect [23, 17]. This variation of dynamics has been considered in model-based approaches in simulation-based studies [9, 10, 11], where linear-matrix-inequality (LMI) design is conducted. Field validation of constant power derating by applying an industrial standard PI controller has been reported [24, 25]. In [26], different operating strategies for power tracking based on extended classical PI control approaches are presented and validated in a wind tunnel. The authors show the turbine's response to stepwise changes in power output demands and compare the loading based on the power tracking strategy.

The wind inflow represents the main disturbance of the system [27], where in addition to the periodic loads from the rotation, the operational loads are governed by turbulent wind interacting with the closed-loop system. Without integrating advanced sensing, such as light detecting and ranging systems, the wind resource cannot be measured for control purposes while governing the nonlinear dynamics. To resolve this operational complexity, disturbance observers and Kalman filters have been designed to estimate the effective wind speed [28, 29, 30]. In [28], different wind speed estimation strategies, including algebraic calculation from stationary power relation, Kalman filtering, and unknown input observers, are compared on the basis of both simulation studies and field measurements. Through experimental measurements, a 20–30% decrease in performance was reported compared to that obtained by simulations.

An observer with a Takagi–Sugeno (TS) structure was proposed for reconstructing wind speed [31, 30, 11]. It is based on a nonlinear description using a convexly weighted combination of linear models.

The wind speed estimate is integrated as a premise variable (PV) in the TS model, which schedules the nonlinear model dynamics. In [31, 30], only the observation problem is discussed without closing the loop, whereas, in [11] the separation principle in the feedback and observer design for TS systems is assumed, which formally holds for only measurable PVs [32]. The consequences for wind turbine control are noted in [2] by discussing the possible interference of the feedforward component and the feedback if acting in the same frequency region. This is also reported in [33], where the disturbance sensitivity function with uncertainties is analyzed for feedback–feedforward individual pitch control.

Few approaches to simultaneous control and observer synthesis for TS systems with unmeasurable PVs have been proposed [34, 35, 36]. The approaches either introduce additional variables as integral constraints inheriting the modeling error due to the unmeasurable PV [35], resulting in relatively complex LMIs with additional design variables [34] or leave the LMI framework yielding bilinear matrix inequalities [36]. However, basic stability constraints reliant on predefined gains for this general nonlinear control problem have been identified for a long time [37], but due to the possibly great number of LMIs inherit a significant conservativeness.

For wind turbine control, basic LMI design constraints with their physically interpretable parameters, such as decay rates and damping ratios, were identified as beneficial in the multivariate design approach [11]. Based on this, load mitigation by the provision of active damping in several turbine components in a large operational range was achieved, and compared to a conventionally applied PI controller. This work extends the observer-based control design discussed in [11] by providing proof of stability both theoretically and experimentally considering the unmeasurable wind speed as PV. To this end, the complexity of the basic stability constraints described in [37] is reduced by exploiting the structural properties of the TS framework when derived based on linearized models under the assumption of a maximum estimation error in PV. The investigated feedback gains are synthesized in a previous step allowing specifically assigned closed-loop dynamics based on LMI performance constraints.

Here, the experimental wind tunnel validation of the LMI-based control contributes to three aspects. First, the robustness of the nonlinear, model-based controller to modeling mismatch and real-time implementation is explored in a large operational range. Second, the adherence of assuming a maximum wind speed estimation error within the LMI-based stability considerations is evaluated. Finally, the power tracking functionality implicitly integrated into the approach is assessed to explore the capability of wind turbines in supporting the dynamic stabilization of the electrical grid.

The rest of the paper is organized as follows: the construction of the nonlinear wind-turbine model in the TS framework is presented in Section 4.2; the LMI-based control design is discussed and used to enforce a desired closed-loop wind-turbine dynamics in Section 4.3; the wind-tunnel setup and inves-

tigated power tracking scenarios are introduced in Section 4.4; the measurement results are displayed and analyzed in Section 4.5; the results are discussed in Section 4.6; conclusions are drawn in Section 4.7.

4.2 Modeling

4.2.1 Model wind turbine Oldenburg (MoWiTO)

The investigated three-bladed MoWiTO is a fully controllable scaled version of the NREL 5-MW reference turbine [38]. With a spatial scaling of 1/70, it has a rotor diameter of 1.8 m and is shown in Figure 4.1. Scaling was performed to preserve operational properties, such as the design tip speed ratio and the lift distribution of the reference turbine in a controllable wind tunnel environment. Within the experiments, an operational strategy that corresponds to a time scaling of 40/1 compared to the 5-MW reference turbine was chosen. MoWiTO has individual pitch capabilities and features strain gauges to measure blade-flap-wise moments, torque, and tower bending moments. A more detailed description of the MoWiTO design is given in [39, 40]. The controller only uses the measurement of the generator speed ω. The collective pitch angle β and generator torque T are governed by the controller.

In the following subsection, we show the derivation of suitable linearized wind turbine models for control design. The models are subsequently interconnected to obtain a nonlinear system. While addressing some specific aspects of the MoWiTO, the treatment of the rotational dynamics shown here is a general approach for wind turbine control. Thus, it can be equivalently applied to other turbines and additionally modeled states [11].

4.2.2 Linearized wind-turbine model

A FAST configuration [41] of the aerodynamic properties of MoWiTO serves as a basis for the control design. A simulation analysis is performed to identify the inputs of the generator torque T_{0i} and collective pitch angle β_{0i} resulting in a stationary model behavior in different chosen constant wind speeds at the desired power output. The operating points considered (Figure 4.2) constitute an extended range, allowing for power tracking operation compared to the commonly evaluated nominal operating trajectory of wind turbines.

A linearization analysis of the rotational dynamics $\dot{x} = f(x, u, d)$ is conducted in a stationary operation using the linearization capability of FAST [41]. This yields the following linear model at the ith

Figure 4.1: Model Wind Turbine Oldenburg (MoWiTO) with a rotor diameter of 1.8 m operated in the WindLab at ForWind Oldenburg.

operating point, determined by the locations x_{0i}, u_{0i}, d_{0i} in the operating range (Figure 4.2)

$$
\begin{aligned}
\dot{x} &= \underbrace{f(x_{0i}, u_{0i}, d_{0i})}_{=0} + \underbrace{\frac{\partial f(x_{0i}, u_{0i}, d_{0i})}{\partial x}}_{A_i}(x - x_{0i}) \\
&+ \underbrace{\left[\frac{\partial f(x_{0i}, u_{0i}, d_{0i})}{\partial u_1} \quad \frac{\partial f(x_{0i}, u_{0i}, d_{0i})}{\partial u_2} \right]}_{B_i}(u - u_{0i}) + \underbrace{\frac{\partial f(x_{0i}, u_{0i}, d_{0i})}{\partial d}}_{B_{di}}(d - d_{0i}),
\end{aligned}
\tag{4.1}
$$

where $x = \omega$ represents the turbine's rotational speed, $u = [u_1 \quad u_2]^{\mathrm{T}} = [T \quad \beta]^{\mathrm{T}}$ is the system input composed of generator torque T and pitch angle β, and the effective wind speed is treated as the disturbance $d = v$. The model describes the rotational dynamics of the turbine at the ith stationary operating point using the state, input, and disturbance matrices A_i, B_i, and B_{di}, respectively.

4.2.3 Takagi-Sugeno-based wind-turbine model

By defining the PV $z = [v \ \Delta p]^{\mathrm{T}}$ as the wind speed v and an externally adjustable power tracking signal Δp, the operational changes that alter the dynamics and stationary points can be embedded in the TS description. Based on the current state of the PV, the contribution of each submodel to the overall nonlinear dynamics is convexly assigned [37].

The PV is used for calculating the triangular weighting functions $w_{l,j}(z_j)$

$$
w_{l,j}(z_j) = \begin{cases} \frac{z_j - z_j^{0(l-1)}}{z_j^{0l} - z_j^{0(l-1)}} & \text{if } z_j^{0(l-1)} < z_j \le z_j^{0l} \\ 1 - \frac{z_j - z_j^{0l}}{z_j^{0(l+1)} - z_j^{0l}} & \text{if } z_j^{0l} < z_j \le z_j^{0(l+1)} \\ 0 & \text{else} \end{cases} , \tag{4.2}
$$

where z_j^{0l} is the value of the jth PV at the lth linearization point in the operating range. The weighting functions for individual PVs and their distribution result from the choice of linearization points (Figure 4.4). Owing to the construction in (4.2), the weighting functions satisfy the convex sum property

$$
\sum_{l=1}^{l_{j,\max}} w_{l,j}(z_j) = 1 , \quad 0 \le w_{l,j}(z_j) \le 1 , \tag{4.3}
$$

where $l_{j,\max}$ denotes the number of operating points for each PV, which is chosen here as $l_{1,\max} = 50$ and $l_{2,\max} = 4$ for v and Δp (Figure 4.4 (a) and (b)). Based on the individual weighting of the PV, the
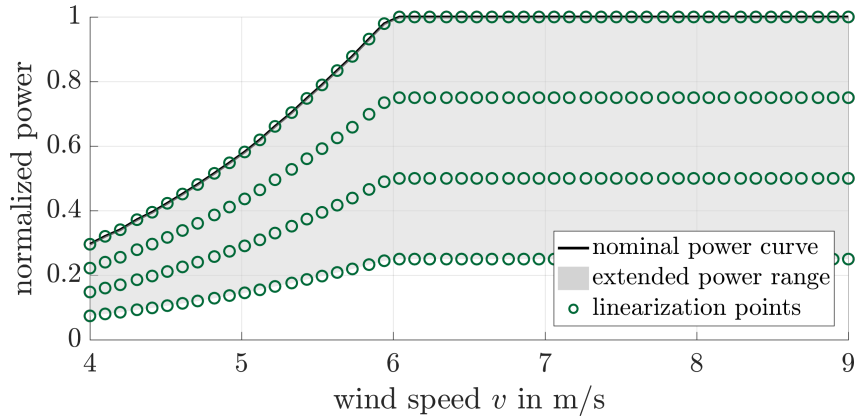
Figure 4.2: MoWiTO power operating range as a function of the wind speed. The nominal operating scenario, i.e., optimization below rated power and limitation to rated power for wind speeds above, is shown along with the extended operating range covered by the proposed TS control strategy.
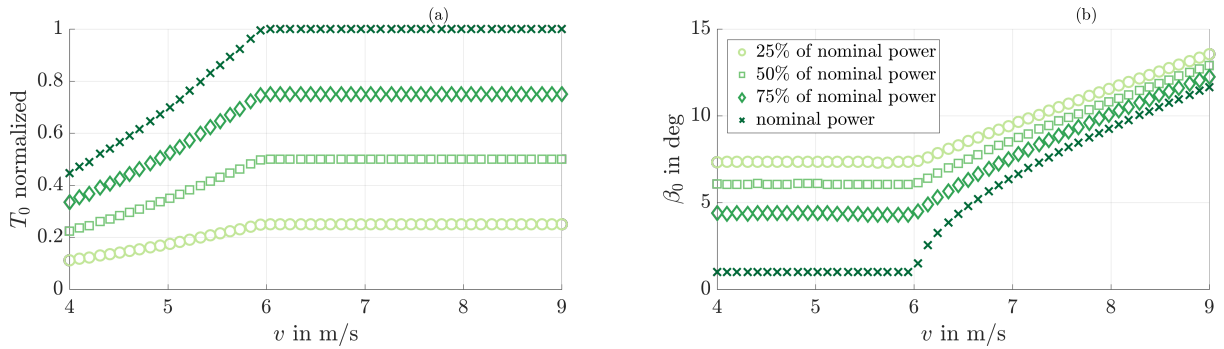
Figure 4.3: Inputs of the MoWiTO model inducing stationary behavior at the linearization points shown in Figure 4.2. (a) normalized generator torque (b) collective pitch angle
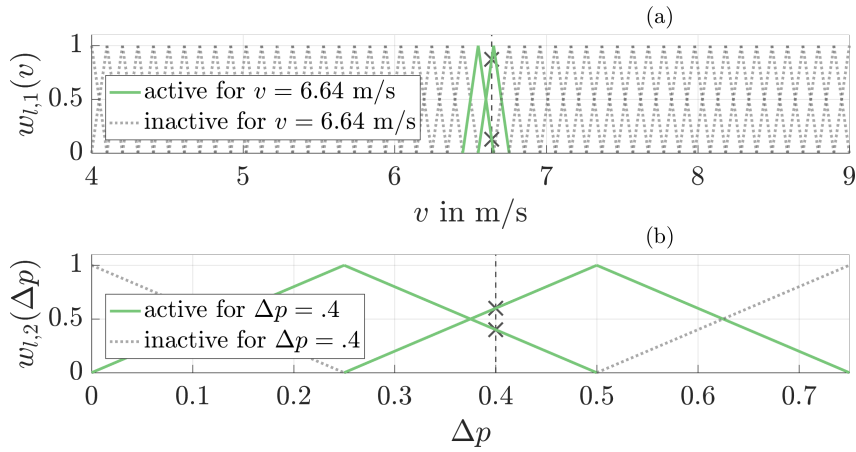
Figure 4.4: Triangular weighting functions of the premise variables $z = [v \ \ \Delta p]^{\mathrm{T}}$ based on (4.2). The active weighting functions for a sample operating point of $z = [6.64\,\mathrm{m/s} \ \ .4]$ are highlighted.

membership functions for blending the linear submodels are expressed as

$$\sum_{i=1}^{N} h_i(z) = \prod_{j=1}^{2} \sum_{l=1}^{l_{j,\max}} w_{l,j}(z_j) \quad , \tag{4.4}$$

which for a two-dimensional premise vector using triangular weighting results in the pyramid-shaped membership functions (Figure 4.5). The membership functions $h_i(z)$ assign the contribution of a linear submodel to the overall nonlinear dynamics depending on the current PVs z, and satisfy the convex property given for the weighting functions in (4.3). The individual number of operating points of the PVs determines the number of submodels in the TS model, which gives $N = \prod_{j=1}^{2} l_{j,\max} = 200$ in this case.

Using the membership functions and linearized models, the rotational dynamics of the wind turbine
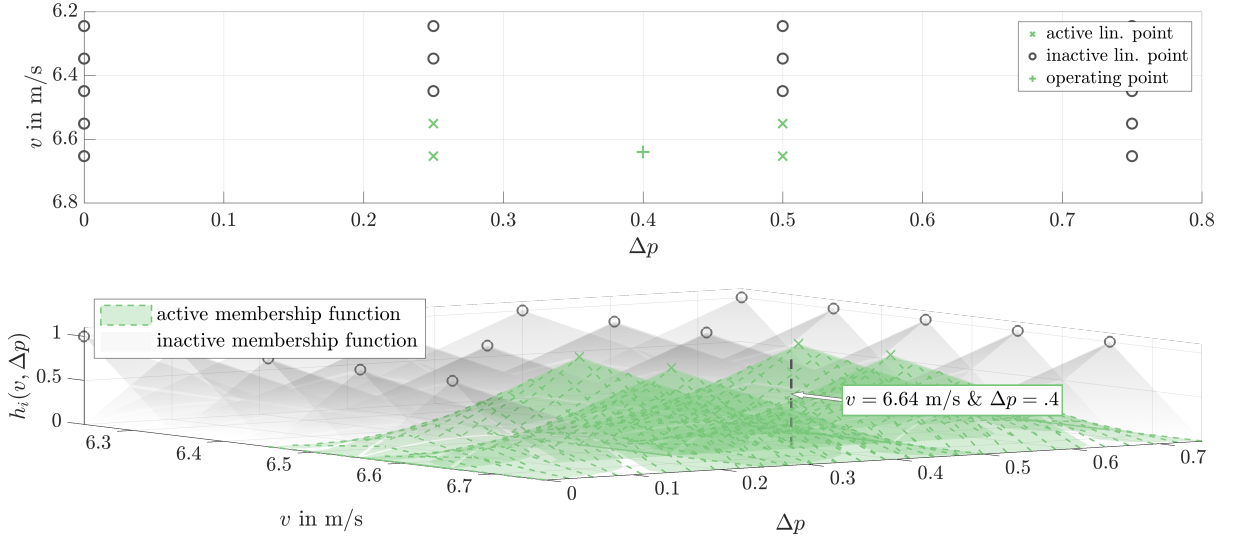
Figure 4.5: Subset of the membership functions $h_i(v, \Delta p)$ resulting from triangular weighting functions for two premise variables within a subregion of the operating range. The circles indicate the linearization points corresponding to Figure 4.2. The active membership functions for a sample operating point of $z = [6.64\,\mathrm{m/s}\ 0.4]$ are highlighted.

in a convex TS form is given as

$$\dot{x} = \sum_{i=1}^{N} h_i(z) \big[A_i(x - x_{0i}) + B_i(u - u_{0i}) + B_{di}(d - d_{0i}) \big] . \tag{4.5}$$

4.3 Control design

The proposed control law comprises a feedback u_{FB} and feedforward u_{FF} component in the system input

$$u = \underbrace{- \sum_{k=1}^{N} h_k(\hat{z}) K_k(\hat{x} - x_{0k})}_{u_{\mathrm{FB}}} + \underbrace{\sum_{k=1}^{N} h_k(\hat{z})\, u_{0k}}_{u_{\mathrm{FF}}} . \tag{4.6}$$

It follows the TS structure using membership functions in the control input calculated based on the estimated wind speed $\hat{v}$, denoted as $h_k(\hat{z})$. This constitutes a general nonlinear observer-based control problem, where the separation principle is formally not applicable. To obtain a certain degree of freedom in shaping a desired closed-loop behavior, we chose a two-step design approach. First, control and observer feedback gains are calculated on the basis of LMI stability conditions assuming measurable PVs, as discussed in Sections 4.3.1 and 4.3.2. The second step is a closed-loop proof of stability consisting of all possible effects shown in the model, including PV and state estimation, and feedback from the estimated states (Section 4.3.3).

4.3.1 Feedback design

A quadratic Lyapunov function approach is used, i.e., $V(x) = x^\mathrm{T} \mathrm{X}^{-1} x$, where $\mathrm{X} = \mathrm{X}^\mathrm{T} \succ 0$ denotes a symmetric positive definite matrix to be determined by the LMI solver. The stability condition $\dot{V}(x) = \dot{x}^\mathrm{T} \mathrm{X}^{-1} x + x \mathrm{X}^{-1} \dot{x} \prec 0$ can be used to derive the following LMI constraints [42]:

$$\mathrm{X} A_i^\mathrm{T} + A_i \mathrm{X} - M_i^\mathrm{T} B_i^\mathrm{T} - B_i M_i \prec 0$$

$$\mathrm{X} A_i^\mathrm{T} + A_i \mathrm{X} + \mathrm{X} A_k^\mathrm{T} + A_k \mathrm{X}$$
$$- M_k^\mathrm{T} B_i^\mathrm{T} - B_i M_k - M_i^\mathrm{T} B_k^\mathrm{T} - B_k M_i \prec 0 \tag{4.7}$$

$$\forall\, i, k = 1...N,\ k > i$$

where the desired feedback gains K_k in (4.6) are captured in $M_k = K_k \mathrm{X}$ to be determined by the LMI solver. To restrict the closed-loop pole location to a region between α_{minC} and α_{maxC} in the complex plane in terms of the decay rate, the following constraints are used:

$$\mathrm{X} A_i^\mathrm{T} + A_i \mathrm{X} - M_k^\mathrm{T} B_i^\mathrm{T} - B_i M_k \prec -2\alpha_{\mathrm{minC}} \mathrm{X}$$
$$\mathrm{X} A_i^\mathrm{T} + A_i \mathrm{X} - M_k^\mathrm{T} B_i^\mathrm{T} - B_i M_k \succ -2\alpha_{\mathrm{maxC}} \mathrm{X} \tag{4.8}$$

To reduce the actuator activity, the design variable M_k is optimized in terms of its Euclidean norm $M_k^\mathrm{T} M_k \prec \gamma \mathrm{I}_{n \times n}$. The number of states and inputs is denoted as n and m, respectively, and the optimization is conducted using the following LMIs:

$$\min(\gamma) \quad \text{subject to} \quad \begin{bmatrix} -\gamma \mathrm{I}_{n \times n} & M_j^\mathrm{T} \\ M_j & -\mathrm{I}_{m \times m} \end{bmatrix} \prec 0 \quad . \tag{4.9}$$

4.3.2 Observer & feedforward design

For wind speed estimation based on a disturbance observer, an augmented system description is defined as $\chi = [x \quad v]^\mathrm{T}$, which captures the unmeasurable wind speed as a system state. The artificial wind dynamics v is assigned as a first-order transfer function with a time constant of $\tau = 4$ s. As a result, an observer in TS form [31, 11]

$$\dot{\hat{\chi}} = \sum_{l=1}^{N} h_l(\hat{z}) \big[\mathcal{A}_l(\hat{\chi} - \chi_{0l}) + \mathcal{B}_l(u - u_{0l}) + \mathcal{L}_l \mathcal{C}(\chi - \hat{\chi}) \big] \tag{4.10}$$

is constructed, where N pairs $(A_l,\ \mathcal{C})$ are observable. The disturbance matrices B_{dl} in (4.1) are used to describe the augmented state space, i.e., $\mathcal{A}_l = \begin{bmatrix} A_l & B_{dl} \\ 0 & -1/\tau \end{bmatrix}$ and $\mathcal{B}_l = [B_l \quad 0]^{\mathrm{T}}$. As the rotational speed is the only system output, $\mathcal{C} = [1 \quad 0]$.

Assigning a quadratic Lyapunov candidate function to the error dynamics $\dot{\varepsilon} = \dot{\chi} - \dot{\hat{\chi}}$, i.e., $V(\varepsilon) = \varepsilon^{\mathrm{T}} P \varepsilon$ with $P = P^{\mathrm{T}} \succ 0$, the following stability constraints can be derived [42, 43]

$$\begin{aligned} \mathcal{A}_l^{\mathrm{T}} P + P\mathcal{A}_l - \mathcal{C}^{\mathrm{T}} N_l^{\mathrm{T}} - N_l\mathcal{C} &\prec -2\alpha_{\mathrm{minO}} P \\ \mathcal{A}_l^{\mathrm{T}} P + P\mathcal{A}_l - \mathcal{C}^{\mathrm{T}} N_l^{\mathrm{T}} - N_l\mathcal{C} &\succ -2\alpha_{\mathrm{maxO}} P \end{aligned}, \tag{4.11}$$

where α_{minO} and α_{maxO} represent the minimum and maximum desired decay rate assigned to the error dynamics. The observer gains in (4.10) are then given by $\mathcal{L}_l = P^{-1} N_l$.

Augmenting the wind-turbine dynamics yields complex-valued poles, which may excite oscillations in the turbine structure. Thus, the observer design uses additional LMIs, constraining the closed-loop dynamics to exhibit a guaranteed damping ratio D. From calculation of the conic sector angle $\theta = \arccos(D)$ (Figure 4.8), in terms of LMIs, this can be formulated as [44, 11]

$$\begin{bmatrix} \sin(\theta)(\mathcal{H}_1) & \cos(\theta)(\mathcal{H}_2) \\ \cos(\theta)(\mathcal{H}_2^{\mathrm{T}}) & \sin(\theta)(\mathcal{H}_1) \end{bmatrix} \prec 0 \tag{4.12}$$

with the definitions

$$\begin{aligned} \mathcal{H}_1 &= P\mathcal{A}_l - N_l\mathcal{C} + \mathcal{A}_l^{\mathrm{T}} P - \mathcal{C}^{\mathrm{T}} N_l^{\mathrm{T}} \\ \mathcal{H}_2 &= P\mathcal{A}_l - N_l\mathcal{C} - \mathcal{A}_l^{\mathrm{T}} P + \mathcal{C}^{\mathrm{T}} N_l^{\mathrm{T}} \end{aligned}.$$

4.3.3   Proof of stability

The previously discussed LMIs for controller and observer design consider stability guarantees for problems, where PV z is measurable, and consequently, the separation principle holds [37]. As the wind speed is an unmeasurable disturbance, this property is violated for the considered control task. However, LMI conditions that verify stability for previously synthesized gains K_k and $\mathcal{L}_l$ can be formulated. In the integrated description of state and observer error dynamics, the membership functions of the real PVs are distinguished from the estimated values, i.e., $h_i(z) \neq h_i(\hat{z})$.

The notation used denotes the multiplication of membership functions as

$$\sum_{i=1}^{N} h_i(x) \sum_{l=1}^{N} h_l(y) = \sum_{il}^{N} h_{il}(x,y)$$

$$\sum_{i=1}^{N} h_i(x) \sum_{l=1}^{N} h_l(y) \sum_{k=1}^{N} h_k(z) = \sum_{ilk}^{N} h_{ilk}(x,y,z)$$

,

whereas the difference terms that occur are given by $\Delta Z_{0xy} = Z_{0x} - Z_{0y}$. The combination of submodels in the design procedure depends on the possibility of two submodels being active simultaneously, which is denoted as $\forall\, i,j = 1,...,N$ such that $h_i h_j \neq 0$ (a more detailed explanation is available in [42]).

The basic model for stability analysis is provided by the augmented system

$$\dot{\chi} = \sum_{i=1}^{N} h_i(z)\big[\mathcal{A}_i(\chi - \chi_{0i}) + \mathcal{B}_i(u - u_{0i})\big] \quad , \tag{4.13}$$

where the state $\mathcal{A}_i$ and input $\mathcal{B}_i$ matrices correspond to the definitions in (4.10). As stability is evaluated in this augmented form, a correction of the control input following

$$u = -\sum_{k=1}^{N} h_k(\hat{z}) \underbrace{K_k[\mathrm{I}_n \quad 0_{n\times 1}]}_{\mathcal{K}_k}(\hat{\chi} - \chi_{0k}) + \sum_{k=1}^{N} h_k(\hat{z})\, u_{0k} \tag{4.14}$$

is defined. The introduction of $\mathcal{K}_k$ accounts for the exclusion of the estimated wind state $\hat{v}$ from the controller feedback.

Substituting (4.14) in (4.13), the closed-loop system dynamics are

$$\dot{\chi} = \sum_{ik}^{N} h_{ik}(z,\hat{z})\big[(\mathcal{A}_i - \mathcal{B}_i\mathcal{K}_k)\chi + \mathcal{B}_i\mathcal{K}_k\varepsilon$$
$$-(\mathcal{A}_i\chi_{0i} - \mathcal{B}_i\mathcal{K}_k\chi_{0k}) + \mathcal{B}_i(u_{0k} - u_{0i})\big] \tag{4.15}$$

and inserting (4.14) into (4.10), the observer dynamics driven by the input is

$$\dot{\hat{\chi}} = \sum_{lk}^{N} h_{lk}(\hat{z},\hat{z})\big[(\mathcal{A}_l - \mathcal{B}_l\mathcal{K}_k)\hat{\chi} + \mathcal{L}_l C\varepsilon$$
$$-\mathcal{A}_l\chi_{0l} + \mathcal{B}_l(\mathcal{K}_k\chi_{0k} + u_{0k} - u_{0l})\big] \quad . \tag{4.16}$$

The estimation error dynamics $\varepsilon = \chi - \hat{\chi}$ with respect to (4.15) and (4.16) are derived as

$$
\begin{aligned}
\dot{\varepsilon} = \sum_{ilk}^{N} h_{ilk}(z, \hat{z}, \hat{z}) \big[& (\mathcal{A}_i - \mathcal{L}_l \mathcal{C} + \Delta\mathcal{A}_{li} - \Delta\mathcal{B}_{li}\mathcal{K}_k)\varepsilon \\
& + (\Delta\mathcal{A}_{il} - \Delta\mathcal{B}_{il}\mathcal{K}_k)\chi + \Delta\mathcal{B}_{il}(\mathcal{K}_k\chi_{0k} + u_{0k}) \\
& + (\mathcal{A}_l\chi_{0l} + \mathcal{B}_l u_{0l}) - (\mathcal{A}_i\chi_{0i} + \mathcal{B}_i u_{0i}) \big]
\end{aligned}
\tag{4.17}
$$

Using (4.15) and (4.17), an integrated closed-loop observer-based system model $\xi = [\chi \quad \varepsilon]^{\mathrm{T}}$ is formulated as

$$
\dot{\xi} = \sum_{ilk}^{N} h_{ilk}(z, \hat{z}, \hat{z}) \big[\mathcal{A}_{ilk}\xi + d_{ilk} \big]
\tag{4.18}
$$

where the state space matrices are given by

$$
\mathcal{A}_{ilk} = \begin{bmatrix} \mathcal{A}_i - \mathcal{B}_i\mathcal{K}_k & \mathcal{B}_i\mathcal{K}_k \\ \Delta\mathcal{A}_{il} - \Delta\mathcal{B}_{il}\mathcal{K}_k & \mathcal{A}_i - \mathcal{L}_l\mathcal{C} + \Delta\mathcal{A}_{li} - \Delta\mathcal{B}_{li}\mathcal{K}_k \end{bmatrix}
$$

and the affine terms are denoted as

$$
d_{ilk} = \begin{bmatrix} -(\mathcal{A}_i\chi_{0i} - \mathcal{B}_i\mathcal{K}_k\chi_{0k}) + \mathcal{B}_i\Delta u_{0ki} \\ (\mathcal{A}_l\chi_{0l} + \mathcal{B}_l u_{0l}) - (\mathcal{A}_i\chi_{0i} + \mathcal{B}_i u_{0i}) + \Delta\mathcal{B}_{il}(\mathcal{K}_k\chi_{0k} + u_{0k}) \end{bmatrix}.
$$

The affine terms characterize two aspects. They consist of two terms, $\mathcal{B}_i\Delta u_{0ki}$ and $(\mathcal{A}_l\chi_{0l} - \mathcal{B}_l u_{0l}) - (\mathcal{A}_i\chi_{0i} - \mathcal{B}_i u_{0i}) + \Delta\mathcal{B}_{il}(\mathcal{K}_k\chi_{0k} + u_{0k})$, which would vanish for $\hat{z} \to z$, i.e., when the wind speed estimation error decays. Additionally, $-(\mathcal{A}_i\chi_{0i} - \mathcal{B}_i\mathcal{K}_k\chi_{0k})$ represents the defined trajectories of the states within the operating range.

System (4.18) can be rewritten with respect to the TS description properties to give [42]

$$
\begin{aligned}
\dot{\xi} = & \sum_{il,k=l}^{N} h_{il,k=l}(z, \hat{z}, \hat{z}) \big[\mathcal{A}_{ill}\xi + d_{ill} \big] \\
& + \sum_{il,k<l}^{N} h_{il,k<l}(z, \hat{z}, \hat{z}) \big[(\mathcal{A}_{ilk} + \mathcal{A}_{ikl})\xi + d_{ilk} + d_{ikl} \big]
\end{aligned}
\tag{4.19}
$$

Assigning a quadratic Lyapunov function $V(\chi) = \xi^{\mathrm{T}} P \xi$ with $P = P^{\mathrm{T}} \succ 0$ for the integrated observer

and feedback closed-loop system (4.19), the following LMI stability constraints are derived [37]

$$\mathcal{A}_{ill}^{\mathrm{T}}\mathrm{P} + \mathrm{P}A_{ill} \prec 0$$

$$(\mathcal{A}_{ilk} + \mathcal{A}_{ikl})^{\mathrm{T}}\mathrm{P} + \mathrm{P}(\mathcal{A}_{ilk} + \mathcal{A}_{ikl}) \prec 0.$$

$$\forall\, i, l, k < l \quad \text{s.t. } h_i h_l h_k \neq 0$$

(4.20)

A global (within the defined operating range of the TS model) proof of stability is obtained by finding a solution including *all* combinations of i, l, and k contained in (4.20). However, the knowledge of the TS construction, along with an assumption on the PV error $e_j = z_j - \hat{z}_j$ can be used to reduce the number of necessary LMIs.

Recalling that i is governed by the unmeasurable PV z_j, whereas l and k are determined by the estimated PV $\hat{z}_j$, we can construct the possible simultaneous occurrences in operation based on the PV error as this activates different weighting functions $w_{l,j}(z_j) \neq w_{l,j}(\hat{z}_j)$. This is conducted by considering all weighting functions, where

$$w_{l,j}(\hat{z}_j) \neq 0,\, \forall\, \hat{z}_j \in \{z_j^{0l} - e_j \leq \hat{z}_j \leq z_j^{0l} + e_j\}$$

(4.21)

holds. This induces the necessary combinations of i, l, and k for which

$$h_i(z)h_l(\hat{z})h_k(\hat{z}) \neq 0$$

(4.22)

possibly holds due to the estimation error. Together with the LMIs expressed in (4.20), these conditions constitute basic stability constraints and obtaining a solution proves closed-loop stability of the observer-based control with unmeasurable PV in a restricted operating region. For the considered turbine control task, this is shown in Figures 4.9 and 4.10. This approach for reducing the number of constraining LMIs applies for TS systems where naturally not all submodels are simultaneously active, i.e., TS models derived by interconnecting locally linearized models. It can be simultaneously used for all unmeasurable variables in the premise space. Thus, an intuitive approach for reducing conservativeness at the cost of restricting the domain of validity to a subspace within the considered operational range is given.

4.3.4 Application of LMI design constraints

The synthesis of the feedback gains K_k and $\mathcal{L}_l$ assumes measurable PVs, i.e., an individual design of feedback and observer is conducted. If triangular membership functions are constructed to interconnect the submodels as in (4.2), for measurable PVs, only adjacent submodels can be simultaneously

active. An example of the resulting combination of submodels within the Lyapunov function-based constraints is depicted in Figure 4.6. The overall design follows a wind-turbine application-specific conception, which is briefly discussed next.
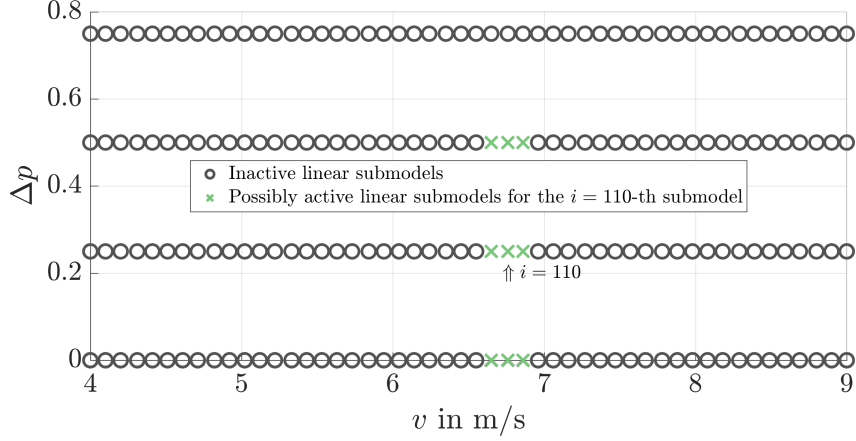

Figure 4.6: Combination of linear submodels in the feedback design for possibly simultaneous active submodels depending on the location in the operating range, i.e., $h_i h_j \neq 0$. The considered submodels in the control design of the i=110$^{\text{th}}$ feedback gain K_i are highlighted.

Depending on the feedback design for either the generator torque or pitch angle, a different input matrix is used to set up the corresponding LMIs, which can be flexibly altered to account for the changing feedback actuator depending on the current operating point. If a feedback gain for the generator torque is designed, the input matrix is composed of the rotation's sensitivity to changes in the generator torque, such that $B_i = \frac{\partial f(x_{0i}, u_{0i}, d_{0i})}{\partial T}$. On the other hand, if feedback gains for the pitch actuator are sought, the input matrices in the LMIs are given by $B_i = \frac{\partial f(x_{0i}, u_{0i}, d_{0i})}{\partial \beta}$. After the design, the obtained feedback gains are arranged into the general feedback structure K_k corresponding to the defined input as $u = [T \quad \beta]^{\text{T}}$.

Base control design   First, desired rotational closed-loop dynamics are assigned, where the generator torque is used to track the optimal tip speed ratio below the rated power. The choice of the linearization points in Figure 4.2 encodes this nominal operating trajectory in the design model. Rotor speed feedback is provided by the pitch in all other operating points, i.e., above-rated wind speed and when power tracking operation is demanded with $\Delta p > 0$. A common Lyapunov function for the entire operating range is assigned, yielding N gains K_k. Therefore, each gain M_k is set to fulfill the stability constraints (4.7) for its adjacent dynamics and the performance constraints (4.8) for $i = k$, while jointly optimized for (4.9). The design parameters of the LMIs in (4.8) are chosen as $\alpha_{\text{minC}} = 2$ s^{-1} and $\alpha_{\text{maxC}} = 8$ s^{-1} (Figure 4.7 (b)).

Add torque feedback for pitch regulated regions To provide some damping to the drive-train in the absence of a corresponding model, minor feedback on the generator torque from the rotational speed is assigned to the operating points that up to this point only feature pitch actuation. This is performed using (4.8) and optimized by (4.9) while embedded in a common Lyapunov function for all considered operating points. The resulting gains are integrated into K_k resulting in slight torque actuation when deviating from nominal rotational speed. It is important to restrict the generator torque activity in those operating points to avoid unintended power oscillations. Thus, the location of the closed-loop eigenvalues λ_i respecting the feedback gains from the previous step is used to assign a desired minimum decay rate. Therefore, in the ith operating point for LMIs (4.8), the desired minimum decay rate is defined as $\alpha_{\text{minC}} = \text{abs}(\text{Re}(\lambda_i)) + 0.1 \text{ s}^{-1}$. This step results in a slight relocation of the closed-loop eigenvalues due to additional torque feedback for operating points with eigenvalues located further left in the complex plane (Figure 4.7 (c)). The operating points where the generator torque performs optimal tip speed tracking remain unchanged and close to the desired minimum decay rate of $\alpha_{\text{minC}} = 2 \text{ s}^{-1}$ from the previous step.
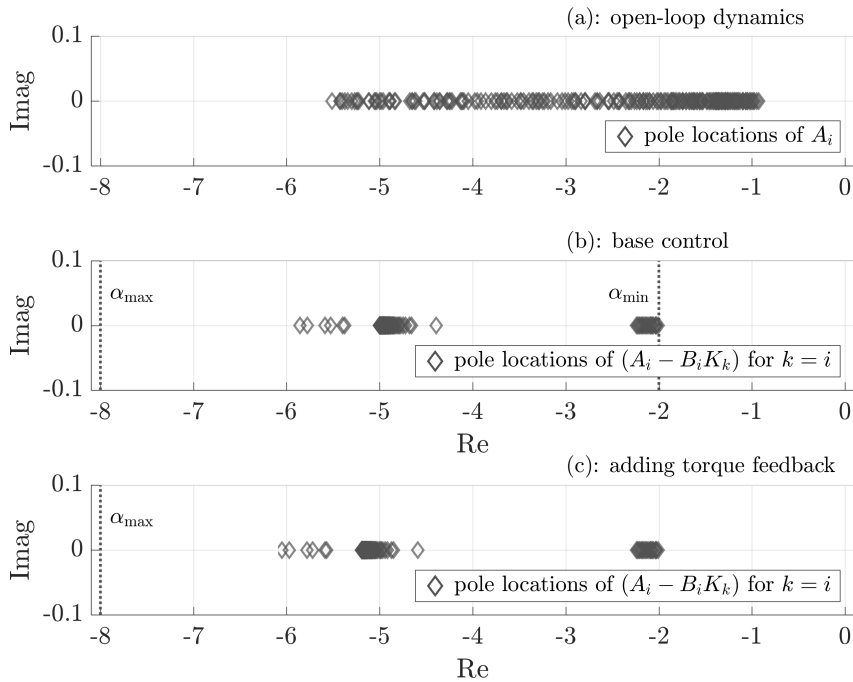
Figure 4.7: Comparison of pole locations in the complex plane before and after feedback gain design. (a) open-loop pole locations (b) closed-loop pole locations after base control design (c) closed-loop pole locations after adding torque feedback.

Observer synthesis LMIs (4.11) and (4.12) with design parameters $\alpha_{\text{minO}} = 10 \text{ s}^{-1}$, $\alpha_{\text{maxO}} = 20 \text{ s}^{-1}$ and $D = 0.9$ are used to embed the entire operating space in a common Lyapunov function yielding N gains $\mathcal{L}_l$ in (4.10). Some closed-loop observer poles that result from the LMI solver

violate the imposed region constraints far in the left half of the complex plane, resulting in slightly different dynamics than imposed (Figure 4.8). However, as the poles are located in the left half of the complex plane and share a common Lyapunov function that satisfies the basic stability constraints $\mathcal{A}_l^{\mathrm{T}} P + P \mathcal{A}_l - \mathcal{C}^{\mathrm{T}} N_l^{\mathrm{T}} - N_l \mathcal{C} \prec 0$, the observer design yields stable estimation error dynamics.
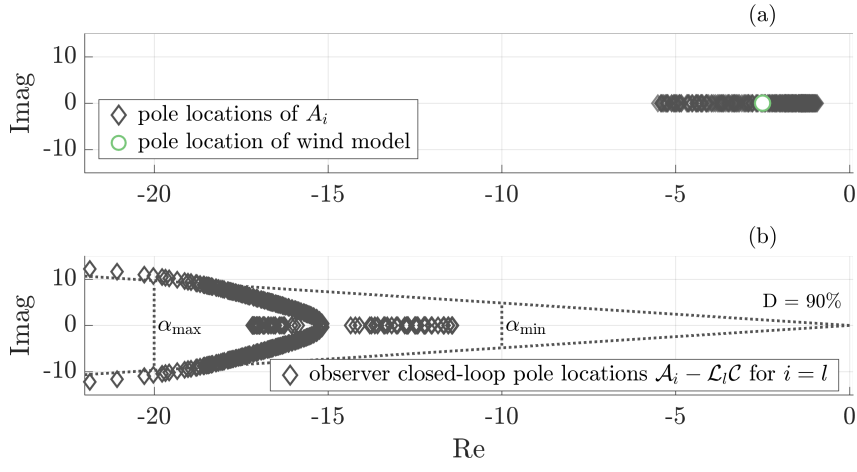

Figure 4.8: Comparison of the pole locations in the complex plane before and after observer gain design. (a) open-loop augmented model and (b) closed-loop estimation error dynamics

Proof of stability   The overall combined observer-based control strategy is formally evaluated for stability using the LMI-constraints (4.20) for all combinations i, l and k induced by the PV estimation error, which, in this case, represents the wind speed. Setting up the LMI solver to search for $P = P^{\mathrm{T}} \succ 0$ constrained by (4.20) and using the previously synthesized gains $\mathcal{K}_k$ and $\mathcal{L}_l$, a well-conditioned solution for the assumption of $|e_v| = |v - \hat{v}| \leq 1.5$ m/s is obtained. The corresponding possibly active weighting functions define the induced combinations of submodels within the design (Figures 4.9 and 4.10). The computational burden connected to the applied proof of stability is reflected by the solver time. While a solution to the LMIs for $e_v = 0$ m/s is obtained within approximately 30 s, the solver time increases up to approximately 20 h when providing a proof of stability up to an estimation error of $|e_v| \leq 1.5$ m/s. For a greater assumption on the estimation error, the LMI solver yields no well-conditioned solution.
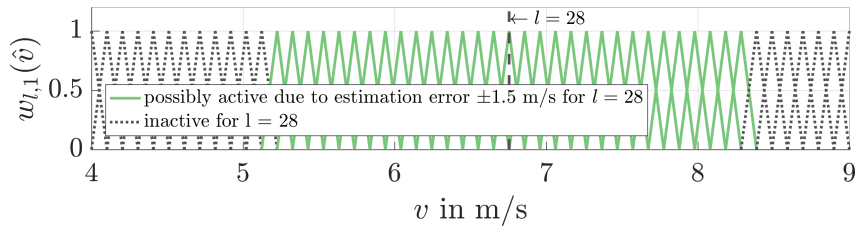
Figure 4.9: Possibly simultaneous active weighting functions due to a wind speed estimation error of 1.5 m/s. The possibly active weighting functions for the $l = 28^{\text{th}}$ operating point are highlighted.
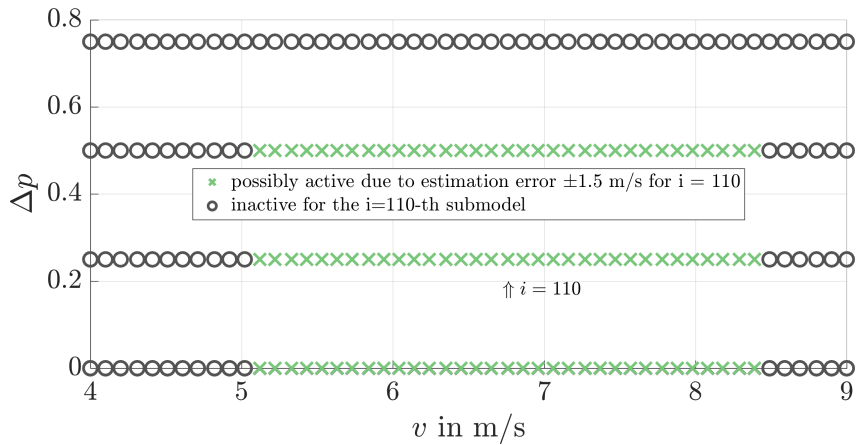

Figure 4.10: Combination of linear submodels in the control design for possibly simultaneous active submodels due to a wind speed estimation error, i.e., $h_i h_j \neq 0$ within the operating range. The combined submodels in the proof of stability for the i=110$^{\text{th}}$ submodel are highlighted for a wind speed estimation error of 1.5 m/s.

4.4 Experimental setup

4.4.1 WindLab wind tunnel

The wind tunnel experiments were performed in the WindLab at the ForWind research facility at the Carl von Ossietzky University of Oldenburg. The wind tunnel has a cross-section of 3×3 m^2 and a test section length of 30 m. In addition to producing constant inflow, an active grid in the setup can generate customized, reproducible inflow conditions [45]. The active grid [46] is designed after Makita [47, 48] producing different flows, from single velocity steps and gusts to atmospheric-like turbulence driven by stochastic processes, and can be tailored for turbine testing [49]. Thus, the interaction of the turbulent wind resource and closed-loop turbine dynamics can be reproduced. This allows for an efficient comparison of control performance at typical operating conditions faced by turbines during the lifetime, where field testing and comparison of controllers involve longer-term data collection due to uncontrollable inflow in a natural environment [50, 40].

Hot-wire measurements placed 1.5 diameters in front of MoWiTO are used to evaluate the wind speed estimation performance. Thus, the assumption on the maximum occurring estimation error used in the stability considerations can be evaluated experimentally.

4.4.2 Power tracking operation

The desired power output in reality depends on the frequency evolution of the electrical grid or a higher-level logic, e.g., a wind farm controller. Here, an artificial power tracking signal is used. Defined as sinusoidal variations, the power tracking signal is used as a PV in the TS method, and therefore, it inherently enforces the desired power output of the turbine in operation. The reproducibility of the WindLab setup allows for investigating the turbine behavior with (almost) identical wind excitation impacted by different power variation scenarios. For this purpose, two test signals are evaluated during the measurements. The scenarios are configured as

$$\Delta p_1(t) = 0.375 \sin(2\pi\,\mathrm{s}^{-1} t) + 0.375$$
$$\text{and}$$
$$\Delta p_2(t) = 0.25 \sin(2\pi 4\,\mathrm{s}^{-1} t) + 0.25$$

which results in maximum power gradients of the turbine in operation of $\max(\frac{\mathrm{d}\Delta p_1}{\mathrm{d}t}) = 2.35$ s^{-1} and $\max(\frac{\mathrm{d}\Delta p_2}{\mathrm{d}t}) = 6.28$ s^{-1}. This means that MoWiTO would vary its power output with a maximum gradient of $235\%\,\mathrm{s}^{-1}$ and $628\%\,\mathrm{s}^{-1}$, corresponding to gradients of $5.8\%\,\mathrm{s}^{-1}$ and $15.7\%\,\mathrm{s}^{-1}$, respectively, for the modeled NREL 5-MW turbine when considering the time scaling of 40/1 for MoWiTO in the chosen configuration. At the lower frequency at Δp_1, the power is reduced to a minimum of 25%, whereas, at Δp_2 a reduction to 50% is demanded.

4.5 Measurement results

4.5.1 Wind ramps

To derive an impression of the stationary behavior in the wind speed range of 4-9 m/s, different stationary operating points are generated. Figure 4.11 shows the wind speed measurement and the estimated wind speed. The estimation follows the inflow sequence while showing a relatively constant offset. The wind speed is underestimated compared to the measurement. At lower wind speeds, the estimation at power tracking $\Delta p_1(t)$ and $\Delta p_2(t)$ slightly oscillates at the corresponding frequency while the reconstruction is identical to nominal operation at $\Delta p = 0$ at higher speeds.
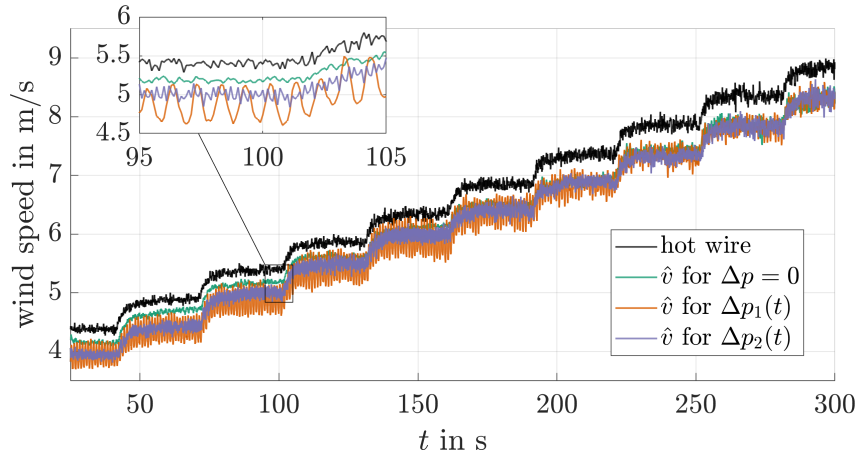
Figure 4.11: Wind ramps performed by the active grid and assessed by hot-wire measurement. The wind speed reconstruction at nominal operation with $\Delta p = 0$ is compared to the results at power tracking operation in scenarios $\Delta p_1(t)$ and $\Delta p_2(t)$.
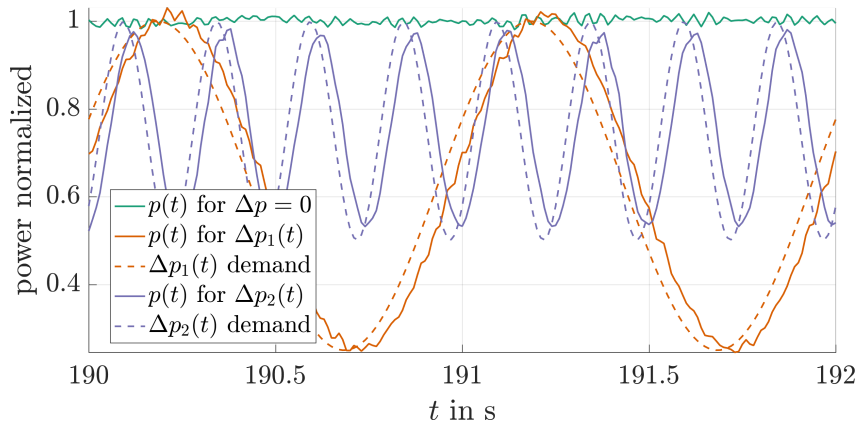
Figure 4.12: Power production at a constant wind of MoWiTO at nominal operation $\Delta p = 0$ compared to operation at power tracking scenarios $\Delta p_1(t)$ and $\Delta p_2(t)$. The evolution of the power demand for $\Delta p_1(t)$ and $\Delta p_2(t)$ are depicted to assess the tracking accuracy.

The variation of the power tracking signal used within the PVs adjusts generator torque and pitch angle while tracking constant rotational speed, causing the transition to the altered power output. Figure 4.12 shows the operation in stationary inflow at 6.8 m/s above rated wind speed. The turbine operates at the rated power for $\Delta p = 0$, whereas the power output follows the tracking signals $\Delta p_1(t)$ and $\Delta p_2(t)$ and exhibits the desired sinusoidal variation. A constant phase shift from the demand to the power output is visible in both tracking scenarios. The evaluation of the cross-correlation of the demand and actual power output yields a delay of 0.04 s for $\Delta p_1(t)$ and 0.03 s for $\Delta p_2(t)$.

Figure 4.13: Operating gust profile executed by the active grid and assessed by hot-wire measurement. The wind speed reconstruction at nominal operation with $\Delta p = 0$ is compared to the results at power tracking operation in scenarios $\Delta p_1(t)$ and $\Delta p_2(t)$.
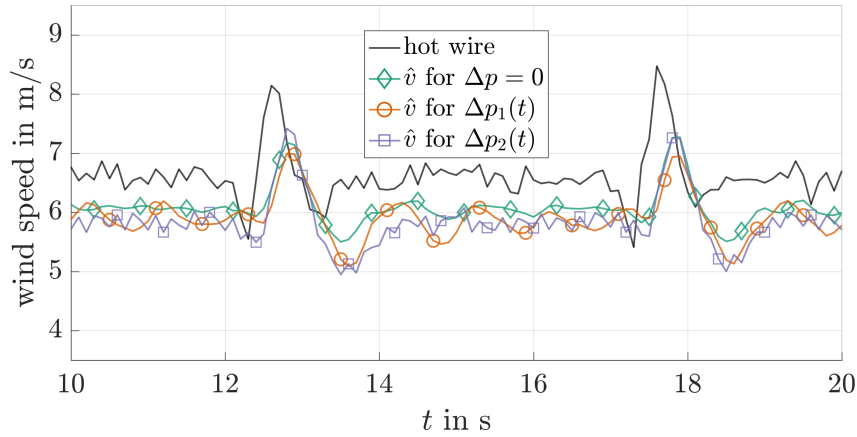
4.5.2 Operating gust

Figure 4.13 shows the operating gust profile, which shows a decline in wind speed before a rapid rise. A constant estimation offset, as experienced previously, is observed. Furthermore, the wind speed reconstruction is delayed compared to the measured wind sequence. This delay is uniform in the three scenarios, where an evaluation of the cross-correlation gives 0.2 s.

The gust is located close to the crucial operating point, where the conceptual change from optimal tip speed ratio tracking to the limitation of the power output is conducted, causing the decreases in the power output (Figure 4.14). At lower wind speeds in this sequence, the power overshoots its desired value, especially at high frequency power tracking $\Delta p_2(t)$. The power demand at tracking operation is calculated from Δp for the two scenarios and the currently estimated wind speed $\hat{v}$. A phase shift in power tracking is observable in Figure 4.14, which was evaluated by cross-correlation to be 0.04 s for $\Delta p_1(t)$ and 0.03 s for $\Delta p_2(t)$.

4.5.3 Turbulent inflow

Finally, the operation in turbulent wind conditions generated by the active grid [46] is evaluated. Figure 4.15 shows the wind sequence. The previously determined offset in wind speed reconstruction is also observed, where the observer underestimates the current effective wind speed. Contrary to the stationary inflow conditions, only a small difference in the wind speed estimation is observed for the different power tracking scenarios. A delay of 0.2 s from the reconstructed wind speed to the measurement was found from the evaluation of the cross-correlation, matching the previous results.
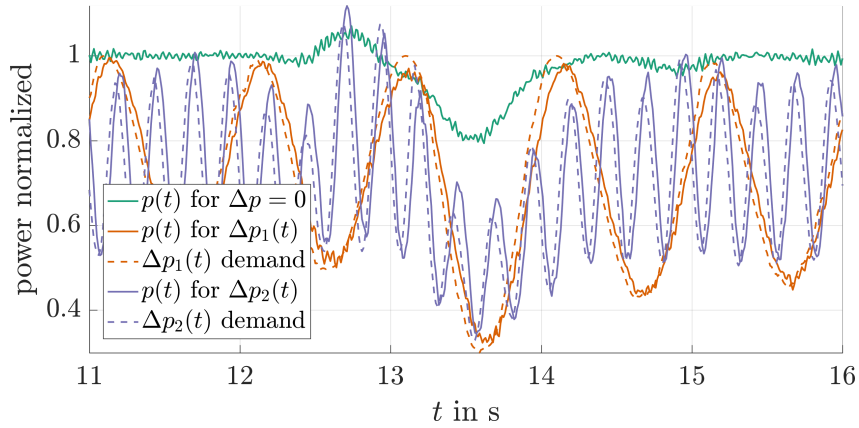
Figure 4.14: Power production of the MoWiTO during the operating gust at the nominal operation $\Delta p = 0$ compared to operation at power tracking scenarios $\Delta p_1(t)$ and $\Delta p_2(t)$. The evolution of the power demand for $\Delta p_1(t)$ and $\Delta p_2(t)$ are shown to assess the tracking accuracy.
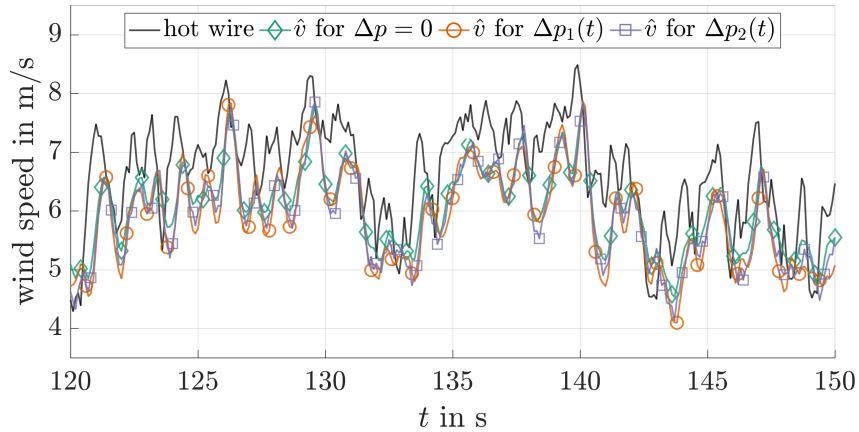
Figure 4.15: Turbulent wind speed generated by the active grid estimated by hot-wire measurements. The wind speed reconstruction at nominal operation with $\Delta p = 0$ is compared to the results at power tracking operation in scenarios $\Delta p_1(t)$ and $\Delta p_2(t)$.

Despite being continuously carried out of the operating point by the turbulent inflow, the controller enforces the power output demanded by the tracking scenarios by following the operating points defined in the design model (Figure 4.16). As observed previously, the delay of the power to its demand is 0.04 s for $\Delta p_1(t)$ and 0.03 s for $\Delta p_2(t)$.

To assess the effects of power tracking operation on the mechanical MoWiTO structure, a frequency analysis of the load signals is performed (Figure 4.17). The power variation propagates into all considered components of the turbine and results in additional loading. The excitation depends on the considered components and the form of the tracking signal. The rotational speed is more sensitive to the excitation at $\Delta p_1(t)$ (Figure 4.17 (a)). On the other hand, the tower base moment in the fore-aft direction shows greater loading for the higher frequency at $\Delta p_2(t)$ (Figure 4.17 (b)). This aligns with

Figure 4.16: Power production at turbulent inflow of the MoWiTO at nominal operation $\Delta p = 0$ compared to operation at power tracking $\Delta p_1(t)$ and $\Delta p_2(t)$. The evolution of the power demand for $\Delta p_1(t)$ and $\Delta p_2(t)$ are shown to assess the tracking accuracy.
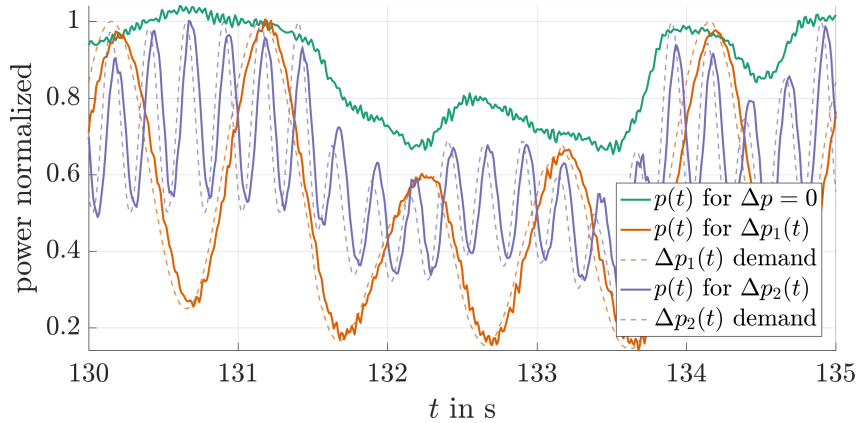
the load spectrum of the tower side-to-side motion (Figure 4.17 (c)), where no additional loading for the lower frequency at $\Delta p_1(t)$ is observed, whereas power tracking at $\Delta p_2(t)$ affects the experienced side-to-side tower loading. Figure 4.17 (d) shows that both tracking scenarios affect the flapwise blade loading equally.

4.5.4 Wind speed estimation error

The proof of stability is valid up to an estimation error $e_v = \pm 1.5$ m/s. This assumption can be evaluated by calculating the difference between the hot-wire measurement and the estimated wind speed at the different operating conditions.

For the wind ramps (Figures 4.11 and 4.18 (a)), small fluctuations in the estimation error at the power tracking frequency can be observed. This oscillation exhibits greater magnitudes in $\Delta p_1(t)$ compared to $\Delta p_2(t)$, indicating the power reduction is dominant rather than the power tracking frequency. This effect is overshadowed by changes caused by the variable inflow in the other scenarios (Figure 4.18 (b) and (c)).

Figure 4.18 (a)–(c) and Table 4.1 show the offset that is observed at all inflow conditions that were considered. Figure 4.18 (a) shows that for the entire wind operating range considered, the offset slightly varies, depending on the mean wind speed, and increases at higher wind speeds. Furthermore, the wind speed estimation is insensitive to the slow inflow variation during the wind ramps, where only small deviations are observed (Figure 4.18 (a)). The basic statistical properties (Table 4.1) show that mean is dependent on the inflow conditions, where an increase in turbulence is observed.
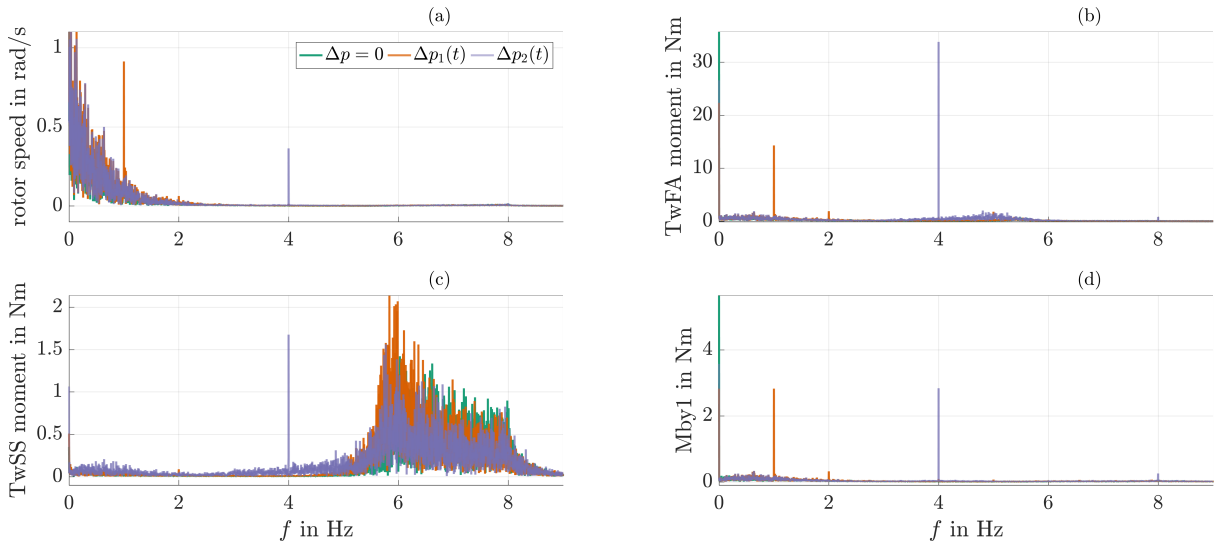
Figure 4.17: Frequency spectrum of the wind turbine's rotational speed at nominal power production $\Delta p = 0$ compared to operation at power tracking scenarios $\Delta p_1(t)$ and $\Delta p_2(t)$ in turbulent inflow conditions. Subplots: (a) rotor speed (b) tower base fore-aft moment (c) tower base side-to-side moment (d) flapwise moment experienced by the first rotor blade.

For gusts and turbulence (Figure 4.18 (b) and (c)), in addition to the offset, the estimation error varies due to inflow transients. The estimation error decays subsequently due to the observer dynamics, but the variance depends on the excitation characteristics (Table 4.1). The estimation error shows increasing variances at turbulence and a greater power reduction at $\Delta p_1(t)$ compared to that at higher frequencies at $\Delta p_2(t)$. During transients, the estimation error temporarily exceeds the assumption used in the stability considerations before converging again toward the offset value. In both gust and turbulent operations, an evaluation of the cross-correlation of the measured and estimated wind speeds shows a time delay of approximately 0.2 s, indicating that the same effect is responsible for the temporary estimation error increase.

4.6 Discussion

4.6.1 Wind speed estimation accuracy

Only rotational speed was measured during the experiments. The observer dynamics force the observer state to the measured trajectory (Figure 4.19). The rotational speed of the observer follows the measurement, and the unavoidable model mismatch condenses in the wind speed estimation error.

The FAST code provides a simplified description of the complex energy conversion process in reality.
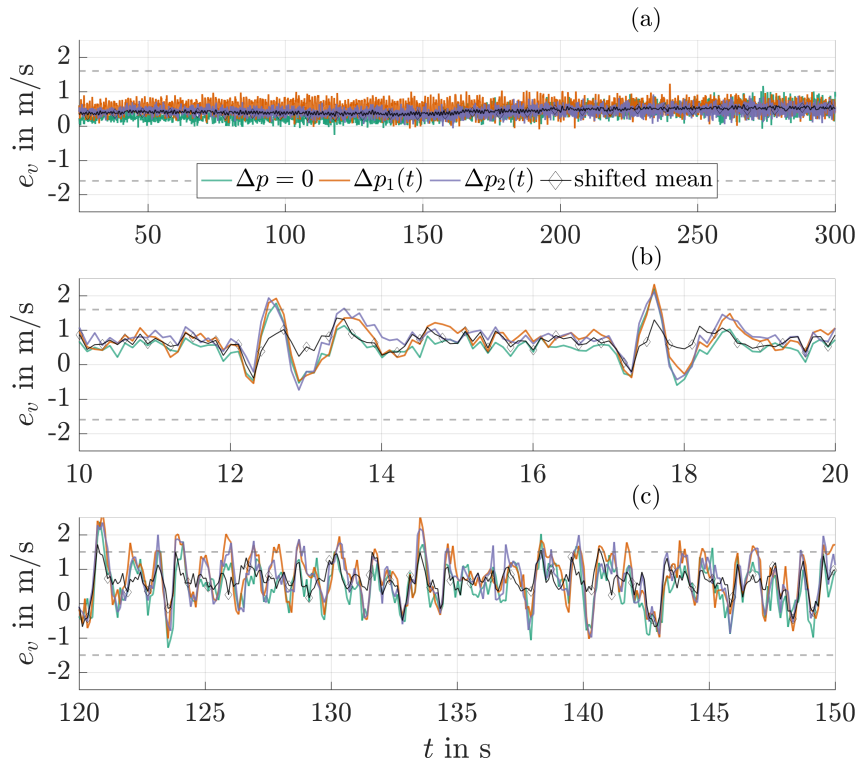
Figure 4.18: Wind speed estimation error e_v at different inflow conditions and power tracking scenarios. The shifted error signal is the mean value of all scenarios, where the reconstructed wind speed is shifted with a delay time of $0.2\,\mathrm{s}$ that was identified from the phase shift of the rotational speed to changes in the wind speed. The dashed lines reflect an estimation error of $e_v = \pm 1.5\,\mathrm{m/s}$ that lead to a feasible solution for the proof of stability. Subplots: (a) wind ramps (b) operating gust (c) turbulent inflow

Table 4.1: Comparison of mean $\mathrm{E}[e_v]$ and variance $\sigma_{e_v}^2$ of the wind speed estimation error e_v at different inflow conditions and power tracking scenarios.

Inflow	Scenario	$\mathrm{E}[e_v]$ in m/s	$\sigma_{e_v}^2$ in m^2/s^2
Wind Ramps	$\Delta p = 0$	0.371	0.044
	$\Delta p_1(t)$	0.537	0.036
	$\Delta p_2(t)$	0.432	0.018
Operating Gust	$\Delta p = 0$	0.538	0.170
	$\Delta p_1(t)$	0.714	0.232
	$\Delta p_2(t)$	0.733	0.203
Turbulent	$\Delta p = 0$	0.460	0.453
	$\Delta p_1(t)$	0.706	0.538
	$\Delta p_2(t)$	0.646	0.520
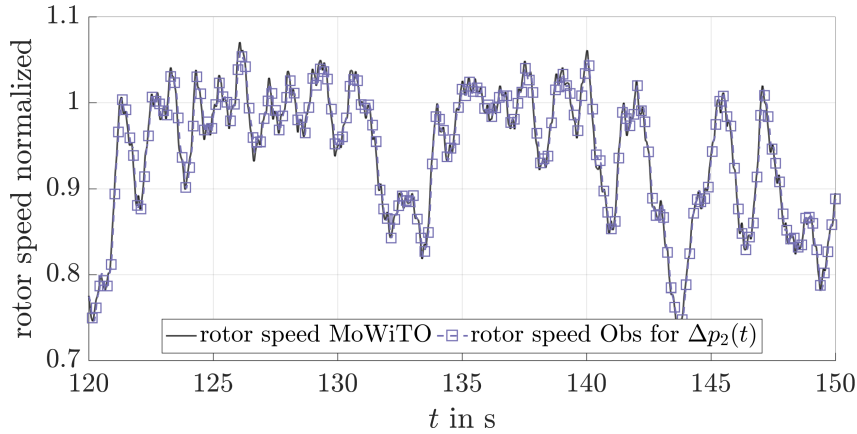
Figure 4.19: Rotational speed of the MoWiTO in turbulent inflow conditions corresponding to the sequence illustrated in Figure 4.15 compared to the evolution of the first observer state representing the rotational speed for power tracking at $\Delta p_2(t)$.

The approximation using the simulation code is also identified to result in a loss of wind speed reconstruction accuracy for different estimation approaches when simulation studies are compared to field test results in [28]. In addition, deriving the TS model by linearization results in a further approximation of the underlying dynamics captured in FAST. The TS model mismatch on the stationary operating curves depends on the distribution of the linearized models [51]. Further, the system description is less accurate when operating the wind turbine in transients, e.g., deviating from the desired rotational speed (Figure 4.19). The underlying FAST turbine model only incorporates an aerodynamical description of the mounted blades of MoWiTO, whereas essential components, such as drive-train dynamics or tower motion are neglected. Therefore, not only the dynamical influence of these components but also the lack of losses in the model overestimates the power generation efficiency. This essentially means the same power production is expected at lower wind speed. It may be the cause of the observed wind speed estimation offset.

During inflow transients, the maximum assumed estimation error used in the proof of stability is temporarily exceeded, but the observer feedback gains force the estimate toward the altered inflow. By evaluating the cross-correlation during turbulent inflow from the rotational speed response (Figure 4.19) to changes in the wind speed (Figure 4.15), a delay of approximately 0.2 s is identified. This delay is similar to the cross-correlation between the reconstructed wind speed and its actual value, indicating that the altered inflow must propagate to the rotational speed before it influences the observer reconstruction. This inertia-induced effect plays a dominant role in the exceedance of the maximum estimation error during transients.

Figure 4.11 shows a fluctuation in the wind speed estimate at the frequency of power tracking, especially at lower wind speeds. Comparing the power coefficient obtained from the FAST model of

MoWiTO to a measured power coefficient surface, we observe differences from -2% to 6%, especially in the area around the optimal tip speed ratio enforced at lower wind speeds. This implies that the FAST model of MoWiTO provides varying efficiency mismatch in the observer design, which results in the oscillations at the power tracking frequency. This is also supported by the more dominant oscillation at higher power reduction at $\Delta p_1(t)$, where the controller moves the turbine further from the nominal operating point. As the wind speed estimate determines the feedforward component, this varying model mismatch is also the primary cause for the rotational speed excitation at the power tracking frequency (Figure 4.17 (a)).

The field test results using different wind speed reconstruction strategies in [28] show varying error means and variances. The mean values that provide satisfactory performance range from -0.25 m/s to 0.5 m/s in [28], with variances ranging from 1.3 m^2/s^2 to 0.5 m^2/s^2. The performance certainly depends on different effects e.g., the turbulence, but a plain comparison with Table 4.1 shows that the TS observer yields slightly greater mean values at variances in the lower range of the field test results in [28]. Although the results are hard to compare as the turbine is not controlled using the estimators, and due to the scaling of turbine and wind conditions in the wind-tunnel experiments, the results obtained here agree well with the findings.

The assumption of a maximum wind speed estimation error in the stability investigation narrows the combination of operational scenarios that are assumed to be encountered. Though experimental validation of the approach provides no guarantee that this bound would not be exceeded, it provides confidence in the observer to converge toward a steady-state offset within the domain of stability. From the experimental investigation, we conclude that the reconstructed wind speed provides useful knowledge for adjusting the feedback gains and feedforward terms to account for the nonlinear turbine dynamics.

4.6.2 Power tracking performance

The controller enforces adequate power tracking. The produced power (Figures 4.12, 4.14, and 4.16), however, reveals a time delay in a range of 0.04 s and 0.03 s for tracking scenarios $\Delta p_1(t)$ and $\Delta p_2(t)$, respectively. An investigation of the measured generator torque showed that this delay is caused by the underlying generator torque control loop.

The power output overshoots during power tracking operation, especially at declining wind speeds (Figures 4.14 and 4.16). A likely cause for this stems from the dynamic inflow effect, which occurs especially at high tip speed ratios associated with declining wind speeds in the partial-load region. This corresponds to an aerodynamic effect, where the flow field inertia results in an axial induction

delay until a stable flow is established when transiting from one operating point to another. The experimental investigation of this effect confirms a first-order time constant $R/v = 0.15$ s at an inflow of 6.1 m /s and a pitching step of 5.9° [52]. Thus, it is located in a crucial time range for the power tracking scenarios, especially at the higher frequency in $\Delta p_2(t)$.

Nevertheless, the experimental results build confidence in wind turbines to provide power tracking capabilities, as also shown in the wind-tunnel campaign in [26]. The power system community studies the impact of frequency stabilization by wind turbines according to frequency evolution after the occurrence of load imbalance [7, 16]. This incorporates power variation at high dynamic requirements to provide support in the inertial and primary time range of the electric grid, i.e., in the range of seconds [53]. The experimental data show the attained accuracy in power tracking at fast scales when operated by an appropriate control strategy, and thus, the capability of wind turbines to supply vital ancillary services at fast scales.

4.6.3 Loading of the wind turbine structure

Power tracking excites the turbine structure, but the components are not equally impacted. Figure 4.17 (a) shows that the rotor speed is more affected at $\Delta p_1(t)$ than at $\Delta p_2(t)$. This effect may be mitigated by considering the varying model mismatch described in the discussion of the wind speed estimation.

The tower fore-aft motion shows the most severe increase in loading (Figure 4.17 (b)), which is consitent with the results for a multi-MW turbine in [11]. There are two main reasons for this. First, there is a strong coupling of the pitch actuation with the tower fore-aft motion [54]. The tower has a different deflection for every power operating point due to the varying thrust at varying pitch angles. This causes a continuous movement of the tower top in the fore-aft direction at the power tracking frequency. The more changes due to the higher frequency at $\Delta p_2(t)$ cause greater additional loading than the fewer changes at a larger magnitude at $\Delta p_1(t)$. Second, power tracking at a frequency of 4 Hz at $\Delta p_2(t)$ is closer to the tower eigenfrequency of 5.7 Hz, which is aerodynamically well-damped in fore-aft direction. As shown in Figure 4.17 (c), this vicinity at $\Delta p_2(t)$ to the eigenfrequency stimulates the tower side-to-side motion coupled to the generator torque, while experiencing no additional excitation for $\Delta p_1(t)$.

The measurement data show an increase in the blade-flap-wise moment (Figure 4.17 (d)). Interestingly, it is almost the same for both scenarios, regardless of the frequency or magnitude, which may be caused by the dynamic inflow effect. At $\Delta p_1(t)$, higher deflections are enforced at lower frequencies, and dynamic inflow causes greater overshoot due to the higher frequency of pitching in $\Delta p_2(t)$ at

lower deflections.

The experimental results demonstrate a significant increase in loading due to the power tracking operation. However, the scenarios considered represent artificial signals designed to investigate the possible dynamics that can be followed. Although the scaled power gradients encountered by MoWiTO represent relevant time scales for supporting frequency stabilization, the continuous variation enforced by the sinusoidal tracking signals is an extreme operation. In reality, power demand changes at such rates and magnitudes are likely to be assigned at singular events and a limited time following e.g., a significant loss of power generation in the electrical grid. The capability to track a power demand even at low rates provides predictability of wind power for the electrical grid's planning and operation.

4.6.4   Applicability and design process

Although the discussed sources of uncertainty are not explicitly considered in the design, the experimental results show that the proposed controller is sufficiently robust. After implementing a discretized version of the observer in (4.10) with a sampling time of 10 ms along with the feedback law in (4.6) in the real-time system, from the first to the last run, the control strategy was not adjusted. The closed-loop turbine showed stable operation in all inflow scenarios considered. The robustness to the modeling mismatch during the experiments is based on a proper definition of the closed-loop system dynamics for both the feedback and observer design. In preparation for the experiment, these dynamics were evaluated by simulations using the MoWiTO FAST model and used, subsequently, in the experiments without any further adjustments.

All discussed measurement results are based on the design specifications given in Section 4.3. In the measurement campaign, the same control approach was tested for different design specifications posed to exhibit a slower closed-loop behavior. This controller also performed stably in all considered operating conditions with slightly greater wind speed estimation errors due to the less aggressive dynamical behavior. This shows the flexibility of the LMI-based design to assign desired closed-loop dynamics.

In the controller and observer design process description, the connection of linear submodels and the influence on the proof of stability's conservativeness is discussed. Although we have thoroughly conducted and used the presented design process for experimental validation, the downstream stability considerations might exceed the reasonable effort necessary for efficient engineering processes from an industrial perspective. This especially holds for multiple-input, multiple-output control design tasks that include several load mitigating feedback loops [11], where the complexity for the LMI

solver due to the increased dimension rises. The evaluated stability guarantees, as usually, hold for the effects covered in the model only, for example, it is assumed that the wind dynamics follow the imposed first-order transfer function while in reality, turbulence shows non-Gaussian statistical properties across several time scales [55]. As a pragmatic approach for the complex wind turbine control design, based on simulation studies, it was found that a connection of adjacent linear submodels in N common Lyapunov functions, one for each linear submodel with respect to its adjacent submodels, allows for an effective control design for the multivariate dynamics. Although this formally does *not* provide global stability guarantees comparable to conventional gain-scheduled PI control approaches, the resulting control design is highly efficient in posing well-defined closed-loop responses in a wide operating range and adaption to different turbine models at a low computational effort.

4.7 Conclusion

The wind tunnel measurement results show the capability of the observer-based control approach to enforce an appropriate wind turbine behavior for a large operational range. The proposed framework comprises power optimization using the generator torque in partial-load operation and limitation of the power output to its rated value in the full load region by pitching the blades. This actuator change is inherited in the control design model. Further, the scalability of the approach allows for a convenient introduction of an enlarged operating region compared to the nominal power trajectory to provide a variable power output vital for supporting electrical grid stabilization. The measurement data show that the power output can be adjusted at a fast scale using an appropriate control algorithm, but also indicates the additional loading resulting from this functionality.

In deriving the control algorithm, proof of stability for TS systems is used, incorporating unknown wind speed estimation as an unmeasurable premise variable. We discussed how an assumption of the maximum estimation error reduces the conservativeness of the LMI constraints. This results in a feasible solution, which is evaluated in the wind tunnel campaign. Despite short violations of this assumption at highly dynamic inflow changes, the measurement data provide confidence in applying the observer to adjust the feedforward term and feedback gains based on the estimated wind speed.

The turbine exhibited a stable operating behavior in all considered scenarios evaluated in the wind tunnel campaign, including wind ramps, operating gusts, and turbulent inflow, while smoothly following the power demand. This shows the usefulness of the proposed approach in enforcing a desired dynamic behavior by appropriate LMI constraints in the control and observer design. The robustness of the model-based strategy to uncertainties and unmodeled dynamics is demonstrated in the experimental setup, and therefore, it builds confidence in applying model-based approaches for current and

future challenges arising in the control of wind turbines.

References

[1] G Sieros, P Chaviaropoulos, J D Sørensen, B H Bulder, and P Jamieson. Upscaling wind turbines: theoretical and practical aspects and their impact on the cost of energy. *Wind Energy*, 2012. DOI: 10.1002/we.527.

[2] K Z Østergaard, J Stoustrup, and P Brath. Linear parameter varying control of wind turbines covering both partial load and full load conditions. *Int. J. Robust and Nonlinear Control*, 2009. DOI: 10.1002/rnc.1340.

[3] L C Henriksen, M H Hansen, and N K Poulsen. Wind turbine control with constraint handling: a model predictive control approach. *IET Control Theory & Applications*, 2012. DOI: 10.1049/iet-cta.2011.0488.

[4] D Schlipf, D J Schlipf, and M Kühn. Nonlinear model predictive control of wind turbines using LIDAR. *Wind Energy*, 2013. DOI: 10.1002/we.1533.

[5] A Koerber and R King. Combined feedback–feedforward control of wind turbines using state-constrained model predictive control. *IEEE Transactions on Control Systems Technology*, 2013. DOI: 10.1109/TCST.2013.2260749.

[6] S Schuler, D Schlipf, P W Cheng, and F Allgöwer. ℓ_1-Optimal Control of Large Wind Turbines. *IEEE Transactions on Control Systems Technology*, 2013. DOI: 10.1109/TCST.2013.2261068.

[7] H Camblong, I Vechiu, A Etxeberria, and M I Martínez. Wind turbine mechanical stresses reduction and contribution to frequency regulation. *Control Engineering Practice*, 2014. DOI: 10.1016/j.conengprac.2014.03.007.

[8] K Selvam, S Kanev, J W van Wingerden, T van Engelen, and M Verhaegen. Feedback–feedforward individual pitch control for wind turbine load reduction. *International Journal of Robust and Nonlinear Control*, 2009. DOI: 10.1002/rnc.1324.

[9] F A Inthamoussou, H De Battista, and R J Mantz. LPV-based active power control of wind turbines covering the complete wind speed range. *Renewable Energy*, 2016. DOI: 10.1016/j.renene.2016.07.064.

[10] B Ibáñez, F A Inthamoussou, and H De Battista. Wind turbine load analysis of a full range LPV controller. *Renewable Energy*, 2020. DOI: 10.1016/j.renene.2019.08.016.

[11] F Pöschke, E Gauterin, M Kühn, J Fortmann, and H Schulte. Load mitigation and power tracking capability for wind turbines using linear matrix inequality-based control design. *Wind Energy*, 2020. DOI: 10.1002/we.2516.

[12] G J van der Veen, J W van Wingerden, P A Fleming, A K Scholbrock, and M Verhaegen. Global data-driven modeling of wind turbines in the presence of turbulence. *Control Engineering Practice*, 2013. DOI: 10.1016/j.conengprac.2012.12.008.

[13] N W Verwaal, G J van der Veen, and J W van Wingerden. Predictive control of an experimental wind turbine using preview wind speed measurements. *Wind Energy*, 2015. DOI: 10.1002/we.1702.

[14] S T Navalkar, E van Solingen, and J W van Wingerden. Wind tunnel testing of subspace predictive repetitive control for variable pitch wind turbines. *IEEE Transactions on Control Systems Technology*, 2015. DOI: 10.1109/TCST.2015.2399452.

[15] J Frederik, L Kröger, G Gülker, and J W van Wingerden. Data-driven repetitive control: Wind tunnel experiments under turbulent conditions. *Control Engineering Practice*, 2018. DOI: 10.1016/j.conengprac.2018.08.011.

[16] J Van de Vyver, J D M De Kooning, B Meersman, L Vandevelde, and T L Vandoorn. Droop Control as an Alternative Inertial Response Strategy for the Synthetic Inertia on Wind Turbines. *IEEE Transactions on Power Systems*, 2016. DOI: 10.1109/TPWRS.2015.2417758.

[17] M Shan, W Shan, F Welck, and D Duckwitz. Design and laboratory test of black-start control mode for wind turbines. *Wind Energy*, 2020. DOI: 10.1002/we.2457.

[18] V Spudić, M Jelavić, and M Baotić. Supervisory controller for reduction of wind turbine loads in curtailed operation. *Control Engineering Practice*, 2015. DOI: 10.1016/j.conengprac.2014.11.005.

[19] V Petrović and C L Bottasso. Wind turbine envelope protection control over the full wind speed range. *Renewable Energy*, 2017. DOI: 10.1016/j.renene.2017.04.021.

[20] J Kazda, K Merz, J O Tande, and N A Cutululis. Mitigating turbine mechanical loads using engineering model predictive wind farm controller. *Journal of Physics: Conference Series*, 2018. DOI: 10.1088/1742-6596/1104/1/012036.

[21] M Vali, V Petrović, G Steinfeld, L Y Pao, and M Kühn. An active power control approach for wake-induced load alleviation in a fully developed wind farm boundary layer. *Wind Energy Science*, 2019. DOI: 10.5194/wes-4-139-2019.

[22] W Munters and J Meyers. Towards practical dynamic induction control of wind farms: analysis of optimally controlled wind-farm boundary layers and sinusoidal induction control of first-row turbines. *Wind Energy Science*, 2018. DOI: 10.5194/wes-3-409-2018.

[23] C Galinos, A M Urbán, and W H Lio. Optimised de-rated wind turbine response and loading through extended controller gain-scheduling. *Journal of Physics: Conference Series*, 2019. DOI: 10.1088/1742-6596/1222/1/012020.

[24] P A Fleming, J Aho, A Buckspan, E Ela, Y Zhang, V Gevorgian, A Scholbrock, L Y Pao, and R Damiani. Effects of power reserve control on wind turbine structural loading. *Wind Energy*, 2016. DOI: 10.1002/we.1844.

[25] D Song, J Yang, M Su, A Liu, Z Cai, Y Liu, and Y H Joo. A novel wind speed estimator-integrated pitch control method for wind turbines with global-power regulation. *Energy*, 2017. DOI: 10.1016/j.energy.2017.07.033.

[26] K Kim, H-G Kim, I Paek C-J Kim, C L Botasso, and F Campagnolo. Design and validation of demanded power point tracking control algorithm of wind turbine. *Int. J. of Precis. Eng. and Manuf.-Green Tech.*, 2018. DOI: 10.1007/s40684-018-0041-6.

[27] K Z Østergaard, P Brath, and J Stoustrup. Estimation of effective wind speed. *Journal of Physics: Conference Series*, 2007. DOI: 10.1088/1742-6596/75/1/012082.

[28] M N Soltani, T Knudsen, M Svenstrup, R Wisniewski, P Brath, R Ortega, and K Johnson. Estimation of rotor effective wind speed: a comparison. *IEEE Transactions on Control Systems Technology*, 2013. DOI: 10.1109/TCST.2013.2260751.

[29] D Jena and S Rajendran. A review of estimation of effective wind speed based control of wind turbines. *Renewable and Sustainable Energy Reviews*, 2015. DOI: 10.1016/j.rser.2014.11.088.

[30] E Gauterin, P Kammerer, M Kühn, and H Schulte. Effective wind speed estimation: Comparison between Kalman Filter and Takagi–Sugeno observer techniques. *ISA Transactions*, 2016. DOI: 10.1016/j.isatra.2015.11.016.

[31] S Georg, M Müller, and H Schulte. Wind turbine model and observer in Takagi-Sugeno model structure. *Journal of Physics: Conference Series*, 2014. DOI: 10.1088/1742-6596/555/1/012042.

[32] X-J Ma, Z-QSun, and Y-Y He. Analysis and design of fuzzy controller and fuzzy observer. *IEEE Transactions on Fuzzy Systems*, 1998. DOI: 10.1109/91.660807.

[33] R Ungurán, V Petrović, S Boersma, J van Wingerden, L Y Pao, and M Kühn. Feedback-feedforward individual pitch control design for wind turbines with uncertain measurements. In *2019 American Control Conference (ACC)*, 2019. DOI: 10.23919/ACC.2019.8814757.

[34] T M Guerra, A Kruszewski, L Vermeiren, and H Tirmant. Conditions of output stabilization for nonlinear models in the takagi–sugeno's form. *Fuzzy Sets and Systems*, 2006. DOI: 10.1016/j.fss.2005.12.006.

[35] C Tseng. A novel approach to H_∞ decentralized fuzzy-observer-based fuzzy control design for nonlinear interconnected systems. *IEEE Transactions on Fuzzy Systems*, 2008. DOI: 10.1109/T-FUZZ.2008.924355.

[36] H K Lam, H Li, and H Liu. Stability analysis and control synthesis for fuzzy-observer-based controller of nonlinear systems: a fuzzy-model-based control approach. *IET Control Theory & Applications*, 2013. DOI: 10.1049/iet-cta.2012.0465.

[37] K Tanaka, T Ikeda, and H O Wang. Fuzzy regulators and fuzzy observers: relaxed stability conditions and LMI-based designs. *IEEE Transactions on Fuzzy Systems*, 1998. DOI: 10.1109/91.669023.

[38] J M Jonkman, S Butterfield, W Musial, and G Scott. Definition of a 5-MW reference wind turbine for offshore system development. Technical report, National Renewable Energy Laboratory, 2009.

[39] F Berger, L Kröger, D Onnen, V Petrović, and M Kühn. Scaled wind turbine setup in a turbulent wind tunnel. *Journal of Physics: Conference Series*, 2018. DOI: 10.1088/1742-6596/1104/1/012026.

[40] V Petrović, F Berger, L Neuhaus, M Hölling, and M Kühn. Wind tunnel setup for experimental validation of wind turbine control concepts under tailor-made reproducible wind conditions. *Journal of Physics: Conference Series*, 2019. DOI: 10.1088/1742-6596/1222/1/012013.

[41] J M Jonkman and M L Buhl Jr. FAST Users Guide. Technical report, National Renewable Energy Laboratory, 2005.

[42] K Tanaka and H O Wang. *Fuzzy Control Systems Design and Analysis: A Linear Matrix Inequality Approach*. John Wiley & Sons, Inc., 2001.

[43] Z Lendek, T M Guerra, R Babuska, and B De Schutter. *Stability Analysis and Nonlinear Observer Design Using Takagi-Sugeno Fuzzy Models*. Springer-Verlag Berlin Heidelberg, 2010.

[44] M Chilali and P Gahinet. H_∞ design with pole placement constraints: an LMI approach. *IEEE Transactions on Automatic Control*, 1996. DOI: 10.1109/9.486637.

[45] L Kröger, L Neuhaus., J Peinke, G Gülker, and M Hölling. Turbulence generation by active grids. In *Progress in Turbulence VIII*, 2019. DOI: 10.1007/978-3-030-22196-6_30.

[46] L Kröger, J Frederik, J W van Wingerden, J Peinke, and M Hölling. Generation of user defined turbulent inflow conditions by an active grid for validation experiments. *Journal of Physics: Conference Series*, 2018. DOI: 10.1088/1742-6596/1037/5/052002.

[47] H Makita. Realization of a large-scale turbulence field in a small wind tunnel. *Fluid Dynamics Research*, 1991. DOI: 10.1016/0169-5983(91)90030-M.

[48] P Knebel, A Kittel, and J Peinke. Atmospheric wind field conditions generated by active grids. *Experiments in Fluids*, 2011. DOI: 10.1007/s00348-011-1056-8.

[49] L Neuhaus, F Berger, J Peinke, and M Hölling. Exploring the capabilities of active grids. *Experiments in Fluids*, 2021. DOI: 10.1007/s00348-021-03224-5.

[50] E A Bossanyi, P A.Fleming, and A D Wright. Validation of individual pitch control by field tests on two- and three-bladed wind turbines. *IEEE Transactions on Control Systems Technology*, 2013. DOI: 10.1109/TCST.2013.2258345.

[51] T A Johansen, R Shorten, and R Murray-Smith. On the interpretation and identification of dynamic Takagi-Sugeno fuzzy models. *IEEE Transactions on Fuzzy Systems*, 2000. DOI: 10.1109/91.855918.

[52] F Berger, D Onnen, G Schepers, and M Kühn. Experimental analysis of radially resolved dynamic inflow effects due to pitch steps. *Wind Energy Science*, 2021. DOI: 10.5194/wes-6-1341-2021.

[53] J Machowski, J Bialek, and J Bumby. *Power System Dynamics: Stability and Control*. John Wiley & Sons, Ltd, 2008.

[54] E A Bossanyi. Wind turbine control for load reduction. *Wind Energy*, 2003. DOI: 10.1002/we.95.

[55] M Wächter, H Heißelmann, M Hölling, A Morales, P Milan, T Mücke, J Peinke, Reinke, and P Rinn. The turbulent nature of the atmospheric boundary layer and its impact on the wind energy conversion process. *Journal of Turbulence*, 2012. DOI: 10.1080/14685248.2012.696118.

5 | Model-based nonlinear filter design for tower load reduction of wind power plants with active power control capability

Abstract

In the light of an increasing share in the electrical grid, wind turbines must be enabled to provide grid stabilizing behavior. This can be achieved by a variation of the turbine's power output depending on the current state of the electrical grid. However, changes of power output excite oscillations in the turbine structure. To reduce the loading caused by the considered frequency droop scheme, in this paper a nonlinear model-based filter design in a Takagi-Sugeno structure is proposed. The design uses Lyapunov function-based linear matrix inequalities for deriving the necessary feedback gains of the filter. The results are obtained for NREL's 5 MW reference turbine. By connecting FAST to an analytic power system model, we study the effects on turbine loading as a result of frequency stabilization in case of a load imbalance. The proposed filter is designed and implemented to reduce the damage equivalent load of the tower fore-aft motion, and its influence on the frequency trajectory is studied.

5.1 Introduction

The increasing share in the energy generation mix necessitates the provision of ancillary services such as active power control (APC) for grid stabilization from wind turbines[1]. An imbalance of load and generation in the electrical grid results in a frequency deviation, which needs to be coped by appropriate control mechanisms to ensure a stable operation of the electrical power system. While these services are typically designed to act at different timescale, these functionalities involve a variation of the turbine's power output depending on the current state of the electrical grid. Several works have discussed turbines capability to provide APC, e.g., [1, 2, 3, 4, 5, 6], and provide promising results with regard to the replacement of conventional power plants in the electrical grid. In [1, 3, 4] the authors discuss the possibility to provide frequency control by equipping the wind turbine with a droop control scheme. By adjusting the power output of the turbine based on the current deviation of the grid frequency, the capability of wind turbines to provide frequency stabilization is shown. Despite being valuable contributions for the power system perspective, the wind turbine's mechanical components and the corresponding control interaction is usually portrayed as simple models involving stationary power curves [1, 2, 3, 4, 5]. Thus, consequences for the loading of the turbine are usually neglected, but are known to be vital for the turbine's lifetime [7], especially if power variation is conducted [6, 8].

A variation of the turbine's power output necessarily excites oscillations in the turbine structure. Especially, the strong coupling of the tower fore-aft motion to actuation by pitch [7] represents a cause of additional fatigue loading through frequency stabilizing behavior[8]. To reduce the loading caused by power output feedback to frequency variations, in this contribution a nonlinear model-based filter design in a Takagi-Sugeno structure is discussed. The design uses Lyapunov functions based on linear matrix inequalities for deriving the necessary feedback gains of the nonlinear filter. For this purpose, the filter design is reformulated as feedback control design with respect to a tower model. The deployed linear matrix inequalities enforce a desired damping on the tower motion by design, such that load reduction in operation can be achieved.

The results are obtained for NREL's 5 MW reference turbine [9]. By connecting FAST [10] to an analytic power system model, we study the effects of turbine loading as a result from frequency stabilization in case of a load imbalance. The proposed nonlinear filter is employed to reduce the damage equivalent load of the tower fore-aft motion. Further, the influence of filter on the frequency trajectory is studied.

5.2 Modeling

5.2.1 Takagi-Sugeno model framework

Throughout this work, the nonlinear state-space model of the plant, as well as the filter model, are formulated in terms of the Takagi-Sugeno (TS) model structure. TS models provide a useful and uniform framework for nonlinear controller, observer and filter design. Originally introduced in the context of fuzzy systems [11], TS models are weighted combinations of linear submodels and can either be derived from input-output data using system identification techniques [11, 12] or from mathematical models of nonlinear systems. Methods based on linear matrix inequalities (LMIs) stability constraints allow for controller and observer design for TS models [13, 14]. The general TS structure of a state-space model is of the form

$$\dot{x} = \sum_{i=1}^{N_r} h_i(z)\,(A_i\,x + B_i\,u)\ , y = \sum_{i=1}^{N_r} h_i(z)\,C_i\,x \tag{5.1}$$

with N linear submodels. Matrices A_i, B_i and C_i of the i-th sub-model have constant coefficients. The vector z of premise variables may comprise states, inputs, and external variables. The functions h_i are the membership functions and fulfill the two conditions [15]

$$\sum_{i=1}^{N} h_i(z) = 1\ , \tag{5.2}$$

$$0 \leq h_i(z) \leq 1\ (i \in \{1,\dots,N\})\ , \tag{5.3}$$

where (5.2) is the convex sum condition.

In order to obtain the TS structure of a nonlinear model, and provided that a mathematical model is given, there are essentially two ways to derive the linear TS submodels. The first method is local Taylor linearization of the nonlinear model around N stationary points and subsequent fuzzy-blending of the linear submodels to a weighted sum according to (5.1). Different types of membership functions can be defined, including e.g., triangular, trapezoidal, sigmoid, or Gaussian functions [15]. The second method is the so-called sector nonlinearity approach [16] (and references therein), [17], which yields an exact representation of the nonlinear model.

In this paper we use the first method, whereby the nonlinear model is not explicitly analytically available and therefore the linear models are numerically extracted from the FAST model [10] of the wind

turbine.

5.2.2 Tower model

The basis for modeling of the wind turbine tower dynamics in fore-aft direction x_T is provided by N second-order linearized models of the nonlinear system dynamics $\dot{x}_T = f(x_T, \beta, v, \Delta p)$ in the operating points $|_{c_i} := |_{\chi_{T0i}, \beta_{0i}, v_{0i}, \Delta p_{0i}}$. In a TS description, the dynamics with respect to the pitch angle β, effective wind speed v and power tracking signal Δp is denoted as

$$
\dot{\chi}_T = \sum_{i=1}^{N} h_i(z) \Big(\underbrace{\begin{bmatrix} 0 & 1 \\ \frac{\partial f(x_T, \beta, v, \Delta p)}{\partial x_T}|_{c_i} & \frac{\partial f(x_T, \beta, v, \Delta p)}{\partial \dot{x}_T}|_{c_i} \end{bmatrix}}_{A_{Ti}}
$$
$$
\cdot (x_T - \chi_{T0i}) + \underbrace{\begin{bmatrix} 0 \\ \frac{\partial f(x_T, \beta, v, \Delta p)}{\partial \beta}|_{c_i} \end{bmatrix}}_{B_{Ti}} \cdot (\beta - \beta_{0i}) \Big)
$$

(5.4)

where the partial derivatives that specify the dynamics in the i-th operating point are gained by FAST's linearization capability [10].

The system description comprises two premise variables that govern the adjustment to varying dynamics in operation, i.e., $z = [v \ \Delta p]^{\mathrm{T}}$. The premise variables span a two dimensional plane, where the investigated number of the operating point on the v-axis and Δp-axis are denoted as i_v and $i_{\Delta p}$ with their maximum number as $i_{v\max} = 54$ and $i_{\Delta p\max} = 15$, respectively. An overview of the considered operating range by a choice of linearization points, and the corresponding pitch angles inducing stationary behavior is given in Fig. 5.1.

To portray the dependence of the tower motion on a varying power demand Δp that results in a variation of the pitch, the model input is reformulated using κ_i, which is depicted in Fig. 5.2, as

$$
\beta - \beta_{0i} = \kappa_i \Delta p \quad ,
$$

(5.5)

where the power tracking signal Δp forms the new input to the system description. The operating point dependent gain κ_i is calculated as the mean of the gradients $m_{i_v, i_{\Delta p}}$ depicted in Fig. 5.2 from power to pitch

$$
\kappa_i = \begin{cases} m_{i_v, 1} & \text{if } i_{\Delta p} = 1 \\ m_{i_v, i_{\Delta p\max}-1} & \text{if } i_{\Delta p} = i_{\Delta p\max} \\ (m_{i_v, i_{\Delta p}-1} + m_{i_v, i_{\Delta p}})/2 & \text{else} \end{cases}
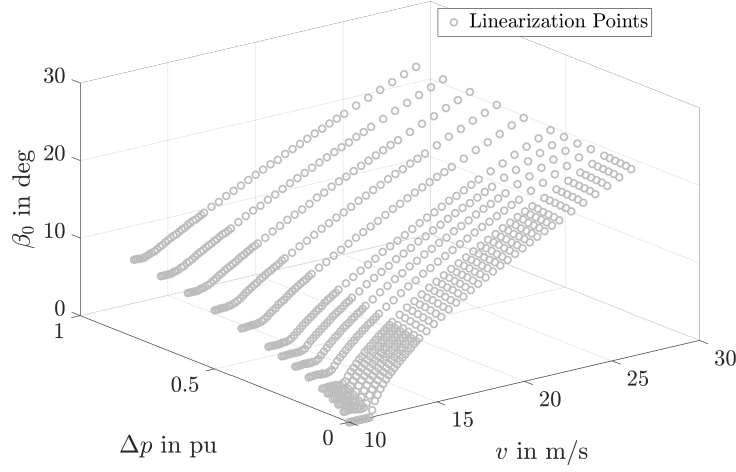$$

(5.6)

Figure 5.1: Linearization points of the wind turbine depending on the wind speed v and power tracking signal Δp. The pitch input values that induce stationary behavior at the given operating points are denoted as β_0.

with $i = (1 - i_v)i_{\Delta p\mathrm{max}} + i_{\Delta p}$. As a result, we derive a tower model with the tracking signal Δp as input in form

$$\dot{x}_T = \sum_{i=1}^{N_r} h_i(z)\big(A_{Ti}(x_T - \chi_{T0i}) + B_{Ti}\kappa_i\Delta p\big) \quad . \tag{5.7}$$

5.2.3 Grid model

The power system's frequency is modeled by a dynamic power balance, see e.g., [18, 2, 3, 4, 6], where a deviation from the electrical synchronous frequency $\Delta\omega = \omega - \omega_s$ can be characterized by the sum of the turbine infeed p_{WT}, power system load p_{L} and power in the grid p_{G}

$$J\frac{\mathrm{d}\Delta\omega}{\mathrm{d}t} = p_{\mathrm{G}} + p_{\mathrm{WT}} - p_{\mathrm{L}} \quad . \tag{5.8}$$

In that form, the evolution of the grid frequency ω is specified in a normalized description in terms of the inertia $J = \bar{J}\omega$ close to the nominal frequency. In accordance with the study in [1], even though we employ simplified dynamics, the excitement of the electrical frequency is initiated by a $\Delta p_{\mathrm{L}} = -10\,\%$ (0.1 pu) load step at a base load of $p_{\mathrm{L}} = 99.5\%$. Before the load step, a wind park, represented by one turbine in FAST [10], provides $p_{\mathrm{WT}} = 15\,\%$, while the grid is assumed to provide $p_{\mathrm{G}} = 85\,\%$. The inertia that characterizes the dynamical response of the frequency is chosen to yield a similar dynamical response compared to the initial slope of the frequency in [1] and is found as $J = 10\,\mathrm{s}$.
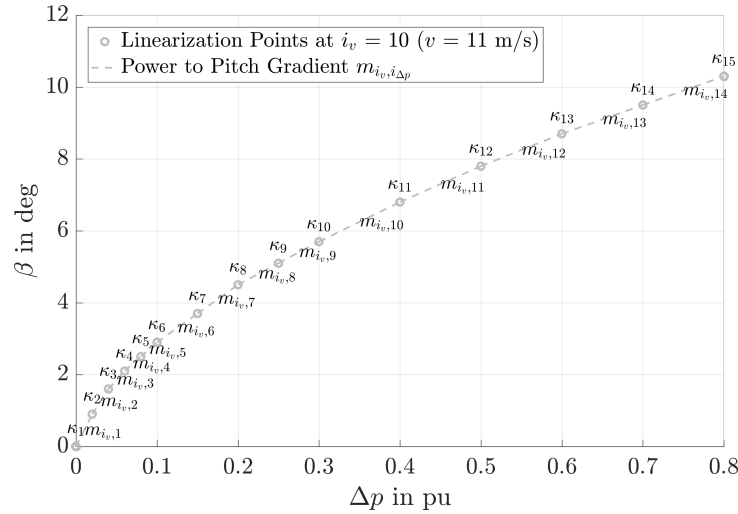
Figure 5.2: Linearization points of the wind turbine at a wind speed of 11 m/s. The gain κ_i, which connects a power output variation to a variation in the pitch angle at each operating point, is calculated from the adjacent gradients m_{i-1}, m_i using the stationary pitch angles of the linearization points.
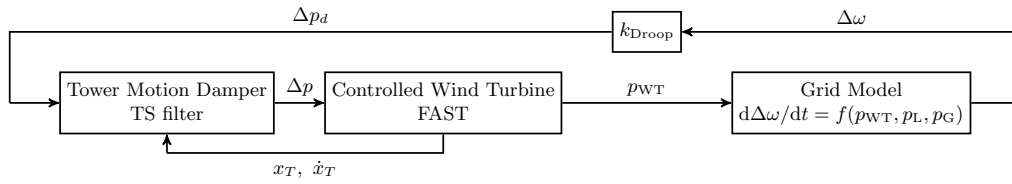

Figure 5.3: Overview of the implemented functionality. APC is provided by the wind turbine according to droop k_{Droop} depending on the current frequency deviation of the grid model.

While in this simplified description of the power system the grid is assumed to provide no stabilizing frequency feedback, i.e., $p_{\mathrm{G}} = \mathrm{const.}$, the wind turbine is equipped with an APC droop control scheme according to the current frequency deviation. This approach emulates an inertial response [3], and thus supports the stabilization of the power grid in case of a frequency event. Depending on the current frequency deviation, the turbine is therefore demanded to vary the current power output by $\Delta p = k_{\mathrm{Droop}} \Delta \omega$, where the proportional gain is defined as $k_{\mathrm{Droop}} = 50$. This corresponds to a power variation of 10% for a frequency deviation of 0.2%, or 0.1 Hz in a 50 Hz-based electrical system. The employed controller for an adjustment of the wind turbine operating point according to Δp varies the generator torque to match the demanded power output, and uses the pitch for balancing of a constant rotational speed in full load region as described in [8]. In that way, the power output can be adjusted to provide APC to the electrical grid. As the filter design is formulated in terms of state feedback, estimated states obtained by a tower observer are used in the scheme. For that purpose, the estimated tower top displacement x_T and speed $\dot{x}_T$ are used in calculation of the filter. An overview of the implemented functionality is given in Fig. 5.3.

5.3 Filter design

The proposed dynamical filter of order n_f is defined as

$$\dot{\chi}_f = \sum_{i=1}^{N_r} h_i(z) \underbrace{\begin{bmatrix} 0_{n_f \times 1} & I_{n_f-1} \\ & 0_{1 \times n_f-1} \end{bmatrix}}_{A_{fi}} \chi_f + \underbrace{\begin{bmatrix} 1 \\ \vdots \\ 1 \end{bmatrix}}_{B_{fi}} u \quad , \tag{5.9}$$

where u is an artificial input, which is subsequently used to shape the dynamical response. The filter employs an integrator chain from the last to the first state of the filter, which is defined as the power tracking signal send to the wind turbine controller, i.e., $\Delta p = x_{f1}$. This allows us to derive a description integrating the nonlinear tower dynamics and filter using (5.7) and (5.9) to form

$$\dot{\chi} = \sum_{i=1}^{N_r} h_i(z) \Big(\underbrace{\begin{bmatrix} A_{Ti} & B_{Ti}\kappa_i & 0_{n \times n_f-1} \\ 0_{n_f \times n} & A_{fi} \end{bmatrix}}_{A_i} (\chi - x_{0i}) + \underbrace{\begin{bmatrix} 0_{n \times 1} \\ B_{fi} \end{bmatrix}}_{B_i} u \Big) \quad . \tag{5.10}$$

The operating trajectory χ_{0i} of $x = [x_T^{\mathrm{T}} \ x_f^{\mathrm{T}}]^{\mathrm{T}}$ is defined by the stationary operating values of the tower derived in the linearization analysis, and the desired filter state. It is adjusted to provide a desired power tracking signal from the APC scheme Δp_d, i.e., $\chi_{0i} = [x_{T0i}^{\mathrm{T}} \ [\Delta p_d \ 0_{n_f-1 \times 1}]^{\mathrm{T}}]$.

System description (5.10) allows us to formulate the filter design as state feedback controller design employing the input u. For that purpose, a system feedback following the parallel distributed compensation control law[17] is defined

$$u = - \sum_{j=1}^{N_r} h_j(z) K_j (\chi - \chi_{0i}) \quad . \tag{5.11}$$

Inserting (5.11) into (5.10) gives us the closed-loop description of the combined tower and filter dynamics

$$\dot{x} = \sum_{i=1}^{N_r} h_i(z) \sum_{j=1}^{N_r} h_j(z) \big((A_i - B_i K_j)(\chi - \chi_{0i}) \big) \tag{5.12}$$

under impact of the feedback gains K_j to be synthesized. From a quadratic Lyapunov function candidate $V(x) = \chi^{\mathrm{T}} X^{-1} \chi$ with $X = X^{\mathrm{T}} \succ 0$ and the corresponding stability condition

$$\dot{V}(x) = \dot{\chi}^{\mathrm{T}} X^{-1} \chi + \chi^{\mathrm{T}} X^{-1} \dot{\chi} \prec 0$$

the following LMI stability constraints can be derived [17]

$$XA_i^{\mathrm{T}} + A_iX - M_j^{\mathrm{T}}B_i^{\mathrm{T}} - B_iM_j \prec 0 \quad , \tag{5.13}$$

where X and M_j are variables to be found. If a solution is obtained by one of various available LMI solvers [19], the necessary feedback gains are calculated from $K_j = M_jX^{-1}$ and stability is verified. Additional LMIs can be used to enforce a desired dynamical response of the closed-loop system. For that purpose, the maximum decay rate of the system can be restricted to α_{max} by

$$XA_i^{\mathrm{T}} + A_iX - M_j^{\mathrm{T}}B_i^{\mathrm{T}} - B_iM_j \succ -2\alpha_{\mathrm{max}}X \quad , \tag{5.14}$$

which is conducted to ensure a proper operation within the numerical environment that the filter is applied. Further, a desired damping on the closed-loop system in operation actively provided by the controller can be formulated in terms of LMIs as [20]

$$\begin{bmatrix} \sin\theta(\Gamma_1) & \cos\theta(\Gamma_2) \\ \cos\theta(\Gamma_2^{\mathrm{T}}) & \sin\theta(\Gamma_1) \end{bmatrix} \prec 0 \tag{5.15}$$

with

$$\Gamma_1 = \left(A_iX - B_iM_j + XA_i^{\mathrm{T}} - M_j^{\mathrm{T}}B_i^{\mathrm{T}}\right)$$
$$\Gamma_2 = \left(A_iX - B_iM_j - XA_i^{\mathrm{T}} + M_j^{\mathrm{T}}B_i^{\mathrm{T}}\right) \quad .$$

The desired damping D is formulated in terms of the angle Θ, that can be calculated according to $\Theta = \arccos(D)$ [20]. It is used to provide damping to the tower dynamics by purposefully shaping the combined tower and filter dynamics through the feedback.

The filter design parameters used for the system (5.12) are a desired damping of at least $D = 12\%$, a maximum decay rate of $\alpha_{\mathrm{max}} = 100$ for the LMIs (5.13), (5.14) and (5.15). The filter is designed of second order, i.e., $n_f = 2$. The LMI solver yields N feedback gains K_j along with the characterization of the Lyapunov function

$$X = \begin{bmatrix} 1.8675 & -0.602 & -0.3815 & -1.1197 \\ -0.602 & 7.7337 & 6.4277 & 5.0647 \\ -0.3815 & 6.4277 & 8.8484 & 3.2063 \\ -1.1197 & 5.0647 & 3.2063 & 14.9906 \end{bmatrix} \succ 0 \quad .$$
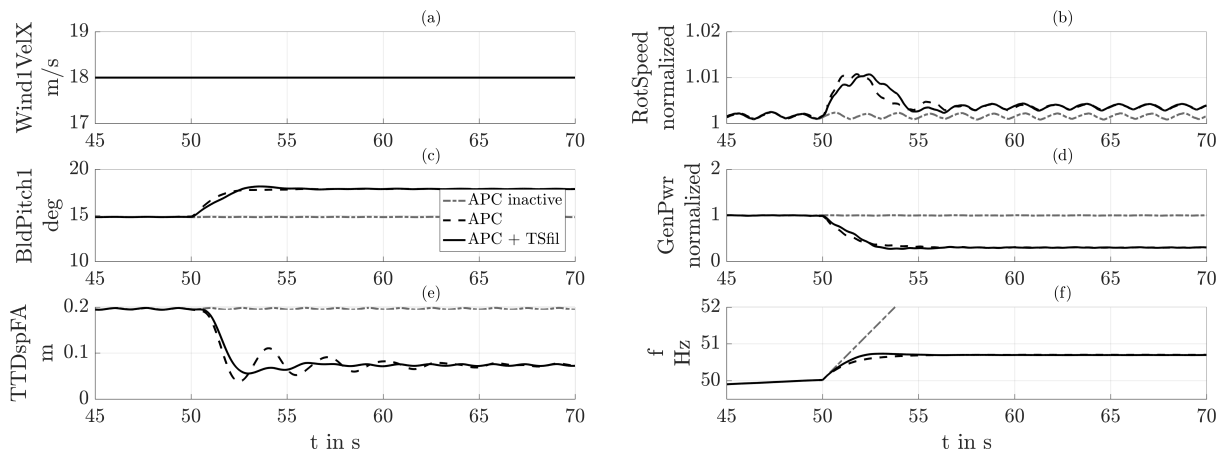
Figure 5.4: Response to a power system load imbalance at t = 50 s and constant wind excitement at 18 m/s. Subplots: (a) downwind hub-height wind speed (b) normalized rotational speed (c) blade 1 pitch angle (d) normalized power output (e) tower-top fore-aft deflection (f) frequency of the grid model

5.4 Results

5.4.1 Constant inflow

Fig. 5.4 depicts the system response to a load imbalance in the electrical grid at a constant wind of 18 m/s. Due to a lack of stabilizing mechanisms without APC, i.e., continuing nominal power production of the wind turbine, the frequency grows continuously at a slope defined by the inertia J in (5.8). The application of APC by the wind turbine is capable of arresting the frequency at 50.7 Hz with the employed slope k_{Droop}. The involved reduction to 30% of the power production can be observed in Fig. 5.4 (d). As one turbine is modeled to provide $p_{\text{WT}} = 15\,\%$ before the load step, the stationary output after the disturbance in the electrical grid corresponds to a total power of $p_{\text{WT}} = 4.5\,\%$. In combination with the power provided by the electrical grid $p_{\text{G}} = 85\,\%$, this yields the demanded power of the load $p_{\text{L}} = 89.5\,\%$. While the APC scheme without applying the filter arrests the frequency at 50.69 Hz, the filtering and thus the differing evolution of the power tracking signal results in a frequency of 50.7 Hz.

Frequency stabilization, however, is conducted at the cost of exciting the structural dynamics of the turbine. As the motion of the tower top in fore-aft direction displays in Fig. 5.4 (e), without the proposed filter the tower top shows a lightly damped oscillation while converging to the altered operating point. The application of the proposed filter, on the other hand, results in an increase of damping, and consequently a smoother transition into the new operating point.

This simulation study in constant wind was repeated for inflow with 14 m/s, 16 m/s and 20 m/s. The
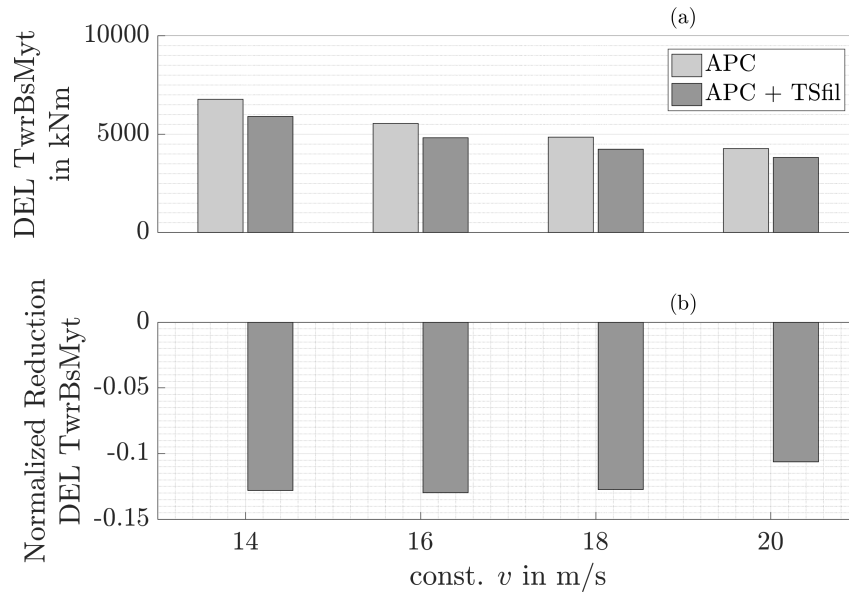
Figure 5.5: Comparison of the tower base fore-aft moment DELs at different constant wind speeds with a power system load imbalance as depicted in Fig. 5.4. Subplots: (a) DEL tower base fore-aft moment (b) reduction of DEL normalized to APC operation without applying filter.

resulting damage equivalent loads in the considered scenarios are depicted in Fig. 5.5. The load analysis reveals a significant decrease along the considered operating range in tower fore-aft loading through the implementation of the proposed filter. The reduction capabilities by applying the filter in constant wind speeds are in a range of 10.5% at 20 m/s and 13% at 16 m/s.

5.4.2   Turbulent inflow

By exciting the turbine with turbulent inflow in identical grid scenarios, the impact of grid stabilization and resulting loads in usual operating conditions of wind turbines can be studied. The varying wind speed, depicted in Fig. 5.6 (a), excites the structural dynamics of the turbine. In addition to a reaction on the frequency deviation, the tower top deflection in fore-aft direction in Fig.5.6 (e) is caused by an interference of the two effects. Despite an additional fluctuation due to the turbulent inflow and thus power production, the frequency evolution in combination with the power produced by the turbine after the load step in the grid is in line with the results obtained at constant wind speed.

In Fig. 5.7 the deviation of the power tracking signal due to the applied filter can be observed. As the evolution of the tower fore-aft motion is used in the filter (see Fig. 5.3), an actuation for providing tower damping is also observed before the load imbalance occurs at t=50 s. While the initial slope of the power tracking signal is very similar compared to applying the scheme without filtering, an excitation of the tower motion due to the variation of the operating point causes a deviation of the
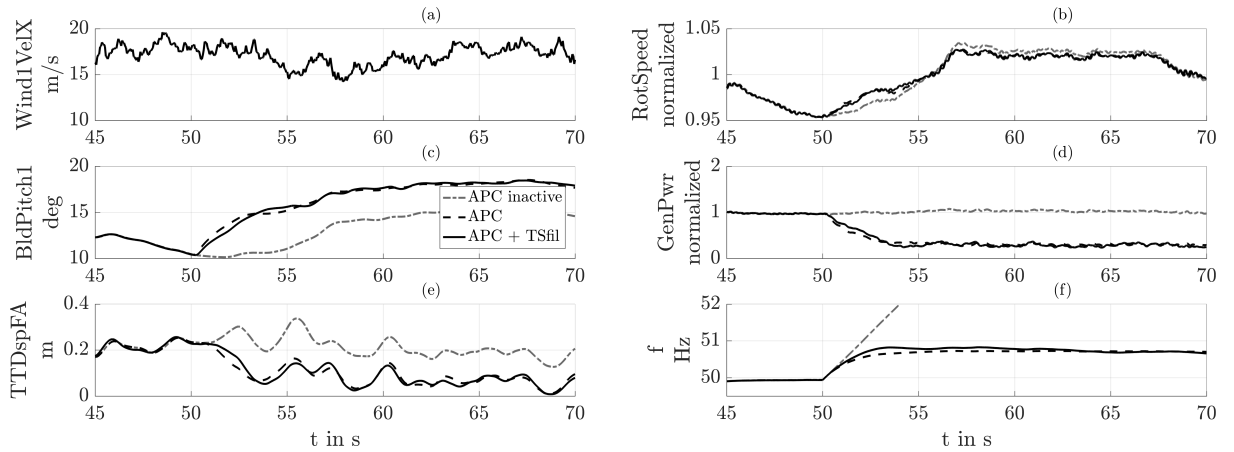
Figure 5.6: Response to a power system load imbalance at t = 50 s and turbulent wind with a mean of 18 m/s. Subplots: (a) downwind hub-height wind speed (b) normalized rotational speed (c) blade 1 pitch angle (d) normalized power output (e) tower-top fore-aft deflection (f) frequency of the grid model
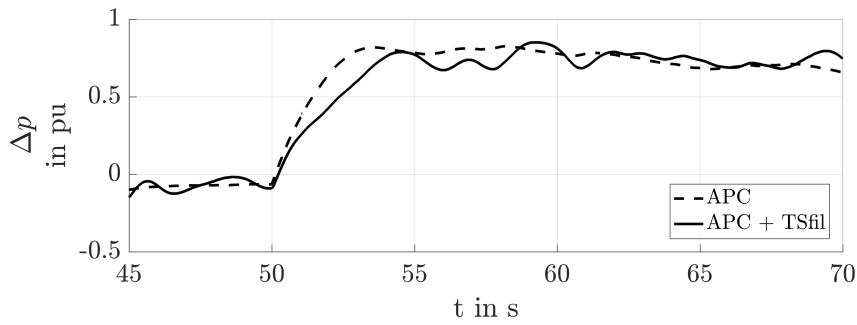

Figure 5.7: Comparison of the power tracking signal Δp processed by the controller with and without application of the filter.

two signals, which effectively results in a reduction of the loading experienced by the turbine tower.

To identify the additional loading through APC in turbulent wind conditions, the resulting damages are normalized to the loads *without* a variation of the power output due to a frequency deviation in Fig. 5.8 (b). An increase of up to 70% at a wind speed of 14 m/s can be observed. As previously reported for the scenarios in constant wind, the TS filter reduces the damage equivalent loads significantly, e.g., 40% reduction at 14 m/s compared to APC without filter. Especially where additional loading due to APC is most striking in lower wind speeds, the model-based filter is capable of mitigating the effects of frequency stabilization. This decreases for medium wind speeds where the additional loading due to APC is small, indicating the stochastic nature of the wind as main source of loading in this operational range. As stated for the state evolution in turbulent inflow, the damage results from an interaction of the grid, turbine and wind dynamics.
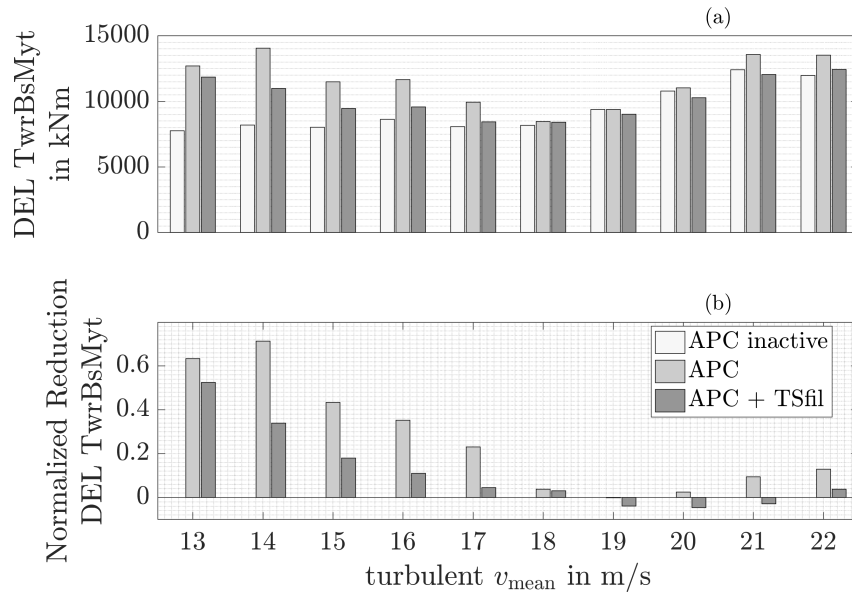
Figure 5.8: Comparison of the tower base fore-aft moment DELs at different turbulent wind speeds with a power system load imbalance, see Fig. 5.6.

5.5   Discussion

The presented results reveal the additional fatigue loading due to application of the droop control scheme in stabilization of the electrical frequency. Especially in lower wind speed, where the pitch magnitudes (see Fig. 5.1) and the distance traveled by the tower due to the changing operating points are greatest, this causes severe additional fatigue loading. It is, however, interesting to notice that ultimate loading of the tower was not negatively affected in the considered scenarios. Except for a slight increase of 1.7% at turbulent inflow with a mean of 21 m/s, ultimate tower loading in fore-aft direction was identified to decrease, ranging up to 24% at a mean turbulent wind of 18 m/s.

In case of constant wind, the damping characteristics of the designed filter shows similar fatigue load reduction along the considered operating range. In turbulent inflow conditions, however, the fatigue loading and the reduction yield are less distinct. As noticed, the loads are caused by an interference of the turbulent wind excitement and the power output demand of the APC scheme, where especially in medium wind the excitement from the wind overshadows the effects from frequency stabilization.

The proposed model-based concept integrates the varying dynamics in the filter design, and thus directly accounts for the characteristics of the considered system in the design step. While the focus in this contribution is on the tower oscillation in fore-aft direction, the basic filter design can be enhanced to include more dynamical effects of the wind turbine, e.g., drivetrain oscillation. By calculation of the membership functions in operation of the TS scheme, a natural approach for handling the varying sys-

tem dynamics is given and consequently, the need for separate scheduler design or tuning of operating point dependent filter loops is avoided.

By reformulation of the filter design as state feedback control scheme, commonly applied LMIs can be used in the filter design. The basic stability constraints restrict the filter dynamics to the left half of the complex plane. While this ensures stability, the range of accessible closed-loop dynamics is indefinite, leaving great design freedom to the LMI solver. For that reason, the application of LMIs that enforce a desired dynamical behavior of the closed-loop system is central to the proposed concept. Especially the LMIs imposing an active damping to the control scheme provide an effective constraint design possibility with regard to load reduction capabilities from the considered scheme.

5.6   Conclusion

In this contribution, the effects of grid stabilizing behavior are studied from a mechanical loading perspective of wind turbines. By equipping the turbine with a droop control scheme, the power output of the turbine is varied according to the current state of the electrical grid frequency. The results show that this feedback enables the turbine to arrest the frequency in a simple analytical grid model. While the output power variation excites the structural dynamics of the turbine, a model-based nonlinear filter in a TS structure is proposed to reduce the resulting loading.

For that purpose, a tower model is reformulated to include the variable power demand as an input to the system. Subsequently, the combined tower and filter dynamics are described, and a feedback control design employing LMIs is used as filter design procedure. This allows for the application of commonly used LMIs for feedback design to the filter design problem.

While the APC functionality increases the fatigue loading of the tower especially in fore-aft direction, the simulation results underline the capability of the proposed filter to reduce the damage by enforcing an active damping from processing the demanded power tracking signal in the filter before passing it to the wind turbine controller.

References

[1] J Morren, J Pierik, and S WH de Haan. Inertial response of variable speed wind turbines. *Electric Power Systems Research*, 2006. DOI: 10.1016/j.epsr.2005.12.002.

[2] P Keung, P Li, H Banakar, and B T Ooi. Kinetic energy of wind-turbine generators for system frequency support. *IEEE Transactions on Power Systems*, 2009. DOI: 10.1109/TPWRS.2008.2004827.

[3] J Van de Vyver, J D M De Kooning, B Meersman, L Vandevelde, and T L Vandoorn. Droop control as an alternative inertial response strategy for the synthetic inertia on wind turbines. *IEEE Transactions on Power Systems*, 2016. DOI: 10.1109/TPWRS.2015.2417758.

[4] P Li, W Hu, R Hu, Q Huang, J Yao, and Z Chen. Strategy for wind power plant contribution to frequency control under variable wind speed. *Renewable Energy*, 2019. DOI: 10.1016/j.renene.2017.12.046.

[5] H Luo, Z Hu, H Zhang, and H Chen. Coordinated active power control strategy for deloaded wind turbines to improve regulation performance in AGC. *IEEE Transactions on Power Systems*, 2019. DOI: 10.1109/TPWRS.2018.2867232.

[6] X Wang, Y Wang, and Y Liu. Dynamic load frequency control for high-penetration wind power considering wind turbine fatigue load. *International Journal of Electrical Power & Energy Systems*, 2020. DOI: 10.1016/j.ijepes.2019.105696.

[7] E A Bossanyi. Wind turbine control for load reduction. *Wind Energy*, 2003. DOI: 10.1002/we.95.

[8] F Pöschke, E Gauterin, M Kühn, J Fortmann, and H Schulte. Load mitigation and power tracking capability for wind turbines using linear matrix inequality-based control design. *Wind Energy*, 2020. DOI: 10.1002/we.2516.

[9] J M Jonkman, S Butterfield, W Musial, and G Scott. Definition of a 5-MW Reference Wind Turbine for Offshore System Development. Technical report, National Renewable Energy Laboratory, 2009.

[10] J M Jonkman and M L Buhl. FAST Users Guide. Technical report, National Renewable Energy Laboratory, 2005.

[11] T Takagi and M Sugeno. Fuzzy identification of systems and its application to modeling and control. *IEEE Transactions on Systems, Man, and Cybernetics*, 1985. DOI: DOI: 10.1109/TSMC.1985.6313399.

[12] M Sugeno and G T Kang. Structure identification of fuzzy models. *Fuzzy Sets and Systems*, 1988. DOI: 10.1016/0165-0114(88)90113-3.

[13] H O Wang, K Tanaka, and M F Griffin. An approach to fuzzy control of nonlinear systems: stability and design issues. *IEEE Transactions on Fuzzy Systems*, 1996. DOI: 10.1109/91.481841.

[14] K Tanaka, T Ikeda, and H Wang. Fuzzy regulators and fuzzy observers: relaxed stability conditions and LMI-based design. *IEEE Transactions on Fuzzy Systems*, 1998. DOI: 10.1109/91.669023.

[15] Z Lendek, T M Guerra, R Babuška, and B De Schutter. *Stability Analysis and Nonlinear Observer Design Using Takagi-Sugeno Fuzzy Models.* Springer-Verlag Berlin Heidelberg, 2010.

[16] K Tanaka and M Sano. A robust stabilization problem of fuzzy control systems and its application to backing up control of a truck-trailer. *IEEE Transactions on Fuzzy Systems*, 1994. DOI: 10.1109/91.277961.

[17] K Tanaka and H O Wang. *Fuzzy Control Systems Design and Analysis: A Linear Matrix Inequality Approach.* John Wiley & Sons, Inc., 2001.

[18] J Machowski, J Bialek, and J Bumby. *Power System Dynamics: Stability and Control.* John Wiley & Sons, Ltd, 2008.

[19] J G VanAntwerp and R D Braatz. A tutorial on linear and bilinear matrix inequalities. *Journal of Process Control*, 2000. DOI: 10.1016/S0959-1524(99)00056-6.

[20] M Chilali and P Gahinet. H_∞ design with pole placement constraints: an LMI approach. *IEEE Transactions on Automatic Control*, 1996. DOI: 10.1109/9.486637.

6 | Synopsis II

6.1 Contextual position of my research

When Katherine Dykes, a Section Head at the Department of Wind Energy of the DTU, was asked in an interview with Siemens Gamesa in March 2020 for her opinion on the scientific challenges that wind energy needs to overcome to realize its full potential, she responded [1]:

"We have got really good at producing wind at a very low cost and we have made it highly competitive compared to conventional energy sources. To take the next step and become the world's foundational energy source, we have to make wind energy even more valuable for electricity systems – making it more predictable, controllable, and available."

Without claiming the presented work is capable of addressing these exciting both practical and scientific challenges as a whole, I want to use the mentioned attributes *controllable*, *available* and *predictable* to locate my research in the current context of wind energy. While all these attributes are research subject for different scientific disciplines [2], the subsequent discussion follows up on the portrayed control perspective in chapter 1.

Controllability In a control-theoretic sense, controllability is a structural property of the system, indicating whether the manipulatable inputs admit for a transition of the system states from any initial value to any other value in finite time [3]. While the TS approach allows for an evaluation of basic system properties like observability or controllability by its local properties [4], from a wind turbine application point of view, this structural analysis is secondary in case of using linearized models. Instead, this criterion refers to a simple thought: enhanced controllability of the wind energy system by increasing the independence from the current wind inflow and eventually making turbines flexible in their power output by following a given demand. The proposed model-based approach is shown to be suitable for enveloping the large operational range that is necessary to enable the power tracking functionality. This introduces an additional degree of freedom in terms of the tracking command Δp related to the change of generated power for the operation of wind turbines, which can be dedicatedly used for different aspects, e.g., grid stabilizing [5], optimized operation of wind farms [6, 7] or preventing animal fatalities from an adjustment of the operational characteristics [8]. In the discussed approach, the trajectory of operation underlying the control design in form of chosen operating points is not unique. This provides the flexibility to assign a desired operational strategy enhancing an efficient adjustment to varying requirements which arise from supplying power to a large-scale dynamically interconnected grid.

To elaborate the flexibility of the control approach, consider the variable and non-unique power track-
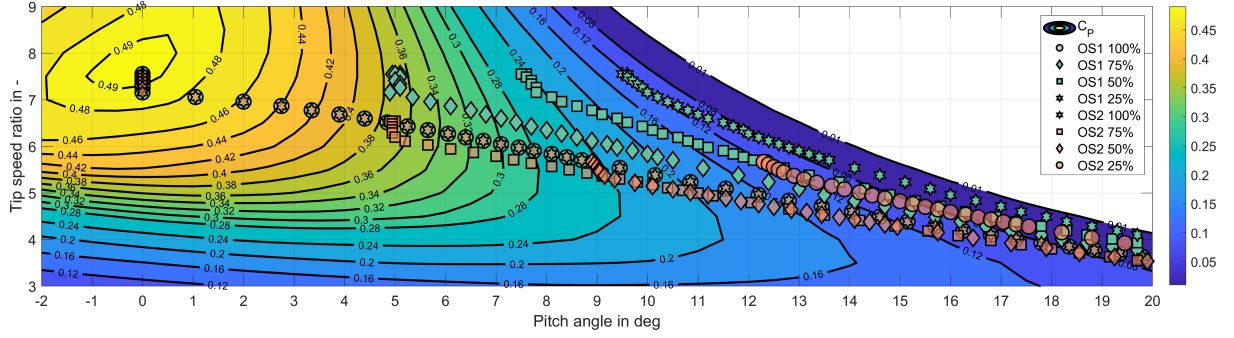
Figure 6.1: Linearization points on the power coefficient surface for the strategies OS1 & OS2.

ing problem of a wind turbine with two distinct strategies. The first operating strategy (OS1) is designed to alter the generator torque T only to provide different levels of desired power p_d (in per unit) and represents the strategy discussed in chapters 3, 4 and 5. The second strategy (OS2) aims at varying both, the generator torque T and rotational speed ω of the turbine in the same proportion to yield the desired power output p_d. Formally, the operating trajectories that form the two strategies can be described as

$$
\text{OS1}: \begin{cases} p(v) = \omega_{\text{opt}}(v) T_{\text{opt}}(v) & \text{if } p_d = 1 \\ p(v) = \omega_{\text{opt}}(v) \underbrace{p_d T_{\text{opt}}(v)}_{=T(v,p_d)} & \text{if } p_d < 1 \end{cases}
$$

$$
\text{OS2}: \begin{cases} p(v) = \omega_{\text{opt}}(v) T_{\text{opt}}(v) & \text{if } p_d = 1 \\ p(v) = \underbrace{\sqrt{p_d}\omega_{\text{opt}}(v)}_{=\omega(v,p_d)} \underbrace{\sqrt{p_d}T_{\text{opt}}(v)}_{=T(v,p_d)} & \text{if } p_d < 1 \text{ and } \sqrt{p_d}\omega_{\text{opt}}(v) \geq \omega_{\min} \\ p(v) = \underbrace{l_\omega(v,p_d)\sqrt{p_d}\omega_{\text{opt}}(v)}_{=\omega(v,p_d)} \underbrace{\frac{\sqrt{p_d}}{l_\omega(v,p_d)}T_{\text{opt}}(v)}_{=T(v,p_d)} & \text{if } p_d < 1 \text{ and } \sqrt{p_d}\omega_{\text{opt}}(v) < \omega_{\min} \end{cases},
$$

(6.1)

where $\omega_{\text{opt}}(v)$ and $T_{\text{opt}}(v)$ denote the optimal steady-state rotational speed and generator torque depending on the wind speed v for maximum power extraction. The operating point depending factor $l_\omega(v,p_d) = \frac{\omega_{\min}}{\sqrt{p_d}\omega_{\text{opt}}(v)}$ is introduced to achieve a limitation of the rotational speed $\omega_{\min}$ to avoid hitting the first tower eigenfrequency with the 3P excitation of the rotation (see the Campbell diagram for the reference turbine in [9]). This formal description serves as a basis for the definition of linearization points. A comparison of these linearization points on the aerodynamic coefficient surface c_P of the 5 MW reference turbine is shown in Fig. 6.1.

The disturbance observer-based control design in the TS framework for OS1 is subject of the previous chapters. For OS2, only the linearization points are altered keeping the rest of the design as discussed. A comparison of the rotational speed, generator torque and generator power of the turbines operating
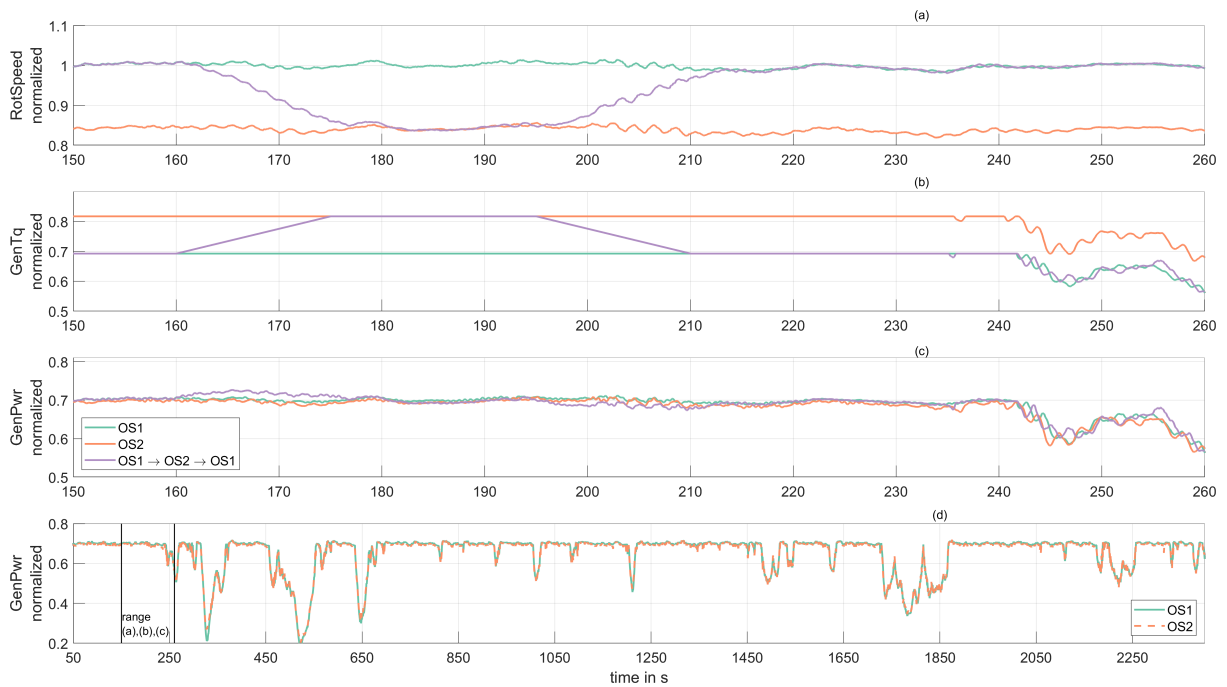
Figure 6.2: Comparison of wind turbine operating trajectories in turbulent wind for OS1 and OS2 at 70% of power production, where additionally a 15 s ramp transition at 160 s from OS1 to OS2 and back at 195 s is shown. (a) Wind turbine rotational speed, (b) generator torque, (c) turbine power output, and (d) 40 min power output time series

at 70% desired power output is shown in Fig. 6.2 (a), (b) and (c), respectively. It can be observed that in OS2 the rotational speed is reduced while in OS1 the nominal rotational speed is kept despite the distance from the optimal power operating point. The power outputs for OS1 and OS2 in Fig. 6.2 (c) show an almost identical trajectory while operated in the same turbulent wind excitation. This is underlined by comparing the 40 min power output time series in Fig. 6.2 (d). The shown trajectories of the power output and variation in the rotational speed are comparable despite operating at different locations on the aerodynamic conversion surface and therefore dynamics of the nonlinear system. This results from the adjustment of the controller and observer feedback gains from the automated model-based design process. The dedicated definition of desired closed-loop dynamics in terms of LMI region constraints plays dominant role in the disturbance rejection properties of the closed-loop wind turbine for both operating strategies.

In Fig. 6.2 (a), (b) and (c), it is shown that the applied controller is capable of blending between the two strategies OS1 & OS2. This transition is initiated at 160 s with a slope corresponding to a 15 s transition time. This command is reversed at 195 s. The trajectories show a smooth transition between the two operating strategies, where the energy released or stored in the rotation due to the variation of the rotational speed can be seen in the power output of the turbine in Fig. 6.2 (c). The possibility to vary the strategy in operation of the turbine provides flexibility to adjust to different external

conditions. The transition functionality is accomplished by integrating an additional externally manipulated premise variable in the TS description that defines the desired operating strategy. Using this framework, the additional operational strategy is provided only by extending the linearization points used for construction of the TS model.

The possibility of integrating additional feedback loops that purposefully alter the dynamic response of certain components illustrate the potential for load mitigation from the application of modern multivariate control approaches as discussed in chapter 3. The integration of additional feedback loops connecting a sensor to an actuator has no effect on the basic control approach: deriving a model of the considered dynamics, integrating it into the TS framework, designing suitable feedback based on the LMI performance constraints, and finally introducing it into the overall closed-loop model description for stability analysis before application to the turbine. Except for the definition of design parameters for the additional actuation and connecting the corresponding sensor to the control scheme, the implementation of the control approach remains unchanged, making it highly adjustable compared to the interconnection of various independently designed and implemented conventional single-input, single-output control loops. Additionally to the flexibility of the design process, this allows for convenient maintenance of the implemented controller code. These considerations indicate the benefits of model-based approaches for efficient development processes.

Finally, the experimental validation of the control scheme shows the robustness of the approach subject to the physically induced uncertainties that even aero-elastic simulators possibly can not depict sufficiently well [10], nor are they easily introduced into control design models. This comprises physical uncertainties originating from, e.g., the aerodynamics, or other unmodeled dynamic loops e.g., the generator torque control underlying the command of the TS controller. Despite these uncertainties, it has been demonstrated that an adequate control performance can be achieved by definition of suitable design specifications. Due to the LMI-based region constraints when used in combination with linearized submodels, the physical interpretability of the design parameters guides the design and can incorporate specific engineering knowledge from other disciplines, e.g., by definition of the desired damping ratio for the tower motion referring to the modeled eigenmode. Opposed to the sometimes formulated concerns regarding robustness of "modern" approaches [11], this thesis highlights that model-based schemes provide a suitable approach for complex control engineering tasks found in wind energy conversion systems at an efficient – both in terms of engineering and computational – control design and thereby can increase controllability in a functional sense.

Availability Possible mitigation of experienced loading by the turbine due to active control is directly coupled to a possible reduction of material expenses [12]. This, among others, determines the overall cost of energy production. Advances led to a steadily decreasing cost of energy for wind power

[13], making wind power an economically attractive option with zero-cost fuel available around the globe. A dedicated control design with load reduction as an explicit objective while respecting the projected loading over lifetime, can help to reduce unplanned maintenance resulting from the loading history experienced by the turbine. This already led to availability levels of above 98 % [12]. Especially for turbines located offshore, failures must be avoided due to the high costs associated with maintenance and to meet the expected annual energy production relevant for the economic returns. As a consequence, for load reduction of increasingly complex dynamical systems, elaborate solutions for tackling the control design task are demanded.

The closed-loop models that result from model-based approaches can be incorporated in condition monitoring systems, where the quality of the model description determines the effectiveness of the approach [14]. In Fig. 6.3 a comparison of a TS wind turbine model to the aero-elastic simulator FAST is shown. Both models are controlled by the disturbance observer-based approach described within this work and excited equally in both power demand and wind speed. Despite being completely decoupled in this comparison, i.e., no feedback loops are incorporated to form an observer, the TS model shows a good approximation of the state trajectories in operation. To increase robustness against model uncertainties and disturbances in a practical implementation, an observer scheme involving a dedicated feedback term as discussed within the thesis would be favorable. From the evolution of the model states, estimates of the experienced loading can be attained supporting the application of condition monitoring systems. A dedicated condition monitoring system supports an effective minimization of the downtime and efforts for the complex logistics involved in the operation of the wind power plants, especially offshore [12].

An additional perspective on possible wear induced effects as actuator faults or sensor drifts is taken by fault-tolerant concepts, where fault detection, isolation, and estimation rely on, possibly closed-loop, models of the considered dynamics. In [15, 16], for example, a sliding-mode observer approach in a TS structure is discussed for the estimation of faults for a wind turbine benchmark. Those and similar techniques are the foundation for an appropriate reaction of the overall control system by compensating for occurring faults and maintaining the operation [17]. By safely operating the turbine despite an identified error, these approaches may yield a further increase in the availability of the individual wind turbine, and may directly incorporate the models resulting from the control design, if not being an integral part of the process itself.

A dedicated treatment of frequency variations by an active power adjustment of the turbine can support the electrical grid, instead of disconnecting in case of e.g., overfrequency [18]. Effectively, this increases the availability of the turbine as time lost from idling and resynchronization with the electrical grid due to a frequency event is avoided [19]. Thus, control schemes capable of integrating the extended power operating range result in a continuous operation of wind turbines even in the event
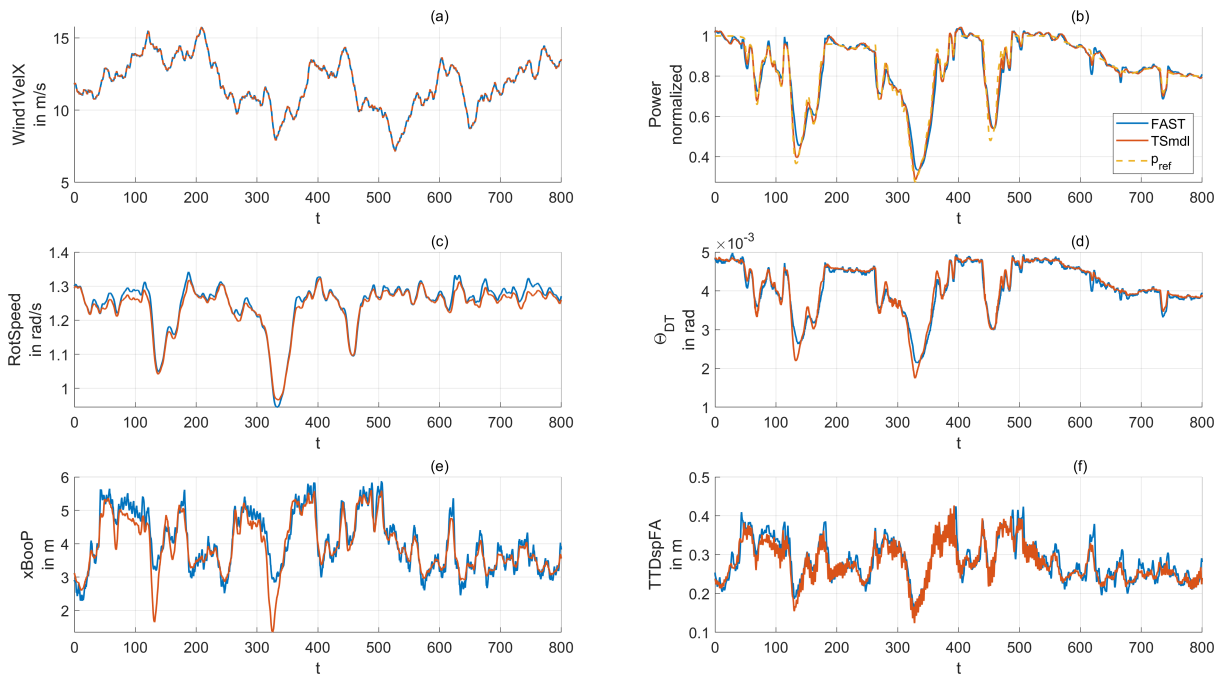
Figure 6.3: Comparison of a TS wind turbine model to the aero-elastic simulator FAST at identical excitation. (a) Wind speed, (b) turbine power and reference, (c) rotor speed, (d) drivetrain torsion, (e) tower-top side-to-side deflection and (f) tower-top fore-aft deflection.

of more severe load imbalances. Additionally, by the possibility to operate the turbine at a large range of operating scenarios, wind energy systems have shown to be capable of black starting an electrical grid [19]. This provides the basis for an islanded operation of a subset of the electrical grid, and a possible reconnection to neighboring power systems after a power system outage. As discussed in [19], this functionality is, among others, limited by the missing authority in conventional control systems to provide varying amounts of active and reactive power. Thus, additionally to the importance of building islanded electrical grids with wind turbines, the availability of the turbines increases when powering a local grid in case of disconnection from the higher-level transmission system instead of terminating its operation.

Predictability An estimate for the future electricity generation from wind power is essential for the reliable and economically feasible operation of the electricity system with high shares of renewables [20], and therefore forecasting and prediction of the wind resource is an important field of study. In [12], the authors note the possible improvement of forecasting from local measurements of the wind resource at the turbine level. The proposed concept within this thesis relies on a wind speed observer and provides this information naturally by relating the structural excitation to the current wind speed using the turbine model without the need for additional sensing devices. Thus, the possibility of improving forecasting is inherently given, provided a wide-spread application of control schemes yielding

an estimate of the current inflow at the turbine.

Instead of disconnecting from the electrical grid in case of e.g., overfrequencies and thereby possibly aggravating the existing problem [18], wind turbines must be equipped with decentralized control schemes that continuously adjust the current power output as a reaction to the state of the electrical grid. For transmission system operators, predictable participation of renewables in grid stabilization is vital for assessing the overall stability measures for the resilience of the electrical grid to disturbances [21]. Conventionally, stabilization was conducted by few, very large power plants, and thus relatively few models are needed for assessment of stability measures. However, due to the decentralized structure of power supply by renewables, many smaller, dynamically interacting units must be portrayed for grasping the relevant dynamical properties. Model-based approaches inherently result in a closed-loop model description of the system dynamics after the control synthesis with low computational complexity in terms of differential equations as shown in Fig. 6.3. This allows for an introduction of the relevant dynamics that determine the grid stabilizing response into large-scale complex simulations that aim for identifying the resilience of the electrical grid to disturbances [22].

For example, consider the structure shown in Fig. 6.4, where a TS wind turbine model is sequentially connected to a generator model, a converter and a voltage source. As the converter decouples the synchronous generator completely from the voltage source, it is modeled as a first-order transfer function [23]. The converter consists of the DC link dynamics depending on the power balance of generated power by the wind turbine and the power injected to the voltage source. The power injection is determined by the output impedance model connecting the voltage source to the terminal voltage of the converter. The terminal voltage is governed by cascaded power and current control loops that are implemented in a rotating reference frame. To synchronize the reference frame with the rotating voltage source, a phase-locked loop can be implemented yielding an estimate of the grid frequency ω_{PLL} and phase angle. Within the setup, the estimated frequency is used to determine the power tracking command for the TS observer-based control scheme designed to enable the discussed operating strategies OS1 & OS2 given in (6.1). The wind turbine is represented by a TS model obtained for control design purposes and captures the dynamics of the tower fore-aft motion, tower side-to-side motion, blade out-of-plane deflection, and drivetrain torsion in nine states at 1200 different operating points distributed along the operating range of interest.

A comparison of the resulting state trajectories for both operating strategies OS1 & OS2 discussed above is given in Fig. 6.5, where at time 35 s and 45 s the frequency of the voltage source is varied by -0.1 Hz and +0.1 Hz, respectively. It is shown that the choice of the operating strategy influences the state trajectories of the wind turbine following a grid event significantly. Especially the turbine's inertia plays a dominant role when adjusting the produced power in OS2, while the adjustment of the generator torque due to its small timeconstant of 20 ms follows the droop-based command precisely in
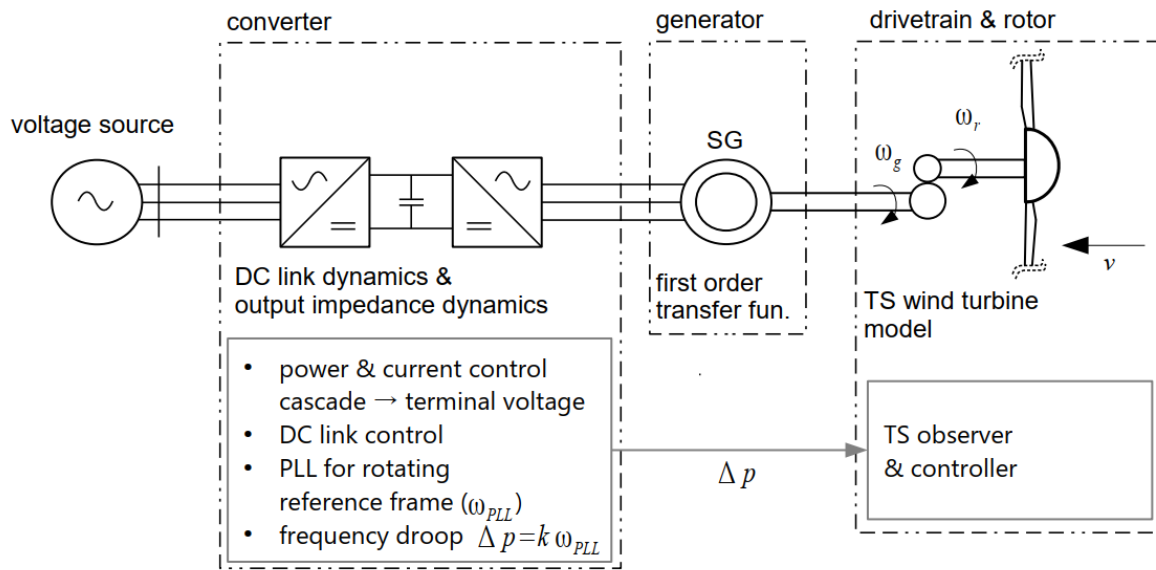
Figure 6.4: Overview of simulation environment for testing of operating strategies OS1 & OS2 to changes in the grid frequency.

both operating strategies. The pitch speed that balances the aerodynamical torque of the rotor remains within reasonable bounds when tracking the droop-based power commands as shown in Fig. 6.4 (e). While relevant dynamical properties like inertia-based effects and control interaction are captured well in the considered wind turbine model, Fig. 6.5 (c) illustrates the limitations. During the variation of active power, there is only small excitation of the turbine's rotational speed as the feedforward term simultaneously varies the generator torque and pitch angle, and thus almost perfectly compensates for the variation of the operating point of the design model. In reality, unmodeled uncertainties and coupling among the different wind turbine components would impede such a perfect transistions among different operating points.

A greater number of degrees of freedom in the control design portrays more interactions of different components and actuators in the design stage. The increasing flexible structures from, e.g., torsion and bend-twist coupling of the blades have effects for stability [2], while moving to offshore locations is further characterized by the need for an integrated analysis including aerodynamics, hydrodynamics and support structures [24]. The stability considerations underlying the control design can be considered as a prediction whether destabilizing couplings due to actuation are identified in the closed-loop model, whereas conventional control approaches rely on simulation studies and possible decoupling by the design of additional filters that process the measurements before deployment to the controller. Therefore, a scalable and computationally efficient algorithm is key for an adaption to the varying relevant dynamics and requirements underlying the complex wind turbine control design task.
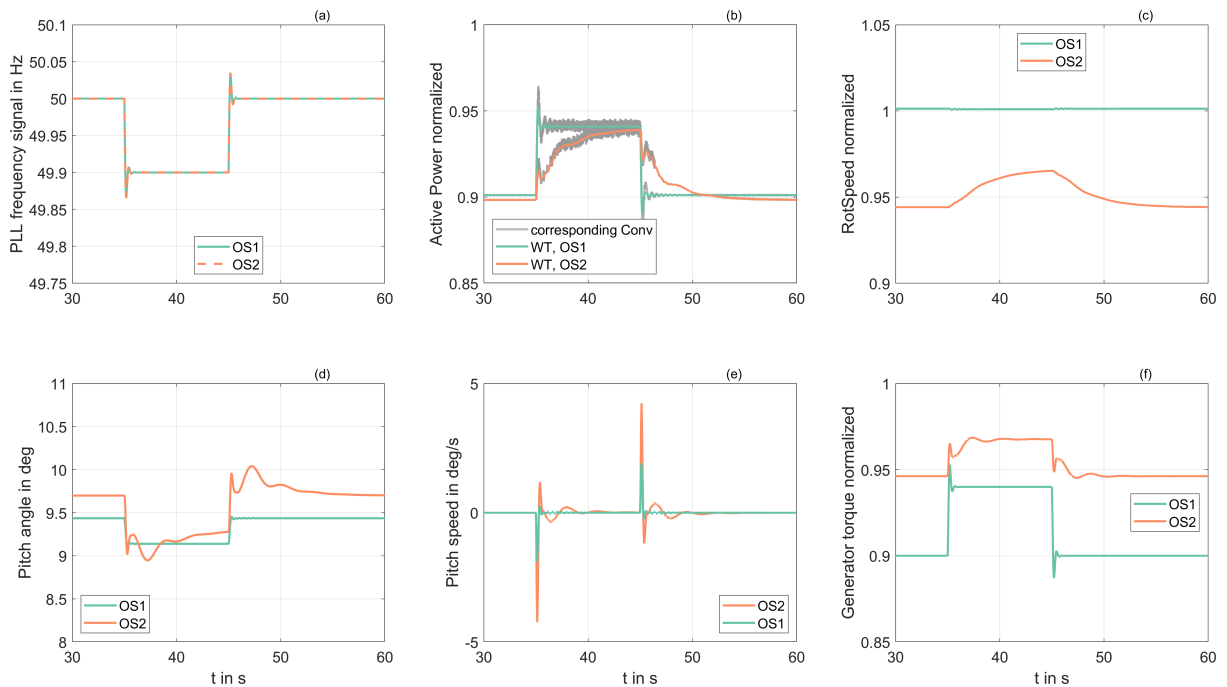
Figure 6.5: Comparison of the TS wind turbine model and FAST. (a) estimated frequency of the phase-locked loop (PLL), (b) active power (c) rotor speed, (d) pitch angle, (e) pitch speed and (f) generator torque.

6.2 Conclusion

The contributions of the thesis are summarized as follows:

- Control and observer design for wind turbine systems in the TS framework (chapter 2)

- Introduction of LMI region constraints in the wind turbine context for a dedicated treatment of operational dynamics and thus loads (chapter 2)

- Integration of a widely extended operational range to support flexible power production for grid stabilization (chapter 3)

- Loading analysis of the wind turbine structure when performing power tracking (chapter 3)

- New conditions for stability of nonlinear TS systems using assumptions on the estimation error (chapter 4)

- Experimental validation of the control scheme (chapter 4)

- Formulation of filter design constraints in terms of TS-based LMI feedback control (chapter 5)

Within the introduction to this thesis, it is discussed that wind energy systems have evolved astonishingly to the largest rotating machines ever build, and are expected to form the backbone of our hopefully near-future energy system. As pointed out in [2], further advancements rely on the expertise of many different disciplines that need to be combined effectively. The stochastic wind is the fuel of the energy conversion process. However, as discussed in the previously presented works, from a control perspective it is also the main disturbance of the system that needs to be rejected appropriately. For this reason, the integration of prediction, based on knowledge about properties of the upcoming wind field like mean wind speed, into the control scheme provides an interesting approach to extend the proposed concept, in cases where an advanced inflow sensing device is exploitable. As argued in [25], this may result in a further reduction of especially the ultimate loading experienced by the turbine. Fatigue loading, however, is greatly determined by the interaction of the closed-loop dynamics with the highly stochastic three-dimensional inflow. Research in the field of physics revealed that the stochastic wind, powering the energy conversion process, exhibits highly intermittent dynamics [26]. Thus, the common assumption concerning Gaussianity underlying a wide range of control approaches, e.g., the combination of a Kalman filter with an LQ controller yielding optimal performance for gaussian disturbances acting on the system [27], do not hold for the disturbances involved in wind turbine control. Further, these properties change depending on the atmospheric conditions, weather, and location of the turbine [26, 12, 2]. Thus, a significant further reduction of fatigue loading by respecting the stochastic properties of the system disturbance by adjusting the controller gains can only be answered using a model-based scheme that is capable of incorporating the relevant turbine *and* wind dynamics. As noted in [2], this interaction is bidirectional as a wind turbine also influences the flow, and thus possibly affects the inflow of nearby located turbines. These considerations underline the need for an integrated approach spanning across several scientific disciplines by combining control engineering with a physical perspective on modeling the stochastic nature of the disturbance.

Research, like presented in [19] that covers grid forming by wind power without conventional sources or the study in [5] comprising up to 80 % of grid penetration by wind power, show that a future electricity generation supplied by renewables only can be feasible. To achieve this, instead of a few central actors that form, supply, and stabilize the grid, many interacting decentralized units need to be enhanced in participating both locally and by exchanging additional information, which is the concept broadly referred to as smart grids [28]. This exciting transformation involves numerous control tasks that need to be addressed efficiently, where communication and distributed intelligence are vital in forming a reliable and stable power system [22]. In both, nature and man-made organisms, it can be observed that well-scaled decentralized structures interacting as a network are a vital aspect for the resilience and stability of systems in general, and enhance an evolutionary optimization process rather than impeding it [29].

The works that form the foundation of this thesis, and the various references therein illustrate the enhancements achieved by the application of modern model-based control approaches to wind energy systems specifically, and to the complex questions that arise from the energy consumption in our life in a broader sense. The employed descriptions of the dynamics have a common ground anchored in the general field of systems theory, which is shared by various disciplines including natural and social sciences that work on understanding and shaping the world we live in [30]. Mankind produced tremendous technological advances that are fascinating in itself and underline the usefulness of the employed models. The regular reports of e.g., the intergovernmental panel on climate change [31], which are substantially based on those common principles, at the same time urge us for a fast transition of the energy sector towards a generation by renewables along with profound consumption patterns that provide the chance to build a sustainable future.

References

[1] F Tømmergaard. Interview with Katherine Dykes, March 2020. `https://www.siemensgamesa.com/en-int/explore/journal/2020/03/siemens-gamesa-katherine-dykes-article` (02.11.2020).

[2] P Veers, K Dykes, E Lantz, S Barth, C L Bottasso, O Carlson, A Clifton, J Green, P Green, H Holttinen, Dl Laird, V Lehtomäki, J K Lundquist, J Manwell, M Marquis, C Meneveau, P Moriarty, X Munduate, M Muskulus, J Naughton, L Pao, J Paquette, J Peinke, A Robertson, J Sanz Rodrigo, A M Sempreviva, J C Smith, A Tuohy, and R Wiser. Grand challenges in the science of wind energy. *Science*, 2019. DOI: 10.1126/science.aau2027.

[3] C-T Chen. *Linear System Theory and Design*. Oxford University Press, 1999.

[4] Z Lendek, T M Guerra, R Babuska, and B De Schutter. *Stability Analysis and Nonlinear Observer Design Using Takagi-Sugeno Fuzzy Models*. Springer-Verlag Berlin Heidelberg, 2010.

[5] V Gevorgian, Y Zhang, and E Ela. Investigating the impacts of wind generation participation in interconnection frequency response. *IEEE Transactions on Sustainable Energy*, 2015. DOI: 10.1109/TSTE.2014.2343836.

[6] W Munters and J Meyers. Towards practical dynamic induction control of wind farms: analysis of optimally controlled wind-farm boundary layers and sinusoidal induction control of first-row turbines. *Wind Energy Science*, 2018. DOI: 10.5194/wes-3-409-2018.

[7] M Vali, V Petrović, G Steinfeld, L Y Pao, and M Kühn. An active power control approach for wake-induced load alleviation in a fully developed wind farm boundary layer. *Wind Energy Science*, 2019. DOI: 10.5194/wes-4-139-2019.

[8] E F Baerwald, J Edworthy, M Holder, and R M R Barclay. A large-scale mitigation experiment to reduce bat fatalities at wind energy facilities. *The Journal of Wildlife Management*, 2009. DOI: 10.2193/2008-233.

[9] J M Jonkman and B J Jonkman. FAST modularization framework for wind turbine simulation: full-system linearization. *Journal of Physics: Conference Series*, 2016. DOI: 10.1088/1742-6596/753/8/082010.

[10] V Petrović, F Berger, L Neuhaus, M Hölling, and M Kühn. Wind tunnel setup for experimental validation of wind turbine control concepts under tailor-made reproducible wind conditions. *Journal of Physics: Conference Series*, 2019. DOI: 10.1088/1742-6596/1222/1/012013.

[11] E A Bossanyi. Wind turbine control for load reduction. *Wind Energy*, 2003. DOI: 10.1002/we.95.

[12] G A M van Kuik, J Peinke, R Nijssen, D Lekou, J Mann, J N Sørensen, C Ferreira, J W van Wingerden, D Schlipf, P Gebraad, H Polinder, A Abrahamsen, G J W van Bussel, J D Sørensen, P Tavner, C L Bottasso, M Muskulus, D Matha, H J Lindeboom, S Degraer, O Kramer, S Lehnhoff, M Sonnenschein, P E Sørensen, R W Künneke, P E Morthorst, and K Skytte. Long-term research challenges in wind energy – a research agenda by the European Academy of Wind Energy. *Wind Energy Science*, 2016. DOI: 10.5194/wes-1-1-2016.

[13] C Kost, S Shammugam, V Jülch, H-T Nguyen, and T Schlegl. Levelized Cost of Eectricity Renewable Energy Technologies. Technical report, Fraunhofer Institute for Solar Energy Systems ISE, 2018.

[14] H E Sánchez Sardi. *Prognostics and Health Aware Model Predictive Control of Wind Turbines*. PhD thesis, Universitat Politècnica de Catalunya, 2017.

[15] F Pöschke, S Georg, and H Schulte. Fault reconstruction using a Takagi-Sugeno sliding mode observer for the wind turbine benchmark. In *2014 UKACC International Conference on Control (CONTROL)*, 2014. DOI: 10.1109/CONTROL.2014.6915183.

[16] H Schulte and F Pöschke. *Variable-Structure Approaches*, chapter Sliding Mode Observer for Fault Diagnosis: LPV and Takagi–Sugeno Model Approaches, pages 213–240. Springer International Publishing, 2016.

[17] P F Odgaard and J Stoustrup. A benchmark evaluation of fault tolerant wind turbine control concepts. *IEEE Transactions on Control Systems Technology*, 2015. DOI: 10.1109/TCST.2014.2361291.

[18] K Das, M Altin, A D Hansen, P E Sørensen, D Flynn, and H Abildgaard. Wind power support during overfrequency emergency events. *CIGRE Science & Engineering*, 9:73–83, 2018.

[19] M Shan, W Shan, F Welck, and D Duckwitz. Design and laboratory test of black-start control mode for wind turbines. *Wind Energy*, 2020. DOI: 10.1002/we.2457.

[20] K D Orwig, M L Ahlstrom, V Banunarayanan, J Sharp, J M Wilczak, J Freedman, S E Haupt, J Cline, O Bartholomy, H F Hamann, B Hodge, C Finley, D Nakafuji, J L Peterson, D Maggio, and M Marquis. Recent trends in variable generation forecasting and its value to the power system. *IEEE Transactions on Sustainable Energy*, 2015. DOI: 10.1109/TSTE.2014.2366118.

[21] J Machowski, J W Bialek, and J Bumby. *Power System Dynamics: Stability and Control.* Wiley, 2011.

[22] J Nutaro, P Teja Kuruganti, M Shankar, L Miller, and S Mullen. Integrated modeling of the electric grid, communications, and control. *International Journal of Energy Sector Management*, 2008. DOI: 10.1108/17506220810892955.

[23] P F Odgaard, J Stoustrup, and M Kinnaert. Fault tolerant control of wind turbines – a benchmark model. *IFAC Proceedings Volumes*, 2009. DOI: 10.3182/20090630-4-ES-2003.00026.

[24] J M Jonkman. Dynamics of offshore floating wind turbines—model development and verification. *Wind Energy*, 2009. DOI: 10.1002/we.347.

[25] A Koerber and R King. Combined feedback–feedforward control of wind turbines using state-constrained model predictive control. *IEEE Transactions on Control Systems Technology*, 2013. DOI: 10.1109/TCST.2013.2260749.

[26] M Wächter, H Heißelmann, M Hölling, A Morales, P Milan, T Mücke, J Peinke, N Reinke, and P Rinn. The turbulent nature of the atmospheric boundary layer and its impact on the wind energy conversion process. *Journal of Turbulence*, 2012. DOI: 10.1080/14685248.2012.696118.

[27] B Friedland. *Control System Design – An Introduction to State-Space Methods.* Dover Publications, Inc., 1986.

[28] X Fang, S Misra, G Xue, and D Yang. Smart grid — the new and improved power grid: a survey. *IEEE Communications Surveys Tutorials*, 2012. DOI: 10.1109/SURV.2011.101911.00087.

[29] G West. *Scale – The Universal Laws of Life, Growth, and Death in Organisms, Cities, and Companies.* Penguin Books, 2017.

[30] L von Bertalanffy. *General System Theory – Foundations, Developement, Applications.* George Braziller, Inc., 1969.

[31] The Intergovernmental Panel on Climate Change. Climate Change 2014: Impacts, Adaptation, and Vulnerability. Part A: Global and Sectoral Aspects. Contribution of Working Group II to the Fifth Assessment Report of the Intergovernmental Panel on Climate Change. Cambridge UniversityPress, Cambridge, United Kingdom and New York, NY, USA, 2014.